

# Reduced-order Models for Simulating Coupled Geometric Instabilities in Steel Beam-columns Under Inelastic Cyclic Straining

Présentée le 30 mars 2021

Faculté de l'environnement naturel, architectural et construit  
Laboratoire des structures métalliques résilientes  
Programme doctoral en génie civil et environnement

pour l'obtention du grade de Docteur ès Sciences

par

**Alexander Riley HARTLOPER**

Acceptée sur proposition du jury

Prof. N. Geroliminis, président du jury  
Prof. D. Lignos, Dr A. de Castro e Sousa, directeurs de thèse  
Prof. A. Elghazouli, rapporteur  
Prof. O.-S. Kwon, rapporteur  
Prof. J.-F. Molinari, rapporteur





To engineers who,  
rather than blindly following  
the codes of practice,  
seek to apply the laws of nature.  
— T.Y. Lin, 1995



## Acknowledgements

I would first like to acknowledge the support of my supervisors, Dimitrios and Albano, for their glorious guidance, energy, and for sharing their expertise with me throughout this journey. The countless discussions we have had over the past four years have had an unquestionable influence on the quality of this work and my growth as a researcher. Thank you. I would also like to thank all the members of my jury for their commitment to reviewing my thesis as well as their insightful comments.

Next, I would like to thank EPFL and the Swiss National Science Foundation (Project No. 200021\_18847) for their support of my research. As well, thanks to the staff of ENAC and the team at GIS-GE for their assistance with experimental activities, particularly Gilles and G  rald. A particular thanks to the staff of RESSLab, Karin and Luisa, who helped with many administrative matters over the years. Thanks to all the members of RESSLab for friendly lunch gatherings, discussions, secret santa, ski trips, and lab parties. Shout-out to my office mate, Hammad, as well as Hiro, Andy, and ex-RESSLab-er/McGill-ian Ahmed. I could not have imagined a better environment for conducting research than I found here at the RESSLab.

Thank you to my friends and family in Vancouver, Calgary, Winnipeg, Montr  al, and elsewhere. It was a pleasure to visit you in these places and it was always a joy to host visitors in Switzerland. Lastly, thank you Anna for being the best person I know—I love you. I certainly could not have completed my thesis without your interventions, love, and support. I will fondly remember the long hours spent socializing in Switzerland and our ability to capitalize on the various natural wonders here. Here's to our next adventure!

*Lausanne, March 2021*

A. H.



## Abstract

Numerical models that can simulate coupled geometric instabilities in steel beam-columns are required for the seismic assessment of certain steel moment-resisting frames. Reliably simulating coupled instabilities requires that the steel material is precisely characterized under inelastic cyclic straining. Full continuum finite element (CFE) models can be used in this context, however, reduced order models are preferred for building-level simulations because of their lower computational cost. Concentrated plasticity models are a typical reduced order approach, although findings from recent full-scale experiments conducted on steel beam-columns have highlighted their limitations in simulating component behavior.

The aim of this thesis is to propose accurate reduced-order simulation models for steel beam-column components to simulate coupled buckling at a diminished computational expense compared to full CFE approaches. This goal is achieved by using component macro models that couple CFEs in critical regions with beam-column elements elsewhere. The specific objectives related to the aim of this thesis are to: (i) advance the state-of-the-art in constitutive modeling for structural steels subjected to earthquake-induced inelastic straining; (ii) develop an efficient method of coupling beam-column and CFE domains that incorporates torsion-warping; and (iii) develop general recommendations for modeling wide flange beam-column components subjected to inelastic cyclic straining using the macro model.

This thesis developed a constitutive model for mild structural steels to improve upon the initial yield behavior of a classic metal plasticity model by accounting for the discontinuous yielding phenomenon. Constitutive model calibration methodologies were developed using constrained optimization for the cases when the material's cyclic behavior is known and when it is unknown. Simulated geometric instabilities were shown to be sensitive to the constitutive model's input parameters in steel beam-columns of particular geometries subjected to multiaxis loading. Coupling methods that included torsion-warping were developed using multipoint constraint equations. Findings indicate that including torsion-warping in the coupling formulation is critical for steel beam-columns that are susceptible to coupled local and lateral-torsional instabilities. The proposed macro model is efficient for the investigated range of steel beam-columns: it reduces computational cost metrics in benchmark CFE analyses by around 50 %. It is also accurate, as the average error between benchmark CFE and macro model analyses is only 3 %.

The advances in material modeling made by this thesis can be used to reduce the uncertainty in steel component simulations. This enables analysts to better comprehend component behavior through simulations and improves simulation-assisted design. Component models that explicitly simulate geometric instabilities and material inelastic behavior at lower computational costs are important in probabilistic assessments and uncertainty quantification. They may be especially useful, for example, in benchmarking concentrated plasticity models and in the process of developing new structural systems.

**Keywords:** reduced-order models, earthquake loading, steel structures, beam-columns, geometric instabilities, multiaxial plasticity, inverse problem, multipoint constraint equations, torsion-warping.



## Résumé

Les modèles numériques qui permettent de simuler les instabilités géométriques couplées dans les poutres-poteaux en acier sont indispensables pour l'évaluation sismique de certaines structures à charpentes métalliques. Afin de simuler les instabilités couplées de manière fiable, il faut caractériser précisément le matériau en acier sous déformation cyclique inélastique. Les modèles d'éléments finis continus (« Continuum Finite Element » ou CFE) peuvent être utilisés pour accomplir ces tâches, cependant, leur coût computationnel dans le contexte des évaluations probabilistes encourage l'utilisation d'approches de modélisation d'ordre réduit. Les modèles de plasticité concentrés sont généralement préférés aux modèles CFE pour cette raison, cependant, les résultats de récentes expériences en échelle réelle menées sur des poutres-poteaux en acier ont fait ressortir leurs limites dans la simulation des comportements des composants.

Le but de cette thèse est de proposer des modèles de simulation d'ordre réduit précis pour les composants poutres-poteaux en acier qui simule les instabilités géométriques couplées à un coût computationnel réduit par rapport aux approches CFE complètes. Ce but est atteint en utilisant des modèles-macro de composants qui couplent des CFE dans des régions critiques avec des éléments de type poutre-poteau situés ailleurs. Les objectifs précis liés au but de cette thèse sont les suivants : (i) faire évoluer l'état des connaissances en ce qui concerne la modélisation constitutive des aciers de charpentes soumis à une déformation inélastique résultant d'un séisme ; (ii) développer une méthode efficace qui permet le couplage des domaines d'éléments de poutre-colonne et des domaines de CFE qui intègre le gauchissement par torsion ; et (iii) rédiger des recommandations générales pour la modélisation des composants poutre-poteau à ailes larges soumis à une déformation cyclique inélastique en utilisant le modèle-macro.

Cette thèse a développé un modèle constitutif pour les aciers de construction afin d'améliorer le comportement du rendement initial d'un modèle classique de plasticité du métal grâce à la prise en compte du phénomène d'écoulement plastique discontinu. Les méthodes de calibration des modèles constitutifs ont été développées en utilisant l'optimisation sous contraintes pour les cas où le comportement cyclique du matériau est directement connu et pour ceux où il est inconnu. Les instabilités géométriques simulées se sont prouvées sensibles aux paramètres de saisie du modèle constitutif dans les poutres-poteaux en acier de géométries particulières sous une charge multiaxiale. Des méthodes de couplage incluant le gauchissement par torsion ont été développées à l'aide d'équations de contraintes multipoints. Les résultats montrent que l'inclusion de la torsion non-uniforme dans la formulation de l'accouplement est essentielle pour les poutres-poteaux en acier qui sont susceptibles de subir des instabilités de voilement et de déversement. Le modèle-macro proposé est efficace pour la gamme de poutres-poteaux en acier examinée : il réduit d'environ 50 % les coûts computationnels des analyses de référence CFE. Il est également précis, car l'erreur moyenne entre les analyses de référence CFE et le modèle-macro n'est que de 3 %.

Les innovations réalisées par cette thèse dans le domaine de la modélisation des matériaux peuvent être utilisées pour réduire l'incertitude dans les simulations de composants en acier. Cela permettra aux analystes de mieux comprendre le comportement des composants grâce à des simulations et à l'amélioration de la conception assistée par simulation. Les modèles de composants qui simulent clairement les instabilités géométriques et le comportement inélastique des matériaux à des coûts informatiques réduits sont importants pour réaliser des

## Résumé

---

évaluations probabilistes et pour quantifier les incertitudes. Ils peuvent être particulièrement utiles, par exemple, dans l'évaluation des modèles d'ordre réduit et dans le développement de nouveaux systèmes structurels.

**Mots clés** : modèles d'ordre réduit, charges sismiques, structure en acier, instabilités géométriques, plasticité multiaxiale, problèmes inverses, équations définissant les contraintes multipoints, gauchissement par torsion, poutres-poteaux.



# Contents

<b>Acknowledgements</b>	<b>i</b>
<b>Abstract (English/Français)</b>	<b>iii</b>
<b>List of figures</b>	<b>xi</b>
<b>List of tables</b>	<b>xvii</b>
<b>1 Introduction</b>	<b>1</b>
1.1 Nonlinear structural analysis in earthquake engineering . . . . .	1
1.2 Modeling steel components subjected to earthquake loads . . . . .	3
1.3 Modeling structural steels subjected to earthquake-induced inelastic cyclic straining . . . . .	4
1.4 Aim and organization of the thesis . . . . .	5
<b>I Structural steel material model</b>	<b>9</b>
<b>2 Constitutive modeling of structural steels: A nonlinear isotropic/kinematic hard-     ening material model and its calibration</b>	<b>11</b>
2.1 Introduction . . . . .	12
2.2 Limitation of the Voce-Chaboche model for mild steels . . . . .	14
2.3 Proposed material model . . . . .	16
2.4 Calibration of material model parameters . . . . .	27
2.5 Finite element analysis case study and implications . . . . .	36
2.6 Discussion of results, limitations, and future work . . . . .	41
2.7 Conclusions . . . . .	43
2.8 Data availability . . . . .	44
2.9 Acknowledgements . . . . .	45
2.10 Notation . . . . .	45
<b>3 Cyclic metal plasticity model parameters with limited information: A constrained     optimization approach</b>	<b>47</b>

## Contents

---

3.1	Introduction . . . . .	48
3.2	Methodology . . . . .	51
3.3	Results . . . . .	61
3.4	Discussion . . . . .	65
3.5	Conclusions . . . . .	76
3.6	Data availability . . . . .	77
3.7	Acknowledgments . . . . .	77
3.8	Notation . . . . .	77
 <b>II Macro model</b>		<b>79</b>
 <b>4 Warping-inclusive kinematic coupling in mixed-dimension macro models for steel wide flange beam-columns</b>		<b>81</b>
4.1	Introduction . . . . .	82
4.2	Proposed coupling method . . . . .	85
4.3	Case studies . . . . .	91
4.4	Case study results . . . . .	102
4.5	Discussion of results . . . . .	112
4.6	Conclusions . . . . .	114
4.7	Data availability . . . . .	115
4.8	Acknowledgements . . . . .	116
4.9	Notation . . . . .	116
 <b>5 Best-fit constraint equations for coupling mixed-dimension simulation models with wide flange cross sections</b>		<b>119</b>
5.1	Introduction . . . . .	120
5.2	Development of the multipoint constraint equations . . . . .	122
5.3	Application of the best-fit constraint equations for nonlinear finite element analysis . . . . .	130
5.4	Summary of the best-fit coupling method . . . . .	137
5.5	Evaluation of the best-fit coupling method . . . . .	138
5.6	Discussion and limitations . . . . .	142
5.7	Summary and conclusions . . . . .	145
5.8	Data availability . . . . .	146
5.9	Acknowledgements . . . . .	146
5.10	Notation . . . . .	146
5.11	Algorithms . . . . .	147
5.12	Linearized constraint equations . . . . .	151

<b>6 Mixed-dimension modeling of steel wide flange beam-columns under multiaxis loading</b>	<b>155</b>
6.1 Introduction . . . . .	156
6.2 Methodology . . . . .	159
6.3 Results . . . . .	170
6.4 Discussion . . . . .	183
6.5 Summary and conclusions . . . . .	192
6.6 Data availability . . . . .	193
6.7 Acknowledgements . . . . .	193
6.8 Notation . . . . .	194
 <b>III Conclusions and backmatter</b>	 <b>197</b>
<b>7 Conclusion and future work</b>	<b>199</b>
7.1 Summary of work completed in this thesis . . . . .	199
7.2 Impact and future research topics . . . . .	204
 <b>Bibliography</b>	 <b>209</b>
<b>Curriculum vitae</b>	<b>225</b>



## List of figures

1.1	Structural components in a steel moment-resisting frame subjected to earthquake loading and their finite element representations. Photos in 1.1a and data in 1.1b from Elkady and Lignos (2018a) and Engelhardt et al. (2000). . . . .	2
1.2	Workflow for calibrating empirical constitutive model parameters, $\mathbf{x}$ , for earthquake-induced inelastic straining. . . . .	6
1.3	Underestimation of the measured yield stress for mild structural steels using the Voce-Chaboche (VC) numerical model. . . . .	6
2.1	Uniaxial 2 % increasing strain amplitude cyclic coupon test on S355J2+N steel and its best-fit Voce-Chaboche model prediction. Experiment data from Grigoriou and Lignos (2017). . . . .	14
2.2	Schematic illustration of initial structural steel material response to cyclic loading.	15
2.3	Schematic illustration of the yield surface progression for structural steels. . . .	16
2.4	Schematic illustration of the radial return mapping algorithm. . . . .	20
2.5	Results from the material model unit cube validation studies. . . . .	23
2.6	Results from the material model column validation study. . . . .	23
2.7	Tangent modulus of the proposed material model subjected to monotonic and cyclic loading histories. . . . .	25
2.8	Comparison of test data and model predictions for the S355J2 HEB500 flange data set. . . . .	34
2.9	Comparison of test data and model predictions for the S355J2 HEB500 web data set. . . . .	35
2.10	Continuum finite element model and elastic buckling modes for the HEB500 column case study. . . . .	37
2.11	Column base moment - chord rotation and column model deformation modes at the first excursion to -4 % chord rotation. Bottom figures: yielding shown in light gray. . . . .	42

## List of figures

---

3.1	Comparison of stress-strain using the S355J2+N 50 mm plate and A992 Gr. 50 W14X82 flange data sets: test data (Test); VC model 2 backstresses, all load protocols used in calibration (All LP); and naive calibration using only a tensile test (Tensile-Naive). . . . .	49
3.2	Workflow of proposed methodology applied to structural steel materials. . . . .	52
3.3	Relevant model metrics for $\sigma_y \approx 355$ MPa materials based on parameters calibrated with all available load protocols. . . . .	70
3.4	Relevant model metrics for $\sigma_y \approx 355$ MPa materials based on parameters calibrated with all available load protocols. (Cont.) . . . . .	71
3.5	Evolution of the constrained optimization solution based on the different starting points using the S355J2+N 50 mm data set. . . . .	72
3.6	Comparison of stress-strain using the S355J2 IPE300 flange data set: test data (Test), VC 2Back Root dataset calibration (HEB500-Flange), and proposed tensile-only calibration with the VC model (Tensile). . . . .	73
3.7	Comparison of stress-strain using the S355J2 IPE300 flange data set: test data (Test), UVC 2Back Root dataset calibration (HEB500-Flange), and proposed tensile-only calibration with the UVC model (Tensile). . . . .	74
4.1	Mixed-dimension component macro model concept for wide flange cross sections. . . . .	86
4.2	Schematic wide flange cross section and mixed-dimension domains. . . . .	87
4.3	Schematic view of prototype frame and overview of Case Studies 2, 3, and 4. . . . .	94
4.4	Details of the nonuniform torsion test, reproduced from Farwell and Galambos (1969). . . . .	96
4.5	Schematic representations of the illustrative examples (extruded view of shell domains shown). . . . .	97
4.6	Representations of the flange imperfection model. . . . .	101
4.7	Imperfections for a 5500 mm length W24X94 analysis model with a 20 % axial load ratio, and (c) reference experimental results from Elkady and Lignos (2018a). . . . .	101
4.8	Comparison of applied torque versus twist angle for models of the Farwell and Galambos (1969) test. . . . .	103
4.9	Comparisons of the von Mises equivalent stress (units of MPa) for the interface shell elements in the nonuniform torsion models at $M_z = 11.25$ kN-m. . . . .	104
4.10	Iteration count for the nonuniform torsion test. . . . .	105
4.11	Comparisons of the DBBW overall subassembly behavior. Test Data retrieved from Engelhardt et al. (2000). . . . .	106
4.12	Comparison of post-test deformed shapes from the DBBW subassembly. Test Data photo used with permission from Engelhardt et al. (2000). . . . .	107

4.13 Comparisons of the DBBW panel zone behavior. Test Data retrieved from Engelhardt et al. (2000). . . . .	107
4.14 Computational resource requirements for Case Studies 2, 3, and 4 normalized by the Full-shell values. . . . .	108
4.15 Results from the W24X136 quasi-static analyses. Test Data retrieved from Elkady and Lignos (2018a). . . . .	110
4.16 Deformed shapes from the W24X146 quasi-static analyses at 11 % SDR. von Mises equivalent stress profile shown on the deformed shape, red regions indicate yielding. Test Data photo used with permission from Elkady and Lignos (2018a). . . . .	111
4.17 Results from the W24X94 column nonlinear response history analyses. . . . .	111
4.18 Deformed shapes from the W24X94 column nonlinear response history analyses at $t = 4.5$ s. von Mises equivalent stress profile shown on the deformed shape, red regions indicate yielding. . . . .	112
5.1 Schematic representation of steel moment-resisting frame and potential component model idealizations. . . . .	121
5.2 Division of component into domains and beam-column element kinematics. . . . .	123
5.3 Schematic representation of an wide flange cross section in the reference, initial, and deformed configurations. . . . .	124
5.4 Visualization of the plane of best-fit for wide flange cross sections. . . . .	125
5.5 Nodal stresses due to an applied beam-column load and the nodal tributary areas. . . . .	132
5.6 Sample assumed elastic shear stress distribution ( $d = 110$ , $b_f = 100$ , $t_w = t_f = 10$ ). . . . .	134
5.7 Results from the elastic cantilever model subjected to a large deformation. Figure (a) shows the Full-shell model (left) and BF-MPC model (right). . . . .	140
5.8 Interface shell element stress distributions for Full-shell, and macro models with built-in Abaqus kinematic coupling (KC) and the proposed MPC (BF-MPC). Values extracted from the final state of Example 1. . . . .	141
5.9 Test setup schematic and results from the Farwell and Galambos (1969) nonuniform torsion test. . . . .	143
5.10 Average axial stress in the interface elements under uniaxial tension when the direct linearization is used in the MPC formulation, values in MPa. . . . .	154
6.1 Component macro model representation for beam-columns with wide flange sections subjected to multiaxis cyclic loading. Photo in 6.1a from Elkady and Lignos (2018a). . . . .	157
6.2 Organization of the steel wide flange column modeling guidelines proposed in this study. . . . .	160

## List of figures

---

6.3	Schematic representation of the error metrics for: peak-strength ( $\epsilon_s$ ), energy ( $\epsilon_e$ ), and axial shortening ( $\epsilon_a$ ). . . . .	161
6.4	Column boundary conditions, applied loading, and base reaction moment. . .	164
6.5	Local and global imperfection shapes and parameter definitions. . . . .	167
6.6	Effect of local imperfection amplitude on full-shell CFE results for the W-8-34-M-C-50 test (W14X61, $P/P_{ym} = 0.5$ ). Test data and photo from Cravero et al. (2020). . . . .	169
6.7	Modeling of critical regions for full-length (Top B.C. = Fixed or Rot; left) and cantilever (Top B.C. = Free; right) members. Photos from Elkady and Lignos (2018a) and Cravero et al. (2020). . . . .	170
6.8	Comparison of A992 Gr. 50 (W14X82 flange) material stress-strain and material model responses using the UVC and VC models. UVC calibrated with tensile and cyclic tests; VC calibrated using only a tensile test. Material data from Suzuki and Lignos (2021). . . . .	172
6.9	Shell element mesh convergence results ( $E = \int M d\theta^*$ ) based on the W-6-25-C1-C test (W14X82, collapse-consistent, $P/P_{ym} = 0.3$ ) by Suzuki and Lignos (2021). . . . .	173
6.10	Solid element mesh convergence results ( $E = \int M d\theta^*$ ), relative to the Solid-Q12 model, based on the W-6-25-S-C test (W14X82, symmetric-cyclic, $P/P_{ym} = 0.3$ ) by Suzuki and Lignos (2021). . . . .	174
6.11	Beam-column element mesh convergence results based on Specimen 1 flexural buckling test by Lamarche and Tremblay (2011). . . . .	174
6.12	Full-shell model average error metric results from the calibration data set (each square is the average of five tests). . . . .	176
6.13	Sample results from the full-shell calibration dataset with $L_{bw} = 1.5b_f$ and $\alpha = 100$ (solid = Test, dashed = Full-shell). . . . .	177
6.14	Full-solid model average error metric results from the calibration data set (average of five tests). $\epsilon_e$ = energy metric, $\epsilon_s$ = peak-strength metric, $\epsilon_a$ = axial shortening metric. . . . .	178
6.15	Effect of global imperfection scale factor, $a_g = L/(\beta \cdot 1500)$ , on columns subjected to multiaxis loading (based on tests from Elkady and Lignos (2018a)). $\epsilon_e$ = energy metric, $\epsilon_s$ = peak-strength metric, $\epsilon_a$ = axial shortening metric. . . . .	179
6.16	Effect of global imperfection on local buckling orientation for the C1 column. Test photo from Elkady and Lignos (2018a). . . . .	179
6.17	Average error metric results from the simulation of the validation dataset. Values above each bar are the mean and standard deviation of the associated log-normal distribution. . . . .	181



6.18 Representative full-shell model results from the “blind” analysis of tests in the validation dataset (solid = Test, dashed = Full-shell). High values of $\epsilon_e$ represent worse predictions of moment-rotation. . . . .	182
6.19 Simulation with lowest error at $L_{\Omega_2} = 3.0b_f$ between the macro and full-shell models (solid = Full-shell, dashed = Macro-shell). . . . .	184
6.20 Simulation with highest energy error ( $\epsilon_e = 0.075$ ) at $L_{\Omega_2} = 4.0b_f$ between the macro and full-shell models (solid = Full-shell, dashed = Macro-shell). . . . .	185
6.21 Probability density of individual errors for $L_{\Omega_2} = 3.0b_f$ , and those when the guidelines proposed in Equation 6.8 are followed. . . . .	185
6.22 Computational efficiency metrics for the macro models. All values normalized by their respective full-shell values. Ref. 1: Suzuki and Lignos (2021), Ref. 2: Elkady and Lignos (2018a), Ref. 3: Cravero et al. (2020), A: added length analyses.	186
6.23 Material results and Voce-Chaboche (VC) model predictions for specimens C1–C4 (W24X146 cross section) tested by Elkady and Lignos (2018a). VC, tensile-only parameters from Table 6.2. . . . .	188
6.24 Zoom on k-area of a W24X84 section to highlight the difference between solid and shell element discretizations. . . . .	189



## List of tables

2.1	Summary of steel material database and metrics for the proposed material model.	32
2.2	Proposed material model parameters for structural steels. . . . .	33
2.3	Comparison of yield stresses and normalized error metrics for the UVC and Voce-Chaboche (VC) models. . . . .	33
2.4	Cross section properties of an HEB500, 7000 mm length. . . . .	38
2.5	Original Voce-Chaboche model parameters for the case study material sets. . .	38
2.6	Imperfection scale factors for lateral-torsional and local buckling modes. . . .	41
2.7	Summary of the error metric from the parametric case study. . . . .	42
3.1	Overview of the Root material database. . . . .	53
3.2	Voce-Chaboche material model parameters with one and two backstresses obtained using the full data sets. . . . .	66
3.3	Voce-Chaboche hardening metrics with one and two backstresses obtained using the full data sets. . . . .	67
3.4	Voce-Chaboche tensile test only calibration with one and two backstresses using the NITRO algorithm and SP1 for mild steels. . . . .	67
3.5	Results from the validation of the tensile test only calibration methodology with one and two backstresses, using the VC model for mild steels. . . . .	68
3.6	Updated Voce-Chaboche full data set calibration with one and two backstresses for mild steels. . . . .	68
3.7	Metrics for the Updated Voce-Chaboche full data set calibration with one and two backstresses. . . . .	69
3.8	Results from the validation of the tensile test only calibration methodology with two backstresses for the UVC model. . . . .	69
4.1	Overview of the case studies. . . . .	93
4.2	Wide flange member geometry used in the analysis cases. . . . .	96
4.3	Case study macro model and imperfection parameters. . . . .	96
4.4	Case study Voce-Chaboche material model parameters. . . . .	100
4.5	Frequencies for selected modes of the W24X94 column. . . . .	110

## List of tables

---

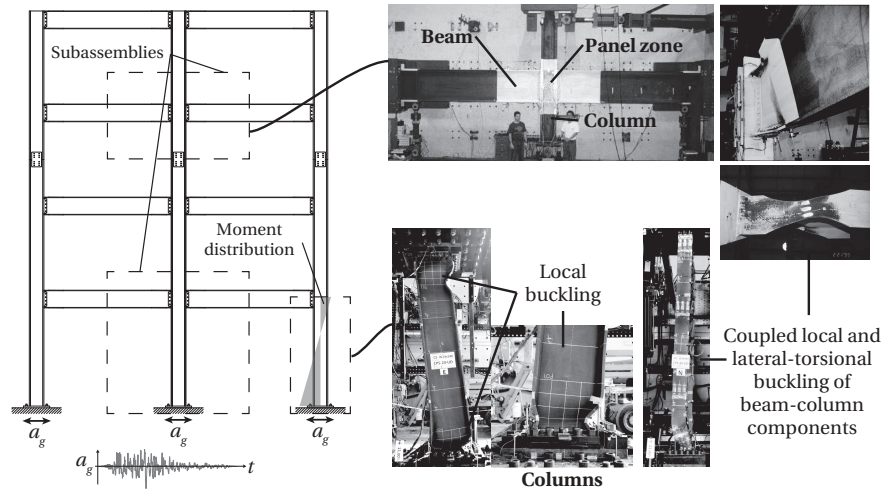
6.1	Wide flange column test database used in this study. Top B.C.: Free = cantilever configuration, Fix = fixed, Rot = rotational B.C.. Mon. = Monotonic, Sym. = Symmetric cyclic, C-C = Collapse-consistent; Dir. = Lateral loading direction: Uni. = Unidirectional, Bi. = Bidirectional. $\bar{\lambda}_{LT}$ from Equation 6.4. . . . .	163
6.2	Results from the calibration of the Voce-Chaboche model using only tensile tests.	171
6.3	Summary of full-continuum modeling parameters determined in this study for modeling columns under multiaxis loading with properties in the ranges of: $0.19 \leq \bar{\lambda}_{LT} \leq 0.38$ , $5.9 \leq b_f/2t_f \leq 8.1$ , $20 \leq h/t_w \leq 44$ , $0.15 \leq P/P_{ym} \leq 0.75$ . . . .	180
6.4	Error metric results from the validation dataset for full-shell and full-solid models as a function of model type and axial load. . . . .	180
6.5	Error metric results for macro-shell models as a function of continuum length ( $L_{\Omega_2}$ ). . . . .	183

# 1 Introduction

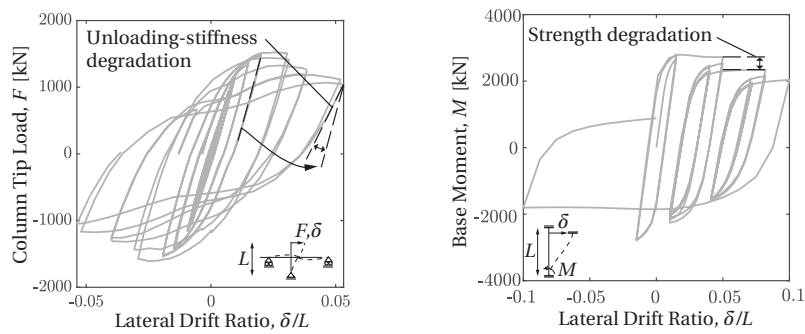
## 1.1 Nonlinear structural analysis in earthquake engineering

Earthquakes cause socioeconomic losses in buildings due to the cost to repair damage in structural and nonstructural components, the inability to utilize buildings during repair time (downtime), and the risk of casualties due to potential collapse. Controlling damage and estimating potential losses can be done using the performance-based earthquake engineering framework (Cornell and Krawinkler, 2000) given that the building's response to earthquake events can be accurately estimated. Physical experiments to predict the behavior of structures and structural components are costly, thus engineers and researchers increasingly turn to numerical models for simulating building behavior to seismic hazards. In this manner, nonlinear structural analysis using the finite element method is integral to the performance-based assessment of buildings subjected to earthquake loads.

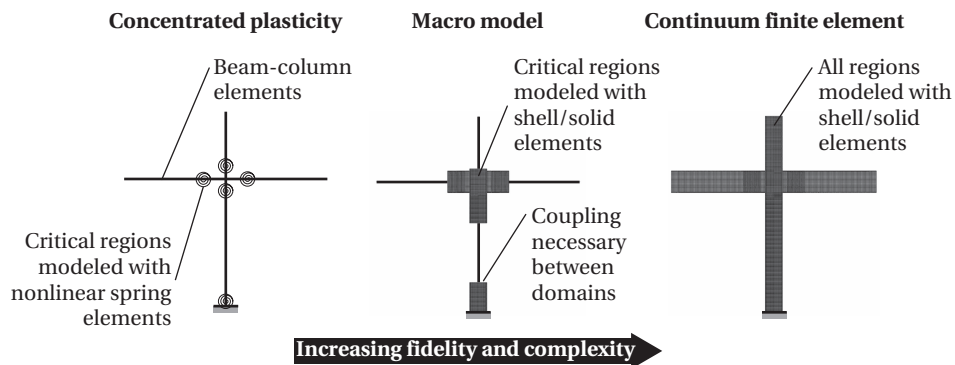
Meaningful simulations require that the nonlinear simulation models accurately portray the behavior of their representative components (e.g., beams, columns, the beam-to-column web panel zone joint—shown in Figure 1.1). Beam and column components, that constitute the focus of the thesis, are subjected to a combination of axial forces, shear forces, and bending moments (multiaxis loading) due to applied gravity loads coupled with lateral drift demands resulting from earthquake-induced displacement of the structure. Collectively, these components are denoted as *beam-columns*. Critical regions in beam-columns are typically at the component ends, due to the moment distributions that arise under lateral displacement of the structure (see Figure 1.1). Components used in seismic design of steel structures are mandated that such damage typically initiates through yielding and inelastic geometric instabilities in these regions (CEN, 2005c; AISC, 2016a; Lignos et al., 2019). Accurately modeling the geometric instabilities interacting with inelastic material behavior is therefore a necessity for reliable nonlinear component simulations.



(a) Structural components and geometric instabilities observed under multiaxis loading



(b) Laboratory response of a subassembly (left) and a column (right)



(c) Potential numerical representations of a first-story subassembly

Figure 1.1 – Structural components in a steel moment-resisting frame subjected to earthquake loading and their finite element representations. Photos in 1.1a and data in 1.1b from Elkady and Lignos (2018a) and Engelhardt et al. (2000).

### 1.2 Modeling steel components subjected to earthquake loads

Complex behaviors in beam-columns, in terms of both material nonlinearity and geometric instabilities, need to be accounted for to accurately predict the behavior of components subjected to multiaxis cyclic loading resulting from earthquakes. A brief overview of these behaviors is provided to contextualize the problem; a thorough review of beam-column behavior under multiaxis cyclic loading can be found in Lignos et al. (2019). Damage in the form of strength degradation in seismically compact beam-columns subjected to lateral drift demands typically initiates through inelastic local buckling at the components' ends due to the moment gradient present in these members (see Figure 1.1). Local instabilities may be coupled with global instabilities, such as lateral-torsional buckling (LTB) and flexural buckling, after further loading. Notably, LTB also leads to unloading-stiffness degradation in seismically compact beam-columns. Modeling coupled local and global instabilities, as well as their interaction, is therefore critical for steel beam-column components.

Yielding and instability phenomena are represented in different ways depending on the class of numerical model. For instance, three classes of simulations models for structural components are shown in Figure 1.1c. Concentrated plasticity models emulate nonlinear material behavior and degradation in component strength/stiffness through zero-length elements at pre-defined locations within the component. Continuum finite element (CFE) component representations utilizing shell and solid elements are more general as they explicitly model both the inelastic material behavior and its interaction with geometric instabilities throughout the entire component. The component macro model approach lies between these two aforementioned methods in terms of fidelity by explicitly modeling critical regions with solid/shell elements and using beam-column elements elsewhere.

Concentrated plasticity approaches are used extensively in performance-based earthquake engineering (FEMA, 2009; ATC, 2017b) owing to their lower computational cost compared to CFE models. The low computational cost is beneficial in this context due to: (i) the number of finite elements needed to model the entire structural system, (ii) the number of earthquake records required to mitigate uncertainty in earthquakes themselves (Eads et al., 2013), (iii) and the number of analyses required to obtain a statistical distribution of structural performance (Vamvatsikos and Cornell, 2002). There are, however, a number of important limitations in concentrated plasticity models that have been highlighted by recent experimental programs on steel beam-columns (Ozkula et al., 2017; Elkady and Lignos, 2018a; Cravero et al., 2020; Suzuki and Lignos, 2021). Addressing the limitations in the concentrated plasticity component modeling approach for steel beam-columns, discussed in detail in Chapter 4, is a primary motivation for the research conducted in this thesis. At the same time, it is desirable to reduce the computational cost of full-CFE approaches for structural models to be better suited for performance-based applications.

One focus of this thesis is on the development of a beam-column macro modeling approach to match the fidelity of full-CFE models at a reduced computational cost. Component macro models are defined by three features: (i) the specification of continuum element (i.e., shell or solid) domains used in the critical regions, (ii) the specification of beam-column element domains used elsewhere, and (iii) the coupling between domains of continuum and beam-column elements. A general procedure, proposed later in this thesis, provides recommendations for these three features given beam-column components subjected to multiaxis loading. One challenge in this regard is the *a priori* partitioning of components into domains of continuum and beam-column elements. Furthermore, as will be introduced in Chapter 4, there are limitations in existing methods (e.g., McCune et al. (2000); Song (2010); Ho et al. (2010); Dassault Systèmes (2014); Liu (2016)) for coupling the continuum and beam-column elements in a manner that includes torsion-warping present in wide flange beam-columns. Including torsion-warping in the coupling formulation is found to be particularly important for beam-columns susceptible to global instabilities such as lateral-torsional buckling.

### 1.3 Modeling structural steels subjected to earthquake-induced inelastic cyclic straining

Frequent reference has thus far been made to the inelastic nature of a beam-column's response to strong earthquake loads. The primary challenge in modeling structural steels subjected to earthquake-induced inelastic cyclic straining is the uncertain nature of the inelastic strain demands. Throughout this thesis, material behavior is represented mathematically using an empirical constitutive modeling approach. In relation to the challenge of uncertain loading, the selected empirical constitutive model, and its parameters, should be selected to accurately represent the expected range of inelastic strain demands regardless of the loading history. This issue was tackled by de Castro e Sousa et al. (2020) by calibrating a classic metal plasticity constitutive model using several strain histories deemed representative of earthquake-induced inelastic strain demands. The reader is directed to de Castro e Sousa et al. (2020) for information regarding the sensitivity in the model calibration to the selected load protocols. The benefit of this approach is that consistent constitutive model parameters are obtained even in the face of parameter non-uniqueness frequently encountered in this domain (Cooke and Kanvinde, 2015).

The overall procedure for determining material model parameters proposed in de Castro e Sousa et al. (2020) is shown in Figure 1.2. A number of structural steel samples (coupons) are extracted from the specified base material (e.g., a wide flange member or a plate). The set of material coupons are subjected to a suite of uniaxial, strain-based loading protocols with different characteristics deemed to be representative of monotonic and earthquake-induced inelastic cyclic straining, an example is shown in Figure 1.3. Constitutive model parameters are



then determined by solving the inverse problem of model calibration using all of the collected stress-strain data for the given material. The objective function in this case is the difference in accumulated squared strain energy between the model and experiment summed over all available uniaxial tests for a given material. Consistent parameters, applicable over a wide range of inelastic strains, tend to result from this procedure.

The classic metal plasticity Voce-Chaboche (VC) (Voce, 1948; Armstrong and Frederick, 1966; Chaboche et al., 1979) constitutive model was calibrated by de Castro e Sousa et al. (2020) for structural steels using the aforementioned methodology. This material model is ubiquitous for modeling structural steel components subjected to earthquake loading (see e.g., Fell et al. (2009); Nip et al. (2010); Fogarty and El-Tawil (2015); Elkady and Lignos (2018b)). However, a particular limitation in the VC model for simulating the inelastic behavior of structural steels was revealed through this work. The initial yield stress is systematically underestimated by at least 10–30 % using this constitutive model, although, for strains past around 0.02 the model performs quite admirably in predicting the stress-strain behavior. Typical results are presented in Figure 1.3 that depict the underestimation of the measured yield stress (most clear under monotonic loading), as well as the reasonably good performance of the VC model for inelastic cyclic loading. There is a need to further comprehend the origins of the discrepancy in yield stress and the impact that it has on component simulations; furthermore, this behavior in the constitutive model should be corrected without sacrificing accuracy in later loading cycles.

A limitation of the framework proposed by de Castro e Sousa et al. (2020) is the requirement of using several cyclic coupon tests to calibrate the material model parameters. Such cyclic coupon tests are scarce, whereas standard tensile tests (ASTM, 2016b; ISO, 2019) are commonplace. Therefore, a calibration method that can make use of standard tensile test results to provide a reasonable estimate of a material's behavior under cyclic loading is considered useful to model situations where the cyclic material behavior cannot be explicitly known. This situation is frequently encountered in modeling laboratory experiments on steel beam-columns subjected to multiaxial cyclic loading, such as those represented in Figure 1.1. Therefore, there is a need for a physically-motivated methodology to calibrate constitutive models under the condition of limited material information.

## 1.4 Aim and organization of the thesis

### 1.4.1 Aim and objectives

The overarching aim of this thesis is to propose reduced-order simulation models for steel beam-column components that match the fidelity of full continuum finite element models at a diminished computational expense. This work is motivated by findings from full-scale experiments conducted on beam-columns that highlighted limitations in concentrated plasticity models. Motivation for a computationally efficient approach comes from the intent to use

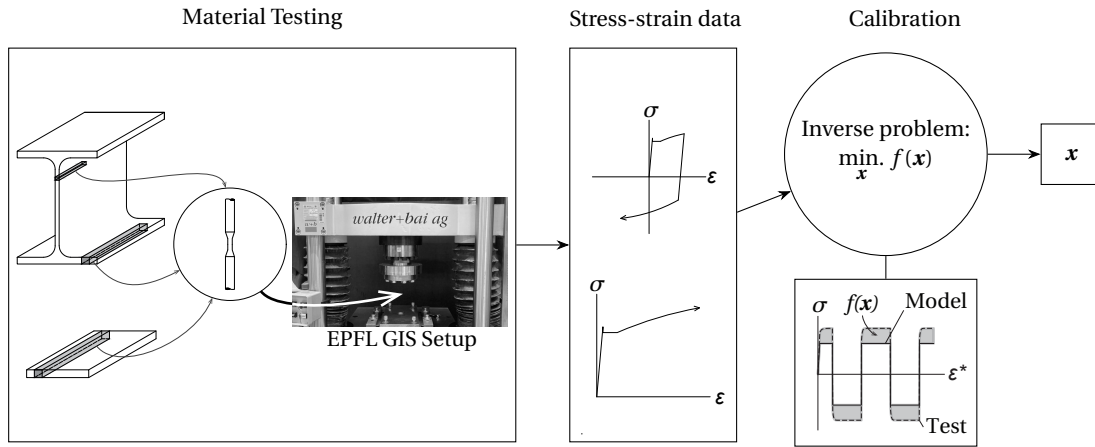
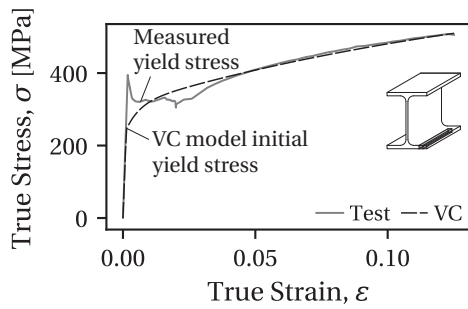
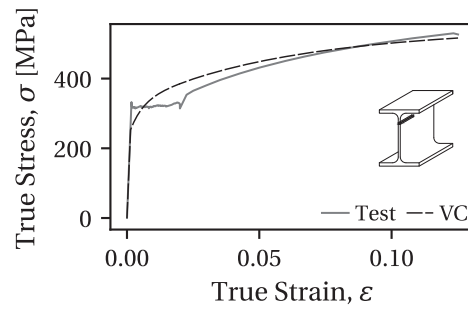


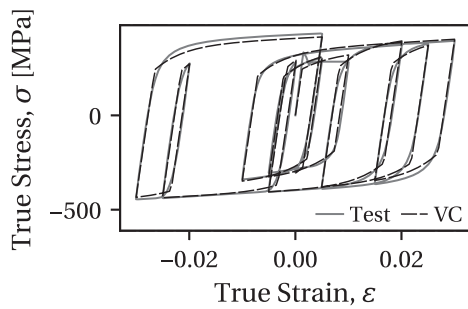
Figure 1.2 – Workflow for calibrating empirical constitutive model parameters,  $x$ , for earthquake-induced inelastic straining.



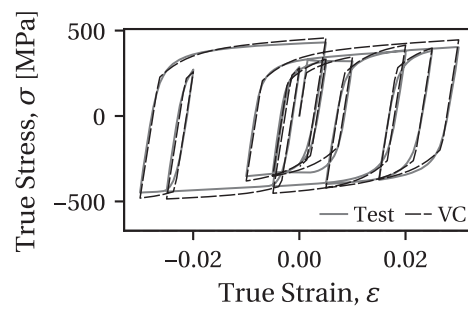
(a) Material sampled from the flange: standard tension test



(b) Material sampled from the web: standard tension test



(c) Material sampled from the flange: cyclic tension/compression



(d) Material sampled from the web: cyclic tension/compression

Figure 1.3 – Underestimation of the measured yield stress for mild structural steels using the Voce-Chaboche (VC) numerical model.

these models in the context of performance-based earthquake engineering. Computationally efficient modeling is achieved in this thesis using the component macro model approach to explicitly represent inelastic material behavior and geometric instabilities in critical regions. Within this paradigm, there is a need for an efficient method to couple beam-column and continuum element domains that accounts for torsion-warping. Reliable component simulations require an updated material model that improves upon the initial yielding behavior of classic metal plasticity models, and a calibration method that accounts for the frequent case when there is limited information available regarding the material behavior.

The specific objectives related to the aim of this thesis are to:

1. advance the state-of-the-art in constitutive modeling for structural steels subjected to earthquake-induced inelastic strain demands;
2. develop an efficient method of coupling beam-column and continuum element domains that incorporates torsion-warping; and
3. develop general recommendations for modeling wide flange beam-column components subjected to inelastic cyclic straining using the macro model concept.

The first objective is achieved by developing a new material model, and a coherent methodology for its calibration, that addresses the limitation in the VC model of underestimating the initial yield stress without sacrificing accuracy in later inelastic loading cycles. A calibration methodology based on constrained optimization is proposed for the cases where the cyclic material behavior is known and when it is unknown. This objective is addressed first as the proposed material model will be used in subsequent developments. The second objective is achieved through new kinematic coupling methods that transfer torsion-warping deformations between the beam-column and continuum element domains. The third objective is achieved by incorporating the developed material model and coupling method into systematic recommendations for the macro modeling of steel wide flange beam-columns.

### 1.4.2 Organization

This thesis is organized by articles. Chapters 2–6 have been, or are planned to be, submitted to high-quality scientific journals. Each chapter is comprised of the preprint or postprint version of an article; and in accordance with EPFL policy, the first page contains: the author list, the thesis author's contributions, and bibliographic information of published articles. Each article's abstract and keywords are also provided at the start of the chapter. References cited in each chapter are contained in the bibliography at the end of the thesis. A notation list is provided at the end of each chapter that corresponds to the specific chapter.

This thesis is thematically divided into two main parts. Part I addresses the first objective stated above through the development of a new constitute model for structural steels and its

calibration (Chapter 2). Part I also includes a novel method that was developed to calibrate material models for cyclic loading when only limited data related to a standard tension test is available (Chapter 3). Part I is mainly concerned with providing material-level results and to highlight the sensitivity of simulations to material model input parameters in particular beam-columns. Further outcomes from these chapters are shown later in the thesis (i.e., in Chapter 6) by comparing simulations using the developments in Part I with beam-columns experiments.

Part II addresses the second and third objectives related to the component macro model. First, two new methods for coupling beam-column element and continuum element domains are developed (Chapters 4 and 5). The best-fit MPC devised in Chapter 5 was developed prior to the development of the warping-inclusive kinematic coupling (WIKC) proposed in Chapter 4. However, the limitations found in the best-fit MPC motivated the WIKC method developed in Chapter 4, and thus the WIKC method was instead used extensively for beam-column macro modeling in this thesis. The presentation of Chapters 4 and 5 therefore follows the chronological order of *article* submission. Afterwards, applications of the component macro model are provided for beam-column components with wide flange cross sections (Chapter 6). Part III of this thesis contains a chapter-by-chapter summary and conclusions, as well as recommendations for future research that resulted from this work.

# **Structural steel material model** **Part I**



## 2 Constitutive modeling of structural steels: A nonlinear isotropic/kinematic hardening material model and its calibration

**Authors:** Alexander R. Hartloper, Albano de Castro e Sousa, Dimitrios G. Lignos

**Postprint version of:** Hartloper, A. R., de Castro e Sousa, A., and Lignos, D. G. (2021a). “Constitutive modeling of structural steels: Nonlinear isotropic/kinematic hardening material model and its calibration.” *Journal of Structural Engineering*, 147(4), 04021031. [https://doi.org/10.1061/\(ASCE\)ST.1943-541X.0002964](https://doi.org/10.1061/(ASCE)ST.1943-541X.0002964). With permission from ASCE.

**Doctoral candidate's contributions:** Literature review, conception and development of the constitutive model, derivation of the parameter constraints, development of the calibration methodology, execution of material testing, production of material parameters, analysis of finite element models, evaluation and interpretation of results. Writing and editing of the manuscript. The co-authors supervised the work carried-out by the doctoral candidate and assisted with the editing of the manuscript.

**Abstract:** Numerical models of structural components that deteriorate primarily due to geometric instabilities under multiaxial cyclic loading are sensitive to both the assumed geometric imperfections and the nonlinear material model assumptions. Accuracy of the constitutive model is, therefore, a desirable feature in finite element simulations. However, the classic Voce-Chaboche metal plasticity model, ubiquitous in commercial finite element software, is found to underestimate the initial yield stress in structural steels by about 10–30 % when calibrated to minimize the overall difference in strain energy between the model and test data of load protocols representative of earthquake loading. This chapter proposes a refined version of the Voce-Chaboche material model. When compared with the original model, the updated one improves the prediction of the initial yield stress, can simulate initial yield plateau behavior, and better estimates experimental cyclic stress-strain data. Constraints on the model parameters are established, a calibration procedure is developed, and model parameters are proposed for nine structural steels used worldwide. Source code for the material model is also made publicly available. A case study demonstrates that steel component behavior is sensitive to subtle differences in the material response that arise between the Voce-Chaboche and the proposed material models.

**Keywords:** Constitutive model; Structural steel; Discontinuous yielding; Multiaxial plasticity; Earthquake loading; Nonlinear inverse problem; Geometric instabilities.

## **2.1 Introduction**

Experimental evaluation and accurate numerical modeling of structural components and systems is necessary in the field of earthquake engineering to evaluate component behavior under multiaxial cyclic loading. In steel structures, that form the basis of this work, parametric full-scale physical experiments would often require an inordinate amount of resources. Furthermore, the complex interactions between nonlinear material behavior and the geometric nonlinearities are challenging to study analytically. Numerical modeling in the form of continuum finite element (CFE) analysis, in contrast, is a well established alternative to investigate these problems in a so-called virtual testing environment (ATC, 2017a). A few prevalent examples demonstrating the use of CFE analysis include modeling braces and brace connections in concentrically braced frames (Fell et al., 2009; Hsiao et al., 2012), studying geometric instability mechanisms in commonly used lateral load resisting systems (Imanpour et al., 2016), extending results from full-scale steel wide flange column tests to a wide range of column geometries and loading conditions (Fogarty and El-Tawil, 2015; Elkady and Lignos, 2015a, 2018b), and aiding the development of component modeling guidelines in support of performance-based earthquake engineering (Lignos et al., 2019).

Accurately simulating the geometric instabilities and nonlinear material behavior is essential to understanding the performance of components subjected to seismic demands through CFE analysis. At the crux of this issue is the choice of initial geometric imperfections to induce an appropriate geometrically nonlinear response, as well as the choice of a material model that rigorously represents the material behavior. Geometric imperfections are typically included by superimposing scaled elastic buckling modes found through eigenvalue analysis, and the sensitivity of simulations to both the shape and amplitude of the imperfections has been acknowledged (Schafer et al., 2010; Kalochairetis and Gantes, 2011; Elkady and Lignos, 2015a, 2018b; Ziemian et al., 2018; Cravero et al., 2020). None of these studies, however, have investigated the sensitivity of steel component simulations to the choice of material model and its parameters—this chapter works towards addressing these questions.

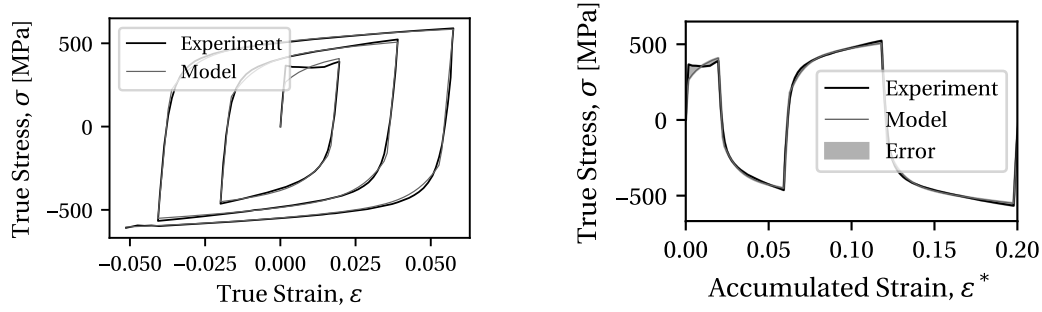
The employed material model should capture pertinent cyclic loading effects, notably the Bauschinger effect, cyclic hardening, and ratcheting (Sowerby et al., 1979; Cofie and Krawinkler, 1985; Hassan and Kyriakides, 1992; Kaufmann et al., 2001). Cyclic softening is another effect observed in particular steels (Hassan and Kyriakides, 1992), however, this effect is not present in the mild structural steels that are the focus of this research. Mild steels are, hereafter, defined as steels that contain less than 0.3 % carbon by mass. The constitutive model combining the nonlinear isotropic hardening law proposed by Voce (1948) to model cyclic hardening with the nonlinear kinematic hardening law of Chaboche et al. (1979) to model the Bauschinger effect and ratcheting, herein the Voce-Chaboche model, is ubiquitous in commercial finite element software.



In the context of earthquake loading, constitutive models for mild structural steels should be able to closely replicate the material's behavior regardless of the load history to account for the effect of ground motion uncertainty on the structural response. de Castro e Sousa et al. (2020) addressed this issue by calibrating the Voce-Chaboche model using data sets of 5–10 uniaxial round-bar coupon tests subjected to distinct cyclic strain histories deemed to be representative of earthquake loading by Suzuki (2018). The reader is directed to de Castro e Sousa et al. (2020) for a detailed discussion of alternative calibration methods. The calibration method of de Castro e Sousa et al. (2020) also reveals that there is an inherent issue in the Voce-Chaboche model for the modelization of mild structural steels in this context.

The issue in the Voce-Chaboche model for mild steels is related to the discontinuous yielding phenomenon (Hall, 1970; Lubliner, 2008), and manifests itself in an underestimation of the initial yield stress with the aforementioned methodology. de Castro e Sousa et al. (2020) demonstrate that the overall difference in accumulated strain energy between the model and the test data is minimized by sacrificing accuracy in the initial yield stress to better predict the behavior in further plastic loading cycles. Their study suggests that the model's optimal initial yield stress underestimates the experimentally measured yield stress by around 10–30 % depending on the data set considered, the reason for this will be discussed shortly. Note that there is no discernible bias in the underestimation based on the steels' yield stress, manufacture provenance, or chemical composition for the sets of structural steels investigated by de Castro e Sousa et al. (2020). The underestimation of the initial yield stress should be addressed in an effort to investigate the sensitivity of steel components to the choice of material model and its input parameters.

The objective of this chapter is to propose an Updated Voce-Chaboche (UVC) material model that better estimates the initial yield stress for structural steels without reducing the fidelity in later loading cycles. Improvement in the prediction of the yield stress at the material level has implications for the extent of member yielding, and subsequently the simulated geometric instabilities in components — both these aspects are demonstrated later on in this chapter through a case study. In turn, accurate predictions of member buckling are important when simulating structures at limit states where such component deterioration is expected. A refined isotropic hardening rule is proposed to achieve this goal, and constraints on the material model parameters that form the sufficient condition to ensure instantaneous hardening of the material model are established. These constraints are considered to be essential for the proper use of the proposed material model for structural steels. A calibration procedure is also proposed that, in combination with the parameter constraints, is general and agnostic with respect to the material model, i.e., no further engineering heuristics are introduced. Finally, we demonstrate that steel components subjected to multiaxial cyclic loading may be highly sensitive to the material model assumptions. A case study utilizing a steel wide flange column model under compressive axial load coupled with cyclic lateral drift



(a) Comparison of test and model responses

(b) Model error in initial cycles

Figure 2.1 – Uniaxial 2 % increasing strain amplitude cyclic coupon test on S355J2+N steel and its best-fit Voce-Chaboche model prediction. Experiment data from Grigoriou and Lignos (2017).

demands demonstrates that seemingly small changes in the material model parameters can have a significant influence on the simulation results.

## 2.2 Limitation of the Voce-Chaboche model for mild steels

The Voce-Chaboche material model underestimates the yield stress in mild structural steels as a compromise to reduce the overall difference in accumulated strain energy between stress-strain data and the model prediction for cyclic loading histories. This issue is illustrated using data from a cyclic uniaxial 2 % increasing strain amplitude test on S355J2+N steel (CEN, 2005d) with a nominal yield stress of  $f_y = 355$  MPa (experimental data from Grigoriou and Lignos (2017)). Test data true stress-strain relations are shown along with the best-fit Voce-Chaboche model prediction in Figure 2.1a. Best-fit in the context of this chapter is defined as the set of parameters that minimizes the accumulated squared area, i.e., squared strain energy, between the experiment and the model prediction. This error is represented by the shaded region in Figure 2.1b restricted on the first few cycles of loading in Figure 2.1a. Notice that the initial yield stress of the test data is underestimated by the model to better match the stress-strain history in subsequent cycles, which tend to present a lower elastic limit with smooth plastic hardening. Consequently, the error is primarily focused in the first loading cycle due to the mismatch of the yield stress. The observation that the initial yield stress is greater than in ensuing cycles, seen in the light of  $J_2$  plasticity, implies that the size of the yield surface diminishes after initial plastic straining.

The reduction in the elastic limit after the initiation of plastic straining is attributed to interstitial carbon and nitrogen atoms in the crystal lattice (Cottrell and Bilby, 1949; Hall, 1970; Lubliner, 2008). These atoms concentrate in the tension field surrounding dislocations, forming a so-called atmosphere, initially locking the dislocations into place (Haidemenopoulos,

## 2.2. Limitation of the Voce-Chaboche model for mild steels

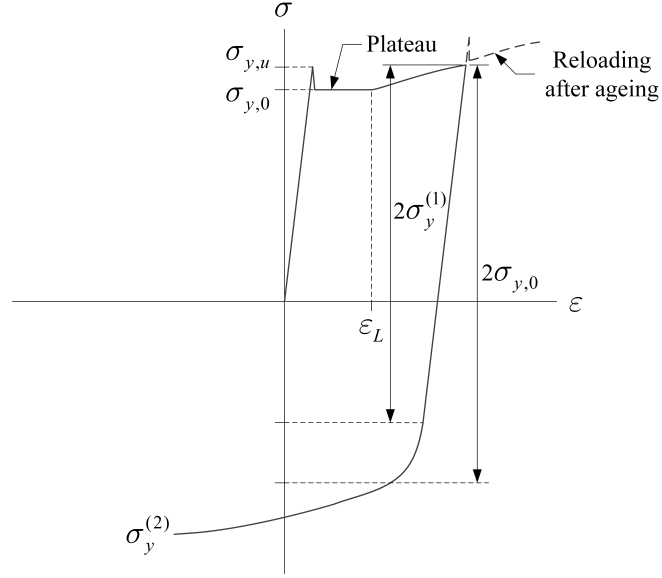


Figure 2.2 – Schematic illustration of initial structural steel material response to cyclic loading.

2018). The yield plateau is the strain range characterized by the growth of Luders bands due to the successive stripping of dislocations from their atmospheres as deformation progresses. A typical stress-strain response for mild structural steels including the plateau region is shown schematically in Figure 2.2. The Luders strain,  $\epsilon_L$ , denoting the end of the yield plateau, is observed to be around 2 % strain in mild steels (Lemaitre and Chaboche, 1990). No plateau is observed upon further loading or immediate reloading once the accumulated plastic strain is greater than the Luders strain. However, a secondary upper yield point is observed if sufficient time is provided for the reformation of atmospheres, this is known as the strain-ageing effect (Hall, 1970; Lubliner, 2008).

The solid load path in Figure 2.2 represents immediate loading up to the second excursion of the test depicted in Figure 2.1a. The dashed loading path in this figure represents the expected behavior if the test was unloaded for a period (on the order of days) then reloaded in tension. Note that the secondary upper yield point formed after ageing exceeds the stress upon immediate reloading. Consideration of the strain ageing effect is potentially critical in studying main-shock/after-shock problems where the steel material has time to age after initial plastic straining, however, this subject is outside the scope of the present chapter.

In Figure 2.1a, the difference between the initial plateau yield stress,  $\sigma_{y,0}$ , and the reduced yield stress upon immediate reloading in compression,  $\sigma_y^{(1)}$  is highlighted. Progression of the size of the yield surface,  $\sigma_y$ , for mild steels undergoing the same loading path is shown schematically in Figure 2.3 with respect to the equivalent plastic strain,  $\epsilon_{eq}^p$ . The initial decrease in size from  $\epsilon_{eq}^p = [0, \epsilon_{min}]$  is intended to simulate the stripping of dislocations from their atmospheres, the later increase after this range accounts for cyclic hardening due to increasing

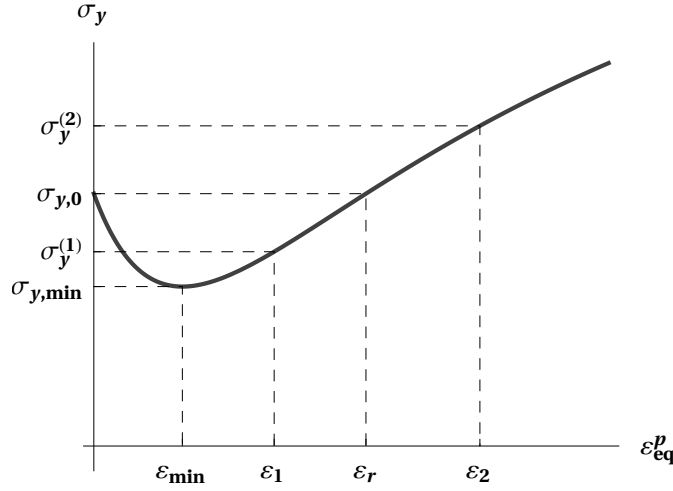


Figure 2.3 – Schematic illustration of the yield surface progression for structural steels.

dislocation densities (Lemaitre and Chaboche, 1990).

We propose a refined material model that accounts for the reduction in the size of the yield surface in mild structural steels by modifying the Voce isotropic hardening rule. The isotropic hardening rule used in Voce (1948) is defined in Equation 2.1,

$$\sigma_y = \sigma_{y,0} + Q_\infty \left( 1 - \exp \left[ -b \varepsilon_{eq}^p \right] \right), \quad (2.1)$$

where  $\sigma_{y,0}$  is the initial yield stress, and  $Q_\infty$ ,  $b$  are material parameters that define the magnitude and rate of isotropic hardening, respectively. The Voce isotropic hardening rule is monotonically increasing and cannot represent the sort of behavior shown in Figure 2.3. Therefore, parameters will be added to this isotropic hardening rule that impose an initial decrease in the size of the yield surface. The following section discusses the formulation of the proposed material model followed by its numerical implementation and calibration.

## 2.3 Proposed material model

The proposed material model follows a classic small-strain, rate independent plasticity formulation (Simo and Hughes, 1998). Geometrically nonlinear problems should be addressed at the material level through an objective integration algorithm as described in Simo and Hughes (1998), however, this discussion is excluded here for brevity. Some notation used in this chapter is established here for clarity before proceeding with the description of the model.

Scalar quantities are not bolded (e.g.,  $a$ ). Bold, serif symbols are first-order tensors (vectors) or second-order tensors (e.g.,  $\mathbf{b}$ ), and capitalized, bold, sans-serif symbols are fourth-order tensors (e.g.,  $\mathbf{C}$ ). The second-order identity tensor is  $\mathbf{1}$ , the fourth-order symmetric identity

tensor is  $\mathbf{I}$ , and the fourth-order deviatoric unit tensor is  $\mathbf{I}_{dev}$ —definitions for each are provided in the Notation section at the end. Contraction on two indices is  $\mathbf{b} : \mathbf{b} = \sum_i \sum_j b_{ij} b_{ij}$ ; the tensor product is  $\mathbf{b} \otimes \mathbf{b} = b_{ij} b_{kl}$ ; the deviatoric part of a tensor is  $\text{dev} [\mathbf{b}] = \mathbf{I}_{dev} : \mathbf{b}$ ; and the 2-norm is always used, i.e.,  $\|\mathbf{b}\| = \sqrt{\mathbf{b} : \mathbf{b}}$ .

### 2.3.1 Constitutive equations

This chapter proposes an Updated Voce-Chaboche model denoted the UVC model. The UVC model uses an additive decomposition of the strain tensor,  $\boldsymbol{\varepsilon}$ , defined in Equation 2.2,

$$\boldsymbol{\varepsilon} = \boldsymbol{\varepsilon}^e + \boldsymbol{\varepsilon}^p, \quad (2.2)$$

where  $\boldsymbol{\varepsilon}^e$  is the elastic strain tensor and  $\boldsymbol{\varepsilon}^p$  is the plastic strain tensor. The elastic stress-strain relation is provided in Equation 2.3,

$$\boldsymbol{\sigma} = \mathbf{C} : (\boldsymbol{\varepsilon} - \boldsymbol{\varepsilon}^p), \quad (2.3)$$

where  $\boldsymbol{\sigma}$  is the stress tensor, and  $\mathbf{C}$  is the isotropic tensor of elastic moduli. A precise definition of  $\mathbf{C}$  is provided in the Notation section at the end. The von-Mises yield condition is used in Equation 2.4 for the yield function  $f$ ,

$$\begin{aligned} f &= \sqrt{(\text{dev} [\boldsymbol{\sigma}] - \text{dev} [\boldsymbol{\alpha}]) : (\text{dev} [\boldsymbol{\sigma}] - \text{dev} [\boldsymbol{\alpha}])} - \sqrt{2/3} \sigma_y \\ &= \|\boldsymbol{\xi}\| - \sqrt{2/3} \sigma_y \leq 0, \end{aligned} \quad (2.4)$$

where  $\boldsymbol{\alpha}$  is the overall backstress,  $\boldsymbol{\xi} = \text{dev} [\boldsymbol{\sigma}] - \text{dev} [\boldsymbol{\alpha}]$  is the deviatoric relative stress, and  $\sigma_y$  is the yield stress of the material. In accordance with the principle of maximum plastic dissipation (Simo and Hughes, 1998), the flow rule in Equation 2.5 associated with  $J_2$  plasticity is

$$\dot{\boldsymbol{\varepsilon}}^p = \lambda \frac{\boldsymbol{\xi}}{\|\boldsymbol{\xi}\|} = \lambda \mathbf{n}, \quad (2.5)$$

where the over-dot indicates the time derivative,  $\lambda$  is the consistency parameter (equivalent to the time derivative of the plastic multiplier), and  $\mathbf{n} = \boldsymbol{\xi} / \|\boldsymbol{\xi}\|$  is the unit normal to the yield surface in deviatoric stress space. For the associative flow rule, the equivalent plastic strain is defined by Equation 2.6,

$$\dot{\varepsilon}_{eq}^p = \sqrt{2/3} \lambda. \quad (2.6)$$

Armstrong and Frederick (1966) defined the nonlinear kinematic hardening rule in Equation 2.7 for a single backstress component  $k$ ,

$$\dot{\boldsymbol{\alpha}}_k = \sqrt{2/3} C_k \dot{\varepsilon}_{eq}^p \mathbf{n} - \gamma_k \dot{\varepsilon}_{eq}^p \boldsymbol{\alpha}_k, \quad (2.7)$$

## Chapter 2. Constitutive modeling of structural steels: A nonlinear isotropic/kinematic hardening material model and its calibration

---

where  $C_k$  and  $\gamma_k$  are the parameters associated with the magnitude and rate of backstress component  $k$ , respectively. Chaboche et al. (1979) later proposed to use a summation of  $N_k$  backstress terms as an improvement to the Armstrong-Frederick rule so that the overall backstress defined in Equation 2.8 is

$$\boldsymbol{\alpha} = \sum_{k=1}^{N_k} \boldsymbol{\alpha}_k. \quad (2.8)$$

We propose an update to the isotropic hardening rule to account for the decrease in the initial yield stress for mild structural steels,

$$\sigma_y = \sigma_{y,0} + Q_\infty \left( 1 - \exp \left[ -b \varepsilon_{eq}^p \right] \right) - D_\infty \left( 1 - \exp \left[ -a \varepsilon_{eq}^p \right] \right), \quad (2.9)$$

where  $D_\infty$  and  $a$  are material parameters that define the magnitude and rate of the decrease in the initial yield stress. As previously discussed, Equation 2.9 is valid for immediate unloading/reloading of the material. The novelty in the proposed model is that the additional term is able to account for the discontinuous yielding phenomenon without leading to a loss of accuracy in later loading cycles by initially reducing the yield surface. This behavior is accomplished through the modification to the isotropic hardening rule and by imposing the proposed constraints on the parameters to enforce nonsoftening behavior. Such a consideration is paramount when calibrating the model using multiple load protocols in an effort to reduce uncertainty in the predicted material behavior when subjected to random strain histories. Additionally, the term is incorporated in a smooth functional form without any discrete imposition of loading stages. Note that the original Voce-Chaboche model can be recovered by simply setting  $D_\infty = 0$  and  $a \neq 0$ , where  $a \neq 0$  is required for numerical reasons in the algorithmic implementation.

Numerous other models exist in the literature for modeling mild structural steels, a nonexhaustive list includes Ohno (1982), Cofie and Krawinkler (1985), Yoshida and Uemori (2002), Ucak and Tsopelas (2011), Mahan et al. (2011), Budaházy and Dunai (2013), and Hu et al. (2018). Most of the reviewed models have a multi-surface formulation, and are not discussed further as the simplicity of the algorithmic implementation for isotropic/kinematic hardening is preferred. The model of Budaházy and Dunai (2013) has a multi-linear isotropic hardening component to simulate the upper yield stress and plateau, and dynamically updates the material parameters depending on the applied load for uniaxial stress states, however, a single set of parameters for all loading scenarios is preferred for its simplicity. The two nonlinear isotropic/kinematic hardening models of Ucak and Tsopelas (2011), Hu et al. (2018) share common features with the UVC model. Notably, both models include a term similar to the  $D_\infty$  term of the proposed model. The highlighted differences with the UVC model are that these two models consider distinct plateau and hardening phases, the term similar to  $D_\infty$  only

provides cyclic softening in the plateau region, and the constraints on the set of parameters are not as general as those discussed later in this chapter because parameter bounds are tied to a particular steel material.

### 2.3.2 Numerical implementation

The numerical implementation of the proposed material model follows two parts: first, solution of the consistency condition to determine the stress for a given strain increment, and second, production of the consistent tangent moduli for use in an iterative nonlinear finite element analysis procedure.

#### Solution to the consistency condition

The return mapping (implicit backward-Euler) time integration algorithm is implemented to provide the stress for given strain states (Simo and Hughes, 1998). Notions of plastic loading and elastic unloading are represented by the Karush-Kuhn-Tucker complementary conditions in (2.10),

$$\lambda \geq 0, \quad f \leq 0, \quad \lambda f = 0. \quad (2.10)$$

These conditions establish the elastic-predictor-plastic-corrector methodology, whereby if the assumed elastic trial state violates the yield condition then plastic loading is active. The algorithm is implemented as a strain driven problem (Simo and Hughes, 1998), i.e., let  $t \in [0, t_1, \dots, T] \subset \mathbb{R}$  be the discretized time interval of interest. At time  $t_n$ , we assume that the total strain, plastic strain, and internal variables are known. If plastic loading is activated, the objective is to solve for the increment in the plastic multiplier,  $\Delta\lambda = \int_{t_n}^{t_{n+1}} \lambda \, dt$ , that constrains the stress state to the yield surface.

Figure 2.4 illustrates the algorithmic counterpart to the consistency condition that arises for multiaxial stress states with a von Mises yield potential in the  $\pi$ -plane (i.e., radial return mapping). Satisfying this condition for  $\Delta\lambda$  is equivalent to finding the orthogonal projection of the trial stress state onto the hardened yield surface (Simo and Hughes, 1998). In this figure,  $\mathbf{s}^{trial}$  is the deviatoric trial stress at the start of a particular increment,  $\mathbf{n} : \Delta\boldsymbol{\alpha}$  is the increment in kinematic hardening,  $\sqrt{2/3}\sigma_y$  is the equivalent yield stress, and  $2\mu\Delta\lambda$  is the reduction in the magnitude of

Starting at time  $t_n$ , Equation 2.11 represents the algorithmic consistency condition to be solved at time increment  $t_{n+1}$ ,

$$g(\Delta\lambda) = \left\| \boldsymbol{\xi}_{n+1}^{trial} \right\| - \left( \sqrt{\frac{2}{3}}\sigma_{y,n+1} + 2\mu\Delta\lambda + \mathbf{n}_{n+1} : \Delta\boldsymbol{\alpha} \right) = 0, \quad (2.11)$$

where  $\Delta\boldsymbol{\alpha} = \boldsymbol{\alpha}_{n+1} - \boldsymbol{\alpha}_n$ . The consistency condition for the time step  $t_{n+1}$  is solved through

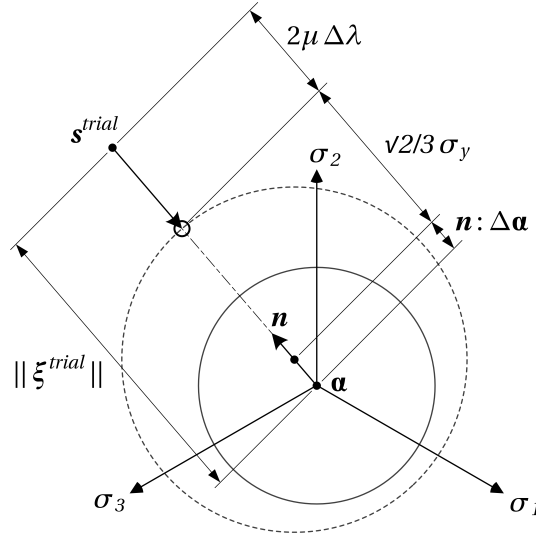


Figure 2.4 – Schematic illustration of the radial return mapping algorithm.

iterations over  $i$  using Newton's local method (Bierlaire, 2015),

$$\Delta\lambda^{(i+1)} = \Delta\lambda^{(i)} - \frac{g(\Delta\lambda^{(i)})}{Dg(\Delta\lambda^{(i)})}, \quad (2.12)$$

where the linearization of Equation 2.11 is provided in Equation 2.13,

$$Dg(\Delta\lambda) = \frac{\partial g(\Delta\lambda)}{\partial \Delta\lambda} = -2\mu \left( 1 + \frac{H'_{n+1} + K'_{n+1}}{3\mu} \right). \quad (2.13)$$

The kinematic and isotropic hardening moduli for multiaxial loading are respectively defined by Equations 2.14 and 2.15,

$$H'_{n+1} = \sum_k (C_k e_{k,n+1}) - \sqrt{\frac{3}{2}} \mathbf{n}_{n+1} : \sum_k (\gamma_k e_{k,n+1} \boldsymbol{\alpha}_{k,n}), \quad (2.14)$$

$$K'_{n+1} = Q_\infty b \exp \left[ -b \varepsilon_{eq,n+1}^p \right] - D_\infty a \exp \left[ -a \varepsilon_{eq,n+1}^p \right], \quad (2.15)$$

where

$$e_{k,n+1} = \exp \left[ -\gamma_k \left( \varepsilon_{eq,n+1}^p - \varepsilon_{eq,n}^p \right) \right]. \quad (2.16)$$

For multiaxial loading, Equation 2.12 is iterated until a tolerance of  $|g(\Delta\lambda)| < 10^{-10}$  is satisfied. Full details of the radial return mapping procedure, along with efficient algorithms for uniaxial, multiaxial and plane-stress, are provided by the authors in Hartloper et al. (2019b).



### Consistent tangent moduli

The elastoplastic tangent moduli consistent with the return mapping algorithm (Simo and Hughes, 1998) are now provided for the case of plastic loading. For brevity, only the final result is shown, details of the derivation can be found in Hartloper et al. (2019b). The consistent elastoplastic tangent moduli is defined by the fourth-order tensor  $\mathbf{C}_{n+1}^{ep}$  in Equation 2.17,

$$\mathbf{C}_{n+1}^{ep} = \kappa (\mathbf{1} \otimes \mathbf{1}) + 2\mu\theta_1 \left( \mathbf{1} - \frac{1}{3} \mathbf{1} \otimes \mathbf{1} \right) - 2\mu\theta_2 (\mathbf{n}_{n+1} \otimes \mathbf{n}_{n+1}) + 2\mu\theta_3 (\mathbf{n}_{n+1} \otimes \Delta \boldsymbol{\alpha}), \quad (2.17)$$

where

$$\theta_1 = 1 - \frac{2\mu \Delta \lambda}{\|\boldsymbol{\xi}_{n+1}^{trial}\|}, \quad \theta_2 = \left( \frac{1}{\beta} + \frac{\mathbf{n}_{n+1} : \Delta \boldsymbol{\alpha}}{\theta_3} \right) - (1 - \theta_1), \quad \theta_3 = \frac{1}{\beta \|\boldsymbol{\xi}_{n+1}^{trial}\|}, \quad (2.18)$$

and

$$\beta = 1 + \frac{K'_{n+1} + H'_{n+1}}{3\mu}. \quad (2.19)$$

A symmetric approximation of the tangent moduli is used since the last term in Equation 2.17 is asymmetric, therefore,

$$\mathbf{C}_{sym.,n+1}^{ep} = \frac{1}{2} \left( (\mathbf{C}_{n+1}^{ep})^T + \mathbf{C}_{n+1}^{ep} \right). \quad (2.20)$$

Hopperstad and Remseth (1995) show that using a symmetric approximation preserves the quadratic convergence of the global Newton solution procedure. This result suggests that the symmetric approximation leads to an overall reduction in both computer memory use and the number of computations required since symmetric matrix storage and solvers can be employed.

### Validation

The proposed material model is implemented in the nonlinear finite element software Abaqus (Dassault Systèmes, 2014) and the Open System for Earthquake Engineering Simulation (OpenSees) (McKenna, 1997) for multiaxial, plane-stress, and uniaxial stress states. User sub-routine files (UMATs) for Abaqus, and C++ source code with compiled dynamic link libraries (.dlls) for OpenSees are made publicly available (Hartloper, 2019). The implementations are validated by comparing the response of several finite element models using the UMAT and NDMaterial with equivalent models using the built-in nonlinear isotropic/kinematic model in Abaqus v6.14 (Dassault Systèmes, 2014). In all these validation cases, the updated isotropic hardening rule of the proposed material model is neglected by simply setting  $D_\infty = 0$  and  $a = 1$  (the choice of  $a = 1$  is made for simplicity as long as  $a \neq 0$ ). Material properties representative of a ASTM A992 Gr. 50 steel (nominal  $f_y = 345$  MPa) are assumed for all analyses:  $E = 179800$  MPa,  $\nu = 0.3$ ,  $\sigma_{y,0} = 318.5$  MPa,  $Q_\infty = 100.7$  MPa,  $b = 8.0$ ,  $D_\infty = 0.0$  MPa,  $a = 1.0$ ,

## Chapter 2. Constitutive modeling of structural steels: A nonlinear isotropic/kinematic hardening material model and its calibration

---

$C_1 = 11608.2$  MPa,  $\gamma_1 = 145.2$ ,  $C_2 = 1026.3$  MPa,  $\gamma_2 = 4.7$ . Only two cases are provided in this chapter for brevity, but several more validations are provided in Hartloper et al. (2019b).

A unit cube model subjected to biaxial loading demonstrates that the material model implementation is accurate when compared with the built-in Abaqus v6.14 material model. Unit cube models consisting of a single fully-integrated brick element (Abaqus: C3D8, OpenSees: SSPbrick) are subjected to two biaxial stress states in Abaqus and OpenSees. Results from both the implemented multiaxial UMAT (“UVC.MA (UMAT)”) and the implemented multiaxial NDMaterial (“UVC.MA (NDM)”) are compared with the results from the built-in nonlinear isotropic/kinematic model in Abaqus v6.14 (“Abaqus”). Comparisons of the results are shown in Figures 2.5a and 2.5b. Both implementations agree with the built-in Abaqus results to the level of machine precision, highlighting the accuracy of the implemented radial return mapping procedure and the consistency of the tangent moduli with the material response.

The material model implementations are also accurate and efficient for component level simulations. The plane stress implementation is validated by modeling a cantilever column using shell elements (S4R) in Abaqus. The column cross section is a W360X122 (W14X82 in U.S customary units), a constant compressive axial load equal to 20 % of the axial yield strength is applied, and the symmetric cyclic load protocol from Chapter K of AISC (2016a) is applied at the column top. The column model is developed according to the recommendations in Elkady and Lignos (2018b). For further details on the modeling procedure, loading, and boundary conditions see Hartloper et al. (2019b). Figure 2.6 shows that there is a negligible difference in the moment-rotation between the models using the built-in material (“Abaqus”) and the implemented material (“UVC.PS (UMAT)”). These differences are attributed to accumulated errors that arise from a difference in the number of required iterations between the two models (UVC.PS UMAT: 4231, Abaqus: 8583). The model run using the UVC.PS UMAT requires approximately 50 % less iterations than the one using the built-in material model, likely because large plastic strain increments can be converged by the implemented UMAT, whereas the built-in material model reduces the time step to achieve convergence. Vis-a-vis the above discussion, the implemented UMAT is more efficient than the built-in Abaqus v6.14 material model in this case.

### 2.3.3 Constraints on the parameter space to ensure nonsoftening

Constraints on the parameter space are necessary because an incorrect choice of parameters for the proposed material model may violate the instantaneous strain-hardening behavior of mild steel materials. Establishing a nonnegative tangent modulus for all plastic strain values, e.g., perfectly-plastic or strain-hardening materials, is used as the starting point for the derivations in this section. This condition is first developed for uniaxial stress states. Afterwards, this condition is shown to enforce uniqueness of the elastoplastic boundary value problem for all stress states.

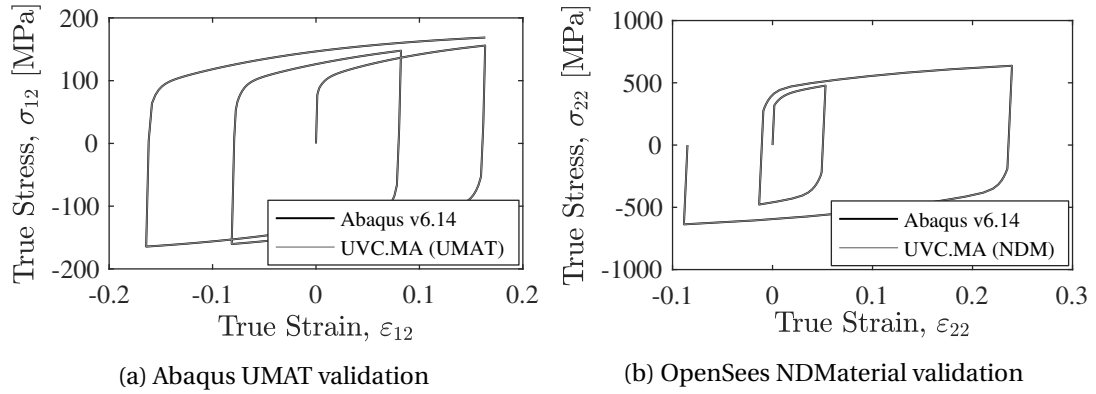


Figure 2.5 – Results from the material model unit cube validation studies.

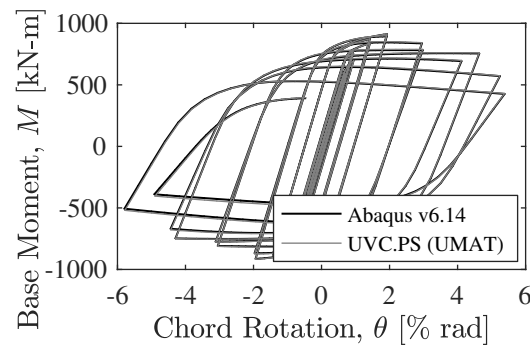


Figure 2.6 – Results from the material model column validation study.

### Uniaxial loading

The algorithmic tangent modulus for a uniaxial stress state is given in Equation 2.21 (Simo and Hughes, 1998),

$$C_u^{ep} = \frac{E(K'_u + H'_u)}{E + K'_u + H'_u}, \quad (2.21)$$

where  $E$  is the elastic modulus, and the kinematic and isotropic hardening moduli are respectively defined for uniaxial loading by Equations 2.22 and 2.23,

$$H'_u = \sum_k (C_k - \text{sign}[\sigma - \alpha] \gamma_k \alpha_k), \quad (2.22)$$

$$K'_u = Q_\infty b \exp[-b \epsilon_{eq}^p] - D_\infty a \exp[-a \epsilon_{eq}^p]. \quad (2.23)$$

If  $K'_u + H'_u \geq 0$ , the tangent modulus in (2.21) is nonnegative since  $E$  is a positive parameter. Therefore, we just seek to impose the condition  $K'_u + H'_u \geq 0$  since the case  $-(K'_u + H'_u) \geq E$  is ignored because we desire a nonsoftening response.

The value of  $K'_u + H'_u$  may be less than zero if the  $D_\infty$  and  $a$  parameters in the isotropic hardening rule are not properly chosen. Ensuring  $C_u^{ep} \geq 0$  is further complicated by the path-dependency of the kinematic hardening term. A key result used to resolve the path-dependency is that the least tangent modulus is found if the strain is monotonically increasing in tension or compression. This fact is shown in Figure 2.7 that illustrates the tangent modulus for monotonic tensile (solid line) and cyclic tension/compression loading histories (dashed line) using Equation 2.21. The peaks and plateaus in the tangent modulus of the cyclic loading history shown in this figure correspond to elastic unloading/reloading. In turn, the plateaus are followed by a gradual decrease in the value of  $C_u^{ep}$  to the limit of monotonic loading with further plastic straining. From Equation 2.7, the monotonic tensile loading provides the lower-bound tangent modulus at all points because reversal in the loading direction decreases the value of  $\alpha$ , thereby increasing the value of  $H'_u$  in Equation 2.22. It follows that the material is nonsoftening under uniaxial loading for all strain histories if the minimum of the monotonic tangent modulus is restricted to be always nonnegative.

Monotonic tensile/compressive loading from an initial state of zero plastic strain is used as a starting point to develop the parameter constraints. Under these two assumptions, the uniaxial kinematic hardening modulus is defined by Equation 2.24,

$$H'_{u,mono} = \sum_k \left( C_k \exp[-\gamma_k \epsilon_{eq}^p] \right), \quad (2.24)$$

while the isotropic hardening modulus is unaffected by this assumption. Replacing Equation 2.22 with Equation 2.24 in Equation 2.21, the constraint that defines nonsoftening behav-

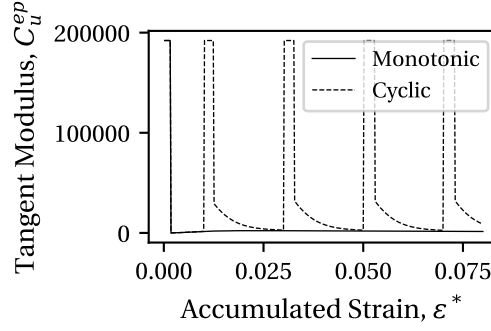


Figure 2.7 – Tangent modulus of the proposed material model subjected to monotonic and cyclic loading histories.

ior is provided in Equation 2.25,

$$\hat{g} = D_{\infty} a \exp \left[ -a \varepsilon_{eq}^p \right] - Q_{\infty} b \exp \left[ -b \varepsilon_{eq}^p \right] - \sum_k \left( C_k \exp \left[ -\gamma_k \varepsilon_{eq}^p \right] \right) \leq 0. \quad (2.25)$$

This constraint implies that the gain in tangent modulus from isotropic and kinematic hardening outweighs the loss from the  $D_{\infty}$  term.

Constraint  $\hat{g}$  defined in Equation 2.25 is still challenging to impose due to its dependency on  $\varepsilon_{eq}^p$ . Two relatively simple constraints that do not depend on  $\varepsilon_{eq}^p$  are developed through an additional assumption that  $a > b$  is placed on the isotropic hardening rate parameters. The assumption  $a > b$  implies that the reduction in yield surface associated with the  $D_{\infty}$  term occurs faster than the increase in the yield surface due to cyclic hardening associated with  $Q_{\infty}$ . This realization is supported by tests on mild steel coupons, and is implied by the behavior shown in Figure 2.3. The relation  $a > b$  is not directly imposed as a constraint to keep the UVC model for more general applications (e.g., for materials exhibiting cyclic softening), however, the calibration results shown later verify this assumption. The two constraints are now presented and afterwards they are proven to provide a nonsoftening response regardless of the applied loading.

Constraints proposed in Equations 2.26 and 2.27 are sufficient to ensure hardening of the material for all feasible strain histories:

$$g_1 = \hat{g} \Big|_{\varepsilon_{eq}^p=0} = -Q_{\infty} b - \sum_k (C_k) + D_{\infty} a \leq 0, \quad (2.26)$$

$$g_2 = \frac{\partial \hat{g}}{\partial \varepsilon_{eq}^p} \Big|_{\varepsilon_{eq}^p=0} = Q_{\infty} b^2 + \sum_k (C_k \gamma_k) - D_{\infty} a^2 \leq 0. \quad (2.27)$$

Note that the constraints  $g_1$  and  $g_2$  are defined in their standard form (i.e.,  $g \leq 0$ ) to be compatible with standard optimization algorithms in anticipation of the calibration procedure

## Chapter 2. Constitutive modeling of structural steels: A nonlinear isotropic/kinematic hardening material model and its calibration

---

to follow. Constraint  $g_1$  ensures that  $C_u^{ep} \geq 0$  when  $\varepsilon_{eq}^p = 0$ , and constraint  $g_2$  ensures that  $\partial C_u^{ep} / \partial \varepsilon_{eq}^p \geq 0$  when  $\varepsilon_{eq}^p = 0$ . These constraints are interpreted to mean that  $g_1$  ensures that the initial tangent modulus is nonnegative, and  $g_2$  ensures that the tangent modulus is initially increasing.

A rigorous evaluation of  $g_1$  and  $g_2$  follows two arguments based on the relationship between the magnitude of the rate parameter  $a$  to the rate parameters  $\gamma_k$ . In what follows,  $a > b$  is always assumed to reduce the number of possible minima to  $C_u^{ep}$  (Hartloper et al., 2019b). The first argument is based on the assumption that  $a \geq \max \gamma_k$ . In this case it can be shown that there is one root to  $C_u^{ep}$  and it is a local maximum of Equation 2.21 (Hartloper et al., 2019b). Therefore, the minimum of  $C_u^{ep}$  occurs as  $\varepsilon_{eq}^p \rightarrow \infty$ ; however, since  $C_u^{ep} \rightarrow 0$  as  $\varepsilon_{eq}^p \rightarrow \infty$ , the tangent modulus is always nonnegative. Accordingly, if  $C_u^{ep} \geq 0$  when  $\varepsilon_{eq}^p = 0$ , the material is always nonsoftening when  $a \geq \max \gamma_k$ .

The second argument is based on the assumption that  $a < \max \gamma_k$ . In this case, there are either zero or two roots to  $C_u^{ep}$  (Hartloper et al., 2019b). For zero roots,  $C_u^{ep} > 0$  for all  $\varepsilon_{eq}^p > 0$ . For two roots, it can be shown that the minimum occurs at a plastic strain less than the maximum, i.e.,  $\varepsilon_{r,min} < \varepsilon_{r,max}$ , where  $C_u^{ep}$  takes local minimum and maximum values at  $\varepsilon_{r,min}$  and  $\varepsilon_{r,max}$ , respectively. The minimum is avoided for physically permissible values of  $\varepsilon_{eq}^p$  if the slope of the tangent modulus,  $\partial C_u^{ep} / \partial \varepsilon_{eq}^p$ , is initially greater than zero. This result follows from Equation 2.6 since  $\varepsilon_{eq}^p \geq 0$  by definition. Therefore, if  $C_u^{ep} > 0$  and  $\partial C_u^{ep} / \partial \varepsilon_{eq}^p > 0$  when  $\varepsilon_{eq}^p = 0$ , the material is always hardening when  $a < \max \gamma_k$ .

The above arguments prove that constraints  $g_1$  and  $g_2$  ensure nonsoftening for monotonic uniaxial loading. Since monotonic loading gives the lower-bound of  $C_u^{ep}$ , we conclude that these constraints ensure nonsoftening for all uniaxial load histories. Specification of these two constraints is only possible if the parameters  $D_\infty$  and  $a$  are added to the original Voce-Chaboche model, otherwise more than two roots to  $\partial C_u^{ep} / \partial \varepsilon_{eq}^p$  may exist. Constraints  $g_1$  and  $g_2$  will later be used in the identification of material parameters based on uniaxial coupon tests.

### Multiaxial loading

Uniaxial results are extended for multiaxial loading based on classical uniqueness of the elastoplastic initial boundary value problem. The condition for uniqueness in Equation 2.28 is that the second-order work density is nonnegative (Simo and Hughes, 1998),

$$\dot{\boldsymbol{\sigma}} : \dot{\boldsymbol{\varepsilon}} = \dot{\boldsymbol{\varepsilon}} : \mathbf{C}^{ep} : \dot{\boldsymbol{\varepsilon}} \geq 0, \quad (2.28)$$

where  $\mathbf{C}^{ep}$  is the fourth-order tensor of *continuum* elastoplastic tangent moduli. The uniaxial interpretation of Equation 2.28 to be true for all strain histories is that  $C_u^{ep} \geq 0$  (i.e., nonsoftening), and for multiaxial loading that the tensor of elastoplastic tangent moduli is positive

semidefinite. We now make use of the property that positive semidefinite matrices have nonnegative eigenvalues to show that condition (2.28) is satisfied for multiaxial loading.

Neilsen and Schreyer (1993) provide two key results. First, that the minimum eigenvalue of  $\mathbf{C}^{ep}$  does not depend on the direction of loading for a von Mises yield condition and an associative flow rule. Second, that the sign of the minimum eigenvalue of  $\mathbf{C}^{ep}$  is equal to the sign of the combined hardening modulus (i.e., the sum of kinematic and isotropic moduli). Therefore,  $K'_u + H'_u \geq 0$  implies that  $\mathbf{C}^{ep}$  is positive semidefinite for the proposed material model since the minimum eigenvalue is nonnegative. Nonsoftening in the uniaxial stress state enforced by the constraints defined in Equations 2.26 and 2.27, therefore, also enforces the uniqueness condition in Equation 2.28 for multiaxial loading.

## 2.4 Calibration of material model parameters

### 2.4.1 Methodology

Model parameters are ideally calibrated from several markedly different load protocols for material models to be representative of material response under random strain histories. The inverse problem of determining the model parameters is stated as a constrained minimization, where the objective is to minimize the difference between the material model prediction and the test data, and the constraints impose that the material model is at no point softening. A gradient-based optimization approach using algorithmic differentiation is found to be most effective for similar problems (de Castro e Sousa et al., 2020), therefore a similar strategy is utilized herein.

The minimization problem to be solved is defined in (2.29),

$$\underset{\mathbf{x} \in \mathbb{R}^n}{\text{minimize}} \quad f(\mathbf{x}) \quad (2.29a)$$

$$\text{subject to} \quad \mathbf{g}(\mathbf{x}) \leq \mathbf{0}, \quad (2.29b)$$

where  $\mathbf{x} = [E, \sigma_{y,0}, Q_\infty, b, D_\infty, a, C_1, \gamma_1, \dots, C_{N_k}, \gamma_{N_k}]$  is the vector of  $n$  parameters for the UVC model under uniaxial loading,  $f(\mathbf{x}) : \mathbb{R}^n \rightarrow \mathbb{R}$  is the objective function, and  $\mathbf{g}(\mathbf{x}) : \mathbb{R}^n \rightarrow \mathbb{R}^m$  is a vector valued function of constraints (i.e., there are  $m$  constraints defined). The goal of the proposed calibration procedure is to find the set of material parameters  $\mathbf{x}$  that is a local minimum of the objective function and satisfy the nonsoftening constraints.

The objective function defined in Equation 2.30 is in keeping with the definition in de Castro e Sousa et al. (2020),

$$f(\mathbf{x}) = \sum_{j=1}^{N_T} \frac{\int_0^{\epsilon_j^*} \left( \sigma_j^{model}(\epsilon_j; \mathbf{x}) - \sigma_j^{test} \right)^2 d\epsilon^*}{\int_0^{\epsilon_j^*} d\epsilon^*}, \quad (2.30)$$

## Chapter 2. Constitutive modeling of structural steels: A nonlinear isotropic/kinematic hardening material model and its calibration

---

where  $N_T$  load histories are considered,  $\sigma_j^{model}(\epsilon_j; \mathbf{x})$  is the stress from the UVC model given strain history  $\epsilon_j$  and parameters  $\mathbf{x}$ ,  $\sigma_j^{test}$  is the stress recorded in the uniaxial test  $j$ , and  $\epsilon^*$  is the accumulated strain

$$\epsilon_j^* = \int_0^{t_j} |\dot{\epsilon}_j| d\tau. \quad (2.31)$$

The objective function  $f(\mathbf{x})$  represents the total squared-area between the model prediction and test data normalized by the total accumulated strain for several tests (see the shaded region in Figure 2.1b for a single test). Constraints to impose nonsoftening are considered for the proposed model,  $\mathbf{g}(\mathbf{x}) = [g_1, g_2]$  defined by Equations 2.26 and 2.27. The parameter space is further limited to  $\mathbf{x} > \mathbf{0}$  to obtain physically meaningful results and to ensure convergence of the return mapping algorithm.

Problem (2.29a) is solved in multiple steps because it is challenging to obtain a solution due to the nonlinearity of the constraints and the indefiniteness of the Hessian of  $f(\mathbf{x})$  (de Castro e Sousa et al., 2020). Numerical testing reveals that solving the problem (2.29a) subjected to (2.29b) directly is not practical, and that the solution time can be significantly reduced by using an appropriate starting point (Hartloper et al., 2019b). The first step is to solve the problem (2.29a) using the Voce-Chaboche model (i.e., without  $D_\infty$  and  $a$ ) following the methodology in de Castro e Sousa et al. (2020). The starting point to the Voce-Chaboche model is chosen as a perfectly plastic material with nominal elastic modulus and initial yield stress. All hardening parameters are initially set to  $10^{-1}$  to represent the perfectly plastic conditions. Once the solution point using the Voce-Chaboche model has been found, the added parameters that constitute the UVC model are set to  $D_\infty = 10^{-1}$  and  $a = 200$ , and this point is denoted as  $\mathbf{x}_{ini}$ . The choice of  $a$  is made on the observation that the Luders strain is typically around 2 % strain for mild steels, corresponding to  $a \approx 230$  for 99 % saturation of  $D_\infty$ .

The second step is to solve problem (2.29a) subjected to (2.29b) with the UVC model starting from  $\mathbf{x}_{ini}$  using the nonlinear interior point trust-region optimizer (NITRO) algorithm described in Byrd et al. (1999) and implemented in the Python package Scipy (Jones et al., 2018). The NITRO algorithm is found to be the most efficient when compared to alternative constrained trust-region (Conn et al., 2000; Bierlaire, 2015) and sequential quadratic programming methods (Bierlaire, 2015). An additional benefit of this algorithm is that solution points can be found starting from infeasible starting points. Solution points are defined by the local minima of the objective function. Minima are defined by the first-order necessary condition,

$$\|\nabla f(\mathbf{x})\| < \epsilon_{tol}, \quad (2.32)$$

and the second-order necessary condition that the Hessian of  $f(\mathbf{x})$  is positive definite. The symbol  $\nabla(\cdot)$  in (2.32) is the gradient operator, and the tolerance is initially defined as  $\epsilon_{tol} = 10^{-8}$ . Even starting from  $\mathbf{x}_{ini}$ , obtaining a solution to Problem (2.29) to  $10^{-8}$  is challenging due to the aforementioned nonconvexity of the objective function and nonlinearity of the



constraints. Experience shows that satisfactory solutions can be found by successively relaxing the tolerance from  $10^{-8}$  to  $10^{-2}$  after 300 iterations, then finally to  $5 \times 10^{-2}$  after a further 1000 iterations. The aforementioned calibration procedure is implemented in the open-source Python package RESSPyLab (de Castro e Sousa et al., 2019).

### 2.4.2 Summary of results for structural steel materials

#### Definition of metrics

Metrics are defined to quantify the model fit and hardening characteristics of each steel material. The quality of fit is defined by the  $\bar{\varphi}$  metric in (2.33) that represents the model error normalized by the total squared-area under all the stress-strain curves in the data set,

$$\bar{\varphi} = \sqrt{f(\mathbf{x}) \times \left( \sum_{j=1}^{N_T} \frac{\int_0^{\varepsilon_j^*} (\sigma_j^{test})^2 d\varepsilon^*}{\int_0^{\varepsilon_j^*} d\varepsilon^*} \right)^{-1}}. \quad (2.33)$$

A value of  $\bar{\varphi} = 0$  indicates a perfect fit, and increasing values indicate decreasing qualities of fit.

The following metrics are defined in terms of the equivalent plastic strain assuming monotonic loading for a fixed set of parameters. Total increase in stress due to hardening is described by the metric (2.34),

$$\sigma_{hard}(\varepsilon_{eq}^p) = Q_\infty \left( 1 - \exp \left[ -b\varepsilon_{eq}^p \right] \right) + \sum_k C_k / \gamma_k \left( 1 - \exp \left[ -\gamma_k \varepsilon_{eq}^p \right] \right), \quad (2.34)$$

the ratios of isotropic and kinematic contributions to the total hardening are respectively defined by the metrics (2.35) and (2.36),

$$\rho_{iso}(\varepsilon_{eq}^p) = \frac{Q_\infty \left( 1 - \exp \left[ -b\varepsilon_{eq}^p \right] \right)}{\sigma_{hard}(\varepsilon_{eq}^p)}, \quad (2.35)$$

$$\rho_{kin}(\varepsilon_{eq}^p) = \frac{\sum_k C_k / \gamma_k \left( 1 - \exp \left[ -\gamma_k \varepsilon_{eq}^p \right] \right)}{\sigma_{hard}(\varepsilon_{eq}^p)}. \quad (2.36)$$

A value of  $\rho_{kin} = 1$  ( $\rho_{iso} = 0$ ) indicates that there is only kinematic hardening present in the material. The total stress at a particular value of  $\varepsilon_{eq}^p$  is defined by (2.37),

$$\sigma_{total}(\varepsilon_{eq}^p) = \sigma_{y,0} + \sigma_{hard}(\varepsilon_{eq}^p) - D_\infty \left( 1 - \exp \left[ -a\varepsilon_{eq}^p \right] \right), \quad (2.37)$$

## Chapter 2. Constitutive modeling of structural steels: A nonlinear isotropic/kinematic hardening material model and its calibration

---

and the ratio of stress at saturation to the initial yield stress is given in (2.38),

$$\rho_{yield}(\varepsilon_{eq}^p) = \frac{\sigma_{total}(\varepsilon_{eq}^p)}{\sigma_{y,0}}. \quad (2.38)$$

A value of  $\rho_{yield} = 2$  would indicate that the stress at the chosen value of  $\varepsilon_{eq}^p$  is twice the initial yield stress.

All the above metrics can be evaluated at any particular  $\varepsilon_{eq}^p$  value. The choice of saturation (i.e.,  $\varepsilon_{eq}^p \rightarrow \infty$ ), indicated by the *sat* superscript, is made for convenience and to compare with de Castro e Sousa et al. (2020). However, the choice of  $\varepsilon_{eq}^p \approx 0.15$  could be more representative of the ultimate material behavior.

### Results and discussion

Parameters for the UVC model based on twelve sets of coupon tests on mild structural steels from Europe, North America, and Japan are provided and evaluated in this section. Nine steel materials are included in this database. These steels can be classified as either carbon structural steels (e.g., S355J2+N, A992 Gr. 50, A500 Gr. B, BCP325, BCR295), or high-strength low-alloy structural steels (e.g., S460NL, S690QL) according to ASTM (2018). The high yield point (HYP) steel is a mild steel for structural applications where the yield stress is enhanced through a thermomechanical control process and grain refinement (Suzuki et al., 2008; Kanno, 2016; Suzuki, 2018). The steel material type, nominal yield stress, load protocols used for calibration, and evaluation metrics for all the data sets are summarized in Table 2.1. Up to ten different strain-based load protocols deemed to be representative of strain histories in steel components subjected to earthquake loading are utilized for each material based on the suggestion in Suzuki (2018). Definitions for the load protocols are found in de Castro e Sousa et al. (2020).

Parameters for the twelve data sets are provided in Table 2.2, note that the identification (ID) number for all the steel materials in this table are in correspondence with Table 2.1. Table 2.3 collects the yield stress measured using the 0.2 % offset method for each dataset (averaged over all tests in each set), along with the  $\sigma_{y,0}$  values and error metric values  $\bar{\varphi}$  for the Voce-Chaboche and UVC models. This table shows that the UVC  $\sigma_{y,0}$  is only 4 % different from the average measured yield stress, while the Voce-Chaboche  $\sigma_{y,0}$  is 17 % different from the average measured yield stress. A 4 % difference in the initial yield stress is notable accuracy, especially considering the discontinuous nature of the stress in the plateau region measured by the 0.2 % offset method. Furthermore, the UVC model leads to a relative reduction in the normalized error metric by about 20 % on average compared to the Voce-Chaboche model.

The proposed UVC material model provides a better fit of the test data, a better estimation of the initial yield stress, and better approximates the initial plateau found in mild carbon steels

## 2.4. Calibration of material model parameters

when compared with the Voce-Chaboche model. Several key points are now highlighted using the Voce-Chaboche model parameters from ten of the same data sets in de Castro e Sousa et al. (2020) as a basis for comparison. Goodness of fit for all the load histories considered is shown in Figures 2.8 and 2.9 for data sets from the flange and web of an HEB500 section that were tested as a part of the current study (IDs 3 and 4 in Table 2.1). In each of these figures, VC is the Voce-Chaboche model prediction. Results from two data sets are shown here for brevity, but comparisons of the remaining data sets are provided in Hartloper et al. (2019b). Although differences between the original and updated models may seem entirely insignificant, in all these figures notice that the plateau yield stress is closely predicted by the updated material model, whereas the same is not true for the original model. A case study later demonstrates that there is a significant impact on the prediction of wide flange column post-peak behavior despite the closeness between the two material predictions.

Values of the ratio of isotropic-to-total hardening,  $\rho_{iso}^{sat}$ , in Table 2.1 show that mild carbon structural steels have a higher ratio of isotropic hardening than the high-strength low-alloy steels. The  $\rho_{iso}^{sat}$  metric is around 25–40 % for the mild carbon structural steels (e.g., S355J2+N, A992 Gr. 50), and is negligible for high-strength steels (e.g.,  $\rho_{iso}^{sat} = 0$  for S690QL). One exception to this observation is the BCR295 data set that does not exhibit cyclic hardening because the coupons were sampled from the corners of a cold-pressed hollow structural section. Recalling that isotropic hardening is a reflection of the amount of cyclic hardening exhibited by the physical material, these results suggest that high-strength steels do not exhibit much cyclic hardening. This finding is in agreement with that of de Castro e Sousa et al. (2020) for the original Voce-Chaboche model, and is visually confirmed by the plots of stress-strain data for the S690QL steel (Hartloper et al., 2019b).

Comparing the UVC and Voce-Chaboche models, there is a larger portion of isotropic hardening in the updated model, and the total stress at saturation is similar. The value of  $\rho_{iso}^{sat}$  varies between 20–25 % for S355J2+N and A992 Gr. 50 steels in de Castro e Sousa et al. (2020) for the Voce-Chaboche model. Ratios of isotropic-to-kinematic hardening tend to be higher in the UVC model since  $Q_{\infty}$  is increased to compensate for the negative effect of  $D_{\infty}$ . Comparing  $\sigma_{total}^{sat}$  from Table 2.1 with their equivalent values in de Castro e Sousa et al. (2020), there is an average of 1 % difference between the two models across all the comparable material data sets. These two results suggest that although the composition of total hardening is different between the two models, the ultimate stress at saturation is comparable.

A reduction in the yield surface is observed in all of the evaluated materials, and the magnitude of  $Q_{\infty}$  seems to be roughly equal to that of  $D_{\infty}$  for the carbon steels (apart from BCR295 due to cold working). Isotropic hardening parameter  $Q_{\infty}$  is greater than  $D_{\infty}$  in seven out of the twelve data sets for the updated material model. These results imply that the decrease in the yield surface due to discontinuous yielding is roughly balanced by the increase due to cyclic hardening. The magnitude of  $D_{\infty}$  is itself significant for all the data sets,

## Chapter 2. Constitutive modeling of structural steels: A nonlinear isotropic/kinematic hardening material model and its calibration

Table 2.1 – Summary of steel material database and metrics for the proposed material model.

ID	Material	$f_{y,n}$ [MPa]	Ref	LP	$\bar{\varphi}$ [%]	$\sigma_{total}^{sat}$ [MPa]	$\sigma_{hard}^{sat}$ [MPa]	$\rho_{yield}^{sat}$	$\rho_{iso}^{sat}$	$\rho_{kin}^{sat}$
1	S355J2+N 50 mm plate	355	1	1–10	6.33	701.93	462.91	2.11	0.26	0.74
2	S355J2+N 25 mm plate	355	1	1–10	6.53	681.02	475.97	2.01	0.28	0.72
3	S355J2 HEB500 flange	355	3	1,2,5,6,9	3.96	636.59	417.72	2.02	0.33	0.67
4	S355J2 HEB500 web	355	3	1,1–3,5–9	5.65	548.55	333.94	1.64	0.42	0.58
5	S460NL 25 mm plate	460	1	1,3–7,9,10	5.46	818.32	515.76	1.86	0.19	0.81
6	S690QL 25 mm plate	690	1	1,3–7,9,10	6.20	896.50	343.41	1.31	0.00	1.00
7	A992 Gr.50 W14X82 web	345	2	1,2,5,6,9	5.21	643.27	407.93	1.70	0.30	0.70
8	A992 Gr.50 W14X82 flange	345	2	1,2,5,6,9	4.76	786.49	548.72	2.10	0.26	0.74
9	A500 Gr.B HSS305X16	315	2	1,2,5,6,9	4.99	832.57	558.90	2.57	0.41	0.59
10	BCP325 22 mm plate	325	2	1,2,5,6,9	3.89	662.04	399.96	1.80	0.28	0.72
11	BCR295 HSS350X22	295	2	1,2,5,6,9	5.21	996.09	687.18	2.42	0.00	1.00
12	HYP400 27 mm plate	400	2	1,2,5,6,9	4.67	797.99	452.81	1.76	0.14	0.86

Notes: Steels 1–6 are European, 7–9 are North American, and 10–12 are Japanese;

HSS = hollow structural section;  $f_{y,n}$  = nominal yield stress;

LP = load protocols tested, see de Castro e Sousa et al. (2020) for definitions;

Ref: 1-Grigoriou and Lignos (2017), 2-Suzuki (2018), 3-Conducted as a part of this study.

indicating that there is some reduction in the yield surface even in high strength steels, e.g., S690QL steel. Although this material does not visually exhibit discontinuous yielding or cyclic hardening (i.e.,  $Q_{\infty} \approx 0$ ), the fact that  $D_{\infty} > 0$  suggests that interstitial impurities may still play a role in restricting dislocation movement that diminishes with increasing accumulated plastic strain. Applications of the proposed material model to other steels that contain a reduction in the yield surface, e.g., due to cyclic softening, is left for future investigations.

### 2.4.3 A note on the number of backstresses

At least two backstresses are necessary to adequately model the kinematic hardening observed in mild steels using the UVC model. One backstress is found to be insufficient to represent

## 2.4. Calibration of material model parameters

Table 2.2 – Proposed material model parameters for structural steels.

ID	$E$ [GPa]	$\sigma_{y,0}$ [MPa]	$Q_\infty$ [MPa]	$b$	$D_\infty$ [MPa]	$a$	$C_1$ [MPa]	$\gamma_1$	$C_2$ [MPa]	$\gamma_2$
1	185.97	332.18	120.48	8.14	93.15	261.75	21102.00	173.60	2300.60	10.42
2	197.41	338.80	134.34	14.71	133.75	229.25	26242.00	199.04	2445.30	11.66
3	192.13	315.04	138.01	11.36	96.16	223.66	18587.84	257.31	1351.98	6.52
4	199.68	334.94	139.32	14.07	120.33	274.73	28528.03	315.17	2569.45	24.68
5	187.61	439.20	97.35	14.02	136.64	226.40	26691.00	188.75	2892.40	10.44
6	188.63	685.39	0.11	0.11	132.30	285.15	34575.00	185.16	3154.20	20.14
7	210.74	378.83	122.63	19.74	143.49	248.14	31638.00	277.32	1548.60	9.04
8	191.02	373.72	141.47	15.20	135.95	211.16	25621.00	235.12	942.18	3.16
9	191.21	324.09	228.02	0.11	50.41	270.40	17707.00	207.18	1526.20	6.22
10	178.61	368.03	112.25	10.78	105.95	221.92	20104.00	200.43	2203.00	11.76
11	178.74	412.21	0.09	0.09	103.30	212.83	20750.59	225.26	1245.04	2.09
12	189.36	454.46	62.63	16.57	109.28	145.74	13860.00	141.61	1031.10	3.53

Note: ID column corresponds to Table 2.1.

Table 2.3 – Comparison of yield stresses and normalized error metrics for the UVC and Voce-Chaboche (VC) models.

ID	$f_{ym,a}$ [MPa]	$\sigma_{y,0}^{UVC}$ [MPa]	$\sigma_{y,0}^{VC}$ [MPa]	Error, $f_y$ UVC [%]	Error, $f_y$ VC [%]	$\bar{\varphi}^{UVC}$ [%]	$\bar{\varphi}^{VC}$ [%]	Error, $\bar{\varphi}$ [%]
1	339	332	271	2	18	6.33	6.37	-1
2	358	339	265	5	22	6.53	6.70	-3
3	305	315	246	3	22	3.96	4.63	-14
4	350	335	252	4	25	5.65	6.16	-8
5	446	439	359	1	18	5.46	6.32	-14
6	714	685	603	4	12	6.20	7.95	-22
7	386	379	339	2	10	5.21	7.01	-26
8	393	374	318	5	15	4.76	7.31	-35
9	343	324	301	6	7	4.99	6.86	-27
10	380	368	306	3	17	3.89	5.05	-23
11	392	412	346	5	16	5.21	8.38	-38
12	463	454	376	2	17	4.67	5.31	-12
Avg.	-	-	-	4	17	-	-	-19

$f_{ym,a}$  = average yield stress for each data set;

$\sigma_{y,0}^{VC}$  and  $\bar{\varphi}$  taken from de Castro e Sousa et al. (2020);

Error,  $f_y$  UVC =  $|\sigma_{y,0}^{UVC} - f_{ym,a}|/f_{ym,a}$ ; Error,  $f_y$  VC =  $|\sigma_{y,0}^{VC} - f_{ym,a}|/f_{ym,a}$ ;

Error,  $\bar{\varphi}$  =  $(\bar{\varphi}^{UVC} - \bar{\varphi}^{VC})/\bar{\varphi}^{VC}$ .

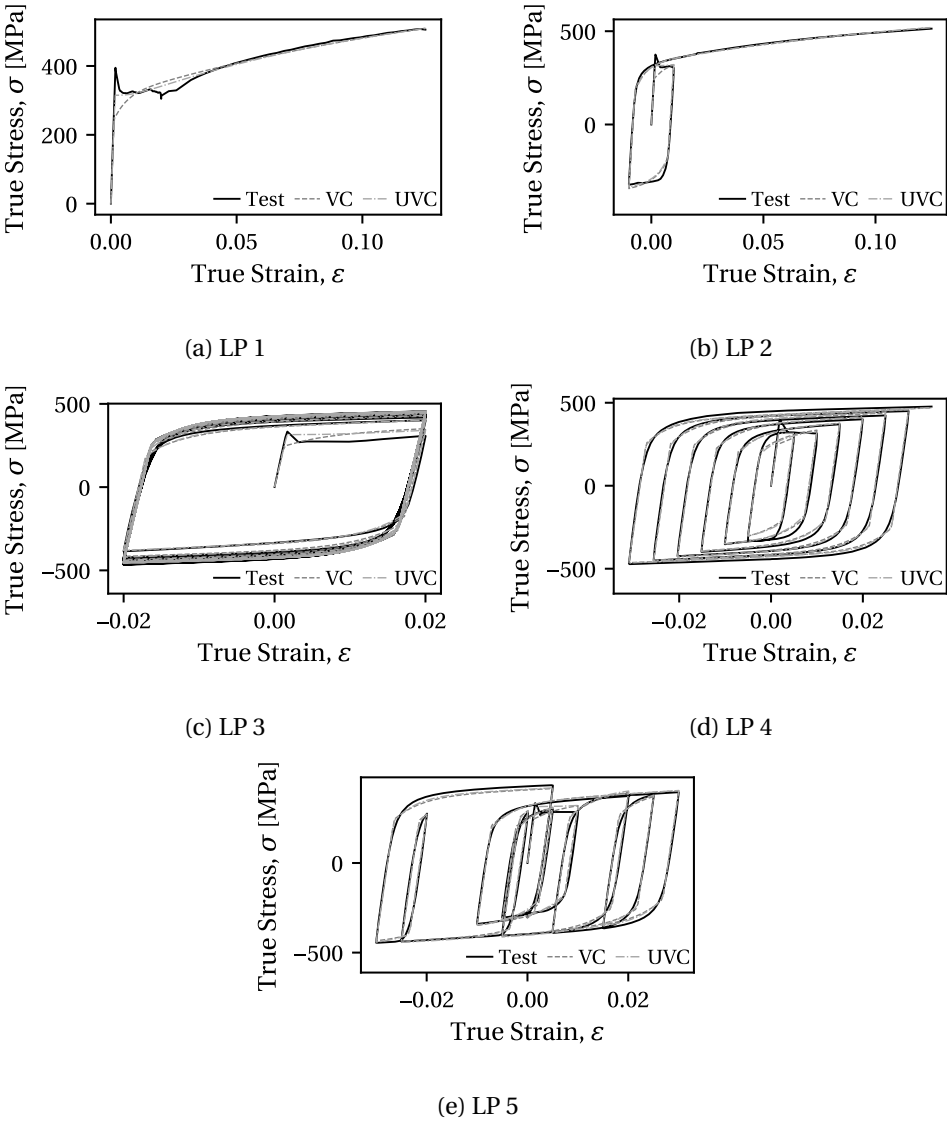


Figure 2.8 – Comparison of test data and model predictions for the S355J2 HEB500 flange data set.

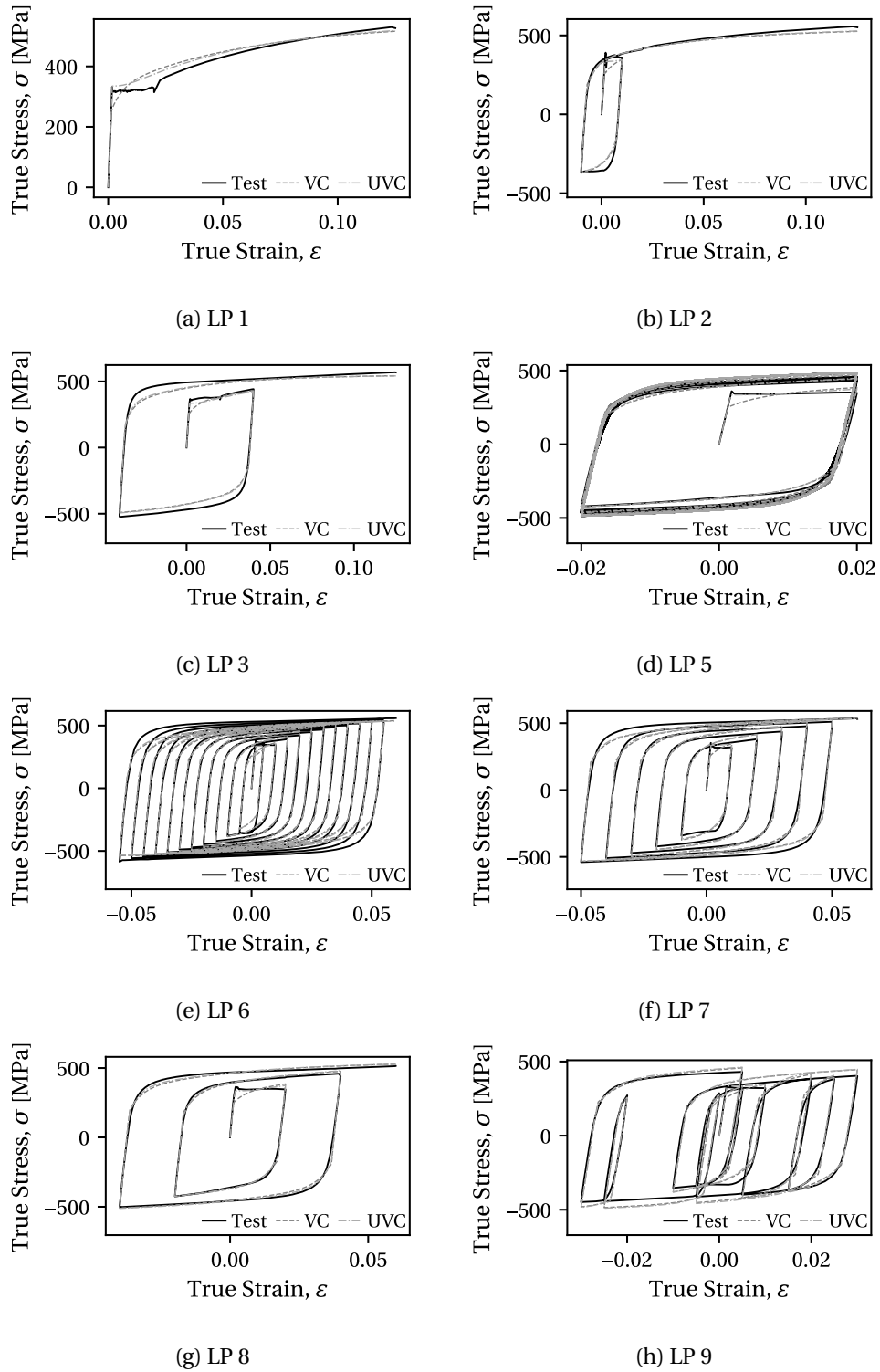


Figure 2.9 – Comparison of test data and model predictions for the S355J2 HEB500 web data set.

the kinematic hardening, leading to irrational estimates of other parameters (Hartloper et al., 2019b). There is little improvement in  $\bar{\varphi}$  when three backstresses are used, echoing the results from de Castro e Sousa et al. (2020) for the original Voce-Chaboche model. Two backstresses, therefore, provide an optimal mix of accuracy and efficiency, while adequately representing the kinematic hardening observed in the test data.

## **2.5 Finite element analysis case study and implications**

The sensitivity of CFE models to their initial material model assumptions is explored in this section through a parametric study. The evaluation is established by comparing the response of two column models with identical geometric characteristics: one using the Voce-Chaboche model, and the other with the UVC model. Variations in the material model parameters as well as the imperfections are considered in this study to conclude whether the differences in the observed behavior consistently arise between simulations carried out with the two material models.

The parametric study focuses on the simulated performance of an HEB500 cross section (similar to a W610X217, or W24X146, in North America) of 7000 mm length subjected to multiaxis loading. Relevant geometric characteristics of this column are provided in Table 2.4. In this table,  $A$  is the cross-sectional area,  $h$  is the section depth,  $b$  is the flange width,  $t_w$  is the web thickness,  $t_f$  is the flange thickness,  $h_1$  is the clear distance between flanges,  $L_b$  is the column unbraced length,  $i_z$  is the radius of gyration in the weak axis, and  $\bar{\lambda}_{LT}$  is the lateral-torsional buckling slenderness calculated according to Eurocode (CEN, 2005a). This cross section satisfies the Eurocode Class 1 criteria for the applied compression and bending (CEN, 2005a), and the AISC highly ductile classification criteria (AISC, 2016a). However, the column has relatively large member slenderness indicated by its  $L_b/i_z$  value, and is susceptible to lateral-torsional buckling (LTB) coupled with plastic local buckling since Eurocode indicates that inelastic LTB should occur when  $0.4 < \bar{\lambda}_{LT} < 1.2$ .

### **2.5.1 Modeling procedure**

Column models for the HEB500 column are developed following the guidelines in Elkady and Lignos (2018b) using the software Abaqus v6.14 (Dassault Systèmes, 2014). Adequacy of these guidelines for similar cross-sections has been established through validations with several columns (Elkady and Lignos, 2018b) and success by the first and third authors in winning a recent blind analysis competition (NIST/ATC, 2018). The models are comprised of quadrilateral reduced integration shell elements (S4R) with a mesh size of approximately 25 mm. Residual stresses are considered in the model based on the Young (1972) stress distribution since de Castro e Sousa and Lignos (2017) suggests that this distribution is adequate for HEB500 cross-sections.



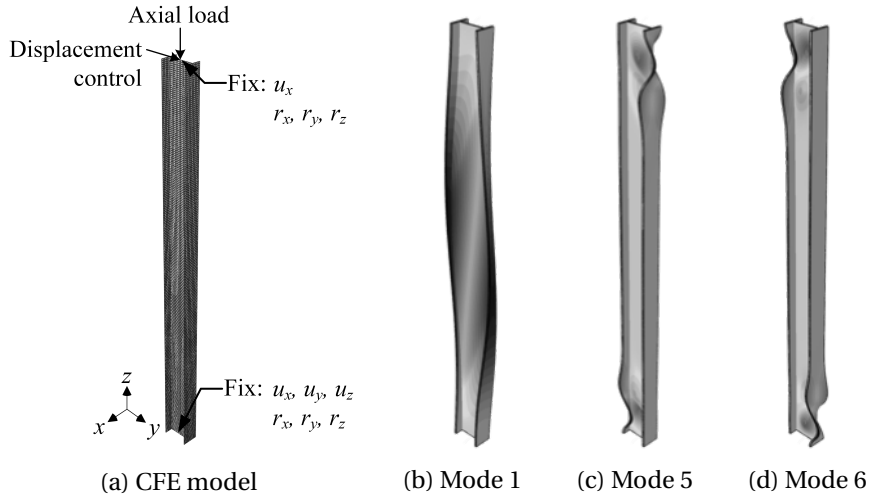


Figure 2.10 – Continuum finite element model and elastic buckling modes for the HEB500 column case study.

Two material data sets are chosen to be consistent with the HEB500 cross section. Parameters constituting Material Set 1 are chosen as the S355J2+N 25 mm plate data set because the plate thickness best matches the flange and web thickness of the HEB500 section given the existing data. Material Set 2 is based on material tests conducted as a part of the present study using 12 and 20 mm diameter round bar coupons (diameter in the reduced section of 6 and 10 mm, respectively) from the web and flange of an HEB500. A second set of parameters is used to establish confidence that the results of this case study hold for multiple data sets. Material parameters for the Voce-Chaboche model are provided in Table 2.5 using the procedure in de Castro e Sousa et al. (2020), and parameters for the UVC model are taken from Table 2.2.

Loading and boundary conditions on the column models are as shown in Figure 2.10a. Rigid-body constraints are applied to the nodes at the top and base of the CFE models to avoid stress concentrations in these regions; all loads and boundary conditions are then applied at the centroid of the cross section. Fixed-end boundary conditions are assumed and the same constant compressive axial load is applied to all models based on 20 % of the axial load at first yield,  $A\sigma_{y,0}$ , where  $A$  is the nominal area and  $\sigma_{y,0}$  is taken as the value from the updated material model for the S355J2+N 25 mm plate data set from Table 2.2. The symmetric cyclic lateral displacement history from Chapter K of AISC (2016a) is applied at the column top after the application of the gravity load as depicted in Figure 2.10a. Default convergence criteria in Abaqus v6.14 is used with automatic time-stepping, however, outputs are generated at the exact same analysis times to make the analyses as comparable as possible.

## Chapter 2. Constitutive modeling of structural steels: A nonlinear isotropic/kinematic hardening material model and its calibration

Table 2.4 – Cross section properties of an HEB500, 7000 mm length.

$A$ [mm <sup>2</sup> ]	$h$ [mm]	$b$ [mm]	$t_w$ [mm]	$t_f$ [mm]	$h_1/t_w$	$b/2t_f$	$L_b/i_z$	$\bar{\lambda}_{LT}$
23900	500	300	14.5	28	26.9	5.4	72.7	1.0

Table 2.5 – Original Voce-Chaboche model parameters for the case study material sets.

Material	$E$ [GPa]	$\sigma_{y,0}$ [MPa]	$Q_\infty$ [MPa]	$b$	$C_1$ [MPa]	$\gamma_1$	$C_2$ [MPa]	$\gamma_2$
S355J2 HEB500 flange	191.85	245.50	119.77	8.67	14019.86	205.39	1247.05	4.45
S355J2 HEB500 web	198.39	251.74	118.43	10.85	17876.51	236.30	2582.61	24.01
S355J2+N 25 mm plate	191.52	265.29	104.44	11.63	12997.99	99.52	1560.41	7.35

### Geometric imperfections

Geometric imperfections are included to induce LTB and local buckling by scaling and superimposing relevant elastic buckling modes (Elkady and Lignos, 2018b). These geometric imperfections are determined by first applying the axial load, then applying a lateral force and conducting an elastic eigenvalue buckling analysis in Abaqus. Modes 1 and 2 corresponding to LTB, and modes 5 and 6 corresponding to local buckling are visually selected. Modes 1, 5, and 6 are shown in Figure 2.10—note that mode 2 is simply the inverse of mode 1. Both modes 1 and 2 are applied independently to the model to consider the random nature of imperfections that could induce LTB in either of the two directions.

For the purpose of this parametric study, geometric imperfections with amplitudes below the manufacturing limits, e.g., CEN (1993), are applied to the column models. The imperfection amplitudes are based on the mean and standard deviation of previously measured imperfections. Five scale factors are considered for both the LTB and local buckling modes,  $a_\mu$ ,  $a_{\mu\pm\sigma}$  and  $a_{\mu\pm\sigma/2}$ , where  $a$  is the scale factor, subscripts  $\mu$  and  $\sigma$  denote the mean standard deviation of the measurements, respectively. The derivation of the imperfection scale factors is now discussed.

Twist measurements from ten full-scale steel columns featuring cross-sections similar to the present study are used to deduce the LTB imperfections scale factors (Elkady, 2016; Elkady and Lignos, 2018a). LTB imperfection scale factors are related to the measured angles of twist through Equation 2.39,

$$a^{LTB} = \frac{\theta_{applied}}{\theta_{ref}}, \quad (2.39)$$

where  $a^{LTB}$  is the scale factor applied to modes 1 or 2,  $\theta_{applied}$  is the intended rotation at column mid-height based on the measured imperfections, and  $\theta_{ref}$  is an estimate of the mid-height rotation for modes 1 and 2 from the buckling analysis. Note that Elkady (2016)

## 2.5. Finite element analysis case study and implications

recorded the initial rotational imperfection at the column top, therefore, the values at mid-height are assumed to be one-half of the values reported at the top. The reference twist angle corresponding to the imperfections in modes 1 and 2 are deduced using (2.40) based on the rotation of the web about its centerline,

$$\theta_{ref} = \arcsin \left[ \frac{2u_w}{h - t_f} \right] = 0.004 \text{ rad}, \quad (2.40)$$

where  $u_w$  is the displacement of the web from the HEB500 model at mid-height due to buckling mode 1. Equation 2.40 is evaluated considering that  $u_w \approx 1.0 \text{ mm}$  due to the normalization of buckling modes in Abaqus. The mean twist for the LTB imperfection is calculated as 0.006 rad, and the standard deviation is 0.005 rad (Elkady, 2016). The scale factors for the LTB imperfections based on the mean and standard deviation using Equation 2.39 are provided in Table 2.6.

Measurements from six European steel wide flange sections are used to deduce the local imperfection scale factors. Local imperfection scale factors are related to the measured flange and web imperfections through Equation 2.41,

$$a^{loc} = \frac{\Delta_{applied}}{\Delta_{ref}}, \quad (2.41)$$

where  $a^{loc}$  is the scale factor applied to modes 5 and 6,  $\Delta_{applied}$  is the intended local imperfection amplitude, and  $\Delta_{ref} = 1.0 \text{ mm}$  is the maximum nodal displacement from modes 5 and 6. Hartloper and Lignos (2019) report the mean measured web imperfections amplitude as  $h/300$  and the standard deviation as  $h/1017$ . From the same study, the mean measured flange imperfection amplitude is  $b/250$ , and the standard deviation is  $b/466$ . The mean measured values are consistent with European manufacturing limits (CEN, 1993) as well as those proposed by Elkady and Lignos (2018b). The scale factors for the local imperfections based on the mean and standard deviation using Equation 2.41 are provided in Table 2.6.

### 2.5.2 Parametric study and results

Both the material properties and geometric imperfections are varied to investigate the consistency of the divergence in buckling modes. With this parametric study we vary the geometric imperfections within expected ranges for common steel profiles. This approach intends to show that if, for a range of variations in the geometric imperfections, there is a consistent divergence in the column behavior for different material models, then it can be reasonably concluded that the accuracy of the material model is the principal cause of the divergence. A total of 15 comparisons are conducted for each material set in which the geometric imperfection scale factors are varied equally for the columns using both the Voce-Chaboche and UVC models. Parameters from two material sets are chosen for a total of 30 comparisons. The

## Chapter 2. Constitutive modeling of structural steels: A nonlinear isotropic/kinematic hardening material model and its calibration

---

parametric study follows three steps for the Material Set 1 (S355J2+N, 25 mm plate). First, five comparisons are made using the imperfection scale factors given in Table 2.6 varying the LTB imperfection mode 1 with constant local imperfection geometry. Second, five comparisons are made in similar fashion but varying LTB mode 2 with constant local imperfection geometry. Third, five comparisons are made varying the local imperfection scale factors for modes 5 and 6 based on Table 2.6, with constant LTB imperfection mode 1 geometry. The same three steps are then carried out using Material Set 2 (S355J2 HEB500 flange and web).

Results from the parametric study indicate that while the pre-peak responses of the simulations are similar, there is a consistent divergence in the simulated buckling modes between the two columns that use different material representations. A comparison of the column base moment - chord rotation for Material Set 2 and all imperfections at mean amplitude is shown in Figure 2.11a. Typical deformed shapes observed from the analyses using the Voce-Chaboche and UVC material models are shown in Figures 2.11b and 2.11c, respectively. The similarity in the pre-peak responses between the two models may seem counterintuitive as the largest difference in material appears in the initial yield stress. However, the initial hardening of the Voce-Chaboche model is increased to compensate its lower initial yield stress so the overall pre-peak component response is relatively similar. Significant differences in the component behavior only arise in this case study after strength deterioration due to buckling in the component has occurred.

Divergence in the component simulations arises primarily due to the difference in initial yield stress between the two material models. Observe in Figures 2.11b and 2.11c that the extent of yielding along the column length from the ends, or plastic hinge length, is around three times greater when the Voce-Chaboche material model is used. Yielding is shown visually in these figures as the light gray regions. At the first excursion to -4 % chord rotation, the spread of plasticity is almost up to 80 % of the column half-length for the Voce-Chaboche model, whereas this value is only around 30 % for the UVC model. The long plastic hinge lengths in the model with the Voce-Chaboche material significantly reduce the torsional stiffness of the column. In-turn, this allows for the initiation of lateral-torsional buckling. Similar observations are made in Elkady and Lignos (2018a) with respect to full-scale wide flange column tests.

The increased initial yield stress of the UVC model does not allow for such a long plastic hinge length to form. Lateral-torsional buckling does not occur in this case, and deterioration in strength and stiffness is due to local buckling followed by column twisting. This case study shows that columns with relatively high member slenderness ratios (e.g.,  $L_b/i_z > 90$ ) can be sensitive to the difference in initial yield stress because these members are prone to experiencing coupled local and lateral-torsional buckling. Such components are, therefore, sensitive to the choice of material model parameters.

Consistency in the difference between simulated component responses is evaluated to

## 2.6. Discussion of results, limitations, and future work

Table 2.6 – Imperfection scale factors for lateral-torsional and local buckling modes.

Imperfection Mode	Basis of Imperfection Scale Factor				
	$\mu - \sigma$	$\mu - \sigma/2$	$\mu$	$\mu + \sigma/2$	$\mu + \sigma$
Lateral-torsional Buckling Modes (1, 2), $a^{LTB}$	0.24	0.83	1.40	2.00	2.59
Local Buckling Modes (5, 6), $a^{loc}$	0.53	0.87	1.20	1.54	1.87

Note:  $\mu$ -mean of measurements,  $\sigma$ -standard deviation of measurements.

assess if the aforementioned sensitivity holds for different material parameters and imperfection geometries. Results from the parametric study are compiled in Table 2.7 in terms of an error metric defined by Equation 2.42 that measures the relative difference in moment between the two analyses over the common load history,

$$E_m = \frac{\|\mathbf{M}_{UVC} - \mathbf{M}_{VC}\|}{\|\mathbf{M}_{VC}\|} \times 100, \quad (2.42)$$

where  $\mathbf{M}$  is the discrete vector of column base moment up-to the last common time increment between the two analyses, and the subscripts denote the analyses using either the Voce-Chaboche (VC) or UVC material model. In Table 2.7, the columns with “VM” indicate the imperfection modes with varied amplitude (e.g., VM1 means that the amplitude of mode 1 is varied, VM56 means that the amplitudes of modes 5 and 6 are varied), and the columns with “CM” indicate the imperfection modes with constant mean amplitude.

Results from the parametric study in Table 2.7 suggest that the difference in base moment over the load history is up to about 20 %. Values in this table of around 15–20 % are the analyses where different buckling modes are observed, while the one value of 6.7 % (Material Set 1,  $\mu + \sigma$  local buckling imperfection amplitude) is a case where the same buckling modes are observed. In this specific case, the response is similar because there is a relatively large local imperfection applied that leads to primarily local buckling even for the column model with Voce-Chaboche material model. The majority of error metrics in Table 2.7 falling into the 15–20 % range, in conjunction with the observed shift in instability models, underscores the high sensitivity of component behavior to minor differences in simulated material response. These results support that a divergence in buckling modes is the most probable outcome when the two different material models are employed, given the assumed member geometry, material properties, and imperfections in this study.

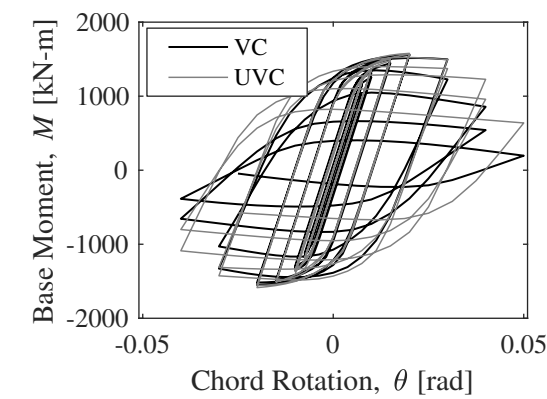
## 2.6 Discussion of results, limitations, and future work

Through this work the proposed material model has been calibrated using multiple tests for each steel material in an effort to better represent the material’s response to random strain histories, such as those expected in steel components during earthquake loading. Using

Table 2.7 – Summary of the error metric from the parametric case study.

VM Scale	Error Metric [%], Material Set 1			Error Metric [%], Material Set 2		
	VM1, CM56	VM2, CM56	CM1, VM56	VM1, CM56	VM2, CM56	CM1, VM56
$\mu - \sigma$	17.5	17.6	19.8	21.3	22.6	15.5
$\mu - \sigma/2$	18.7	18.8	19.6	24.5	22.6	24.2
$\mu$	19.0	18.9	19.0	23.6	25.3	23.6
$\mu + \sigma/2$	19.3	19.2	17.6	22.8	21.0	22.4
$\mu + \sigma$	19.3	19.3	6.7	21.1	20.7	16.3

Notes: VM = Varying Mode, CM = Constant Mode(s), all the constant modes at mean scale factor.  
 $\mu$ -mean of measurements,  $\sigma$ -standard deviation of measurements.



(a) Moment-rotation, Material Set 1, mean imperfection amplitudes



Figure 2.11 – Column base moment - chord rotation and column model deformation modes at the first excursion to -4 % chord rotation. Bottom figures: yielding shown in light gray.

this method, the proposed material model has been shown to improve the predicted stress-strain behavior over the classic Voce-Chaboche model for all the data sets considered. This comes as a result of the model's ability to initially reduce the yield surface while maintaining nonsoftening behavior. The same comparisons cannot yet be made with other structural steel material models referenced in this chapter because the authors consider that meaningful comparisons can only be made when evaluating the same set of data and error measures.

Through an investigation of the component-level sensitivity to material model assumptions, this chapter shows that seemingly minute differences in the material-level response can be magnified in the component-level response. This difference is mainly attributed to the difference in the initial yield stress parameter between the classic Voce-Chaboche and proposed models. The case study in this chapter demonstrates that this difference in initial yield stress may have a significant impact on simulated column instability modes. This result is notable because, to the authors' knowledge, such a result regarding CFE component-level sensitivity has not yet been investigated for the structural steel constitutive models referenced in this chapter.

The above considerations notwithstanding, one limitation of this work is that no rigorous assertion can presently be made on whether the modifications to the Voce-Chaboche material model result in more accurate representations of component level responses compared to test data. Assessing the relative merits of different modeling approaches in component level experiments, though, requires test data where the material properties are fully known (i.e., several uniaxial or multiaxial coupons have been tested with different loading protocols for both the flange and web), the geometric imperfections in the member have been measured, and the residual stresses in the section are known. To the authors' knowledge, to date, such data do not exist for any full-scale steel column test. Conducting experiments in the future that include the data noted above is considered essential to assess and validate the material level sensitivity that has been postulated in this chapter. The component-level sensitivity uncovered in this study is very likely to depend on the component under consideration, therefore, this matter should also be investigated for other steel components. Finally, the proposed model does not consider time-dependent effects (i.e., strain rate effects, strain ageing). These effects, including their impact on pre- and post-peak component behavior, should be addressed in the future.

## **2.7 Conclusions**

Prior work (de Castro e Sousa et al., 2020) shows that calibration of the Voce-Chaboche material model parameters consistently underestimate the initial yield stress in mild steels when the calibration method is based on minimizing the difference in strain energy across multiple tests that include strain demands deemed representative of those expected in steel components

## **Chapter 2. Constitutive modeling of structural steels: A nonlinear isotropic/kinematic hardening material model and its calibration**

---

subjected to earthquake loading. This issue can be attributed to the permanent decrease in the yield stress because of the discontinuous yielding phenomenon present in these metals. In this chapter we propose an Updated Voce-Chaboche (UVC) nonlinear isotropic/kinematic hardening material model as well as its calibration methodology. The main outcomes are summarized as follows:

- Constraints on the parameters of the UVC model are essential to ensure a hardening response consistent with the behavior of mild steels. Two constraints are formulated to ensure nonsoftening behavior regardless of the steel material.
- The material model implementation is validated in commercial and open-source finite element analysis programs Abaqus (as UMATs) and OpenSees (as a UniaxialMaterial and NDMaterials) for uniaxial, plane-stress, and multiaxial stress states. The code is made publicly available (Hartloper, 2019).
- Parameters for the UVC material model are provided for a database of nine structural steels used in North America, Japan, and Europe. The initial yield stress is increased by 17 % using the UVC model over the Voce-Chaboche model. A 19 % relative improvement in the overall material model accuracy is found when compared to the Voce-Chaboche model. The full calibration procedure of the UVC model is made available in the open source Python package RESSPyLab (de Castro e Sousa et al., 2019).
- At least two backstresses are necessary for the UVC model to accurately represent the behavior of the investigated steel materials. One backstress leads to an underfitting of the kinematic hardening component.
- Results from the conducted parametric study suggest that the simulated geometric instabilities in steel wide flange columns that arise under multiaxial loading are sensitive to the material model and input parameters for the studied column geometry.
- Findings from the case study should be supported by full-scale tests where the imperfections, residual stresses within the cross section, and material characteristics are fully quantified beforehand to reliably evaluate the effect of material initial conditions. Furthermore, effects that influence the hardening mechanisms and spread of plasticity within the plastic hinge length of columns, such as the rate of applied loading, should also be explored in the future by means of large-scale physical testing.

### **2.8 Data availability**

Some or all data, models, or code generated or used during the study are available in a repository or online in accordance with funder data retention policies. This includes: the code used for the calibration procedure available in RESSPyLab (de Castro e Sousa et al., 2019); the



finite element models used for validation, and the implemented material models available in Hartloper (2019).

Some or all data, models, or code that support the findings of this study are available from the corresponding author upon reasonable request. This includes: the finite element models used in the case study section, and the uniaxial stress-strain data used for calibration of parameters in Tables 2.1 and 2.2.

## 2.9 Acknowledgements

This study is based on work supported by EPFL and by the Swiss National Science Foundation (Project No. 200021\_188476). The financial support is gratefully acknowledged. Any opinions, findings, and conclusions or recommendations expressed in this chapter are those of the authors and do not necessarily reflect the view of sponsors.

## 2.10 Notation

*The following symbols are used in this chapter:*

- $a$  = Isotropic hardening rate parameter for yield surface reduction;
- $a_{(c)}^{(c)}$  = Buckling mode scale factor for geometric imperfections;
- $b$  = Isotropic hardening rate parameter for cyclic hardening;
- $\mathbf{C}$  =  $\kappa \mathbf{1} \otimes \mathbf{1} + 2\mu \mathbf{I}_{dev}$ , fourth-order tensor of elastic moduli;
- $\mathbf{C}^{ep}$  = Fourth-order tensor of elastoplastic moduli;
- $C_k$  = Kinematic hardening magnitude for  $k$ 'th backstress;
- $D_\infty$  = Isotropic hardening magnitude for yield surface reduction;
- $E_m$  = Case study error metric;
- $\mathbf{e}_i$  = First-order standard basis tensor;
- $e_k$  = Update to kinematic hardening;
- $f$  = von Mises yield function;
- $f(\mathbf{x})$  = Objective function in minimization problem;
- $\mathbf{g}(\mathbf{x})$  = Vector of constraint functions;
- $g(\Delta\lambda)$  = Equation for the consistency condition in radial return mapping;
- $\hat{g}, g_1, g_2$  = Constraints to ensure nonsoftening;
- $H'$  = Kinematic hardening modulus;
- $\mathbf{I}$  =  $1/2(\delta_{ik}\delta_{jl} + \delta_{il}\delta_{jk})\mathbf{e}_i \otimes \mathbf{e}_j \otimes \mathbf{e}_k \otimes \mathbf{e}_l$ , fourth-order sym. identity tensor;
- $\mathbf{I}_{dev}$  =  $\mathbf{I} - 1/3 \mathbf{1} \otimes \mathbf{1}$ , fourth-order deviatoric identity tensor;
- $K'$  = Isotropic hardening modulus;
- $\mathbf{M}$  = Discrete base-moment history vector;
- $N_T$  = Number of load protocols used in calibration;

## Chapter 2. Constitutive modeling of structural steels: A nonlinear isotropic/kinematic hardening material model and its calibration

---

- $\mathbf{n}$  = Unit vector-field normal to the yield surface;
- $Q_\infty$  = Isotropic hardening magnitude for cyclic hardening;
- $T$  = End of time interval;
- $t$  = Time variable;
- $\mathbf{x}$  = Parameter vector for the proposed material model (uniaxial);
- $\boldsymbol{\alpha}$  = Second-order total backstress tensor;
- $\gamma_k$  = Kinematic hardening rate parameter for  $k$ 'th backstress;
- $\Delta\lambda$  = Increment in the plastic multiplier;
- $\delta_{ij}$  = Kronecker delta;
- $\epsilon_{tol}$  = Tolerance in optimization problem;
- $\boldsymbol{\epsilon}$  = Second-order strain tensor;
- $\boldsymbol{\epsilon}^e$  = Second-order elastic strain tensor;
- $\boldsymbol{\epsilon}^p$  = Second-order plastic strain tensor;
- $\epsilon_L$  = Luders strain;
- $\epsilon_{eq}^p$  = Equivalent plastic strain;
- $\epsilon^*$  = Accumulated absolute strain;
- $\kappa$  = Bulk modulus;
- $\lambda$  = Consistency parameter (time derivative of plastic multiplier);
- $\mu$  = Shear modulus;
- $(\cdot)_{\mu/\sigma}$  = Mean/standard deviation for imperfections;
- $\boldsymbol{\xi}$  = Second-order relative stress tensor;
- $\rho$  = Hardening metrics;
- $\boldsymbol{\sigma}$  = Second-order stress tensor;
- $\sigma_y$  = Yield stress;
- $\sigma_{y,0}$  = Initial yield stress;
- $\bar{\phi}$  = Normalized calibration error metric;
- $\mathbf{1}$  =  $\delta_{ij}\mathbf{e}_i \otimes \mathbf{e}_j$ , second-order identity tensor; and
- $(\dot{\cdot})$  = Time derivative.

### 3 Cyclic metal plasticity model parameters with limited information: A constrained optimization approach

**Authors:** Albano de Castro e Sousa, Alexander R. Hartloper, Dimitrios G. Lignos

**Postprint version of:** de Castro e Sousa, A., Hartloper, A. R., and Lignos, D. G. (2021). "Cyclic metal plasticity model parameters with limited information: A constrained optimization approach." *Journal of Engineering Mechanics*, (In-press). [https://doi.org/10.1061/\(ASCE\)EM.1943-7889.0001922](https://doi.org/10.1061/(ASCE)EM.1943-7889.0001922). With permission from ASCE.

**Doctoral candidate's contributions:** Refinement of the methodology, addition of the UVC model, implementation of methodology, generation of all data, contribution to data analysis, contribution to discussion and interpretations of results. Writing of the Methodology and Results sections, editing of the manuscript. Note that the first author wrote the Introduction and Discussion sections. The co-authors supervised the work carried-out by the doctoral candidate and assisted with the editing of the manuscript.

**Abstract:** Tensile test data for structural steels are ubiquitous. Yet, the information monotonic loading provides with respect to the material's characteristics is limited. Notably, features of inelastic response to cyclic loading, such as the Bauschinger effect, can not be determined without testing with a load reversal protocol. This chapter aims at addressing this shortcoming by formulating a constrained optimization problem that provides best-fit material parameters to a tensile test, while simultaneously imposing representative cyclic properties for structural steels. Recommendations on constraints are given. Results demonstrate that improvements can be achieved when compared to: (1) direct fits to tensile data and (2) input model parameters from the same steel material but from different batches calibrated to a wide range of strain-based protocols. Given the available data, it is concluded that simpler models with one backstress tend to perform best with the proposed constraints.

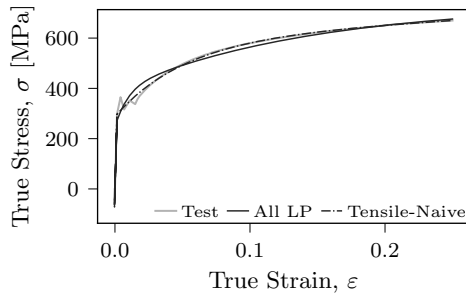
**Keywords:** Inverse problem; structural steel; tensile test; material constitutive modeling; Earthquake loading; cyclic hardening; constrained optimization.

### **3.1 Introduction**

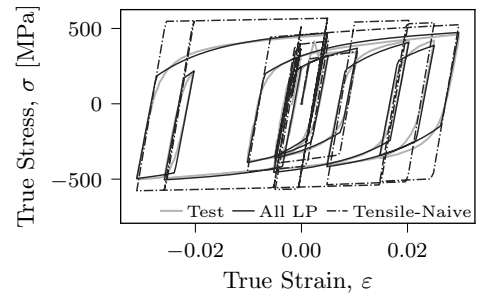
Seismic response of steel structures to extreme events is often nonlinear in nature. The sources of the nonlinearity can be classified mainly into two categories: (1) material and (2) geometric. Without accurate material and geometric properties, reliable physics-based modeling of the hysteretic response of a component or sub-assembly can not be established. Consequently, their impact at the system level can be the source of accumulated errors that may lead to misleading conclusions of overall structural performance. Yet, all too often are structural steel's nonlinearities oversimplified or all together overlooked. In situations where material and geometric nonlinearities strongly interact (e.g., open-section beam-columns), it has been shown that such oversimplifications can lead to distinct member failure modes (Hartloper et al., 2019a).

Accurate material modeling depends both on the constitutive model and on the ability to obtain its characteristic input parameters. Solving inverse problems, however, are marred with nonuniqueness issues (Cooke and Kanvinde, 2015), i.e., a different set of parameters can yield the same overall material response for a particular loading history— *c.f.* e.g., Figure 3.1. This feature can significantly hamper modeling efforts in situations where loading histories differ from the calibrated cases. For earthquake applications this is naturally an issue of concern due to the stochastic character of seismic action. To mitigate this problem, a methodology has been proposed to calibrate parameters to a rich set of protocols that are representative of seismic loading (de Castro e Sousa et al., 2020). While this approach shows promise, obtaining test data can be challenging since it can be costly both in terms of the number of specimens and of specialized testing equipment in order to achieve high compressive strains. Furthermore, there are situations, like the performance assessment of existing steel structures (CEN, 2005c; ASCE, 2017), where collecting the required amount of samples may be challenging. Given that there is a need for accurate material modeling, on one hand, and that the ability to carry out extensive testing campaigns may be restricted, on the other hand, a way to use limited test information, such as monotonic tensile tests, is of particular interest to the research and practice communities.

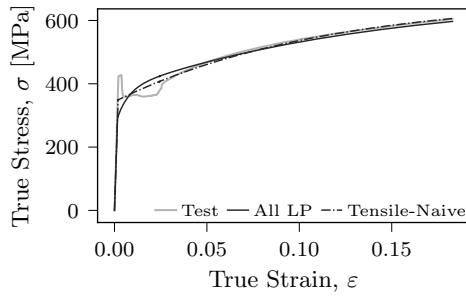
Most of steel's mechanical design characteristics are typically obtained by tensile tests. These tests are both common and standardized (ASTM, 2016b; CEN, 2001), meaning they are relatively economical and the testing methodology is established. Their main shortcoming, however, is that they can not depict how the material would behave under cyclic loading. Importantly, the extent of the Bauschinger effect and isotropic versus kinematic hardening saturation levels are information that cannot be derived solely from monotonic loading. This chapter proposes addressing this challenge by determining material parameters from a specific tensile test but that, at the same time, satisfy some *a priori* knowledge pertaining to its cyclic properties. It is envisioned that this *a priori* knowledge should be directly related to



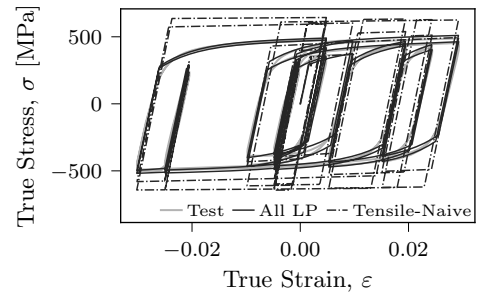
(a) S355J2+N, tensile (Load Protocol 1)



(b) S355J2+N, variable amplitude (Load Protocol 9)



(c) A992Gr.50, tensile (Load Protocol 1)



(d) A992Gr.50, variable amplitude (Load Protocol 9)

Figure 3.1 – Comparison of stress-strain using the S355J2+N 50 mm plate and A992 Gr. 50 W14X82 flange data sets: test data (Test); VC model 2 backstresses, all load protocols used in calibration (All LP); and naive calibration using only a tensile test (Tensile-Naive).

### Chapter 3. Cyclic metal plasticity model parameters with limited information: A constrained optimization approach

---

the steel grades' general material characteristics, e.g., its microstructure (in its grain size and crystalline structure) or its chemical composition. As will be shown more concretely in the methodology and results sections, different steel grades commonly present different ratios of isotropic to kinematic hardening, a behavior believed to be closely related to the material's grain refinement (Bouaziz et al., 2008).

The interpretation of material parameters is inextricably tied to the chosen model representation. Herein, two materials models are used: (1) the Voce-Chaboche (VC) (Voce, 1948; Chaboche et al., 1979) and (2) an Updated Voce-Chaboche (UVC) (Hartloper et al., 2021a). Both are part of the rate independent,  $J_2$  plasticity framework, but differ on their hardening rules - the isotropic, in particular. The first is a widely used material model in the context of nonlinear analysis of steel structures (*c.f.* e.g., Fell et al. (2009), Araújo et al. (2017), Elkady and Lignos (2018b)). Among its most important features is its ability to adequately capture cyclic loading behavior with exponentially saturating hardening laws. The second builds upon the VC by adjusting the material response to more accurately capture the discontinuous yielding phenomenon present in mild steels (Lubliner, 2008). Both models aim at representing physical mechanisms that lead to work hardening - e.g., the Bauschinger effect through the kinematic hardening representation. However, the interpretation of material parameters through these models should only be made if they can be determined in a reliable and consistent manner.

The approaches made in de Castro e Sousa et al. (2020) and Hartloper et al. (2019b) are focused toward consistency of the parameters obtained for the VC and UVC models, respectively. Therein, unconstrained optimization procedures, based on Newton Trust-Region (NTR) framework, are presented that are able to navigate the non-convex parameter search space both efficiently and reliably, given a diverse set of strain-based load protocols. The parameters obtained for each of these models, with those methodologies, are considered to be intrinsic to the material since they are both reliable and physically motivated. While differences between steel production batches are to be expected, the hypothesis is made that certain behavioral aspects are directly transferable between materials of the same grade; that is to say that, specific material parameters might be different but, for example, ratios of isotropic to kinematic hardening should remain largely of the same magnitude for a given steel grade.

This chapter concerns itself with answering mainly one question: can parameter optimization of a single tensile test, holding constant characteristic material ratios for cyclic loading, return satisfactory stress-strain responses for a wide range of cyclic load protocols? There is a pressing need for an answer to this question. Consider, for example, Figure 3.1 which depicts test results for two load protocols (Figure 3.1a /3.1c- monotonic; Figure 3.1b/3.1d - cyclic variable amplitude)<sup>1</sup>. On top of the test results, two uniaxial VC model responses for the tests' strain histories are also depicted, whose parameters are determined with (1) a wide range of cyclic load protocols and (2) naively with only the tensile test data. It can be seen that,

---

<sup>1</sup>load protocol designations can be consulted in de Castro e Sousa et al. (2020)

although the parameters perform similarly in the tensile case, the tensile fitting's response deviates largely from the variable amplitude response. Naive tensile-only calibrations do not perform well when simulating cyclic loading because monotonic tensile tests do not contain information regarding the Bauschinger effect nor cyclic hardening, therefore, it can be taken for granted that naively using a tensile test to calibrate a cyclic material model is an inadequate approach. Since it has been shown that even small differences in a material model can have a disproportionate effect on the overall member behavior and influence simulated geometric instabilities (Hartloper et al., 2019a), this aspect may be crucial in the accuracy of structural responses in the nonlinear regime.

To address the problem stated above, an approach is proposed in this chapter that makes use of (1) material performance metrics and (2) a constrained optimization procedure using the developed metrics in order to solve for the corresponding model parameters. Their efficacy is evaluated by using appropriate error metrics. Additionally, comparisons are made to material model performance using parameters from known databases for nominally identical materials. It is shown that the proposed method outperforms a “naive” optimization, and is on-or-above par with the use of relevant parameters from databases, for the case-study addressed herein. Details for the approach are given in the Methodology section. After, results of the application of the methodology to a number of materials are presented and a discussion of those results is given in the subsequent section. The chapter concludes with a brief section summarizing the main outcomes of this research.

## 3.2 Methodology

A solution to the problem of determining a set of constitutive model parameters representative for cyclic loading using only a tensile test is proposed in this section. The workflow of the proposed methodology is shown in Figure 3.2 applied to structural steel materials. The workflow consists of three stages for a given steel material: Stage 1: determine the *a priori* cyclic hardening characteristics of the material for a set constitutive model, Stage 2: use this *a priori* information to inform the model calibration using only a tensile test, and Stage 3: validate the results.

In Stage 1, the metrics to quantify the behavior of steel materials subjected to cyclic loading, and the associated constraints, are proposed. An existing database of uniaxial cyclic tests, denoted as the Root dataset, is used to calculate the bounds in these constraints for selected materials through established calibration methods (Hartloper et al., 2019b; de Castro e Sousa et al., 2020). In Stage 2, the constraints are used with tensile tests to form a constrained optimization problem using this limited data. The solution to this minimization problem yields the constitutive model parameters that match a tensile test with cyclic loading information embedded. In Stage 3, an assessment of the methodology is made by comparing the predicted

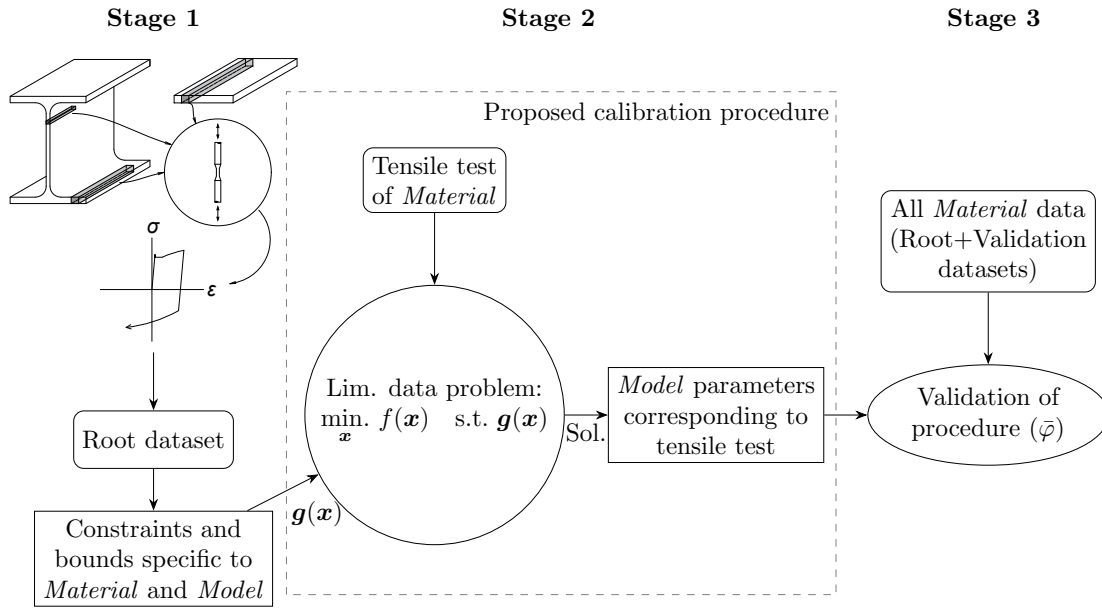


Figure 3.2 – Workflow of proposed methodology applied to structural steel materials.

steel material response using the tensile-only parameters with uniaxial coupon tests from the Root dataset in addition to a separate dataset (denoted the Validation dataset) to avoid bias in the results.

### 3.2.1 Database of steel materials

As shown in Figure 3.2, data regarding the cyclic and tensile behavior of steel materials is required at each step of the process, therefore, a database of such information is a necessary starting point. An existing database of uniaxial tensile tests on structural steel materials, in combination with several uniaxial cyclic tests conducted on round-bar coupons, is utilized in this chapter (Grigoriou and Lignos, 2017; Suzuki, 2018; Hartloper et al., 2021a). This database contains the original data used in the authors' research in the domain of inverse problems and is thus coined the Root dataset. A further description of the database, including the definitions of the cyclic load protocols used, is provided in de Castro e Sousa et al. (2020). In brief, the strain-based load protocols are cataloged numerically into 10 different histories that are deemed to be representative of strain histories in steel frame structural components when subjected to earthquake loading. In total, nine sets of different steel materials (some materials having multiple samples) are included in the database, as summarized Table 3.1.

The Root dataset (Table 3.1) is largely comprised of low-carbon (or mild) low-alloy structural steels that are commonly used in Europe (e.g., S355J2 and S355J2+N), North America (e.g., A992 Gr. 50 and A500 Gr. B), and Japan (e.g., BCR295 and BCP325) (CEN, 2005d; ASTM, 2016a, 2018). These mild steel materials are the focus of this study. Other materials included



Table 3.1 – Overview of the Root material database.

ID	Material	Source	Tested By <sup>a</sup>	Load Protocols	$f_{y,n}$ <sup>b</sup> [MPa]	$f_{u,n}$ <sup>c</sup> [MPa]
1	S355J2+N	50 mm plate	1	1–10	355	470–630
2	S355J2+N	25 mm plate	1	1–10	355	470–630
3	S355J2	HEB500 flange	3	1,2,5,6,9	355	470–630
4	S355J2	HEB500 web	3	1,1–3,5–9	355	470–630
5	S460NL	25 mm plate	1	1,3–7,9,10	440	540–720
6	S690QL	25 mm plate	1	1,3–7,9,10	690	770–940
7	A992 Gr.50	W14X82 web	2	1,2,5,6,9	345	450 <sup>d</sup>
8	A992 Gr.50	W14X82 flange	2	1,2,5,6,9	345	450 <sup>d</sup>
9	A500 Gr.B	HSS305X16	2	1,2,5,6,9	315	400 <sup>d</sup>
10	BCP325	22 mm plate	2	1,2,5,6,9	325	490–610
11	BCR295	HSS350X22	2	1,2,5,6,9	295	400–550
12	HYP400	27 mm plate	2	1,2,5,6,9	400	490–640

<sup>a</sup> 1: Grigoriou and Lignos (2017), 2: Suzuki (2018), 3: Hartloper et al. (2021a).

<sup>b</sup>: nominal yield stress, <sup>c</sup>: nominal tensile stress, <sup>d</sup>: minimum value.

in Table 3.1 are high-strength low-alloy steels (S460NL and S690QL) (CEN, 2019b,a), and a high-performance steel that is manufactured with a thermomechanically controlled process and grain refinement (HYP400) (Suzuki et al., 2008) that are of emerging interest in structural earthquake engineering. However, only a single set of tests is available for each of these materials, and therefore, the hardening characteristics of these materials cannot be reliably established at this time. Informative results for these materials are included for use in future work that may expand on the present study.

### 3.2.2 Definition of the constitutive models

Implementation of the VC and UVC models has already been extensively described in the literature (Hartloper et al., 2019b; de Castro e Sousa et al., 2020), therefore, only pertinent details are covered herein for brevity. The model implementation outlined in this section is specific to uniaxial stress states owing to the nature of the data included in the previously described database.

Both the VC and UVC models use a von Mises yield condition,  $\phi^{VM}$ ,

$$\phi^{VM} := |\sigma - \alpha| - (\sigma_{y,0} + K) \leq 0, \quad (3.1)$$

where  $\sigma$  is the uniaxial stress,  $\alpha$  is the backstress defining the kinematic hardening component,  $\sigma_{y,0}$  is the initial yield stress, and  $K$  is the isotropic hardening. The isotropic hardening rule

### Chapter 3. Cyclic metal plasticity model parameters with limited information: A constrained optimization approach

---

defined in the UVC model is

$$K = Q_{\infty} \left( 1 - \exp \left[ -b \dot{\varepsilon}_{eq}^p \right] \right) - D_{\infty} \left( 1 - \exp \left[ -a \dot{\varepsilon}_{eq}^p \right] \right), \quad (3.2)$$

where  $\dot{\varepsilon}_{eq}^p = |\dot{\varepsilon}^p|$  is the equivalent plastic strain,  $Q_{\infty}$  is the magnitude of isotropic hardening at model saturation,  $b$  is the associated rate parameter,  $D_{\infty}$  and  $a$  are parameters to account for discontinuous yielding in structural steels. The over-dot indicates the derivative with respect to time. The parameter  $D_{\infty}$  imposes an initial reduction in the yield surface that saturates quickly when the rate parameter  $a$  is properly chosen. Isotropic hardening in the classic VC model is attributed to Voce (1948), and is simply recovered by removing the  $D_{\infty}$  term from Equation 3.2. Removal of this term is the only difference in the hardening rules between the VC and UVC models.

Both of the material models employ the nonlinear kinematic hardening rule proposed by Chaboche et al. (1979) based on the work of Armstrong and Frederick (1966). The Chaboche hardening rule is  $\alpha = \sum_k^{N_k} \alpha_k$ , where  $\alpha_k$  are backstress components,  $k = 1, 2, \dots, N_k$ . Each component is defined by the Armstrong-Frederick rule for uniaxial loading,

$$\dot{\alpha}_k = \text{sign}[\sigma - \alpha] C_k \dot{\varepsilon}_{eq}^p - \gamma_k \alpha_k \dot{\varepsilon}_{eq}^p, \quad (3.3)$$

where  $C_k$  is the magnitude of contribution to the total backstress for component  $k$ , and  $\gamma_k$  is the corresponding rate parameter. In this chapter, the backstress rate parameters are defined such that  $\gamma_1 > \gamma_2 > \dots > \gamma_{N_k}$ .

Two constraints on the set of UVC parameters are required for modeling structural steels (Hartloper et al., 2019b); they are denoted  $g_1$  and  $g_2$ , and are respectively defined as

$$g_1 := -Q_{\infty} b - \sum_k C_k + D_{\infty} a \leq 0, \quad (3.4)$$

$$g_2 := Q_{\infty} b^2 + \sum_k C_k \gamma_k - D_{\infty} a^2 \leq 0. \quad (3.5)$$

These two constraints are sufficient conditions for the set of UVC model parameters to lead to a non-softening stress-strain response, therefore, they are considered an essential component of the UVC model for structural steels. Constraints (3.4) and (3.5) do not apply to the VC model.

Considering the uniaxial stress state, the addition of the elastic modulus,  $E$ , completes the set of parameters. The set of parameters for the VC and UVC models are respectively

$$\mathbf{x}^{VC} = [E, \sigma_{y,0}, Q_{\infty}, b, C_1, \gamma_1, \dots, C_{N_k}, \gamma_{N_k}],$$

and

$$\mathbf{x}^{UV\mathcal{C}} = [E, \sigma_{y,0}, Q_{\infty}, b, D_{\infty}, a, C_1, \gamma_1, \dots, C_{N_k}, \gamma_{N_k}].$$

### 3.2.3 Definition of the inverse problem

Following de Castro e Sousa et al. (2020), an objective function is defined that represents the error in the model prediction based on the squared strain energy. The objective function  $f(\mathbf{x}) : \mathbb{R}^n \rightarrow \mathbb{R}$  is

$$f(\mathbf{x}) = \sum_{j=1}^{N_T} \frac{\int_0^{\varepsilon_j^*} \left( \sigma_j^{model}(\varepsilon_j; \mathbf{x}) - \sigma_j^{test} \right)^2 d\varepsilon^*}{\int_0^{\varepsilon_j^*} d\varepsilon^*}, \quad (3.6)$$

where  $\sigma_j^{model}(\varepsilon_j; \mathbf{x})$  is the predicted model stress given a strain history  $\varepsilon_j$  and parameters  $\mathbf{x}$ ,  $\sigma_j^{test}$  is the stress recorded in the uniaxial test  $j$ , and  $\varepsilon^*$  is the accumulated strain

$$\varepsilon_j^* = \int_0^{t_j} |\dot{\varepsilon}_j| d\tau. \quad (3.7)$$

Note that Equation 3.6 is defined for  $N_T$  load histories allowing for multiple cyclic tests to be used in the calibration simultaneously.

We seek the set of parameters that minimizes the defined objective function, i.e., the inverse problem of parameter calibration is posed as the constrained minimization problem

$$\underset{\mathbf{x} \in \mathbb{R}^n}{\text{minimize}} \quad f(\mathbf{x}) \quad (3.8a)$$

$$\text{subject to} \quad \mathbf{g}(\mathbf{x}) \leq \mathbf{0}, \quad (3.8b)$$

where  $\mathbf{g}(\mathbf{x}) : \mathbb{R}^n \rightarrow \mathbb{R}^m$  is a vector valued function of  $m$  constraints given  $n$  parameters in  $\mathbf{x}$ . These constraints are an essential component of the proposed methodology as they embed characteristics of the material subjected to cyclic loading into just a single tensile test.

### 3.2.4 Definition of the constraints to embed cyclic loading information

Metrics are proposed to characterize the behavior of structural steels subjected to cyclic loading. These metrics should be derived from tests that are representative of the expected loading conditions of the material. In the context of the current chapter, the load protocols should be consistent with the expected inelastic strain demands in steel components under earthquake loading. Constraints on these metrics are then defined to embed this information into the calibration process when only a tensile test is used.

### Material hardening metrics

The metrics defined herein are consistent with those used in de Castro e Sousa et al. (2020) to quantify the isotropic and kinematic hardening found in structural steels. Given a set of parameters for either the UVC or VC models, the following metrics are defined in terms of the equivalent plastic strain assuming monotonic loading from an initially strain free state. This assumption is necessary to define metrics independent of the strain history for the kinematic hardening component because the time-integration of Equation 3.3 is not a monotonically increasing function under cyclic loading. Where applicable, the metrics for the VC model are calculated neglecting  $D_\infty$  and  $a$ .

The total increase in stress due to combined isotropic and kinematic hardening is described by the metric

$$\sigma_{hard}(\varepsilon_{eq}^p) = Q_\infty \left(1 - \exp\left[-b\varepsilon_{eq}^p\right]\right) + \sum_k C_k / \gamma_k \left(1 - \exp\left[-\gamma_k \varepsilon_{eq}^p\right]\right), \quad (3.9)$$

and the ratio of isotropic-to-total hardening is defined by the metric

$$\rho_{iso}(\varepsilon_{eq}^p) = \frac{Q_\infty \left(1 - \exp\left[-b\varepsilon_{eq}^p\right]\right)}{\sigma_{hard}(\varepsilon_{eq}^p)}. \quad (3.10)$$

A value of  $\rho_{iso} = 1$  indicates that there is only isotropic hardening present in the material, and  $\rho_{iso} = 0$  indicates purely kinematic hardening (e.g., in high-strength steels). The total stress at a particular value of  $\varepsilon_{eq}^p$  is defined by

$$\sigma_{total}(\varepsilon_{eq}^p) = \sigma_{y,0} + \sigma_{hard}(\varepsilon_{eq}^p) - D_\infty \left(1 - \exp\left[-a\varepsilon_{eq}^p\right]\right), \quad (3.11)$$

and the ratio of total stress to the initial yield stress is defined as

$$\rho_{yield}(\varepsilon_{eq}^p) = \frac{\sigma_{total}(\varepsilon_{eq}^p)}{\sigma_{y,0}}. \quad (3.12)$$

A value of  $\rho_{yield} = 2$  would indicate that the stress at the chosen value of  $\varepsilon_{eq}^p$  is twice the initial yield stress. In this chapter, all the metrics are defined at their saturation value,  $\varepsilon_{eq}^p \rightarrow \infty$ , this is indicated by the *sat* superscript, e.g.,  $\rho_{iso}^{sat} = Q_\infty / (Q_\infty + \sum_k C_k / \gamma_k)$ .

A further metric is introduced relating the rates of kinematic and isotropic hardening. This metric quantifies the rates at which the different hardening components saturate assuming monotonic loading, and is defined as

$$\rho_{\gamma_1 b} = \frac{\gamma_1}{b}. \quad (3.13)$$

If  $\rho_{\gamma_1 b} > 1$  this indicates that the kinematic hardening saturates at a lower equivalent plastic strain than the isotropic hardening under monotonic loading. A metric is proposed to define the rate of saturation for various kinematic hardening components if more than one backstress is specified in the constitutive model:

$$\rho_{\gamma_1 \gamma_2} = \frac{\gamma_1}{\gamma_2}. \quad (3.14)$$

This constraint is necessary to prevent duplication of the backstress rate terms, for instance, if  $\gamma_1 = \gamma_2$ , then essentially the two-backstress model reduces to a one-backstress model. This issue arises because there is not enough information in a single tension test to differentiate the kinematic hardening components since a near-perfect fit can be obtained with a single component (see Figures 3.1a and 3.1c). Whereas, this same issue only appears to occur after four backstresses are included when the full set of load protocols are used in the calibration effort (de Castro e Sousa et al., 2020).

An additional metric is proposed for the UVC model that specifies the ratio of the initial reduction in the yield surface to the total hardening at saturation. More specifically,

$$\rho_D(\varepsilon_{eq}^p) = \frac{D_\infty \left(1 - \exp \left[-a \varepsilon_{eq}^p\right]\right)}{Q_\infty \left(1 - \exp \left[-b \varepsilon_{eq}^p\right]\right) + \sum_k C_k / \gamma_k \left(1 - \exp \left[-\gamma_k \varepsilon_{eq}^p\right]\right)}. \quad (3.15)$$

Another possible constraint is to specify the ratio between  $D_\infty$  and  $Q_\infty$ , however, this constraint is not valid for steels with very low isotropic hardening (e.g., high strength steels). This is also common in the case of cold-forming, such as in the corners of press-bent products.

#### Constraints on the hardening metrics

Constraints are imposed on each of the metrics described in the previous section for use in the constrained minimization problem. All the constraints are posed as bound constraints in the standard form specified in (3.8b), therefore, two constraints are defined for the lower and upper bound of each metric,  $g^{inf}$  and  $g^{sup}$ , respectively. Each of the following constraints consists of a metric,  $\rho$ , and a constant that specifies the lower/upper bound of the metric,  $c^{inf/sup}$ .

In total, there are ten constraints specified assuming a maximum of two backstresses in

the constitutive model:

$$g_{yield}^{inf} := c_{yield}^{inf} - \rho_{yield}^{sat}; \quad g_{yield}^{sup} := \rho_{yield}^{sat} - c_{yield}^{sup}; \quad (3.16a)$$

$$g_{iso}^{inf} := c_{iso}^{inf} - \rho_{iso}^{sat}; \quad g_{iso}^{sup} := \rho_{iso}^{sat} - c_{iso}^{sup}; \quad (3.16b)$$

$$g_{\gamma_1 b}^{inf} := c_{\gamma_1 b}^{inf} - \rho_{\gamma_1 b}^{sat}; \quad g_{\gamma_1 b}^{sup} := \rho_{\gamma_1 b}^{sat} - c_{\gamma_1 b}^{sup}; \quad (3.16c)$$

$$g_{\gamma_1 \gamma_2}^{inf} := c_{\gamma_1 \gamma_2}^{inf} - \rho_{\gamma_1 \gamma_2}^{sat}; \quad g_{\gamma_1 \gamma_2}^{sup} := \rho_{\gamma_1 \gamma_2}^{sat} - c_{\gamma_1 \gamma_2}^{sup}; \quad (3.16d)$$

$$g_D^{inf} := c_D^{inf} - \rho_D^{sat}; \quad g_D^{sup} := \rho_D^{sat} - c_D^{sup}; \quad (3.16e)$$

The constants in each of (3.16a)–(3.16e) depend on the constitutive model (e.g., VC or UVC, including the number of backstresses assumed), and the equivalent plastic strain used in computing the corresponding metrics (e.g., at saturation). Both these factors should be consistent with the calibration at hand when computing the constants.

### 3.2.5 Proposed calibration procedure

The optimization problem (3.8a) subjected to (3.8b) is solved with the NITRO algorithm (Byrd et al., 1999) as implemented in Scipy (Virtanen et al., 2020). The NITRO algorithm requires an initial starting point, and is an iterative method where the stopping point for a local minimum is determined by the first- and second-order necessary conditions (i.e., the norm of the objective function's gradient is less than a specified tolerance, and the objective function's Hessian is positive definite). Gradients and Hessians required in this algorithm are computed using algorithmic differentiation, as previous studies have demonstrated the efficacy of this approach when combined with gradient-based optimization methods (Hartloper et al., 2019b; de Castro e Sousa et al., 2020).

The use of a minimization algorithm requires an initial starting point. Two starting points are used in this study to assess if similar optimal parameters are obtained from different initial conditions. The first starting point, denoted as SP1, is feasible with respect to the constraint set. To generate SP1, an initial set of parameters is chosen that represents an elastic perfectly-plastic material as assumed in de Castro e Sousa et al. (2020); this set is then modified according to Algorithm 1 so that the initial point is feasible with respect to the constraints. The basis for this algorithm is to set the parameters such that the constraints are set to their mean of the upper and lower bound values. The second starting point, SP2, is a potentially infeasible point that is just the set of parameters leading to a nearly perfectly-plastic response (SP1 prior to applying Algorithm 1).

With reference to Stage 2 of the workflow shown in Figure 3.2, the proposed procedure for calibration of the VC and UVC model parameters using only a tensile test is as follows:

#### 1. Specify the constraints:

- (a) VC model: The constraint vector,  $\mathbf{g}(\mathbf{x})$ , is composed of constraints (3.16a)–(3.16c) regardless of the model and number of backstresses. Constraints defined in (3.16d) are added if two backstresses are considered.
  - (b) UVC model: The constraint vector,  $\mathbf{g}(\mathbf{x})$ , is composed in the same manner as the VC model for either one or two backstresses. Additionally,  $g_1$  and  $g_2$  are added to ensure non-softening of the material.
2. **Set the material cyclic hardening metric constraint bounds:** The bounds on the constraints are defined using the minima and maxima of relevant metrics from prior calibrations on similar materials using relevant cyclic loading histories. The metrics used to establish the bounds should match the employed material model and number of backstresses for the constraints to be meaningful.
  - (a) VC model:
    - One backstress:  $c_{yield}^{inf}, c_{yield}^{sup}, c_{iso}^{inf}, c_{iso}^{sup}, c_{\gamma_1 b}^{inf}, c_{\gamma_1 b}^{sup}$ ,
    - Two backstresses: VC model one backstress, additionally  $c_{\gamma_1 \gamma_2}^{inf}, c_{\gamma_1 \gamma_2}^{sup}$
  - (b) UVC model:
    - One backstress: VC model one backstress, additionally  $c_D^{inf}, c_D^{sup}$
    - Two backstresses: VC model two backstresses, additionally  $c_D^{inf}, c_D^{sup}$
3. **Select the starting point:** The starting point is intended to represent a material with nominal elastic and yield properties, and a nearly-perfectly plastic behavior. Nominal values for the elastic modulus and yield stress are selected as  $E_n = 200$  GPa and  $f_{y,n} = 355$  MPa for all materials in this study.
  - (a) VC model:
    - One backstress:  $\mathbf{x}_{SP2}^{VC} = [E_n, f_{y,n}, 1, 1, 1, 1]$
    - Two backstresses:  $\mathbf{x}_{SP2}^{VC} = [E_n, f_{y,n}, 1, 1, 1, 1, 1, 1]$
  - (b) UVC model: Note that the initial value for “ $a$ ” is set to 200 to approximately reach 99 % saturation of  $D_\infty$  at 2 % strain (typical plateau strain in mild steels).
    - One backstress:  $\mathbf{x}_{SP2}^{UVC} = [E_n, f_{y,n}, 1, 1, 1, 200, 1, 1]$
    - Two backstresses:  $\mathbf{x}_{SP2}^{UVC} = [E_n, f_{y,n}, 1, 1, 1, 200, 1, 1, 1, 1]$
4. **(Optional) Make the starting point feasible:** If desired, Algorithm 1 can be applied to  $\mathbf{x}_{SP2}^{VC} / \mathbf{x}_{SP2}^{UVC}$  so that the starting point satisfies the hardening metric constraint bounds. The basis of this algorithm is to set the material properties to the average of the relevant bounds. The feasible starting point is denoted  $\mathbf{x}_{SP1}^{VC} / \mathbf{x}_{SP1}^{UVC}$ .

### Chapter 3. Cyclic metal plasticity model parameters with limited information: A constrained optimization approach

5. **Determine the optimal set of parameters:** The minimization, Problem (3.8), is solved using the NITRO algorithm starting from SP1 or SP2 with a tolerance on the convergence criteria of  $10^{-8}$  and a maximum of 600 iterations. Note that the solution point typically converges to a local minima within 200 iterations for the steel materials examined in this work (on average, approximately 5 minutes on a desktop computer with a 4 GHz processor), therefore, the 600 iterations is deemed to be adequate.

---

**Algorithm 1** Generate a feasible starting point with respect to  $g_{yield}$ ,  $g_{iso}$ ,  $g_{\gamma_1 b}$ ,  $g_{\gamma_1 \gamma_2}$ .

---

- 1:  $\rho_{yield,avg}^{sat} \leftarrow 0.5 \times (c_{yield}^{inf} + c_{yield}^{sup})$
  - 2:  $\rho_{iso,avg}^{sat} \leftarrow 0.5 \times (c_{iso}^{inf} + c_{iso}^{sup})$
  - 3:  $\rho_{\gamma_1 b,avg}^{sat} \leftarrow 0.5 \times (c_{\gamma_1 b}^{inf} + c_{\gamma_1 b}^{sup})$
  - 4:  $\rho_{\gamma_1 \gamma_2,avg} \leftarrow 0.5 \times (c_{\gamma_1 \gamma_2}^{inf} + c_{\gamma_1 \gamma_2}^{sup})$
  - 5:  $\gamma_{2,0} \leftarrow \gamma_{1,0} / \rho_{\gamma_1 \gamma_2,avg}$
  - 6:  $C_{1,0} \leftarrow -\gamma_{1,0} \sigma_{y,0,0} (-1 + \rho_{iso,avg}) (-1 + \rho_{yield,avg})$
  - 7:  $Q_{\infty,0} \leftarrow C_{1,0} \rho_{iso,avg} / (\gamma_{1,0} (-1 + \rho_{iso,avg}))$
  - 8:  $b_0 \leftarrow \gamma_{1,0} / \rho_{\gamma_1 b,avg}$
- 

#### 3.2.6 Metrics used for procedure evaluation

Referring to Stage 3 of the proposed workflow shown in Figure 3.2, the normalized form of the objective function is used to assess the accuracy of the proposed calibration procedure using only a tensile test. The normalized error metric is

$$\bar{\varphi} = \sqrt{\frac{f(\mathbf{x})}{E_{total}}}, \quad (3.17)$$

where the total normalized strain energy of all the considered tests in a data set is

$$E_{total} = \sum_{j=1}^{N_T} \frac{\int_0^{\epsilon_j^*} (\sigma_j^{test})^2 d\epsilon^*}{\int_0^{\epsilon_j^*} d\epsilon^*}. \quad (3.18)$$

The metric  $\bar{\varphi}$  represents the error in strain energy calculated over the entire data set (i.e., tensile and cyclic tests), normalized by the total strain energy of all the tests.

Consistency between sets of parameters is evaluated using the  $\xi_2$  metric defined in de Castro e Sousa et al. (2020). This metric is computed between two sets of parameters  $\mathbf{x}_{base}$  and  $\mathbf{x}_{sample}$  as

$$\xi_2 = \frac{(\mathbf{x}_{sample} - \mathbf{x}_{base})^T \nabla_{xx} f(\mathbf{x}_{base}) (\mathbf{x}_{sample} - \mathbf{x}_{base})}{E_{total}}, \quad (3.19)$$

where  $\nabla_{xx} f(\mathbf{x}_{base})$  is the Hessian of the objective function for a given data set evaluated at



the local minimum of  $f(\mathbf{x})$ ,  $\mathbf{x}_{base}$ . The  $\xi_2$  metric represents the normalized increase in the minimum value of the objective function when choosing  $\mathbf{x}_{sample}$  instead of  $\mathbf{x}_{base}$ . If this increase is insignificant, then the two sets of parameters are said to be consistent.

### 3.2.7 Validation of the results

The main objective of this chapter is to answer the question of whether calibrations of single tensile tests, constrained by cyclic material characteristics, will yield *satisfactory* responses for a wide range of cyclic protocols. Here, the proposed tensile-only calibration procedure is satisfactory if the results out-perform, in the  $\bar{\varphi}$ -sense for all LPs, parameters derived for other materials using all available load protocols. The satisfactory condition defined above reflects the common situation where a modeler selects input model parameters from a nominally identical steel grade that have been calibrated in a prior study for an entirely different production batch. For instance, parameters from de Castro e Sousa et al. (2020) for a hot-rolled HEB500 section of S355J2 ( $f_y = 355$  MPa) steel may be selected to model an IPE300 section from a different production heat of the same steel grade. In this hypothetical situation, we would like to demonstrate that, on average, there is less error in the  $\bar{\varphi}$ -sense by using the proposed tensile-only calibration with a supplied tensile test than using alternative parameters from the same steel grade.

Since the cyclic characteristics are obtained *a priori*, validation of the proposed methodology is done using data sets of S355J2 steel that are separate from the database summarized in Table 3.1 to avoid bias in the results. The characteristics are derived from the Root dataset (see Figure 3.2) and used to analyze steel materials from another set, coined the Validation dataset. The Validation dataset consists of tests conducted on round-bar coupons of S355J2 steel (with same group of ten uniaxial cyclic load protocols) sampled from two alternative sources: (1) the web of an IPE300 hot rolled profile and (2) the flange of the same IPE300. The proposed calibration procedure described above is subsequently applied to estimate the model parameters using a single tensile test. Comparisons are then made to parameters that would be obtained if all available load protocols were used, as well as using the parameters from Tables 3.2 and 3.6 for S355 steels calibrated from the Root dataset.

## 3.3 Results

The methodology proposed in the previous section is applied to the database of steel materials summarized in Table 3.1. Results for the VC material model are presented first, followed by the UVC model. In all cases, discussion of the results is delayed to the Discussion section.

### **3.3.1 Voce-Chaboche model results**

#### **Constraint bounds**

Bounds on the metrics used to form the constraints defined in (3.16a)–(3.16d), i.e., the  $c$  values, are calculated using the parameters obtained for mild structural steels. As mentioned in the Methodology section, only the S355J2(+N), A992 Gr. 50, and BCP325 steels are utilized for the tensile-only calibration because these materials are consistent in terms of their nominal chemical compositions and yield/tensile stresses (see Table 3.1) (CEN, 2005d; ASTM, 2016a). The other materials included in Table 3.1 are excluded from the metric bounds, and the tensile-only calibration is not conducted. The materials are excluded on the basis that: (1) they are high-strength low-alloy steels (e.g., S460NL and S690QL), (2) are cold worked from the corners of hollow structural sections (e.g., A500 Gr. B and BCR295), or (3) were manufactured with a thermomechanically controlled process and grain refinement (e.g., HYP400). However, parameters and hardening metrics using all available protocols are provided for each material in the Root dataset for use in future research.

Parameters for the VC model with one and two backstresses computed using the methodology in de Castro e Sousa et al. (2020) are recorded for all the Root materials in Table 3.2. The material hardening metrics computed for the subset of mild steels are summarized in Table 3.3, and a summary of the metrics can be viewed graphically in Figure 3.3. Most importantly, observe that the computed metrics in Table 3.3 depend on the number of backstresses included in the model, therefore, a separate set of bounds are used for either one or two backstresses. Notice that there is an increase in the ratio of kinematic hardening when two backstresses are included in the model, this is because the kinematic hardening is more accurately represented by two backstress components, thus increasing its relevance and magnitude. The total hardening,  $\sigma_{total}^{sat}$ , is also greater when two backstresses are included. The reason for this is that  $\gamma_1$  in the one-backstress model is greater than  $\gamma_2$  in the two-backstress model, therefore, the two-backstress model saturates at a much greater plastic strain than the one-backstress model. This issue could be addressed by evaluating this metric at a finite equivalent plastic strain value, but for simplicity, this is not taken into account herein. As for the initial yield stress, comparing the  $\sigma_{y,0}$  values in Table 3.2 with the nominal yield stresses in Table 3.1, the VC model values are close to, but consistently lower than, the nominal yield stress values. This is a known issue with the VC model for structural steels, and is the motivation behind the development of the UVC model (Hartloper et al., 2019b).

Low coefficient of variation (CoV) values for the metrics imply consistency across the steel materials, thereby providing an indication of the link between the physical material properties and the proposed hardening metrics. Results in Figure 3.3 suggest that a reasonably low variance in all metrics is found for the VC one-backstress model, while this variance is significantly larger for the  $\rho_{yield}^{sat}$  and  $\rho_{\gamma_1 b}$  metrics of the two-backstress model. Furthermore,

the metric  $\rho_{\gamma_1\gamma_2}$  applicable to the VC two-backstress model does not appear to be reliable given that the CoV is slightly lower than 90 %. Recall, however, that this constraint should be considered to avoid duplication of the  $\gamma_k$  parameters when two backstresses are used in the tensile-only calibration.

The constraint bounds applicable to mild steels contain the minima and maxima of the metrics in Table 3.3 for S355J2(+N), A992 Gr. 50, and BCP325 steels. For the VC one-backstress model, these bounds are:  $1.5 \leq \rho_{yield}^{sat} \leq 2.5$ ,  $0.35 \leq \rho_{iso}^{sat} \leq 0.50$ , and  $2.25 \leq \rho_{\gamma_1b} \leq 3.25$ . Similarly, the bounds used in this study for the VC model and two backstresses are:  $1.75 \leq \rho_{yield}^{sat} \leq 2.3$ ,  $0.15 \leq \rho_{iso}^{sat} \leq 0.30$ ,  $8.5 \leq \rho_{\gamma_1b} \leq 25.0$ , and  $13 \leq \rho_{\gamma_1\gamma_2} \leq 92$ .

### Tensile-only calibration results

Bounds on the metrics are used to establish the constraint vector  $\mathbf{g}(\mathbf{x})$  used in the proposed calibration procedure (Stage 2, Figure 3.2) for the subset of *Root* data. Results for the tensile-only calibration of the seven selected steel materials are provided in Table 3.4. The normalized error metric values,  $\bar{\phi}$ , in Table 3.4 are evaluated using the parameters in this table along with all the available load protocols for each steel material. Similarly, the values of the  $\xi_2$  metric are calculated using Equation 3.19 with  $\mathbf{x}_{base}$  taken from Table 3.2 for the full data calibration (the base), and  $\mathbf{x}_{sample}$  taken from Table 3.4 for the tensile-only calibration (the sample). The results in Table 3.4 suggest that there is no benefit in this approach to use two versus only one backstress in terms of the value of the error function—in fact it is worse to use two backstresses. Also, if one takes the threshold value of  $\xi_2 = 5\%$  discussed in de Castro e Sousa et al. (2020), these results show that the tensile only parameters are inconsistent with those retrieved from a calibration a full set of load protocols. The implications of these findings are further expounded in the Discussion section.

The influence of the two starting points is shown in Figure 3.5 for the S355J2+N 50 mm plate data set, and similar results hold for the other data sets although they are not shown herein. The convergence criteria at each iteration of the NITRO algorithm is shown in Figure 3.5a, and the results imply that the starting point does not have a major influence on the rate of convergence for the algorithm. Furthermore, the convergence criteria of  $10^{-8}$  for Problem (3.8) are satisfied in all but one case (S355J2+N 25 mm plate). In this case, the exit convergence criterion value was about  $10^{-5}$  after 600 iterations. The plot of the objective function value at each iteration, Figure 3.5b, indicates that the same level of error is reached regardless of the starting point. The reason is that the model parameters also converge to the same value for both SP1 and SP2, as shown in Figure 3.5c that tracks the model parameters at each iteration. Therefore, the chosen starting points do not appear to be influential on the obtained solution point in this calibration procedure.

### **Validation**

Data sets of uniaxial coupon tests conducted on samples from the flanges and web of an IPE300 profile of S355J2 steel are used as the *Validation* set for our proposed tensile-only calibration. The results of the validation are summarized in Table 3.5 via the  $\bar{\varphi}$  metric. Values of the  $\bar{\varphi}$  metric in this table are computed using all available load protocols for the IPE300 flange/web, and parameters that are either: (1) calibrated using the methodology in this chapter using only the tensile test of the IPE300 flange or web data sets (tensile-only), or (2) calibrated using all available load protocols of other S355J2(+N) steel materials. For instance, the error computed across the entire IPE300 flange dataset using the parameters from the IPE300 tensile-only calibration is  $\bar{\varphi} = 10.53 \%$ , while the error computed using the parameters from the S355J2+N (50 mm plate) dataset is  $\bar{\varphi} = 11.25 \%$ . The implications of these results will be discussed shortly.

Figure 3.6 is provided to compare the level of fit between different options for selected tests from the IPE300 flange data set. Material model predictions in these figures are computed with the parameters from the VC 1-backstress model tensile-only calibration using the IPE300 flange (“Tensile”), and the VC 2-backstress model parameters calibrated to the S355J2 HEB500 flange data (“HEB500-Flange”). For the case shown in Figure 3.6, the proposed tensile-only calibration leads to results that are in closer agreement with the test data regardless of the load protocol. Moreover, a stark contrast is apparent between the poor results of the “naive” approach, where no information is used to guide the tensile-only calibration (see Figure 3.1b/3.1d), and the reasonably good results shown in Figure 3.6c when the proposed methodology is employed.

### **3.3.2 Updated Voce-Chaboche model results**

#### **Constraint bounds**

The same materials and methodology as discussed above for the VC model is applied to the UVC model to derive appropriate bounds of the model’s material performance metrics. UVC material model parameters are provided in Table 3.6 for one and two backstresses, and the hardening metrics are summarized in Table 3.7. A summary of the metrics can also be viewed in graphical form in Figure 3.3.

Many observations regarding the link between the calibration results and the physical material properties made for the VC model also apply to the UVC model. However, a quick review of the obtained metrics shows a significant dispersion in the ratios in the material metrics  $\rho_{iso}^{sat}$  and  $\rho_D^{sat}$  when only one backstress is included in the UVC model (see Figures 3.3b and 3.4b). The later metric essentially measures the decay in isotropic hardening stress with respect to the other hardening components of the model, and the accuracy of this parameter

is crucial to the UVC functioning as intended since it is the main differentiator with respect to the VC model. Furthermore, considering that these two metrics cannot be defined with precision, the initial hypothesis that these metrics are an intrinsic property of the material cannot be made with any degree of confidence when only one backstress is included in the UVC model. It follows, then, that it is pointless to pursue analyses with one backstress using the UVC model. This is not the case, however, for the two backstress condition, where  $\rho_D^{sat}$  and  $\rho_{iso}^{sat}$  are defined within a narrow CoV range.

Following the above argument, the recommended bounds used in this study to assess tensile-only calibrations for the UVC model are based solely on a two-backstress model. For the steels in question (S355J2(+N), A992 Gr. 50, and BCP325) these are:  $1.8 \leq \rho_{yield}^{sat} \leq 2.1$ ,  $0.25 \leq \rho_{iso}^{sat} \leq 0.30$ ,  $13.0 \leq \rho_{\gamma_1 b} \leq 20.0$ ,  $15.0 \leq \rho_{\gamma_1 \gamma_2} \leq 30.0$ , and  $0.2 \leq \rho_D \leq 0.3$ .

#### Tensile-only calibration and validation results

In contrast with the VC model, UVC tensile-only parameters are not presented herein. The reason for this decision follows from the results in Table 3.8 for the validation of the UVC two-backstress model. This table indicates that, in terms of the error metric  $\bar{\varphi}$ , the performance of the tensile-only parameters is significantly worse than using the parameters from a different steel from a database derived with full load protocols (i.e., using any of the two-backstress parameter sets from Table 3.6). For example, the error in the IPE300 web data set is around  $\bar{\varphi} = 25\%$  when the proposed tensile-only calibration procedure is used with the UVC model, while the error is around  $\bar{\varphi} = 10\text{--}18\%$  using the parameters calibrated from other data sets. Poor results of the UVC tensile-only calibration are apparent in Figure 3.7: despite matching the tensile test, the other cyclic load protocols are not accurately represented by the model predictions. These results demonstrate that UVC tensile-only calibrations, even with two backstresses, are inadequate with the methodology and data presented herein, and should not be used when parameters from a material with a similar microstructure are available.

### 3.4 Discussion

The methodology presented in this chapter assumes a strong link between physical material response and the parameters used in its representation by a material constitutive model. This assumption is crucial in order to obtain accurate cyclic model responses by performing a constrained optimization with limited information (in this case a tensile-only test of a material sample). From the results presented in the previous section, it was shown that while precise performance metrics can be found for the material models under analysis (VC with one backstresses, and UVC with two backstresses), when these metrics are used in the constrained optimization with tensile-only test data, the results are not universally satisfactory. In fact, the poor performance of the UVC under these conditions leads to the inescapable conclusion that

### Chapter 3. Cyclic metal plasticity model parameters with limited information: A constrained optimization approach

Table 3.2 – Voce-Chaboche material model parameters with one and two backstresses obtained using the full data sets.

ID	$\bar{\varphi}$ [%]	$E$ [GPa]	$\sigma_{y,0}$ [MPa]	$Q_{\infty}$	$b$ [MPa]	$C_1$	$\gamma_1$	$C_2$ [MPa]	$\gamma_2$
1	8.21	177.54	296.62	123.26	7.17	6501.83	27.90	-	-
	6.31	184.98	270.96	107.22	5.97	14327.30	115.12	1771.06	7.56
2	8.49	182.11	285.67	125.79	11.80	6801.09	29.78	-	-
	6.57	191.52	265.29	104.45	11.63	12997.99	99.51	1560.41	7.35
3	6.02	186.13	272.57	132.55	9.10	3738.39	28.95	-	-
	4.63	191.85	245.50	119.77	8.67	14019.86	205.39	1247.05	4.45
4	7.38	193.82	275.65	104.97	14.29	8437.43	62.41	-	-
	6.86	200.39	265.46	103.29	11.18	11996.11	104.79	627.33	1.14
5	8.02	172.85	376.44	106.09	11.08	6857.43	23.44	-	-
	6.18	185.86	358.93	68.04	10.02	14202.40	104.22	2259.11	8.01
6	7.56	184.88	607.47	0.50	0.58	15648.17	60.98	-	-
	7.29	184.70	602.64	0.48	0.55	16107.81	78.81	937.51	6.32
7	7.78	194.55	328.83	101.76	16.73	5159.90	38.80	-	-
	6.23	207.32	299.86	88.30	13.96	14878.98	166.00	1424.51	8.57
8	7.69	178.64	324.68	127.20	11.89	3943.98	30.59	-	-
	5.75	189.95	292.75	110.54	9.71	15142.58	170.54	1117.53	5.86
9	7.72	180.57	321.68	36.64	0.94	3995.53	24.59	-	-
	5.43	191.39	286.87	24.08	0.84	11934.29	160.01	1585.62	7.71
10	6.67	173.87	325.05	103.34	8.75	5945.26	32.19	-	-
	4.88	177.92	306.09	94.16	5.81	11613.11	122.00	1744.03	8.29
11	7.75	173.46	355.97	0.56	0.60	5135.19	44.95	-	-
	6.24	177.88	329.13	0.57	0.61	12773.06	196.86	1746.22	11.96
12	7.02	187.13	401.29	44.20	9.64	5758.71	38.19	-	-
	5.22	189.35	376.22	29.12	6.41	13711.66	139.70	1147.15	4.59

Table 3.3 – Voce-Chaboche hardening metrics with one and two backstresses obtained using the full data sets.

ID	One Backstress			Two Backstresses			
	$\rho_{yield}^{sat}$	$\rho_{iso}^{sat}$	$\rho_{\gamma_1 b}$	$\rho_{yield}^{sat}$	$\rho_{iso}^{sat}$	$\rho_{\gamma_1 b}$	$\rho_{\gamma_1 \gamma_2}$
1	2.20	0.35	3.89	2.72	0.23	19.27	15.22
2	2.24	0.36	2.52	2.69	0.23	8.56	13.55
3	1.96	0.51	3.18	2.91	0.26	23.70	46.13
4	1.87	0.44	4.37	3.90	0.13	9.37	92.16
7	1.71	0.43	2.32	2.15	0.26	11.89	19.37
8	1.79	0.50	2.57	2.33	0.28	17.56	29.12
10	1.89	0.36	3.68	2.31	0.24	21.00	14.72
Avg.	1.95	0.42	3.22	2.72	0.23	15.91	32.90
StD.	0.19	0.06	0.73	0.54	0.05	5.52	26.46
CoV.[%]	9.49	14.76	22.61	20.05	19.44	34.72	80.44

Table 3.4 – Voce-Chaboche tensile test only calibration with one and two backstresses using the NITRO algorithm and SP1 for mild steels.

ID	$\bar{\varphi}$ [%]	$\xi_2$ [%]	$E$ [GPa]	$\sigma_{y,0}$ [MPa]	$Q_\infty$ [MPa]	$b$	$C_1$ [MPa]	$\gamma_1$	$C_2$ [MPa]	$\gamma_2$
1	12.4	13.5	206.38	298.28	201.10	7.10	4692.07	23.07	-	-
	14.31	37.0	199.38	308.79	60.68	1.79	5183.37	15.21	0.01	1.17
2	12.4	14.4	200.40	299.99	193.89	8.15	4861.80	25.00	-	-
	13.65	44.0	200.87	311.37	82.02	1.96	5380.87	16.67	0.04	1.28
3	9.5	10.9	220.12	300.02	157.51	3.07	2018.60	6.90	-	-
	18.05	20.9	200.00	289.05	55.60	0.41	3081.98	9.85	0.16	0.76
4	11.5	7.5	204.86	290.20	118.20	6.23	3078.12	14.02	-	-
	19.01	37.5	200.00	291.16	77.46	1.09	3666.21	12.24	0.69	0.94
7	8.68	4.6	200.95	356.51	104.04	6.90	2999.91	15.53	-	-
	14.97	7.4	200.00	357.10	60.84	0.54	3619.24	13.25	0.91	1.02
8	10.1	9.3	200.15	339.64	114.86	5.61	2690.49	12.61	-	-
	19.45	13.0	200.00	331.53	78.09	0.51	3656.42	12.51	0.81	0.96
10	10.5	12.1	212.62	353.76	114.24	6.21	2965.99	13.98	-	-
	14.30	10.2	200.00	352.67	81.40	0.51	3662.68	12.33	1.33	0.95

### Chapter 3. Cyclic metal plasticity model parameters with limited information: A constrained optimization approach

Table 3.5 – Results from the validation of the tensile test only calibration methodology with one and two backstresses, using the VC model for mild steels.

Calibration Data Set	Material	Load Protocols	Model	IPE300 flange $\bar{\varphi}$ ,[%]	IPE300 web $\bar{\varphi}$ ,[%]
Validation	S355J2 (IPE300 flange)	Tensile only	VC, 1bk	10.53	-
Validation	S355J2 (IPE300 web)	Tensile only	VC, 1bk	-	11.82
Validation	S355J2 (IPE300 flange)	Tensile only	VC, 2bk	18.31	-
Validation	S355J2 (IPE300 web)	Tensile only	VC, 2bk	-	19.92
Validation	S355J2 (IPE300 flange)	All available	VC, 2bk	5.46	6.94
Validation	S355J2 (IPE300 web)	All available	VC, 2bk	6.03	6.26
Root	S355J2+N (50 mm plate)	All available	VC, 2bk	11.25	11.86
Root	S355J2+N (25 mm plate)	All available	VC, 2bk	10.71	11.50
Root	S355J2 (HEB500 flange)	All available	VC, 2bk	16.91	18.36
Root	S355J2 (HEB500 web)	All available	VC, 2bk	11.99	13.64

Table 3.6 – Updated Voce-Chaboche full data set calibration with one and two backstresses for mild steels.

ID	$\bar{\varphi}$ [%]	$E$ [GPa]	$\sigma_{y,0}$ [MPa]	$Q_{\infty}$ [MPa]	$b$	$D_{\infty}$ [MPa]	$a$	$C_1$ [MPa]	$\gamma_1$	$C_2$ [MPa]	$\gamma_2$
1	8.18	177.51	327.15	128.25	7.86	37.28	203.33	6572.34	28.32	-	-
	6.33	197.41	338.8	134.34	14.71	133.75	229.25	26242.00	199.04	2445.30	11.66
2	8.43	182.96	330.42	146.77	13.72	67.20	133.57	6962.12	30.65	-	-
	6.53	185.97	332.18	120.48	8.14	93.15	261.75	21102.00	173.60	2300.60	10.42
3	5.81	186.17	304.96	153.96	12.13	59.91	98.68	4044.49	32.44	-	-
	3.96	192.13	315.04	138.01	11.36	96.16	223.66	18587.84	257.31	1351.98	6.52
4	7.00	193.91	341.22	454.07	34.70	419.75	56.92	8907.58	66.38	-	-
	6.61	199.68	334.94	139.32	14.07	120.33	274.73	28528.03	315.17	2569.46	24.68
7	7.43	194.62	376.35	623.86	38.46	574.87	51.64	5690.09	44.29	-	-
	5.21	210.72	378.83	122.63	19.74	143.49	248.14	31638.00	277.32	1548.60	9.04
8	7.53	178.75	360.64	195.99	20.52	113.60	74.36	4425.80	36.83	-	-
	4.76	191.02	373.72	141.47	15.20	135.95	211.16	25621.00	235.12	942.18	3.16
10	6.51	173.95	360.85	123.00	12.50	60.74	127.27	6193.34	34.44	-	-
	3.89	178.61	368.03	112.25	10.78	105.95	221.92	20104.00	200.43	2203.00	11.76



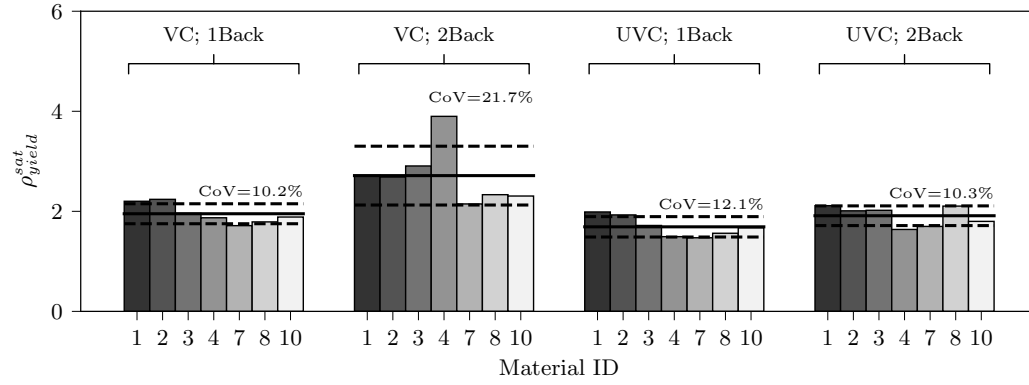
Table 3.7 – Metrics for the Updated Voce-Chaboche full data set calibration with one and two backstresses.

ID	One Backstress				Two Backstresses				
	$\rho_{yield}^{sat}$	$\rho_{iso}^{sat}$	$\rho_{\gamma_1 b}^{sat}$	$\rho_D^{sat}$	$\rho_{yield}^{sat}$	$\rho_{iso}^{sat}$	$\rho_{\gamma_1 b}^{sat}$	$\rho_D^{sat}$	$\rho_{\gamma_1/\gamma_2}$
1	1.99	0.36	3.60	0.10	2.11	0.26	21.33	0.20	16.67
2	1.93	0.39	2.23	0.18	2.01	0.28	13.53	0.28	17.08
3	1.72	0.55	2.68	0.22	2.02	0.33	22.65	0.23	39.49
4	1.49	0.77	1.91	0.71	1.64	0.42	22.39	0.36	12.77
7	1.47	0.83	1.15	0.76	1.70	0.30	14.05	0.35	30.66
8	1.56	0.62	1.80	0.36	2.10	0.26	15.47	0.25	74.44
10	1.67	0.41	2.76	0.20	1.80	0.28	18.60	0.26	17.05
Avg.	1.69	0.56	2.30	0.36	1.91	0.30	18.29	0.28	29.74
StD.	0.19	0.17	0.73	0.25	0.18	0.05	3.66	0.06	20.26
CoV. [%]	11.28	31.00	31.87	68.39	9.43	17.20	20.01	20.04	68.14

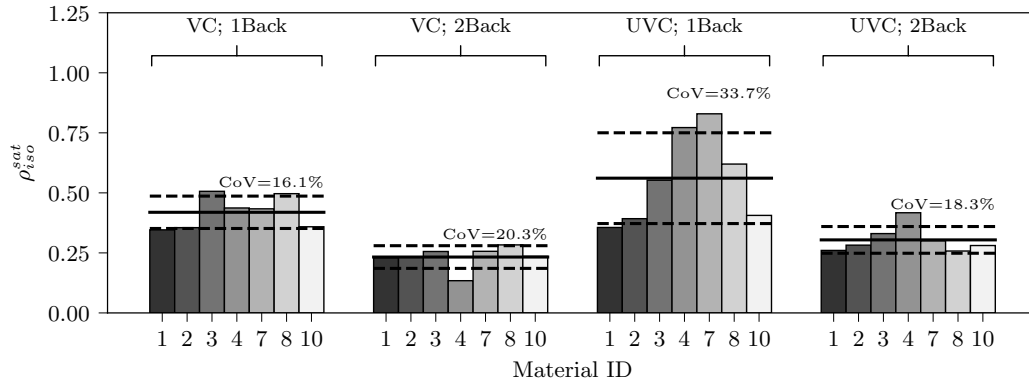
Table 3.8 – Results from the validation of the tensile test only calibration methodology with two backstresses for the UVC model.

Calibration Data Set	Material	Load Protocols	Model	IPE300 flange $\bar{\phi}, [\%]$	IPE300 web $\bar{\phi}, [\%]$
Validation	S355J2 (IPE300 flange)	Tensile only	UVC, 2bk	19.80	-
Validation	S355J2 (IPE300 web)	Tensile only	UVC, 2bk	-	24.69
Validation	S355J2 (IPE300 flange)	All available	UVC, 2bk	4.94	6.35
Validation	S355J2 (IPE300 web)	All available	UVC, 2bk	5.59	5.42
Root	S355J2+N (50 mm plate)	All available	UVC, 2bk	10.86	11.31
Root	S355J2+N (25 mm plate)	All available	UVC, 2bk	10.19	10.69
Root	S355J2 (HEB500 flange)	All available	UVC, 2bk	16.42	17.86
Root	S355J2 (HEB500 web)	All available	UVC, 2bk	10.40	12.19

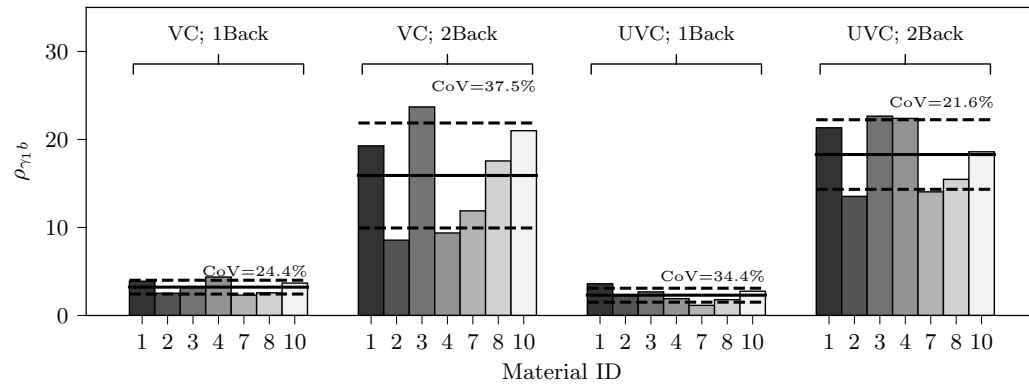
### Chapter 3. Cyclic metal plasticity model parameters with limited information: A constrained optimization approach



(a)



(b)



(c)

Figure 3.3 – Relevant model metrics for  $\sigma_y \approx 355$  MPa materials based on parameters calibrated with all available load protocols.

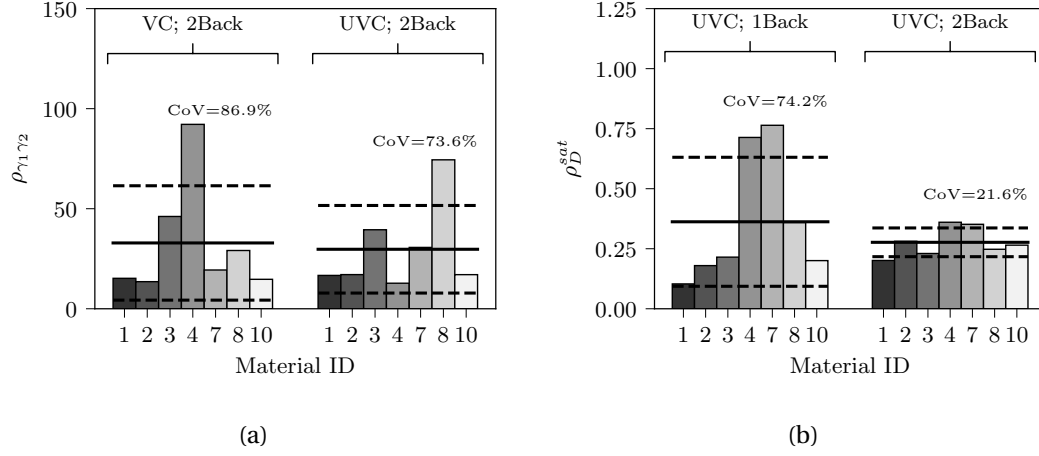


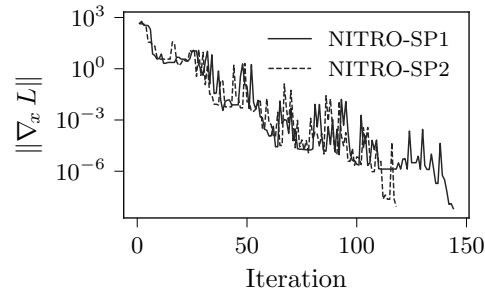
Figure 3.4 – Relevant model metrics for  $\sigma_y \approx 355$  MPa materials based on parameters calibrated with all available load protocols. (Cont.)

it should not be used for calibrations under limited information. This is not the case for the VC model– some nuances notwithstanding .

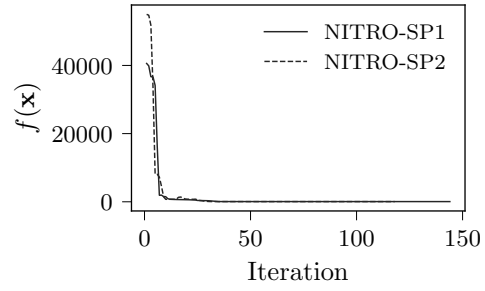
The results depicted in Table 3.4 for the VC show persistently that tensile-only calibrations with two backstresses underperform, in error-metric terms ( $\bar{\varphi}$ ), the model with a single backstress. One key observation in this Table is that the second backstresses parameters are close to zero, meaning that the model response is close to a single-backstress condition. A probable cause for this result is the significant dispersion in the  $\rho_{\gamma_1\gamma_2}$  performance metric in Table 3.3 and depicted in Figure 3.4a, since it is the only metric that relates both backstresses. Furthermore, the consistency of the solutions, as measured by  $\xi_2$  metric with respect to the parameters calibrated with all available load protocols, is significantly worse than the one-backstress case. Moreover, the results from the validation dataset shown in Table 3.5 show overwhelmingly that the tensile-only two-backstress VC, underperforms models with parameters unrelated to the specific sample, i.e., taken from another (Root) dataset. All-in-all, these findings seem to indicate that there just isn't enough information in a tensile test to accurately provide two-backstress VC model parameters and that, under conditions in which the modeler is faced with a single tensile-only test, it is preferable to use known database parameters rather than attempting to calibrate a two-backstress VC model. This conclusion, however, does not hold for the one-backstress VC model.

The one-backstress VC model performance, shown in Tables 3.4 and 3.5, suggests that error levels are typically smaller than the two-backstress tensile-only VC model. Moreover, in the validation cases the one-backstress model performs at error levels on or above par with respect to known two-backstress database parameters established with many more load protocols (the recommended VC calibrations strategy of de Castro e Sousa et al. (2020)). These results seem to indicate that a limited information calibration procedure with a one-backstress

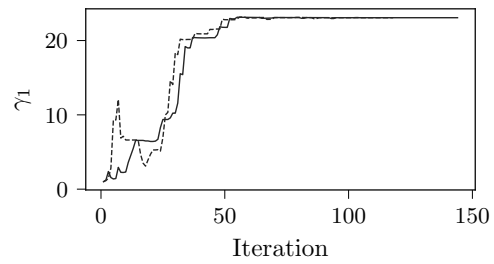
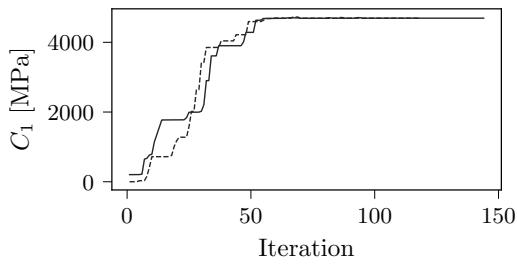
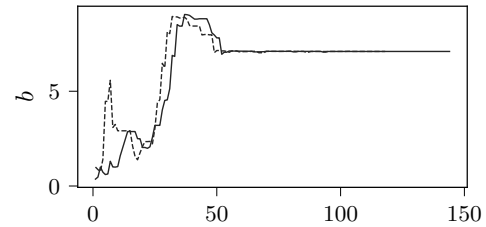
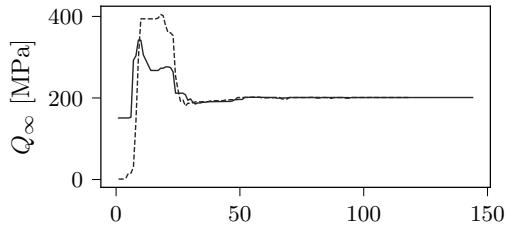
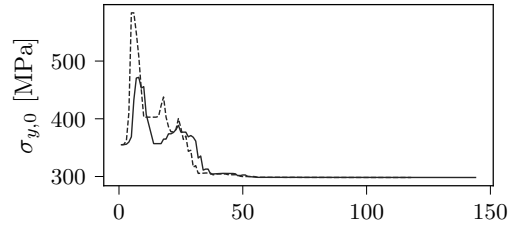
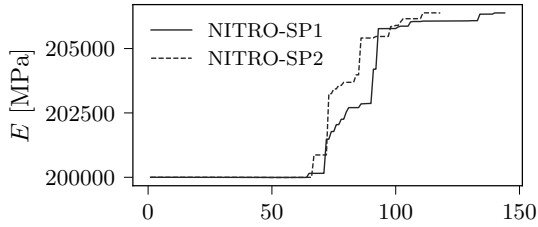
### Chapter 3. Cyclic metal plasticity model parameters with limited information: A constrained optimization approach



(a) Convergence criteria



(b) Objective function



(c) Parameter values

Figure 3.5 – Evolution of the constrained optimization solution based on the different starting points using the S355J2+N 50 mm data set.

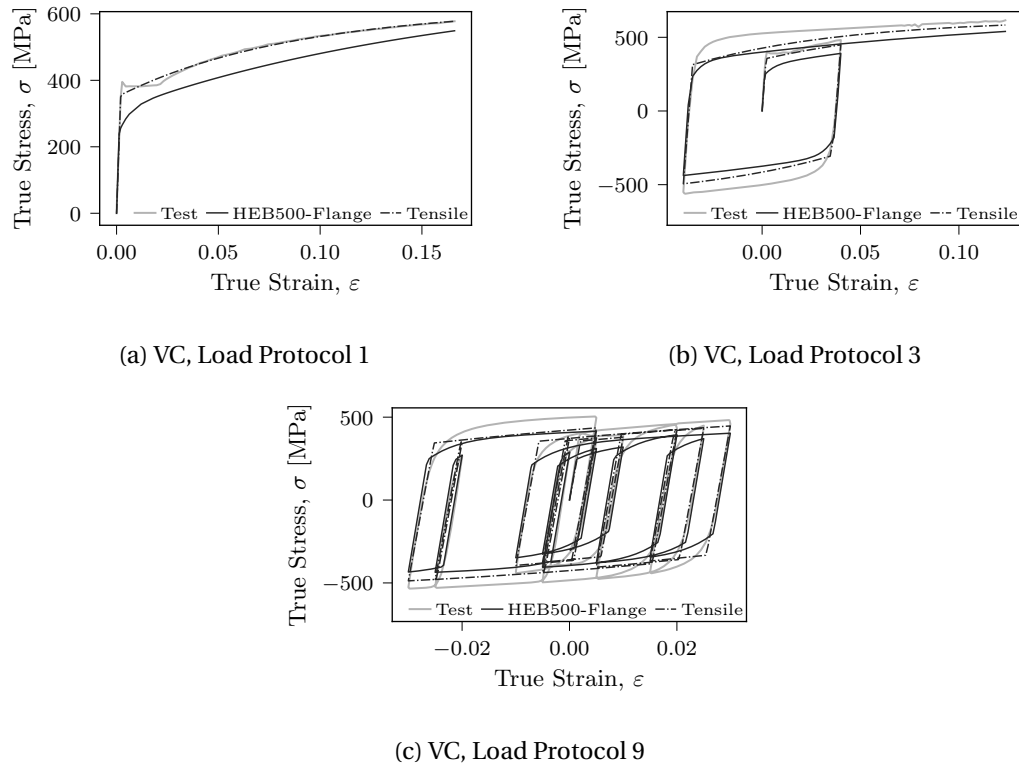
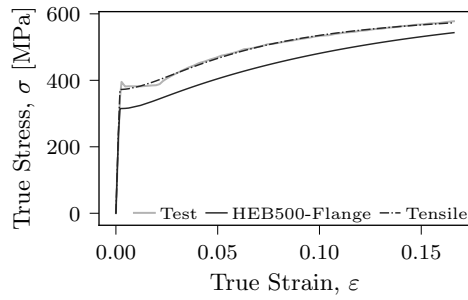
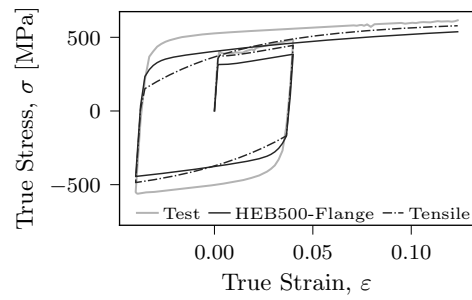


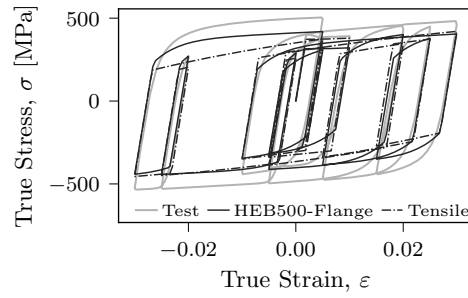
Figure 3.6 – Comparison of stress-strain using the S355J2 IPE300 flange data set: test data (Test), VC 2Back Root dataset calibration (HEB500-Flange), and proposed tensile-only calibration with the VC model (Tensile).



(a) UVC, Load Protocol 1



(b) UVC, Load Protocol 3



(c) UVC, Load Protocol 9

Figure 3.7 – Comparison of stress-strain using the S355J2 IPE300 flange data set: test data (Test), UVC 2Back Root dataset calibration (HEB500-Flange), and proposed tensile-only calibration with the UVC model (Tensile).

VC model is, in fact, a suitable approach to modeling material response when only monotonic test data is available. Indeed it could be said, also with respect to the UVC results, that the simplest model is the one that performs best under limited information conditions.

Why, then, should one find the possibility of using a single test result to calibrate a material model worthwhile? The main advantage of using the constrained optimization procedure advocated in this chapter, instead of using known database parameters, is that it diminishes the uncertainty related to the steel making process. Consider, for instance, using database parameters for S355J2 taken from an HEB500 flange and applying them to an S355J2 IPE300 flange. The results in Table 3.5 show that an error of  $\bar{\varphi} = 16.91\%$  is obtained, whereas if the tensile-only IPE300 flange test is used, one obtains an error  $\bar{\varphi} = 10.53\%$ . This suggests that, although the materials are “*theoretically*” the same, variations in manufacturing conditions (e.g., differences between production batches or profile rolling schemes) can affect a material’s cyclic response and that the methodology presented herein can mitigate this effect.

The facts above notwithstanding, if a modeler can have access to a material’s cyclic response using multiple load protocols, the modeler should not hesitate in using them (de Castro e Sousa et al., 2020). The accuracy of the parameters obtained using multiple load protocols is substantially better than the alternatives (constrained optimization or established material databases). This can also be seen in Table 3.4, where mid-single-digit errors are obtained if a two-backstress solution with all available load protocols is used. Moreover, it should be noted that, although satisfactory results are obtained using the one-backstress VC model tensile-only method, the values of  $\xi_2 > 5\%$  in Table 3.4 indicate that the parameters are inconsistent with those obtainable from more protocols – *c.f.* de Castro e Sousa et al. (2020) for details on the 5 % bound. In other words, the proposed method is acceptable **only** in situations where limited information is available on the material at hand, but it is not without its shortcomings.

Another disadvantage of this methodology is the fact that best-fit is only achieved with a one-backstress solution for the VC model. The feature restricts the possible shapes of the hardening material, which in certain applications may reveal crucial. Here, care should be taken on the range of plastic strains to which the model is to be applied. For instance, hardening slopes play a significant role in localization problems and, as such, this approach is likely not suitable in studying cases like ultra low cycle fatigue of materials where significant plastic strains ranges coupled with damage occurs. It should be stated, in fact, that the most suitable cases to use in this approach would be cases where nominal strains (as opposed to strain riser regions, such as sharp geometry changes or welds) are fairly bounded (between -5/+5 % plastic strains, the range of most cyclic calibration tests).

Lastly, it should be noted that the best-fit constrained optimization method presented herein is geared toward obtaining better cyclic material properties than otherwise obtained with a tensile test or from existing databases, which may not directly translate itself to a

"best-fit" component behavior. The material will be better characterized (as shown above), but how this relates to a better hysteretic response on the component side is a different issue. Component behavior depends not only on material characteristics, but also on how these interact with other features like its slenderness, geometric imperfections or residual stresses and demand histories. As such, one can only point out to the component modeler that some care should be taken with regards to the sensitivity of the component response to material parameters, because cases can arise where different failure modes can be triggered as a function of the material response (Hartloper et al., 2019a).

## **3.5 Conclusions**

This chapter presented a methodology to obtain material model parameters under limited information conditions. The models discussed herein are the Voce-Chaboche (VC) and an Updated Voce-Chaboche (UVC) in the context of structural steel applications. Limited information conditions can arise when one intends to study the behavior of steel structures under large amplitude cyclic loading, but knowledge of the employed steel material is restricted to a single tensile test. A procedure is proposed herein that allows the calibration of material parameters taking into account its cyclic properties with a single monotonic test using a constrained optimization scheme. This procedure has been incorporated into the open-source Python library, RESSPyLab de Castro e Sousa et al. (2019), which is made publicly available. The following conclusions can be made from this work:

- The definition of adequate material cyclic-performance metrics is an essential part in the constrained optimization procedure. Metrics are proposed herein that relate typical ratios of isotropic to kinematic hardening and their rates in order to inform the constrained optimization procedure;
- The number of backstresses used in the kinematic part of the models plays a significant role in the accuracy of tensile-only parameter estimates;
- The UVC model does not provide satisfactory results in parameter estimates in the tensile-only constrained optimization, regardless of the number of backstresses employed;
- The VC model with two backstresses does not provide satisfactory estimates of material response for tensile-only calibrations with the constraints presented herein. More data can however motivate different constraints;
- The VC model with one backstress, however, yields satisfactory results and is the recommended material model if a modeler is faced with a situation where tensile-only data is available.



It should be underscored that this methodology is a best-fit approximation in limited information cases. Whenever possible, material testing taking into account multiple load protocols should, nevertheless, be used.

### 3.6 Data availability

Some or all data, models, or code generated or used during the study are available in a repository or online in accordance with funder data retention policies (de Castro e Sousa et al., 2019).

### 3.7 Acknowledgments

The authors recognize and are grateful for the financial support of this study by the Nippon Steel Corporation, internal grants from École Polytechnique Fédérale de Lausanne (EPFL), as well as an exploratory grant from EPFL's School of Environmental, Architectural and Civil Engineering, and the Swiss National Science Foundation (Project No. 200021\_188476). Any opinions, findings, and conclusions or recommendations expressed in this chapter are those of the authors and do not necessarily reflect the views of sponsors.

### 3.8 Notation

*The following symbols are used in this chapter:*

- $a$  = isotropic saturation rate parameter associated with  $D_\infty$ ;
- $b$  = isotropic saturation rate parameter associated with  $Q_\infty$ ;
- $C_k$  = kinematic stress parameter for the  $k$ -th backstress;
- $c$  = constant in hardening metric constraint;
- $D_\infty$  = isotropic differential stress at saturation for discontinuous yielding;
- $E$  = Young's modulus;
- $E_{total}$  = total normalized strain energy in stress-strain data;
- $f(\mathbf{x})$  = objective function in minimization problem with vector variable  $\mathbf{x}$ ;
- $g$  = constraint on hardening metric;
- $Q_\infty$  = isotropic differential stress at saturation;
- $\gamma_k$  = kinematic saturation rate parameter for the  $k$ -th backstress;
- $\varepsilon$  = uniaxial true strain;
- $\varepsilon^*$  = error-metric strain;
- $\dot{\varepsilon}_{eq}^p$  = equivalent plastic strain;
- $\xi_2$  = consistency distance metric;
- $\rho$  = constitutive model hardening metric;
- $\sigma$  = uniaxial true stress;

### Chapter 3. Cyclic metal plasticity model parameters with limited information: A constrained optimization approach

---

$\sigma_{y,0}$  = initial yield stress;

$\varphi$  = error function;

$\bar{\varphi}$  = normalized error function;

$\phi^{VM}$  = Von Mises yield criterion;

$\nabla_x f(\mathbf{x})$  = gradient of function  $f$  with respect to vector variable  $\mathbf{x}$ ; and

$\nabla_{xx} f(\mathbf{x})$  = hessian of function  $f$  with respect to vector variable  $\mathbf{x}$ .

## Macro model Part II



## 4 Warping-inclusive kinematic coupling in mixed-dimension macro models for steel wide flange beam-columns

**Authors:** Alexander R. Hartloper, Albano de Castro e Sousa, Dimitrios G. Lignos

**Preprint version of:** Hartloper, A. R., de Castro e Sousa, A., and Lignos, D. G. (2021b). “Warping-inclusive kinematic coupling in mixed-dimension macro models for wide-flange beam-columns.” *Journal of Structural Engineering*, (Under review).

**Doctoral candidate's contributions:** Literature review, development of the warping-inclusive kinematic coupling method, finite element modeling and analysis, evaluation and interpretation of results. Writing and editing of the manuscript. The co-authors supervised the work carried-out by the doctoral candidate and assisted with the editing of the manuscript.

**Abstract:** A warping-inclusive kinematic coupling method to be used in finite element analysis of members featuring wide flange cross-sections is proposed in this chapter. This coupling method is used in mixed-dimension macro models that combine continuum and beam-column elements to reduce the computational cost of purely continuum finite element models. The proposed coupling method, utilizing either linear or nonlinear constraint equations, is implemented and validated in a commercial finite element software; the source code is made publicly available. Case studies indicate that including warping in the coupling formulation is critical for components that may experience coupled local and lateral-torsional buckling. Also highlighted is the potential of macro models to reduce the total degrees-of-freedom by up-to about 60 %, and computational memory use by up-to around 80 %, while retaining solution fidelity for beam, column, and panel zone components in steel moment-resisting frames. The case studies show that the linear constraint equation formulation may not be suitable for all problems, however, it may still yield acceptable results as long as the level of twisting is insignificant and lateral-torsional buckling is not critical.

**Keywords:** Continuum finite element analysis; Steel structures; Nonlinear geometric instabilities; Kinematic coupling; Beam-columns.

## **4.1 Introduction**

### **4.1.1 Background**

Simulation-based infrastructure design against natural hazards, such as earthquakes, relies heavily on the development of representative models of various fidelities (Krawinkler et al., 2006). Additionally, numerical models are necessary to evaluate the vulnerability of buildings and bridges and the social vulnerability of populations in at-risk communities (Deierlein and Zsarnóczy, 2019). Within the scope of steel structures subjected to earthquake hazards, geometric instabilities are a significant source of structural damage, therefore, modeling this effect is a necessity. Models that simulate nonlinear geometric instabilities in steel structures under cyclic loading can be divided into three main categories of increasing fidelity and complexity: (a) point hinge models (concentrated plasticity); (b) distributed plasticity models (commonly using fiber beam-column elements); and (c) continuum finite element (CFE) models. Although fracture can be critical for steel components, the focus of this chapter is mainly on models simulating component-level strength and stiffness deterioration due to local and/or member instabilities (member and lateral torsional buckling), as well as their interaction.

Point hinge models are placed at predefined locations of anticipated plasticity along a member. Concentrated plasticity models are known to be computationally efficient for parametric nonlinear analyses of metal structures (e.g., Ibarra and Krawinkler (2005)), and do not suffer from spurious localization issues during component deterioration. Sivaselvan and Reinhorn (2000) and Ibarra et al. (2005) proposed hysteretic models that capture the basic modes of cyclic deterioration in steel components, namely strength, post-peak strength and unloading stiffness deterioration. Others (Lignos and Krawinkler, 2011; Lignos et al., 2019) have proposed ad hoc modifications to the Ibarra et al. model's hysteretic rules in an effort to properly describe the hysteretic behavior of steel members.

Point hinge models have become the main workhorse in collapse-risk assessment studies (FEMA, 2009; NIST, 2010), however, they exhibit considerable limitations. First, their calibration requires large component datasets (Lignos and Krawinkler, 2013) that may not be always available. Second, point hinge models do not capture coupled geometric instabilities, and the effects of residual stresses on steel structures (Mathur et al., 2012). Third, the above approaches do not consider varying axial loads and bi-directional loading effects, nor do they capture axial shortening that may be influential in estimating earthquake induced losses (Elkady et al., 2020). These are major drawbacks, considering the findings from recent full-scale experimental studies (Suzuki and Lignos, 2015; Ozkula et al., 2017; Elkady and Lignos, 2018a; Cravero et al., 2020), along with corroborating CFE analyses (Elkady and Lignos, 2015a; Fogarty and El-Tawil, 2015; Elkady and Lignos, 2018b; Wu et al., 2018).

The capability of standard flexibility- (Spacone et al., 1996) and displacement-based (Mari, 1984) fiber-based beam-column elements to simulate the inelastic behavior of steel and composite-steel structures is well established (Hajjar et al., 1998; Sivaselvan and Reinhorn, 2002). Numerical accuracy, for a viable computational expense, can be achieved by properly selecting the number of fibers to discretize the cross section (Kostic and Filippou, 2012). Standard fiber beam-column elements employ the plane-sections-remain-plane assumption that is violated by torsion warping present in wide flange steel profiles. Theoretical developments have been proposed to address this challenge for fiber-based beam-column elements (Le Corvec, 2012; Di Re et al., 2018). Inclusion of the warping component is critical for evaluating wide flange steel components subjected to torsion and those that are susceptible to lateral-torsional buckling.

Continuum finite element component models are currently the only viable way to provide insights into complex instability interactions prior to global and partial structural collapse (Miyamura et al., 2015; Stoakes and Fahnstock, 2016; Wu et al., 2018). CFE models are also suitable for detailed studies of critical regions of metal structures (Kalochairetis and Gantes, 2011; Elkady and Lignos, 2015a, 2018b; Fogarty and El-Tawil, 2015; Araújo et al., 2017). Furthermore, it is acknowledged that CFE simulations can serve as benchmarks for theoretical developments of advanced fiber beam-column elements, and for the further development of advanced experimental techniques (Whyte et al., 2016).

A current difficulty in employing CFE models in structural analysis is that they are computationally expensive for multiple nonlinear dynamic analyses of structures. Reducing the computational expense of simulation models in aforementioned studies (Miyamura et al., 2015; Wu et al., 2018) would be beneficial to increase the number of structural configurations and ground motions that can be investigated within any time-frame. Such a consideration is particularly important in, e.g., incremental dynamic analysis (Vamvatsikos and Cornell, 2002), in which the computational complexity is further increased through the number of intensity levels analyzed for each ground motion. There is a clear need to reduce the computational demands from CFE component models while retaining the solution fidelity of this modeling approach. To achieve this goal, methods to reduce the associated computational cost in CFE simulations should be further developed.

The approach advocated in this chapter is to employ a mixed-dimension component macro model, that combines domains of 1D beam-column elements with continuum domains comprised of 2D shell or 3D solid elements. Here, the dimensionality of the element refers to the number of dimensions used to parametrize the element geometry: 1D elements are lines, 2D elements are surfaces, and 3D elements are volumes. The mixed-dimension macro model idea is illustrated in Figure 4.1a that shows the beam-column ( $\Omega_1$ ) and continuum ( $\Omega_2$ ) element domains for a wide flange cross section. Macro models can capture material plasticity and local instabilities in the continuum domains, while maintaining the

computational efficiency of beam-column elements. A chief issue in mixed-dimension macro models, and the focus of this chapter, is that there is a need to select an accurate coupling method between the beam-column and continuum domains that is also computationally friendly.

### **4.1.2 Review of coupling methods**

Coupling between the beam-column and continuum domains is typically accomplished through one of two means: the transition element approach, or the multipoint constraint (MPC) approach. One-dimension-to-continuum transition elements have been developed by Wagner and Gruttmann (2002), and were later extended by Chavan and Wriggers (2004) to include warping, and Koczubiej and Cichoń (2014) further extended these elements to the total Lagrangian formulation. More recently, Sadeghian et al. (2018) developed transition elements between 1D beam-column elements and 2D membrane elements for the analysis of reinforced concrete members. One limitation of transition elements is that they are typically less efficient than MPC approaches due to the proliferation of elements that connect all the nodes across both domains at the interface. Further limitations of transition elements include a proclivity to locking, and the need to treat such effects (Ho et al., 2010).

The MPC coupling approach specifies constraint equations among the relevant degrees of freedom (DOFs) between the two domains on the beam-column/continuum interface. The MPCs that form the coupling between domains can be implemented through any common constraint method (e.g., elimination, Lagrange multipliers, and the penalty method). Mixed-dimension MPC coupling methods have been developed by Monaghan et al. (1998) for coupling beam-column and solid domains by balancing the work done on the interface of each region. McCune et al. (2000); Shim et al. (2002) expanded on Monaghan et al. (1998)'s formulations to generalize for 1, 2, and 3D coupling. The notable limitations of this method are that linear constraint equations are enforced (i.e., the dependent DOFs have a linear relation to the independent DOFs), and that deformations due to warping are not transferred between the beam-column and continuum domains. Ho et al. (2010) proposed a multi-dimensional coupling for use with explicit time integration methods. Warping and shear deformations are not included in this method, and the reliance on explicit time integration limits the applicability of this approach. Song (2010) developed coupling between Timoshenko beam-column elements and 3D solid elements using transformation matrices. Again, warping was not included, and only linear material behavior and small deformations are considered. The lack of warping transfer between the two domains limits the applicability of any coupling method for components experiencing nonuniform torsion or susceptible to lateral-torsional buckling.

Kinematic coupling constitutes another class of MPC methods. In this method, displacement and/or rotation continuity of a dependent region of continuum element nodes is enforced based on the displacements and rotations of an independent beam-column node.



Existing formulations (Dassault Systèmes, 2014; Liu, 2016) fall under the category of kinematic coupling as they enforce displacement continuity in static problems, and a mixture of velocity and displacement continuity in dynamic problems. Liu (2016) showed the capability of kinematic coupling utilizing nonlinear constraint equations for solving problems involving finite-rotations. However, torsion warping is again absent in these formulations. Incorporating warping into kinematic coupling, and studying the effect of doing so, are two aims of this chapter.

### 4.1.3 Chapter objectives

Component models that mix elements of varying fidelity have been used previously in the assessment of steel structures (see e.g., Tada et al. (2008), Krishnan (2010), Sreenath et al. (2011), Imanpour et al. (2016)), however, such studies have not focused on the effect of the coupling method between the different domains. Further investigation into this matter is necessary to develop accurate and efficient modeling recommendations for a wide range of steel beam-column components. The main issues apparent in the reviewed coupling methods are that transition elements that include warping may not be computationally efficient when compared with the MPC approach, and that existing MPC approaches do not consider warping that can be critical for beam-columns susceptible to coupled local and lateral-torsional buckling. Furthermore, nonlinear constraint equations should be employed for modeling collapse limit states often of interest in earthquake engineering.

An MPC kinematic coupling method that includes torsion warping is proposed to address the aforementioned considerations. This chapter focuses on answering the following questions: What is the effect of warping-inclusive coupling on simulation results? When are formulations with linear constraint equations acceptable? What are the computational benefits of the component macro model approach? Linear and nonlinear versions of the proposed coupling method are implemented; the proposed coupling method is found to be easily compatible with existing finite element analysis software typically used in practice. A series of computational case studies are then used to evaluate each of questions posed above using the proposed MPC formulation and an existing coupling method that is available in commercial software.

## 4.2 Proposed coupling method

### 4.2.1 Beam-column element kinematics

A coupling strategy for beam-column and continuum elements requires an understanding of the governing element kinematics. The beam-column kinematics used herein are based on a line of centroids and a set of cross section planes that rotate about each of the centroid

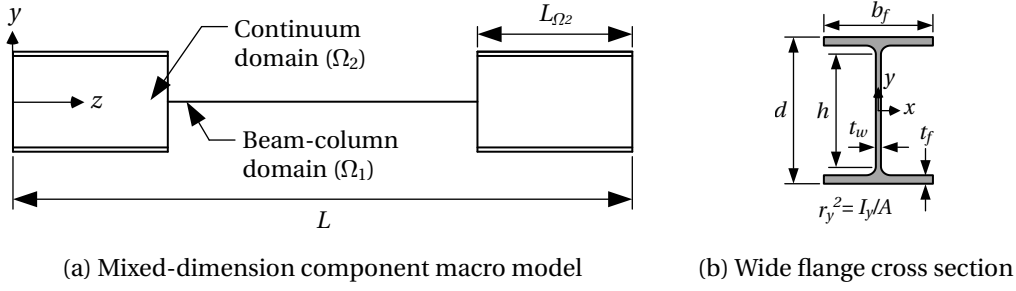


Figure 4.1 – Mixed-dimension component macro model concept for wide flange cross sections.

points, see e.g., Simo and Vu-Quoc (1991). Following this reference, a warping function is also defined on the cross section to incorporate out-of-plane torsion warping. Each beam-column element node is assumed to have three displacement DOFs, three rotation DOFs, and one torsion warping DOF.

Beam kinematics are defined by material points, denoted  $\mathbf{x}_{mp}^b$ , where the subscript indicates that this is a material point and the superscript indicates the beam-column element. The position of any material point in the cross section defined by the beam element formulation is as follows:

$$\mathbf{x}_{mp}^b(\xi, \eta, \zeta) = \mathbf{x}(\zeta) + \xi \mathbf{n}_1(\zeta) + \eta \mathbf{n}_2(\zeta) + w(\zeta) \psi(\xi, \eta) \mathbf{t}(\zeta), \quad (4.1)$$

where  $\zeta$  is the coordinate along the element centerline,  $\xi$  and  $\eta$  are the distances measured along the  $\mathbf{n}_1$ ,  $\mathbf{n}_2$  axes in the undeformed configuration,  $\mathbf{x}(\zeta)$  is the position of the centroid along the centerline in the undeformed configuration,  $w(\zeta)$  is the warping amplitude,  $\psi(\xi, \eta)$  is the warping function, and  $\mathbf{t}(\zeta)$  is the axis in the direction of the cross section normal. The representation of these parameters is shown in Figure 4.2a for a wide flange profile, and leads to the limits of  $0 \leq \zeta \leq L$ ,  $-b_f/2 \leq \xi \leq b_f/2$  and  $-d/2 \leq \eta \leq d/2$ , where  $L$  is the member length;  $b_f$  is the flange width; and  $d$  is the full cross section depth. The first term in Equation 4.1 is the position of the cross section with respect to the centerline, the second and third terms represent the cross section plane spanned by  $\mathbf{n}_1$  and  $\mathbf{n}_2$ , and the fourth term is the out-of-plane deformation due to torsion warping.

Only wide flange sections are considered within the scope of this chapter, however, the proposed coupling method may be used with other cross-sections provided that the warping function is readily available at each point on the cross section. The warping function used in this chapter is based on elastic homogeneous thin-walled open cross-sections, and for wide flange cross-sections can be simply defined as (Chen and Atsuta, 2008)

$$\psi(\xi, \eta) = \xi \eta. \quad (4.2)$$

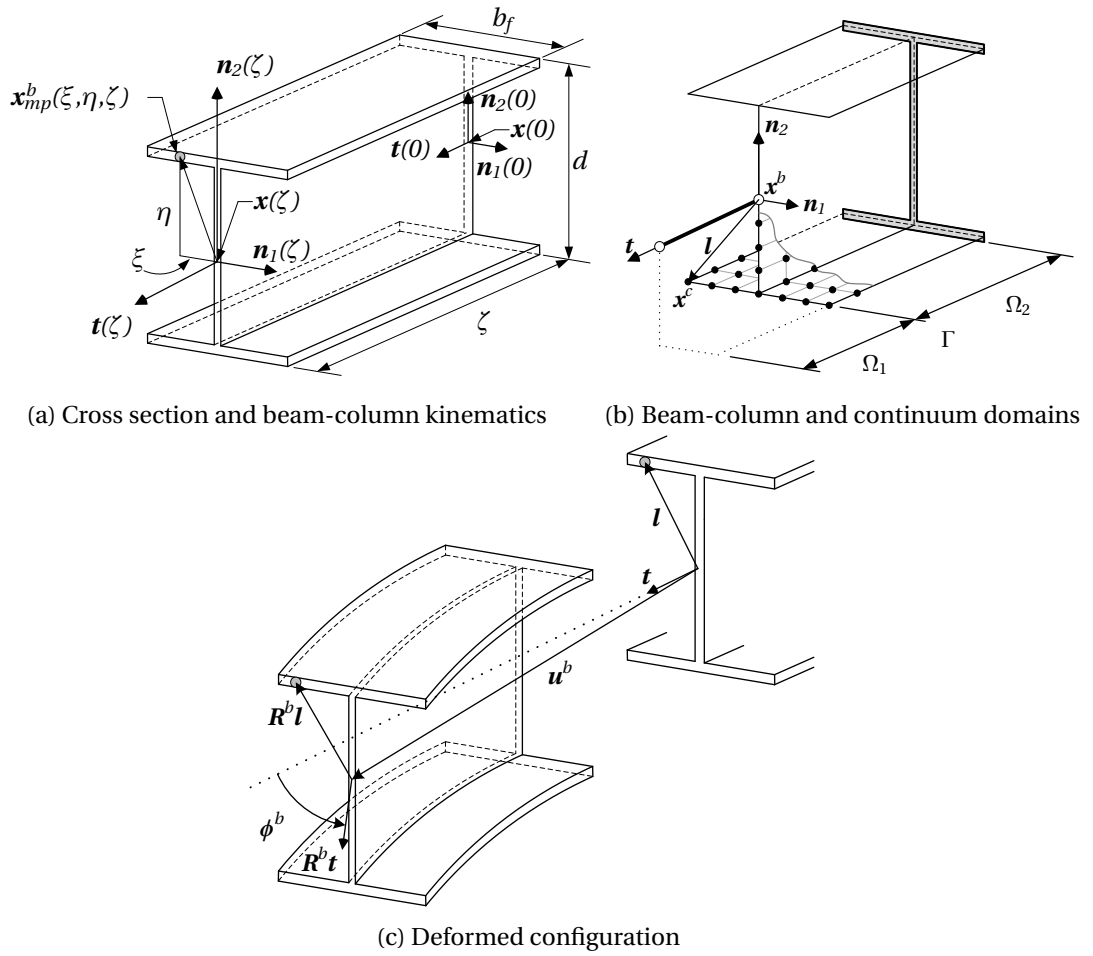


Figure 4.2 – Schematic wide flange cross section and mixed-dimension domains.

### 4.2.2 Nonlinear definition of the constraint equations

The kinematic coupling method proposed in this chapter is composed of constraint equations that relate the beam-column and continuum domains, as defined in Figure 4.2b. The beam-column domain is  $\Omega_1$ , the continuum domain is  $\Omega_2$ , and the interface between these two domains is  $\Gamma$ . The proposed coupling method stipulates that the beam-column node is coupled to the three displacement DOFs of the continuum nodes on the interface, therefore, coupling of rotation DOFs in the continuum domain are neglected (e.g., in shell elements). This method is referred to as the Warping-Inclusive Kinematic Coupling, or WIKC, herein, and can be identified as an enhancement to kinematic coupling methods, for instance, in Abaqus (Dassault Systèmes, 2014). Each of the constraint equations are a function of seven variables owing to the seven DOFs of the beam-column node, and in total  $3N$  equations are defined for  $N$  continuum nodes.

First, the constraints for a single continuum node are presented without warping, and afterwards the warping term is included. The nonlinear, rigid-body coupling constraint equations without warping are written succinctly in matrix-vector form for a single node as

$$\mathbf{u}^c = \mathbf{u}^b + \mathbf{R}^b \mathbf{l} - \mathbf{l}, \quad (4.3)$$

where  $\mathbf{u}^c$  is the vector of continuum displacements,  $\mathbf{u}^b$  is the vector of beam-column node displacements,  $\mathbf{l}$  is the link vector that relates the continuum node initial position to the beam-column node initial position, ( $\mathbf{l} = \mathbf{x}^c - \mathbf{x}^b$ ,  $\mathbf{x}^c$  is the initial position of the continuum element node, and  $\mathbf{x}^b$  is the initial position of the beam-column node, as shown in Figure 4.2a). The term  $\mathbf{R}^b \mathbf{l}$  is the link rotated into the deformed configuration by the rotation matrix  $\mathbf{R}^b$ . The definition of each of these variables is shown in Figure 4.2b, and the deformed configuration is shown in Figure 4.2c.

The rotation matrix,  $\mathbf{R}^b$ , is formed from the rotation vector of the beam-column node,  $\boldsymbol{\phi}^b$ , using the well-known Rodrigues formula (Rodrigues, 1840):

$$r = \|\boldsymbol{\phi}^b\|, \quad \mathbf{r} = \boldsymbol{\phi}^b / r, \quad (4.4a)$$

$$\mathbf{R}^b = \cos[r] \mathbf{I} + (1 - \cos[r]) \mathbf{r} \mathbf{r}^T + \sin[r] [\mathbf{r}]_{\times}, \quad (4.4b)$$

where  $\mathbf{I}$  is the  $3 \times 3$  identity matrix, and  $[\mathbf{r}]_{\times}$  is the skew-symmetric matrix formed from  $\mathbf{r}$ , i.e.,

$$[\mathbf{r}]_{\times} = \begin{bmatrix} 0 & -r_3 & r_2 \\ r_3 & 0 & -r_1 \\ -r_2 & r_1 & 0 \end{bmatrix}. \quad (4.5)$$

Including warping, the constraint equations that constitute the warping-inclusive kine-

matic coupling method become

$$\mathbf{u}^c = \mathbf{u}^b + \mathbf{R}^b \mathbf{l} - \mathbf{l} + \psi w^b \mathbf{R}^b \mathbf{t}, \quad (4.6)$$

where  $\psi$  is the warping function evaluated at  $\xi$  and  $\eta$  of the node,  $w^b$  is the value of the warping DOF at the beam-column node, and the term  $\mathbf{R}^b \mathbf{t}$  is the orientation of the local  $\mathbf{t}$ -axis in the deformed configuration. Finally, the standard, or homogenous, form of the constraint equations is

$$\mathbf{f} := \mathbf{u}^c - \mathbf{u}^b - \mathbf{R}^b \mathbf{l} + \mathbf{l} - \psi w^b \mathbf{R}^b \mathbf{t} = \mathbf{0}. \quad (4.7)$$

### 4.2.3 Linearized constraint equations

Linearized constraint equations are necessary for implementation of the coupling in a non-linear incremental-iterative analysis (e.g., Newton-Raphson). The key components of the linearized constraint equations are the constraint coefficient matrices,  $\mathbf{A}_1$  and  $\mathbf{A}_2$ , that are based on the standard form of the constraint equations. These two matrices are the coefficients of the beam-column and continuum nodes, respectively, from the linearized constraint equation. Linearizing Equation 4.7,  $\mathbf{A}_1$  and  $\mathbf{A}_2$  are defined in Equation 4.8 as follows:

$$\delta \mathbf{f} = \mathbf{A}_1 \delta \mathbf{u}^c + \mathbf{A}_2 \begin{bmatrix} \delta \mathbf{u}^b \\ \delta \boldsymbol{\theta}^b \\ \delta w^b \end{bmatrix} = \mathbf{0}, \quad (4.8)$$

where  $\delta \boldsymbol{\theta}^b$  is the linearized rotation vector. Carrying out the linearization, the following expression is obtained:

$$\delta \mathbf{f} = \delta \mathbf{u}^c - \delta \mathbf{u}^b - \mathbf{R}^b \mathbf{l} \times \delta \boldsymbol{\theta} - \psi w^b \mathbf{R}^b \mathbf{t} \times \delta \boldsymbol{\theta} - \psi \mathbf{R}^b \mathbf{t} \delta w^b, \quad (4.9)$$

where, for any rotation field,  $\delta(\mathbf{R}^b \mathbf{l}) = \delta \boldsymbol{\theta} \times \mathbf{R}^b \mathbf{l}$  (see, e.g., Sec. 1.3.1 of Dassault Systèmes (2014)). Additionally in Equation 4.9, the term  $\delta \mathbf{l} = \mathbf{0}$  because this vector is considered to be constant throughout the analysis (i.e., deformation of the cross section due to Poisson's effect is neglected). From Equation 4.9, the  $\mathbf{A}_1$  matrix related to the displacement  $\mathbf{s}$  of the beam-column node is equal to the identity matrix,  $\mathbf{I}$ , since all the coefficients are equal to unity. Collecting the remaining terms in Equation 4.9, and using the matrix definition of the cross-product, the  $\mathbf{A}_2$  matrix of dimension  $3 \times 7$  becomes

$$\mathbf{A}_2 = \left[ \mathbf{A}_2^{disp}, \mathbf{A}_2^{rot}, \mathbf{A}_2^{warp} \right] = \left[ -\mathbf{I}, -[\mathbf{R}^b \mathbf{l} + \psi w^b \mathbf{R}^b \mathbf{t}]_{\times}, -\psi \mathbf{R}^b \mathbf{t} \right]. \quad (4.10)$$

To close, a few remarks are made regarding  $\mathbf{A}_2$ :

- The  $[\mathbf{R}^b \mathbf{l}]_{\times}$  term can be interpreted as forces acting at the continuum node due to

bending/(pure)torsion acting on the beam-column node in the current deformed configuration.

- The  $[\psi w^b \mathbf{R}^b \mathbf{t}]_{\times}$  term can be interpreted as a nonlinear effect of warping that arises because of the displacement component in the local  $\mathbf{t}$ -axis between the continuum and beam-column nodes.
- The coupling method is nonlinear because the  $\mathbf{A}_2^{rot}$  and  $\mathbf{A}_2^{warp}$  matrices depend on the current rotation  $\mathbf{R}^b$ , therefore, the  $\mathbf{A}_2$  matrix needs to be re-computed at each iteration in the analysis.
- Force, moment, and bi-moment equilibrium are satisfied at the interface considering that the forces, moments, and bi-moment acting on the interface beam-column node are determined through the constraint coefficient matrix  $\mathbf{A}_2$ . For example,  $\mathbf{A}_2^{disp} = -\mathbf{I}$  implies that the beam-column node forces are equal to the sum of the forces acting on each continuum element node;  $\mathbf{A}_2^{rot}$  implies the moments will be equal to the continuum node forces multiplied by the rotated link vector plus the nonlinear effect due to warping; and  $\mathbf{A}_2^{warp}$  implies that the bi-moment will be equal to the warping function multiplied by the force in the direction of  $\mathbf{R}^b \mathbf{t}$ .

### Linear Coupling Method

A linear version of the WIKC method is derived for use in evaluating linear coupling methods. The linear constraint coefficient matrix,  $\mathbf{A}_2^{lin}$ , can be recovered from Equation 4.10 by considering the current configuration always equal to the initial configuration. This is done by replacing  $-\left[\mathbf{R}^b \mathbf{l} + \psi w^b \mathbf{R}^b \mathbf{t}\right]_{\times}$  with  $-\left[\mathbf{l}\right]_{\times}$  in  $\mathbf{A}_2^{rot}$ , and replacing  $-\psi \mathbf{R}^b \mathbf{t}$  with  $-\psi \mathbf{t}$  in  $\mathbf{A}_2^{warp}$ . With these considerations, the linear version of the  $\mathbf{A}_2$  matrix becomes

$$\mathbf{A}_2^{lin} = \left[ -\mathbf{I}, -\left[\mathbf{l}\right]_{\times}, -\psi \mathbf{t} \right]. \quad (4.11)$$

The governing linear constraint equations can be recovered by applying  $\mathbf{A}_2$  to the vector of beam-column DOFs, and considering that  $l_3 = 0$  as the continuum and beam-column nodes are assumed to be in the same plane initially:

$$\mathbf{u}_c = \mathbf{A}_2^{lin} \begin{bmatrix} \mathbf{u}^b \\ \boldsymbol{\phi}^b \\ w^b \end{bmatrix} \Rightarrow \mathbf{u}_c = \begin{bmatrix} u_1^b - \phi_3^b \eta, \\ u_2^b + \phi_3^b \xi, \\ u_3^b + \phi_1^b \eta - \phi_2^b \xi + \xi \eta w^b \end{bmatrix}. \quad (4.12)$$

### 4.3 Case studies

A series of case studies are investigated in this chapter to: (a) validate the proposed WIKC method, illustrate the importance of including warping in the constraint equations, (b) assess the applicability of the linear coupling method, (c) and highlight the computational efficiency of the proposed macro models. To achieve these objectives, four computational models are compared for each of the cases described in subsequent sections: (1) a full-shell model that represents the continuum “benchmark” analysis (denoted as Full-shell); (2) a beam-shell macro model using a “built-in” kinematic coupling formulation that does not transfer warping across the interface (denoted as Macro Built-in); (3) a beam-shell macro model using the proposed nonlinear WIKC (denoted as Macro Warping); and (4) a beam-shell macro model using the proposed linear WIKC (denoted as Macro Lin. Warping). All of the computational work in this chapter is carried out using Abaqus v6.14 (Dassault Systèmes, 2014). Both the linear and nonlinear versions of the WIKC method are implemented in Abaqus using MPC user subroutines; the source code, instructions for use, and examples are available in Hartloper (2020). The following sections provide a description of the case studies, their links with practical applications, and a set of general modeling recommendations. Afterwards, the results for each case are presented and discussed.

#### 4.3.1 Case studies overview

The case studies investigated in this chapter are summarized in Table 4.1. This table gives a brief description of the primary mode of deformation, the components and their respective cross-sections, and the stability of the anticipated equilibrium path. The objectives of Case Study 1 are to demonstrate the error in the elastic torsional stiffness of mixed-dimension macro models when warping is not included in the coupling formulation, and to identify the limits of the proposed macro model approach when twisting is significant. Case Studies 2–4 demonstrate the implications of this issue in the context of steel components subjected to cyclic loading. These examples are based on structural components in steel moment-resisting frames (MRFs), subjected to both quasi-static and dynamic loading, as shown schematically in Figure 4.3. Through these four case studies, the proposed macro model approach and coupling method are evaluated for main structural components in steel MRFs.

##### Case study 1: Nonuniform torsion

Case Study 1 is based on a seminal experiment conducted by Farwell and Galambos (1969) using a  $6 \times 6$ -25 beam of ASTM-A36 (nominal  $f_y = 250$  MPa) steel subjected to a central torque. The geometric properties of the  $6 \times 6$ -25 beam are provided in Table 4.2, and a schematic of the test set-up is provided in Figure 4.4. The test consists of a steel beam fixed against

## Chapter 4. Warping-inclusive kinematic coupling in mixed-dimension macro models for steel wide flange beam-columns

---

rotation at the ends but free to warp. A torque is applied at the center of the beam through the circular loading plate. The beam ends are assumed to be restricted in axial displacement due to friction at the beam end supports, as this condition provides the best match with the test data. For this reason the centroid of the beam is considered as axially fixed at the ends. The equilibrium path in Case Study 1 is stable (i.e., no buckling occurs) as the beam is only subjected to torsion. The continuum lengths are nominally chosen as  $L_{\Omega_2} = 0.25L = 482.5$  mm at both member ends for the macro models.

### Case study 2: Interior subassembly

Case Study 2 focuses on an interior subassembly, in this case represented by the DBBW specimen tested by Engelhardt et al. (2000) as a part of the SAC<sup>1</sup> Program (FEMA, 2000). The beams in the subassembly have a W36X150 cross section, and the column is a W14X398, dimensions of the components are provided in Table 4.2, and a schematic of the subassembly is shown in Figure 4.5b. This table also includes the normalized LTB slenderness per CEN (2005a), the ratio of unbraced length to weak-axis radius of gyration ( $L_b/r_y$ ), and the limiting length for inelastic LTB ( $L_r$ ) per ANSI/AISC 360-16 (AISC, 2016b). The material for all components is ASTM A572 Gr. 50 steel ( $f_y = 345$  MPa). The beams have roller supports near the ends and lateral supports at the ends, and a cyclic displacement-controlled load is applied at the column top. The column bottom is pinned, and the top is fixed against out-of-plane displacements and has a flexible torsional support that is modeled with a stiffness equivalent to two 1.5 m W14X150 beams. Both beam-to-column connections include radius-cut reduced beam sections (RBS), and the subassembly was designed with a balanced panel zone concept that leads to yielding in the panel zone and buckling in the RBS region, therefore, the equilibrium path is designated as unstable. Based on observations of the Full-shell model, the continuum lengths are chosen to be approximately 400 mm greater than the extend of the RBS cut-out in the beams ( $L_{\Omega_2} = 1300$  mm), and approximately 400 mm greater than the beams on both sides for the column ( $L_{\Omega_2} = 1700$  mm).

### Case study 3: Quasi-static collapse-consistent loading of first-story column

Case Study 3 focuses on a typical first-story column with a relatively compact cross section ( $b_f/2t_f = 5.92$ ,  $h/t_w = 33.2$ ), in this case represented by the C5 test carried out by Elkady and Lignos (2018a). The column cross section is a W24X146, with a length of 3.9 m, the geometric properties are summarized in Table 4.2. The column is not critical for LTB since  $\bar{\lambda}_{LT} < 0.4$ . A unidirectional collapse consistent load protocol (Suzuki and Lignos, 2020) is applied in the strong axis of the column ( $u_y$ ), and a constant compressive 20 % of the measured axial yield load is applied at the column top ( $-F_z$ ), as illustrated in Figure 4.5c. Rotations

---

<sup>1</sup>Joint venture between the Structural Engineers Association of California (SEAOC), the Applied Technology Council (ATC), and California Universities for Research in Earthquake Engineering (CUREe)



Table 4.1 – Overview of the case studies.

Case Study ID	Description	Component(s)	Material	Equilibrium Path
Case 1	Nonuniform torsion	Beam: $6 \times 6-25$	A36	Stable
Case 2	Interior subassembly	Column: W14X398, Beam: W36X150	A572 Gr. 50	Unstable
Case 3	First-story column, quasi-static loading	Column: W24X146	A992 Gr. 50	Unstable
Case 4	First-story column, dynamic loading	Column: W24X94	A992 Gr. 50	Unstable

and displacements are fixed at the column base, and a rotationally flexible boundary in the strong axis is assumed at the column top by synchronizing  $\phi_x$  with  $u_y$ . The basis of the flexible boundary is to obtain an inflection point at  $z = 3/4L$  when the column is elastic, representative of first-story columns in steel moment-resisting frames (Elkady and Lignos, 2018a). The equilibrium path is classified as unstable because local buckling is observed in the test, thereby causing cyclic deterioration in strength and stiffness. The continuum lengths are chosen as  $L_{\Omega_2} = 0.25L = 900$  mm at both member ends for the macro models to capture the local buckling at the member ends.

#### Case study 4: Column nonlinear response history analysis

Case Study 4 focuses on an equivalent single-degree-of-freedom type representation of a typical first story column. The column selected for this example is based on the interior first-story column in a prototype four-story steel MRF designed for urban California (Elkady and Lignos, 2015b). The column cross section is a W24X94 with a length of 5500 mm, the geometric properties are summarized in Table 4.2, and a schematic of the model is provided in Figure 4.5d. The criticality of including warping in the coupling formulation is demonstrated in this case since the column has a typical cross section and is susceptible to inelastic lateral-torsional buckling ( $\bar{\lambda}_{LT} > 0.4$ ).

All displacements and rotations are fixed at the column bottom, and out-of-plane displacements and all rotations are fixed at the column top. A constant axial load corresponding to 20 % of the expected axial yield strength of the cross section ( $F_z = 1300$  kN) is applied at the top of the column, and the Northridge 1994 Canoga Park record is applied to the base of the column ( $a_{g,y}$ ). The first-mode period of the target prototype structure is about 1.5 s (Elkady, 2016), therefore, the mass of the column is chosen such that the first-mode period is equal to 1.5 s. This procedure results in a mass of  $766.5 \text{ s}^2\text{N/mm}$ , and 2 % mass proportional damping is assumed. A frequency analysis is conducted to validate the computed mass and the results are presented later. The shell lengths are chosen as  $L_{\Omega_2} = 0.3L = 1650$  mm at both member ends for the macro models to capture the coupled buckling along the member length.

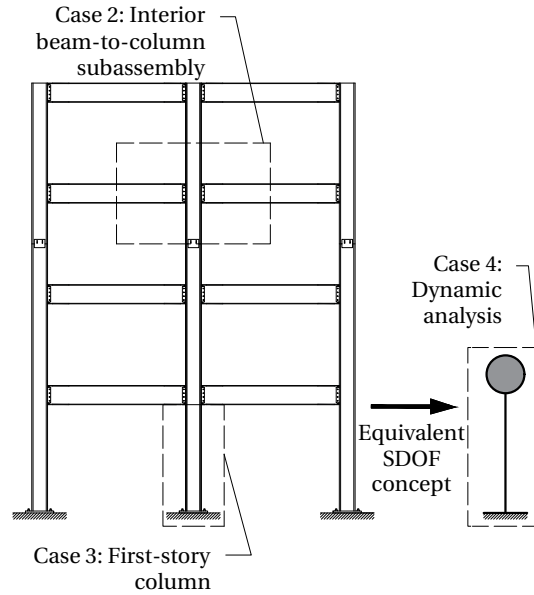


Figure 4.3 – Schematic view of prototype frame and overview of Case Studies 2, 3, and 4.

#### 4.3.2 Nonlinear finite element modeling approach

Modeling guidelines for the Full-shell models are based on those of Elkady and Lignos (2018b), and the macro models are then adapted from the full-shell models. A later section also includes a methodology for generating and imposing imperfections for continuum mechanics problems containing an unstable equilibrium path, and afterwards a summary of the model and imperfection properties is provided for all the case studies.

Numerical details of the analyses carried out in Abaqus v6.14 are outlined for clarity. Implicit time integration is used for both the quasi-static and dynamic problems. The system of equilibrium equations is solved using Newton's method with double precision. The default convergence criteria of 0.5 % on the relative force and moment residuals is used for all analyses.

Based on Elkady and Lignos (2018b), four-node reduced integration shell elements (S4R) are used in the continuum domains. The Abaqus enhanced hourglass stiffness control is used (Dassault Systèmes, 2014), and five Simpson integration points are used throughout the shell thickness. A mesh size of <25 mm is used in the continuum domains where buckling may occur, and the element size is relaxed in the column of Case Study 2 since only yielding of the panel zone occurs. Linear, two-node beam-column elements with torsion warping (B31OS) are used in the beam-column element domains. These are displacement-based beam-column elements with a single integration point at the center of the element, and 7-DOFs at each node. Cross section properties and forces are evaluated in these beam-column elements at five integration points in each flange, and five integration points along the web (Dassault Systèmes, 2014). A minimum of four beam-column elements are used in each  $\Omega_1$  domain so that possible

member buckling can be captured in the macro model. Extents of the beam-column and shell element domains, i.e., the length  $L_{\Omega_2}$  in Figure 4.1a, are provided for all the cases in Table 4.3.

The Voce-Chaboche (VC) nonlinear kinematic/isotropic hardening material model native to Abaqus v6.14 is used in all the beam-column and shell domains to represent the ASTM A992 Gr. 50 and ASTM A572 Gr. 50 materials subjected to cyclic straining. Consistent model parameters for the A992 Gr. 50 steel are taken from de Castro e Sousa et al. (2020). VC model parameters for the A572 Gr. 50 steel are calibrated using the tensile-only approach of de Castro e Sousa et al. (2021) using the SAC average stress-strain curve (Engelhardt et al., 2000). Employed parameters for both materials are provided in Table 4.4, where a Poisson's Ratio of  $\nu = 0.3$  is always assumed. One limitation of the employed Abaqus v6.14 beam-column elements is that only one material may be specified for the element. The flange material properties are assumed throughout the beam-column domains because yielding is primarily expected to occur in the flanges due to the axial stress gradient from bending. Residual stresses are not considered in any of the numerical models because the beam-column elements in Abaqus v6.14 do not allow for residual stress variations through the cross section, this issue is discussed later in the Limitations section.

#### Modeling exceptions for case study 1

The following exceptions to the aforementioned guidelines are made for Case Study 1: the mesh size is slightly smaller than that recommended by Elkady and Lignos (2018b) due to the smaller cross section dimensions, and an increased number of quadratic beam-column elements (B32OS) are used in  $\Omega_1$ . The increased elements and additional integration point along the length are required to capture the yielding throughout the member, whereas this is not necessary for the other case studies since yielding is focused at the member ends in the continuum domains. Furthermore, a beam-column element only model (denoted “Full-beam”) is used in this case study to compare a beam-column element only model with a shell element only model. An exception is also made for the ASTM-A36 material properties in this case study: a piece-wise isotropic hardening model is used to represent this steel material since only monotonic loading is applied. The parameters for the ASTM-A36 material are  $E = 213400$  MPa,  $\nu = 0.3$ ,  $\sigma_{y,0} = 285$  MPa and hardening defined by 289 MPa at  $\epsilon^p = 0.01329$  and 876.2 MPa at  $\epsilon^p = 0.094$  as assumed in Pi and Trahair (1995).

#### 4.3.3 Imperfection methodology

Imperfections are critical when geometric instabilities are expected in nonlinear analysis problems (Galambos, 1998; Ziemian, 2010; AISC, 2016b), for this reason, care is taken in describing the approach used to apply imperfections. Member out-of-straightness and out-of-plumbness imperfections are deemed critical for flexural buckling modes, and local flange and web im-

## Chapter 4. Warping-inclusive kinematic coupling in mixed-dimension macro models for steel wide flange beam-columns

Table 4.2 – Wide flange member geometry used in the analysis cases.

Case	Section	$d$ [mm]	$b_f$ [mm]	$t_f$ [mm]	$t_w$ [mm]	$L_b$ [mm]	$b_f/2t_f$ -	$h/t_w$ -	$L_b/r_y$ -	$\bar{\lambda}_{LT}^b$ -	$L_r$ [m]
1	6 × 6-25	152	151	12.2	8.0	1930	6.20	16.0	50	0.20	10.7
2	W14X398	465	442	72.4	45.0	3708	2.92	6.44	34	0.15	41.8
2	W36X150	912	305	23.9	15.9	3962	6.37	51.9	63	0.31	7.7
3	W24X146 <sup>a</sup>	627	325	27.1	17.6	3900	5.92	33.2	51	0.29	10.2
4	W24X94	617	230	22.2	13.1	5500	5.18	41.9	109	0.50	6.4

<sup>a</sup>: measured  $d, b_f, t_f, t_w$ . <sup>b</sup>:  $\bar{\lambda}_{LT} = \sqrt{Z_x f_y / M_{cr}}$

$M_{cr} = C_1 \pi^2 E I_y / (k_y L)^2 \sqrt{(k_y / k_w)^2 I_w / I_y + (k_y L)^2 G I_t / (\pi^2 E I_y)}$ ,  $C_1 = 2.55$ ,  $k_y = 0.5$ ,  $k_w = 1.0$

Table 4.3 – Case study macro model and imperfection parameters.

Case Study ID	$L_{\Omega_2}$ [mm]	$\Delta_{shell}$ [mm]	Shell Type	$N_{beam}$	Beam Type	$L_{bw}$ [mm]	$\theta_{twist}$ [%rad]
Case 1	482.5	<20	S4R	8	B32OS	-	-
Case 2, column	1700	<50	S4R	4	B31OS	-	-
Case 2, beams	1300	<25 <sup>a</sup>	S4R	6	B31OS	686	-
Case 3	800	<25	S4R	4	B31OS	752	0.05
Case 4	1650	<25	S4R	4	B31OS	740	0.6

<sup>a</sup>: <25 mm in the RBS region, <50 mm elsewhere.

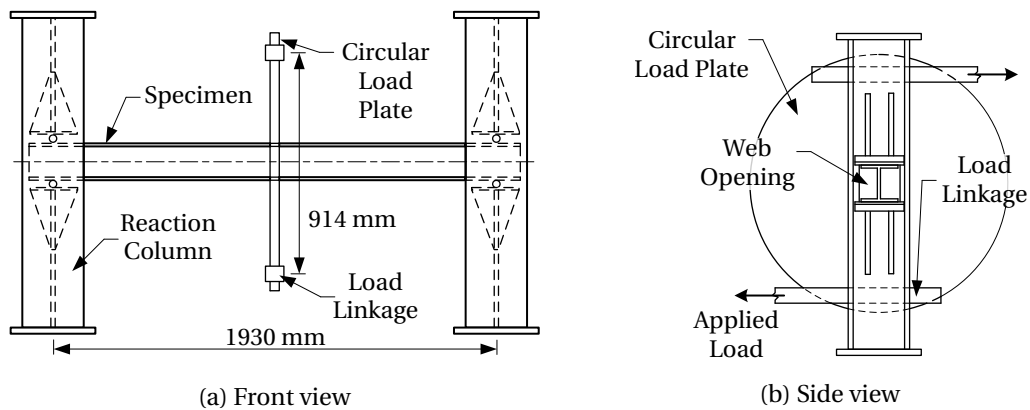


Figure 4.4 – Details of the nonuniform torsion test, reproduced from Farwell and Galambos (1969).

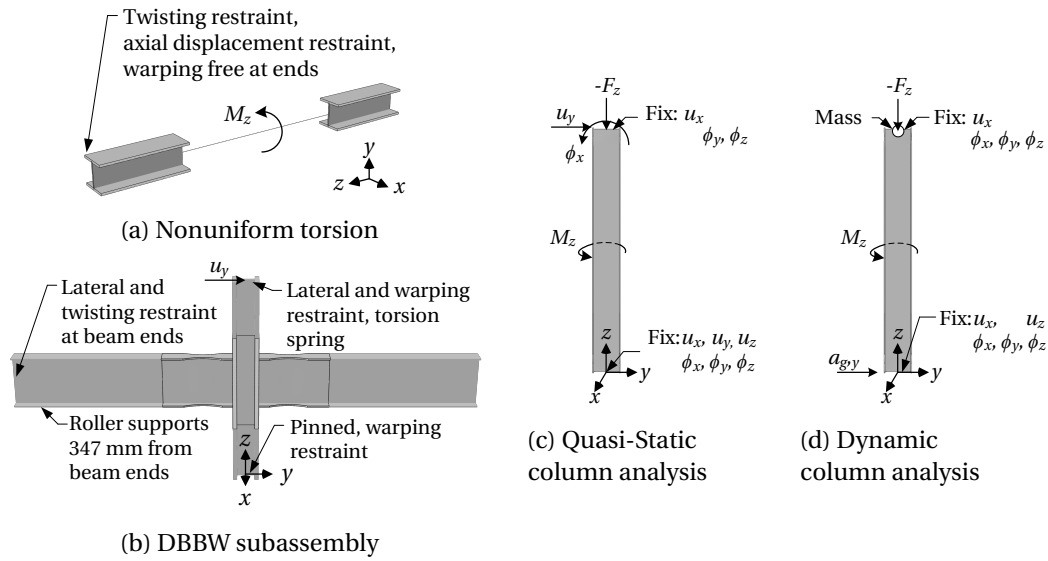


Figure 4.5 – Schematic representations of the illustrative examples (extruded view of shell domains shown).

perfections are deemed critical for local buckling modes. Twisting imperfections are also considered to be critical for modes associated with lateral-torsional buckling. Flexural buckling modes are not critical in the analyses examined herein, and therefore, out-of-straightness and out-of-plumbness imperfections are not considered.

Typically, imperfections may be included by applying scaled buckling modes from elastic eigenvalue analysis to the geometrically perfect model (Fogarty and El-Tawil, 2015; Elkady and Lignos, 2018b; Cravero et al., 2020). One issue with this typical method is that the similitude between the full-continuum and macro models is not guaranteed because the presence of the beam-continuum interface will influence the computed buckling modes. Using the exact same imperfections in the full-shell and macro models is considered important to remove a potential source of bias when comparing the two modeling approaches. An alternative method is proposed in this study to derive local imperfection geometries that are applied directly to the shell domains. This proposed method also addresses an anticipated challenge of applying geometric imperfections to members in system-level simulation studies where the member buckling modes may not be available for each individual component.

The proposed imperfection method, implemented in the Python package *pywikc* (Hartloper, 2020), defines a local imperfection geometry according to elastic plate buckling theory. The shape of the imperfection is defined as a function of the buckling wavelength,  $L_{bw}$ , and the maximum imperfection amplitude. The buckling wavelength is determined using elastic eigenvalue buckling analysis of the component, and the maximum imperfection amplitude is based on previous studies and measurements of wide flange cross-sections (Hartloper and Lignos, 2019). First, the imperfection shapes are defined, then methods for obtaining the

## Chapter 4. Warping-inclusive kinematic coupling in mixed-dimension macro models for steel wide flange beam-columns

maximum amplitudes and  $L_{bw}$  are defined.

Equations describing the buckled shape along the width of the flanges and web are adapted from Hill (1940) and Haaijer (1956). The mathematical model for the half-flange plate is shown in Figure 4.6. A uniform compressive stress,  $\sigma$ , is assumed to act along the two fixed edges, while one edge is free and the other edge has a rotational restraint (RR) from the web. The shape along the flange width in the  $\mathbf{n}_1$  direction is described by

$$v_\xi(\tilde{\xi}) = \tilde{\xi} + \frac{\epsilon}{2a_3} (\tilde{\xi}^3 + a_1\tilde{\xi}^4 + a_2\tilde{\xi}^3 + a_3\tilde{\xi}^2), \quad (4.13)$$

where  $a_1 = -4.963$ ,  $a_2 = 9.852$ ,  $a_3 = -9.778$ ,  $\epsilon$  is the relative restraint per unit width provided by the web, and  $\tilde{\xi} = \xi/(b_f/2)$ . The model for the web plate is similar to that of the flange, but both unloaded edges have a rotational restraint due to the flanges. The shape along the width of the web in the  $\mathbf{n}_2$  direction is

$$v_\eta(\tilde{\eta}) = \frac{\pi\epsilon}{2} (\tilde{\eta}^2 - 0.25) + (1 + \epsilon/2) \cos(\pi\tilde{\eta}), \quad (4.14)$$

where  $\epsilon$  is the relative restraint per unit width provided by the flanges, and  $\tilde{\eta} = \eta/(d - t_f)$ . The shape of both the flange and web plates in the  $\mathbf{t}$  direction is needed to complete the imperfection. A function is defined to represent a single buckling wave that satisfies the fixed boundary conditions at the loaded edges, a suitable function is

$$v_\zeta(\zeta) = \sin^2[\pi\zeta/L_{bw}]. \quad (4.15)$$

The final buckled shape is obtained by multiplying  $v_\xi$  with  $v_\zeta$  for the flange, and  $v_\eta$  with  $v_\zeta$  for the web. The complete buckled shape for the flange is shown in Figure 4.6b. Contours of the two functions  $v_\xi$  and  $v_\zeta$  are shown projected onto the axes to give a sense of the effect of these functions on the imperfection geometry. The normalized vector of the flange imperfection is obtained from Equations 4.13 and 4.15:

$$\mathbf{v}_f(\tilde{\xi}, \zeta) = \frac{v_\xi(\tilde{\xi})v_\zeta(\zeta)}{\max[v_\xi(\tilde{\xi})v_\zeta(\zeta)]} \mathbf{n}_2. \quad (4.16)$$

The normalized vector of the web imperfection is obtained from Equations 4.14 and 4.15:

$$\mathbf{v}_w(\tilde{\eta}, \zeta) = \frac{v_\eta(\tilde{\eta})v_\zeta(\zeta)}{\max[v_\eta(\tilde{\eta})v_\zeta(\zeta)]} \mathbf{n}_1. \quad (4.17)$$

The max is used in these equations so that the maximum imperfection amplitude can easily be made equal to a pre-specified value.

Finally, local imperfection fields for the entire member are defined through  $\mathbf{v}_{flange}$  and

$\mathbf{v}_{web}$ :

$$\mathbf{v}_{flange} = \begin{cases} a_f \mathbf{v}_f(\tilde{\xi}, \zeta) & \text{if } 0 \leq \zeta \leq L_{bw} \\ -a_f \mathbf{v}_f(\tilde{\xi}, \zeta - (L - L_{bw})) & \text{if } L - L_{bw} \leq \zeta \leq L \end{cases} \quad (4.18a)$$

$$\mathbf{v}_{web} = \begin{cases} a_w \mathbf{v}_w(\tilde{\eta}, \zeta) & \text{if } 0 \leq \zeta \leq L_{bw} \\ -a_w \mathbf{v}_w(\tilde{\eta}, \zeta - (L - L_{bw})) & \text{if } L - L_{bw} \leq \zeta \leq L \end{cases} \quad (4.18b)$$

where  $a_f$  is the maximum flange imperfection amplitude, and  $a_w$  is the maximum web imperfection amplitude. The different cases in these equations lead to an anti-symmetric in-plane local imperfection pattern at the bottom and top of the member, i.e., the imperfection is “in-wards” at one end and “out-wards” at the other. This mode is chosen on the basis of recommendations validated with beam-column experiments (Suzuki and Lignos, 2015; Elkady and Lignos, 2018a; Cravero et al., 2020), and also agrees with expected cross section imperfections due to the hot-rolling process and manufacturing (e.g., welding) (CEN, 1993; ASTM, 2016a). Figure 4.7b illustrates the anti-symmetric buckling pattern applied to an analysis model, and Figure 4.7c shows the local buckling pattern present at the base of a W24X84 column subjected to 20 % axial load and a symmetric cyclic lateral loading history.

The local buckling wavelength,  $L_{bw}$ , of the local imperfections is unknown through the aforementioned procedure, and is determined in this study by matching with elastic eigenvalue buckling analysis in Abaqus. The length  $L_{bw}$  is chosen as the wavelength of the end-most local buckle present in a local buckling dominated mode. This end-most wavelength is deemed to be critical because local buckling is known to initiate at the member ends due to the moment gradient in columns subjected to lateral loads (Elkady and Lignos, 2018a). A local buckling dominated mode from eigenvalue analysis is shown in Figure 4.7a with the proposed method for applying local imperfections in Figure 4.7b.

The last ingredient of the local imperfections are the maximum amplitudes  $a_f$  and  $a_w$ . The local imperfection amplitudes are based on the compatible minimum of  $d/300$  and  $b_f/250$  that have been used in prior studies based on measured imperfections (Hartloper and Lignos, 2019), and are similar to those in Elkady and Lignos (2018b). Compatibility in this proposed method is defined by maintaining the 90 degree angle between the flange and web plate centerlines, therefore, only one of the maximum amplitudes  $a_f$  or  $a_w$  will be reached depending on the section geometry. Note that these imperfection amplitudes are below the tolerances set forth in standards such as (CEN, 1993; ASTM, 2016a).

Local imperfections are incorporated into the simulation models by applying the imperfection fields, Equations 4.18a and 4.18b, to the continuum domains. This method generates a set of nodal perturbations that can be easily applied to the initially perfect geometry. The computation of the local imperfection geometries has been implemented by the authors in the Python package `pywikc` for wide flange cross-sections (Hartloper, 2020).

## Chapter 4. Warping-inclusive kinematic coupling in mixed-dimension macro models for steel wide flange beam-columns

Table 4.4 – Case study Voce-Chaboche material model parameters.

Material	$E$ [GPa]	$\sigma_{y,0}$ [MPa]	$Q_{\infty}$ [MPa]	$b$ -	$C_1$ [MPa]	$\gamma_1$ -	$C_2$ [MPa]	$\gamma_2$ -
A572 Gr.50 <sup>a</sup>	207.34	352.01	61.60	8.96	2305.55	20.15	-	-
A992 Gr.50 Flange <sup>b</sup>	179.75	318.47	100.72	8.00	11608.17	145.22	1026.33	4.68
A992 Gr.50 Web <sup>b</sup>	182.97	339.18	77.52	9.29	8716.08	118.47	1182.05	5.22

<sup>a</sup>: calibrated as a part of this study, <sup>b</sup>: from de Castro e Sousa et al. (2020).

Twisting imperfections, occurring due to base plate welding, have typically been applied similarly to local imperfections by applying a scaled buckling mode, or the nodal perturbation could be specified directly. In the context of beam-shell macro models, however, the twisting imperfection cannot be applied as an initial geometric imperfection in Abaqus because only initial displacements can be specified to the nodes. This is an issue because the twisting imperfection is specified about the member centerline, and therefore, the beam-column element centerline only has a rotation, and does not have a displacement.

Similitude between the full-shell and macro models is obtained in this case by applying a torque at the center of the model that leads to a twist equivalent to those measured in full-scale experiments, similar to the notional load concept (AISC, 2016b). Twist magnitudes measured in Elkady (2016) are used as a basis of expected amplitudes. The average twist magnitude measured at the column top was 0.6 %rad, the minimum was 0.0 %rad, and the maximum was 1.5 %rad. Torques are applied that lead to a mid-height twist equal to half the top twist assuming that initial angle of twist is constant along the member. Concentrated torques are simple to apply to the beam-column elements by ensuring a node exists at the center of the beam-column domain, and a distributed coupling in Abaqus v6.14 is used to apply the concentrated torque to the full-shell models in a region around the mid-height of the member.

The imperfection parameters for all the components included in the case studies are provided in Table 4.3. For the beams in Case Study 2,  $v_{flange}$  and  $v_{web}$  are applied to the entire RBS region ( $L_{bw} = 686$  mm) with an offset equal to the distance from the beam end to the start of the radius cut. For Case Studies 3 and 4, the length of the local buckling wave was found to be around  $1.2d$ . The twisting imperfection in Case Study 3 is based on the measured value, while the twisting imperfection in Case Study 4 is chosen near the maximum of the measured values in Elkady and Lignos (2018a). Finally, no imperfections are included in components with stable equilibrium paths because geometric instabilities are not expected, thereby diminishing the importance of imperfections (Galambos, 1998; Gantes and Fragkopoulos, 2010; Ziemian, 2010).



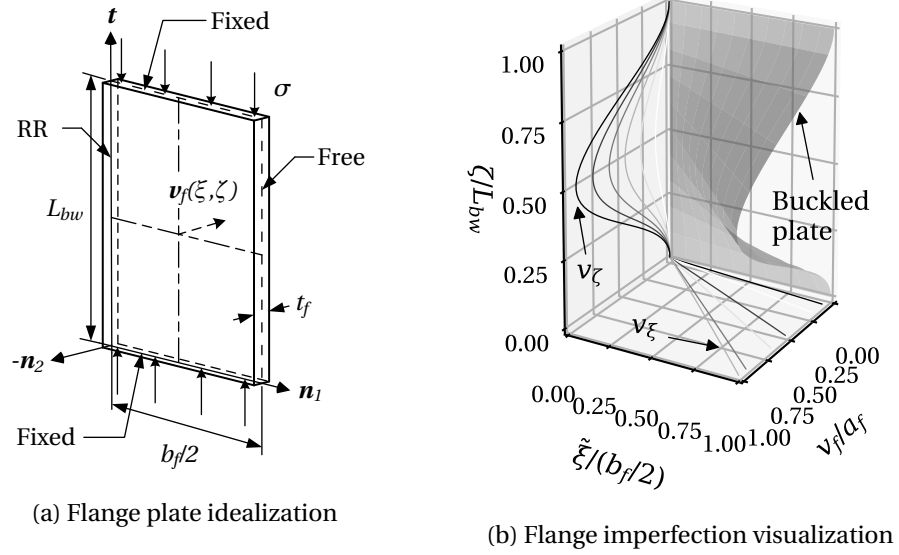


Figure 4.6 – Representations of the flange imperfection model.

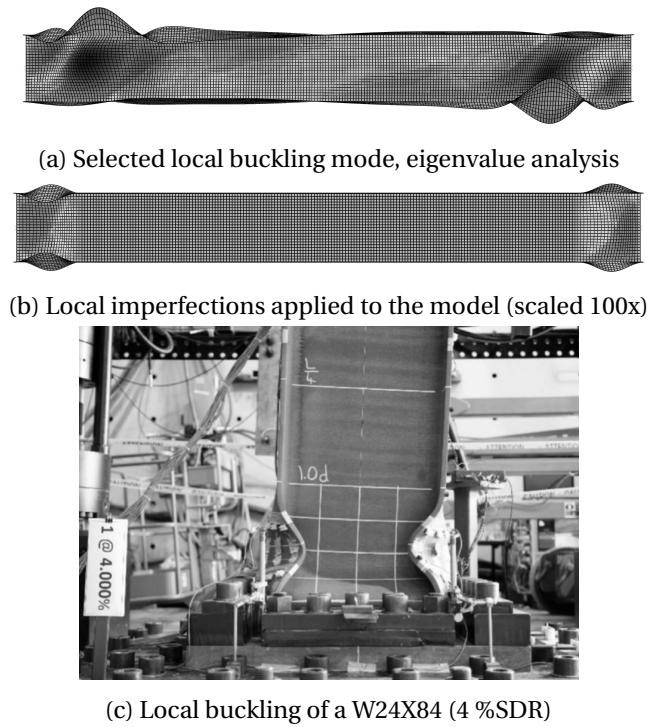


Figure 4.7 – Imperfections for a 5500 mm length W24X94 analysis model with a 20 % axial load ratio, and (c) reference experimental results from Elkady and Lignos (2018a).

## **4.4 Case study results**

Results in the form of component behavior and computational effort are reported for each of the case studies. Computational effort in each case is measured in three possible ways: the total number of DOFs in the model, the amount of memory required to run the analysis, and the number of iterations required throughout the analysis. The total number of DOFs is representative of the size of the problem being solved, and is correlated to the effort required to solve each iteration of the Newton-Raphson method. The memory required represents a base-line requirement to run the numerical model. The number of iterations required is indicative of the rate of convergence; the rate of convergence can be used to validate the implementation of the WIKC method, and is a major factor in the total analysis time. Direct measurements of the analysis time are not given herein because they are highly dependent on the computational system used to solve the problem, whereas the included metrics are independent of the utilized system.

### **4.4.1 Case study 1: Nonuniform torsion results**

Torque-twist responses of the finite element models along with the physical data is shown in Figure 4.8. From Figure 4.8a, it is clear that the Full-shell model captures the component behavior throughout the entire load path, while the other modeling options may only be accurate in the initial loading stages (see Figure 4.8b). The Macro (Warping) model with nonlinear WIKC begins to lose accuracy with respect to the Full-shell model after a twist of around 0.25 rad because the Abaqus beam-column elements are only valid for small angles of twist (Dassault Systèmes, 2014), as seen in the Full-beam model response as well. Results in Figure 4.8b also indicate that the linear WIKC method is viable for components that experience twists of up-to around 0.05 rad. In the context of steel MRF components, the maximum observed twist in full-scale experiments on wide flange columns is in the neighborhood of 0.10 rad (Elkady, 2016; Elkady and Lignos, 2018a), therefore, the Macro (Warping) model employing the nonlinear WIKC at beam-continuum interfaces should be suitable for most applications, while the linear version presents a limitation in this regard.

A notable divergence is found in the elastic torsional stiffness of the Macro (Built-in) model compared with the other options, as the elastic torsional stiffness is computed to be 226 kN-m/rad and this quantity is around 90 kN-m/rad for the Full-shell model. Differences in the elastic stiffnesses is clearly visible in Figure 4.8b. The built-in kinematic coupling in Abaqus, that does not transfer warping, creates a warping-fixed boundary in the continuum domains at the interface, this in-turn leads to the increase in the torsional stiffness. This issue will have later implications in the response of steel MRF components subjected to cyclic loading.

Accuracy of the coupling method can also be assessed in this case by comparing the von Mises equivalent stress distributions at the interface shell elements in Figure 4.9 near the

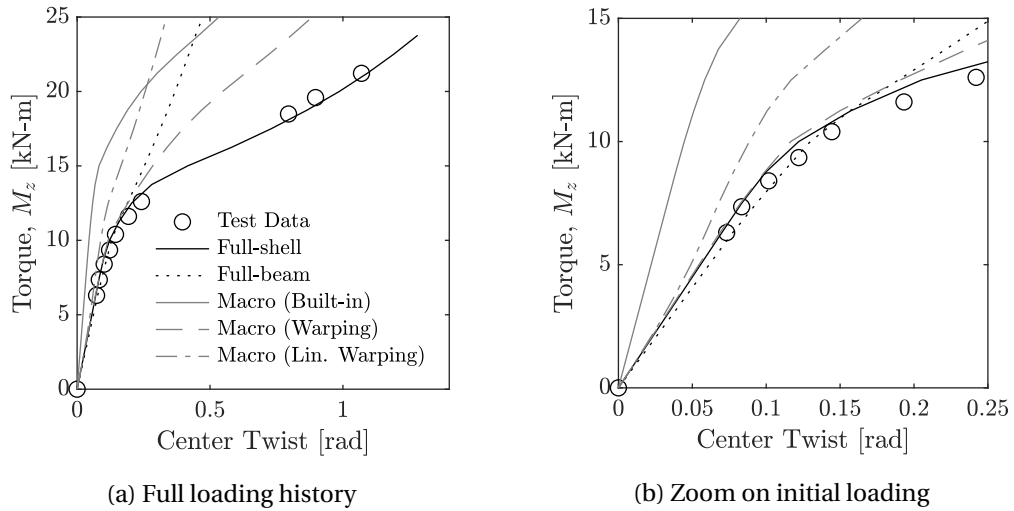
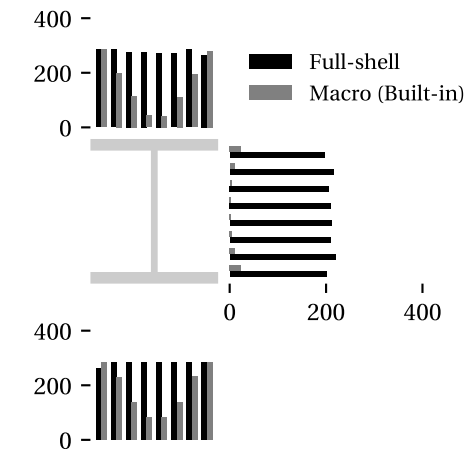


Figure 4.8 – Comparison of applied torque versus twist angle for models of the Farwell and Galambos (1969) test.

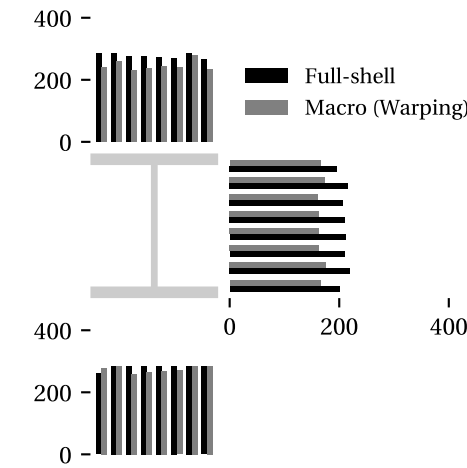
point of yielding ( $M_z = 11.25$  kN-m). The stress distribution of the Macro (Warping) model is closer to the Full-shell model when compared with the Macro (Built-in) model, particularly in the web elements. The rate of convergence is also important for validating the implementation of the proposed WIKC method and to assess the overall computational effort required. To this end, a plot of the total number of iterations in the analysis with respect to the applied torque is provided in Figure 4.10. This figure shows that the convergence rate of the Macro (Warping) model is comparable to the Full-shell model up to the point of divergence between these models at around 12 kN-m.

#### 4.4.2 Case study 2: Interior subassembly results

The overall subassembly behavior in terms of story drift ratio (SDR = column tip displacement / initial column length) and column tip load is shown in Figure 4.11. The Full-shell model is able to capture reasonably well the pre- and post-peak behavior of the subassembly, note that the relative error in the maximum absolute column tip load is around 2 % between the Full-shell and Test Data. There is also good agreement between the Full-shell model unloading stiffness and the test data prior to the last cycle of loading, indicating that the Full-shell model is able to capture the progression of local buckling in the RBS region and twisting of the beams and column. This observation is reflected by the apparent match between the post-test deformed shapes found in the Full-shell model and the experiment itself, as shown in Figure 4.12. Certain features of the test data are not replicated by the model (e.g., the apparent stiffening of the test response in cycles after 2 %SDR), although, this is attributed to boundary condition effects that are not fully captured by the model, as this particular test was stopped after the cycles to 5 %SDR due to damage in the lateral support system (Engelhardt et al., 2000).



(a) Full-shell and Macro (Built-in) models



(b) Full-shell and Macro (Warping) models

Figure 4.9 – Comparisons of the von Mises equivalent stress (units of MPa) for the interface shell elements in the nonuniform torsion models at  $M_z = 11.25$  kN-m.

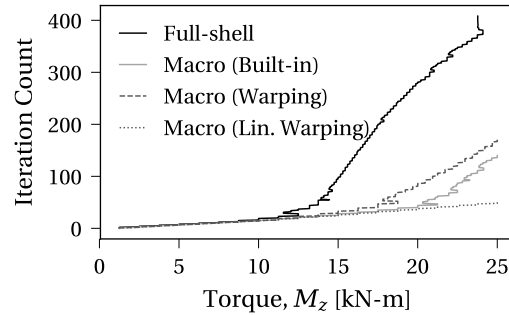


Figure 4.10 – Iteration count for the nonuniform torsion test.

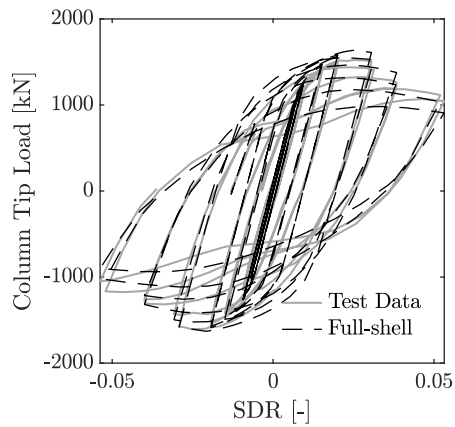
The angle of twist predicted by the Full-shell model at the column bottom is approximately 0.12 rad at the final excursion to -5 %SDR, and the beam angle of twist is approximately 0.22 rad (see also Figure 4.12), indicating that torsional effects are expected to be significant. The Full-shell model is also able to capture the panel zone behavior of the subassembly, as shown in Figure 4.13a, although the peak shear rotation is slightly overestimated.

The Macro (Built-in) and Macro (Warping) models are compared with the Full-shell model in Figures 4.11b and 4.11c. Both models predict reasonably well the Full-shell model's response, although, the Macro (Built-in) model overestimates the overall unloading/reloading stiffness after the initiation of beam twisting due to the increased torsional stiffness of the beams and column. Additionally, the Macro (Warping) model is able to represent the Full-shell model panel zone behavior, as indicated in Figure 4.13b. Note that results for the Macro (Lin. Warping) model are not shown for this case, as convergence issues were experienced for this model due to the linear coupling formulation.

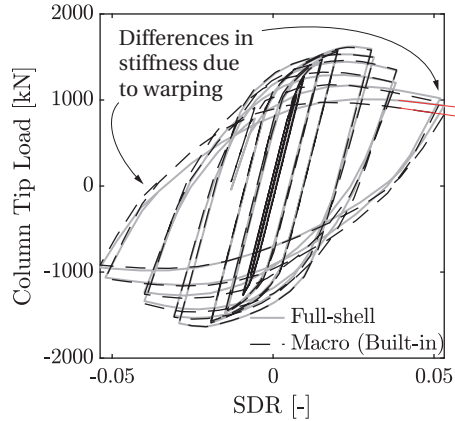
The memory and DOF requirements for Case Study 2 are provided in Figure 4.14. This figure plots the memory required by the analyses normalized by the requirement of the Full-shell model, and similarly with the total DOFs in the models. Results are shown for the Macro (Warping) model only, however, they are very similar for the Macro (Built-in) model barring differences of around 1 % in the DOF and memory requirements that may be attributed to the use of a user subroutine in Abaqus v6.14. For Case 2, a reduction in the number of DOFs required is around 55 %, and the reduction in memory required is around 48 %.

#### 4.4.3 Case study 3: Quasi-static collapse-consistent loading of first-story column results

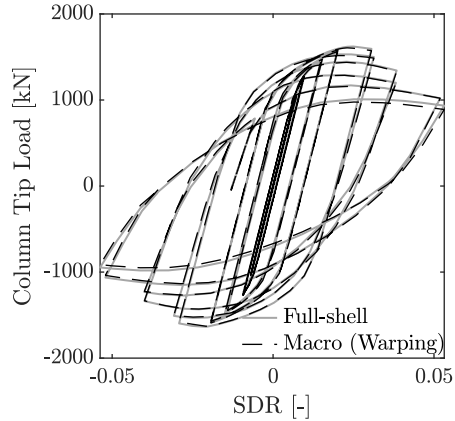
Column reaction moments at the base without the second-order contribution,  $M_{col}$ , are reported herein. For clarity,  $M_{col} = M_{total} - M_{PD}$ , where  $M_{total}$  is the total base reaction moment, and  $M_{PD} = u_y F_z$  is the second-order moment about the column base. The SDR is computed as  $SDR = (u_y^{top} - u_y^{base})/L_0$ , and axial shortening is reported as a percent of the



(a) Test and Full-shell model



(b) Full-shell and Macro (Built-in) models



(c) Full-shell and Macro (Warping) models

Figure 4.11 – Comparisons of the DBBW overall subassembly behavior. Test Data retrieved from Engelhardt et al. (2000).

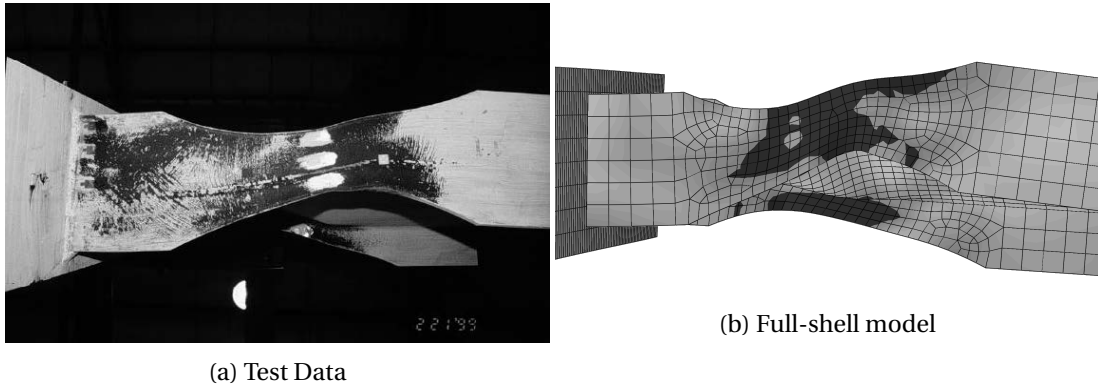


Figure 4.12 – Comparison of post-test deformed shapes from the DBBW subassembly. Test Data photo used with permission from Engelhardt et al. (2000).

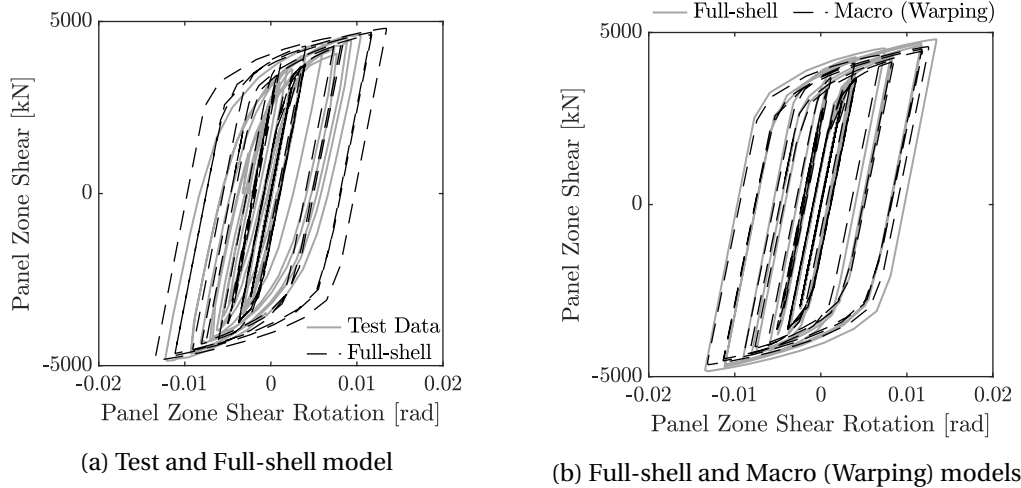


Figure 4.13 – Comparisons of the DBBW panel zone behavior. Test Data retrieved from Engelhardt et al. (2000).

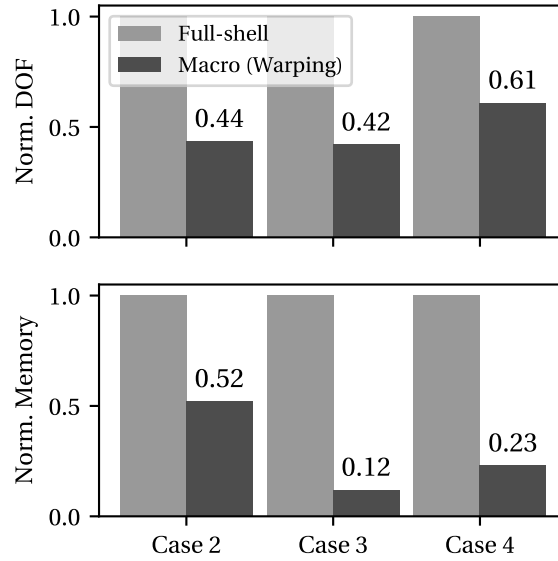


Figure 4.14 – Computational resource requirements for Case Studies 2, 3, and 4 normalized by the Full-shell values.

initial length,  $u_z/L_0$ .

The column moment vs. story drift ratio (SDR) is plotted in Figure 4.15 including the test data and comparisons between the Full-shell model and different macro models. Relative error between the maximum absolute moment of the Full-shell and test data is around 7 %, indicating the models' ability to capture the initial flexural yielding behavior of the steel material and initiation of local buckling in the column. Furthermore, agreement of the loading/unloading stiffness between the Full-shell results and Test Data indicates that the progression of local buckling is reasonably well captured by the Full-shell model. Computation of the column response is also validated through the deformed shape of the column models at the excursion at +10 %SDR with a photograph from the test at the same point in Figures 4.16a and 4.16b. Agreement between the deformed shapes and the test results is notable. The maximum angle of twist observed in this test and finite element analyses is around 0.10 rad in the last loading excursion, although the effect of torsion is not significant in this case as the problem is dominated by local buckling (Elkady and Lignos, 2018a).

Each of the macro modeling options are also compared individually with the Full-shell model in Figure 4.15. In this case that the strength/stiffness deterioration is dominated by local buckling, there are no significant differences between the Full-shell and macro model responses in terms of moment-rotation throughout the entire loading history, regardless of the coupling method. Despite the agreement in overall component behavior, the stress at the interface may be significantly in error with the linear coupling method, as noted in Figure 4.16e. The number of DOFs in the model and the computer memory demands are



extracted from information provided by the Abaqus analysis and presented in Figure 4.14 above the label “Case 3”. A savings of around 60 % in the number of DOFs is obtained by the macro models since around 2/3 of the total length is modeled with beam-column elements, and the memory savings is around 80 % in this case (see Figure 4.14).

#### **4.4.4 Case study 4: Column nonlinear response history analysis results**

Modal frequencies determined through eigenvalue analysis of the four W24X94 models are provided in Table 4.5, Mode 1 is the primary lateral mode of deformation, and Mode 3 is the twisting mode provided for comparison purposes. In all cases the first mode period is approximately equal to 1.5 s validating the assumed mass. The Mode 3 frequency of the Macro (Built-in) model is around 50 % larger than the Full-shell frequency because of the difference in elastic torsional stiffness. Note that the linear WIKC model's Mode 1 and Mode 3 frequencies are consistent with the Full-shell model.

The SDR, column base moment, and axial displacement as a percentage of the initial column length are provided with respect to the applied ground motion time in Figure 4.17. The point at which the column loses load carrying capacity is evident as the slopes of the SDR and axial displacement approach  $-\infty$ . The Full-shell model point of collapse is reasonably well computed by the Macro (Warping) model, as evident in Figure 4.17, however, the same cannot be said for the Macro (Built-in) model.

In contrast with Case Study 3, divergence in the response of the Macro (Built-in) and Macro (Lin. Warping) models from the Full-shell model is found in Case Study 4. Divergence at the point indicated in Figure 4.17 stems from the computation of different buckling modes: the W24X94 Macro (Built-in) and Macro (Lin. Warping) models deform in a primarily local buckling mode, while the Full-shell and Macro (Warping) model have a coupled buckling response, as shown in Figure 4.18. Differences in the buckling modes subsequently leads to differences in the column base moment responses, as highlighted in Figure 4.17, while the Macro (Warping) model agrees well with the Full-shell model until near the point of the loss of load carrying capacity. The W24X94 column Full-shell model stress distribution is also reasonably well predicted by the Macro (Warping) model as indicated by comparing the von Mises stress contours in Figure 4.18. Computational resource demands of the column models are summarized in Figure 4.14 with respect to the Full-shell model. The number of DOFs are reduced by around 40 % are obtained for the W24X94 macro models compared to the Full-shell model, and the memory requirements are reduced by around 75 %.

## Chapter 4. Warping-inclusive kinematic coupling in mixed-dimension macro models for steel wide flange beam-columns

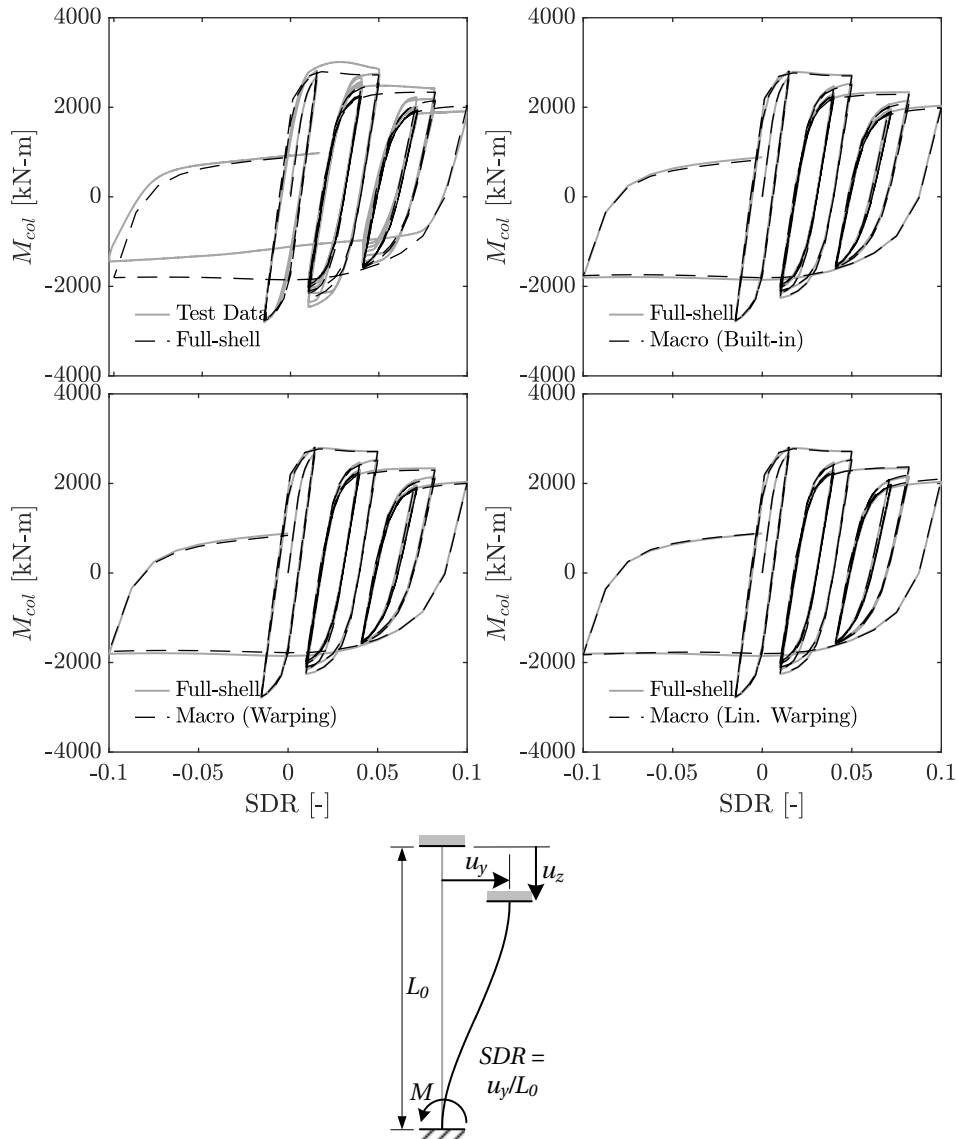


Figure 4.15 – Results from the W24X136 quasi-static analyses. Test Data retrieved from Elkady and Lignos (2018a).

Table 4.5 – Frequencies for selected modes of the W24X94 column.

Model	Mode 1 (Lateral)		Mode 3 (Twisting)	
	Freq. [Hz]	$E_{fs}$ [%]	Freq. [Hz]	$E_{fs}$ [%]
Full-shell	0.667	-	1094	-
Macro (Built-in)	0.668	0.15	1661	51.83
Macro (Warping)	0.668	0.15	1109	1.37
Macro (Lin. Warping)	0.668	0.15	1118	2.19

$$E_{fs} = (\text{Full-shell} - \text{Macro}) / \text{Full-shell}.$$

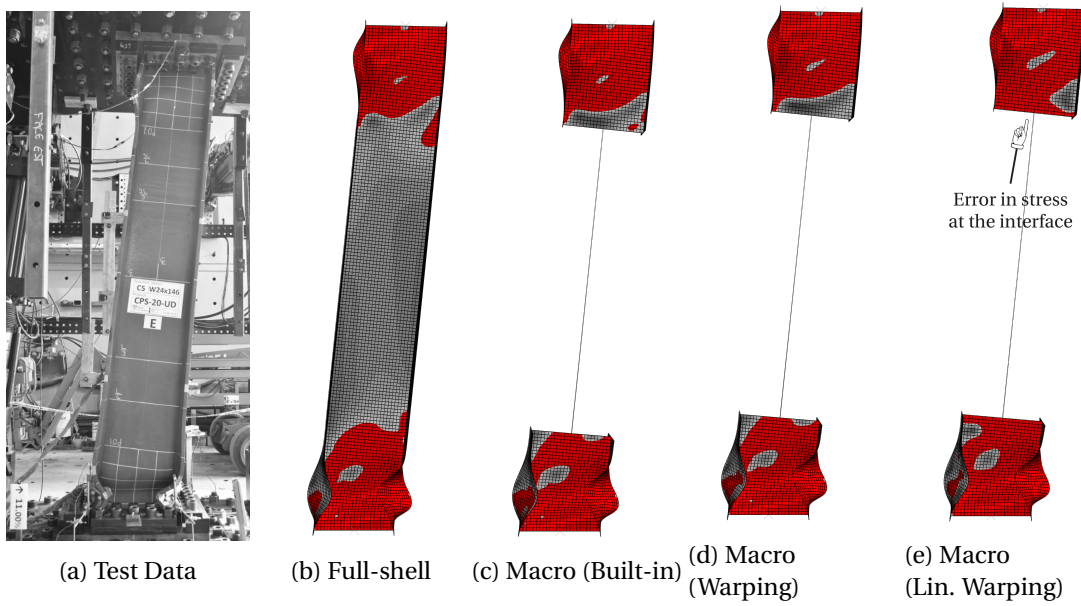


Figure 4.16 – Deformed shapes from the W24X146 quasi-static analyses at 11 % SDR. von Mises equivalent stress profile shown on the deformed shape, red regions indicate yielding. Test Data photo used with permission from Elkady and Lignos (2018a).

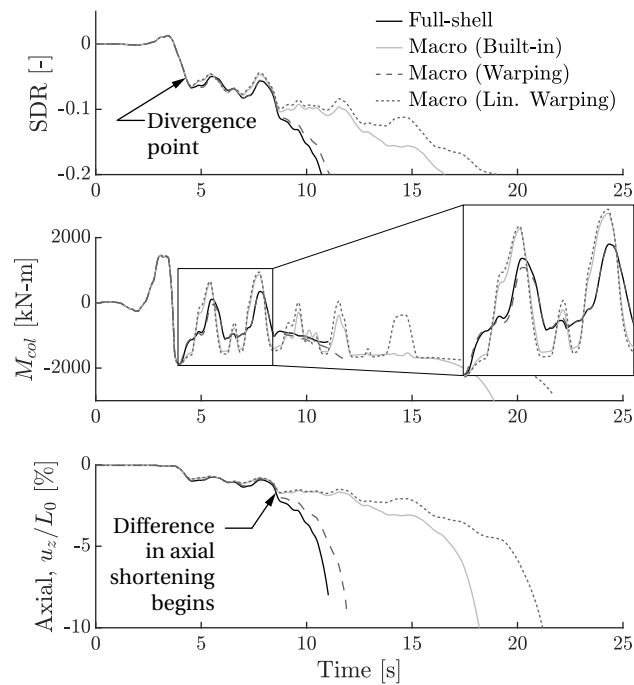


Figure 4.17 – Results from the W24X94 column nonlinear response history analyses.

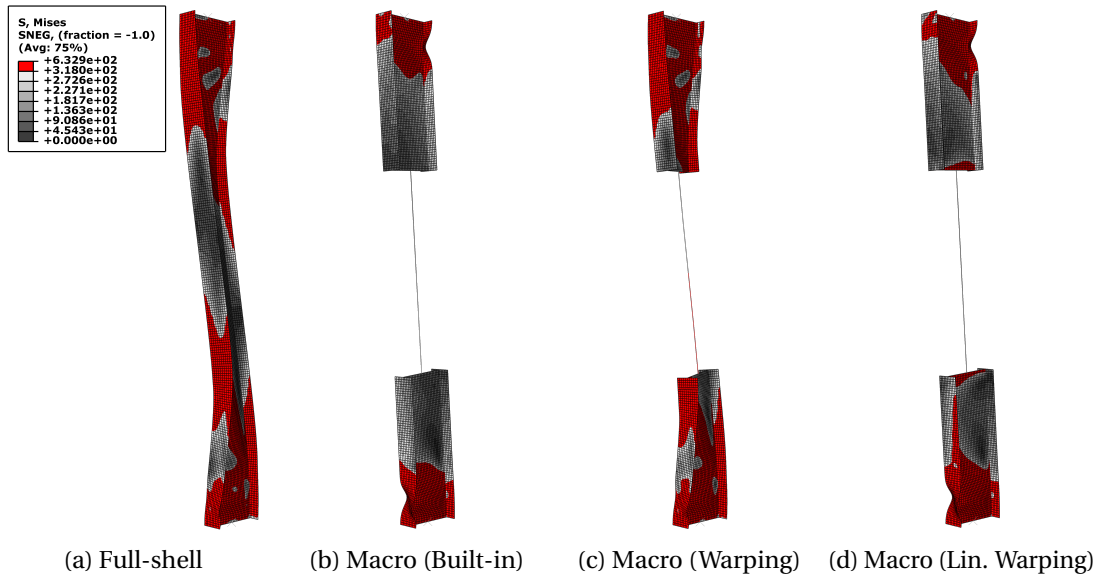


Figure 4.18 – Deformed shapes from the W24X94 column nonlinear response history analyses at  $t = 4.5$  s. von Mises equivalent stress profile shown on the deformed shape, red regions indicate yielding.

## 4.5 Discussion of results

### 4.5.1 Macro model accuracy

Case studies investigated in this chapter show that, as long as the coupling between beam-column and continuum elements can account for all relevant mechanical phenomena, the component macro models represent well the Full-shell model. This statement is made with regards to parameters that have been identified as critical in collapse simulations of steel frame buildings (Ibarra and Krawinkler, 2005), such as a component's: pre-peak stiffness, peak strength, and post-peak stiffness. These results indicate that the macro models can replicate the Full-shell model's initiation and progression of local and lateral-torsional buckling, as well as the progression of axial shortening. This is true even in the complex case of coupled local and lateral-torsional buckling. Therefore, component macro models can be used to address the limitations outlined in the introduction for concentrated and distributed plasticity approaches provided that a suitable coupling method is used, and the component deformation is within the range of its constitutive elements.

More specifically, from the cases investigated, there is little-to-no difference between the different coupling methods when computing the pre-peak response and initiation of *local* instabilities in wide flange beam-column components subjected to axial load and/or lateral drift demands. However, the influence of warping in the constraint formulation is paramount in the case of nonuniform torsion and coupled buckling mechanisms due to the

increase in torsional stiffness found using the Abaqus v6.14 built-in coupling. The stiffness increase is a result of the warping-fixed boundary enforced on the continuum domains, as seen in the results of case studies, as well as the Mode 3 frequency in Table 4.5 for the W24X94 column. The increase in torsional stiffness decreases the member's proclivity to LTB, this in-turn leads to the divergence in buckling modes between the Macro (Built-in) and Macro (Warping) models in the W24X94 dynamic analyses, as shown in Figure 4.7. Differences of stiffness in the descending portion of the post-peak response, such as the ones shown in Figure 4.11b for the Macro (Built-in) model, are critical in collapse simulations (Ibarra and Krawinkler, 2005), alternatively, this stiffness is well predicted by the Macro (Warping) model in Figure 4.11c. An initial recommendation based on the results presented in this chapter is that a warping-inclusive coupling method should be used for beam-column components that have a significant torsional load, or that have a normalized LTB slenderness  $\bar{\lambda}_{LT} > 0.4$  that is considered susceptible to inelastic LTB according to CEN (2005a).

From an accuracy point of view, it appears that if torsion is not dominant in the component response and there is no coupled buckling, the choice of coupling method is not influential in the column post-peak region. This result suggests that including warping in the coupling can be neglected for beam-column components if  $\bar{\lambda}_{LT} \leq 0.4$ . Furthermore, linear coupling methods are found to be acceptable under the following conditions: local buckling is dominant in the member response, the lateral deformation is below 10 %SDR, and the angle of twist does not exceed 0.10 rad. If torsion is dominant, the linear coupling method may be used as long as the angle of twist does not exceed 0.05 rad (see Figure 4.8b). The linear WIKC method can also be employed in eigenvalue analyses, as supported by the results of the frequency analysis in Table 4.5.

#### 4.5.2 Macro model computational efficiency

Results of the computational resource metrics shown in Figure 4.14 illustrate that the number of DOFs in the macro models are reduced in approximate proportion to the ratio  $L_{\Omega_1}/L$  for single components. For instance, the number of DOFs are approximately 2/3 for the W24X94 macro models compared to the Full-shell model in Figure 4.14 since 1/3 of the length is modeled with beam-column elements. This ratio of 2/3 is increased for the W24X94 analyses owing to the increased beam-column domain length. The memory savings are expected to be larger than the DOF savings, although the relationship is not clear, as elements of the square matrices need to be saved in addition to state variables for each element. For these reasons, the memory reduction using component macro models in Case Study 2 is less pronounced than the other cases, potentially due to the increased complexity and number of constraints present in this model to form the subassembly.

In the context of frame analysis, additional computational savings can be gained if the macro model approach is applied selectively depending on the desired level of modeling

fidelity and available computational resources. For instance, the macro model approach could be useful to model the torsion induced on columns due to buckling of beams with RBS connections, as well as first-story columns that experience deterioration in capacity-designed MRFs. This selective approach focuses the computational effort where it is most useful, while lower fidelity component models (i.e., concentrated and distributed plasticity approaches) can be used elsewhere in the structural model. Furthermore, the number of iterations required for convergence of the Macro (Warping) model appears similar to the Full-shell and Macro (Built-in) models, see Figure 4.10. Therefore, the reduced number of DOFs in macro models is expected to also reduce the required CPU time compared to full-shell models. Finally, the linear WIKC method may lead to issues with global convergence in certain nonlinear problems. The linear WIKC method is, therefore, not computationally advantageous in these cases, and is recommended only if the nonlinear method is unavailable.

### 4.5.3 Limitations

The following limitations uncovered through this study are stated:

- Residual stresses have not been included in the beam-column elements used in this study. This limitation could be addressed using a beam-column element formulation such as in Lamarche and Tremblay (2011). Residual stresses may influence the Wagner constant (Trahair, 1993; de Castro e Sousa and Lignos, 2017), that in-turn, could substantially reduce the torsional stiffness of beam-columns. This reduction may be critical for slender members as it further increases their susceptibility to LTB.
- The limitation of using beam-column elements is that local deformations cannot be captured in the beam-column domains, therefore, the length of the continuum domains need to be chosen appropriately *a priori*. This challenge has yet to be addressed because the extent of local instabilities in the member depends on the primary mode of deterioration (e.g., local buckling, lateral-torsional buckling, flexural buckling) that is ultimately influenced by the member geometry, material properties, initial imperfections, loading, and boundary conditions.
- The results presented herein are for shell elements in the continuum domain only, solid elements have not yet been investigated by the authors. However, the proposed coupling method is valid for these elements since only the displacement DOFs of the continuum domain are coupled with the beam-column element domain.

## 4.6 Conclusions

Continuum finite element models address the limitations in available concentrated and distributed plasticity component models for steel wide flange beam-columns, however, they

may be computationally expensive in the context of earthquake engineering analysis. Mixed-dimension macro models employing 1D beam-column and 2D/3D continuum elements are promising to reduce this computational expense. A review of existing coupling methods highlights that there is a need for a multi-point constraint method that also incorporates torsion warping. In this chapter, we propose a warping-inclusive kinematic coupling (WIKC) formulation to transfer warping deformations between the beam-column and continuum element domains. The beam-shell macro models used in this study reduce the model degrees-of-freedom by up-to around 60 % and the computational memory requirement by up-to around 80 % compared to their full-shell counterparts, while retaining the solution fidelity of full-continuum finite element models even for coupled local and lateral-torsional buckling.

The main conclusions drawn from this chapter with respect to steel wide flange beam-columns and subassemblies are as follows:

- Including warping in the coupling formulation may be critical in accurately estimating the full-continuum model failure mode and, therefore, should be included for general use. This is especially true for components subjected to nonuniform torsion, or that are susceptible to coupled local and lateral-torsional instabilities, i.e., if  $\bar{\lambda}_{LT} > 0.4$ .
- A nonlinear, finite-rotation constraint formulation appears to be necessary for nonlinear problems, and there does not appear to be any computational advantages offered by the linear coupling method. Linear, small-rotation coupling methods appear to be acceptable for eigenvalue analyses, as well as problems not dominated by torsion if: (i) LTB is not critical, (ii) the angle of twist is less than 0.10 rad, and (iii) the column drift is below 10 %. If twisting is the dominant mode of deformation, the angle of twist should remain below 0.05 rad if a linear coupling method is employed.
- The macro model approach leads to a reduction in the DOFs and memory usage proportional to the ratio of the beam-column element domain length to the total component length. The macro model approach does not appear to negatively affect the rate of convergence compared to the full-continuum model, therefore, the computational time savings are expected to be a function of the DOF reduction.

Macro model parameters (e.g., proportion of continuum domain, mesh discretization, imperfections, etc.) need to be calibrated in a future study based on the member geometry, boundary conditions, material properties, and loading. Such guidelines will allow for the practical use of component macro models in frame simulations.

## 4.7 Data availability

Some or all data, models, or code that support the findings of this study are available from the corresponding author upon reasonable request.

## **4.8 Acknowledgements**

The Authors sincerely thank Professor Michael Engelhardt from the University of Texas at Austin for allowing for the use of Figure 4.12 and providing the experimental data for the DBBW subassembly. The Authors also sincerely thank Professor Ahmed Elkady from the University of Southampton for allowing use of Figures 4.7c/4.16a and providing the experimental data from specimen C5. This study is based on work supported by EPFL and by the Swiss National Science Foundation (Project No. 200021\_188476) for the first author, and an EPFL internal grant for the second author. The financial support is gratefully acknowledged. Any opinions, findings, and conclusions or recommendations expressed in this chapter are those of the authors and do not necessarily reflect the view of sponsors.

## **4.9 Notation**

*The following symbols are used in this chapter:*

- $A_1, A_2$  = constraint coefficient matrices;
- $b_f$  = flange width;
- $(\cdot)^b$  = beam quantity;
- $(\cdot)^c$  = continuum quantity;
- $d$  = wide flange section depth;
- $f$  = constraint equations for a continuum node;
- $I$  =  $3 \times 3$  identity matrix;
- $L$  = member length;
- $l$  = link vector;
- $n_1, n_2$  = cross-sectional plane vectors;
- $R$  = rotation matrix;
- $t$  = cross-sectional normal vector;
- $t_f$  = flange thickness;
- $t_w$  = web thickness;
- $u$  = nodal displacement vector;
- $v$  = nodal initial imperfection vector;
- $w$  = warping DOF;
- $x$  = nodal position vector;
- $\delta(\cdot)$  = infinitesimal quantity;
- $\Gamma$  = beam-continuum interface;
- $\xi$  = distance along  $n_1$  axis;
- $\theta$  = infinitesimal nodal rotation vector;
- $\eta$  = distance along  $n_2$  axis;



- $\psi$  = warping function;
- $\boldsymbol{\phi}$  = nodal rotation vector;
- $\zeta$  = distance along  $\boldsymbol{n}_3$  axis;
- $\Omega_1$  = beam-column element domain;
- $\Omega_2$  = continuum element domain; and
- $[(\cdot)]_{\mathbf{x}}$  = matrix representation of cross-product.



## 5 Best-fit constraint equations for coupling mixed-dimension simulation models with wide flange cross sections

**Authors:** Alexander R. Hartloper, Albano de Castro e Sousa, Dimitrios G. Lignos

**Preprint version of:** Hartloper, A. R., de Castro e Sousa, A., and Lignos, D. G. "Best-fit constraint equations for coupling mixed-dimension simulation models with wide flange cross sections." *Finite Elements in Analysis and Design*, (In preparation).

**Doctoral candidate's contributions:** Literature review, problem definition, development of constraint equations and constraint coefficient matrix, implementation and validation of methodology, evaluation and interpretation of results. Writing and editing of the manuscript. The co-authors supervised the work carried-out by the doctoral candidate and assisted with the editing of the manuscript.

**Abstract:** A new mixed-dimension coupling method is formulated for members with wide flange cross sections based on the idea of least squares transformations between two sets of point clouds. This coupling method imposes the minimum number of constraint equations required to link the displacement, rotation, and torsion-warping degrees-of-freedom of the dependent node. At the heart of the formulation is the solution of a  $4 \times 4$  eigenvalue problem and the deduction of torsion-warping deformations. The proposed method is implemented and validated for nonlinear finite element analysis; open-access source code is provided. Examples demonstrate that the proposed coupling method can improve interface stress distributions over alternative methods, and is suitable for the coupling of elastic continuum finite elements.

**Keywords:** Reduced-order model; Multipoint constraint equations; Warping; Quaternions; Steel structures; Finite element analysis.

## **5.1 Introduction**

Simulation models that incorporate material nonlinearity and geometric instabilities are increasingly important for the design and analysis of infrastructure. For instance, finite element models that account for nonlinear geometric effects can be used in the stability design and evaluation of members (CEN, 2005b; AISC, 2016b), particularly if a closed-form expression for the member's critical load is not readily available (Ziemian and Abreu, 2018; Ziemian et al., 2018). Furthermore, nonlinear finite element analysis has long-since been an integral tool in the performance-based assessment and design of infrastructure (Krawinkler et al., 2006). Performance-based assessments entail a probabilistic approach due to the uncertain nature of natural hazards—see e.g., Vamvatsikos and Cornell (2002); Zareian and Krawinkler (2007). The computational complexity of performance-based assessments is therefore increased due to the number of simulations that must be run for any given case. Thus, the need for a computationally friendly modeling approach is warranted in this context.

Concentrated plasticity and continuum finite element (CFE) modeling approaches are two possible numerical representations used in state-of-the-art analysis of buildings for resisting natural hazards (Deierlein and Zsarnóczyay, 2019). Mathematical models for steel moment-resisting frames (MRFs) based on the concentrated plasticity approach, for instance, are generated using beam-column elements combined with zero length elements that represent regions of anticipated nonlinear component behavior, as shown schematically in Figure 5.1. The concentrated plasticity modeling approach is oftentimes favoured owing to its computational simplicity, however, it has several limitations for steel beam-column components as discussed in Hartloper et al. (2021b). These limitations can be addressed by using a CFE model, as illustrated in Figure 5.1, constructed with either 2D shell or 3D solid elements (the following nomenclature is used herein: 1D elements are lines, 2D elements are surfaces, and 3D elements are volumes). Continuum finite element models overcome the limitations of the concentrated plasticity approach by explicitly modeling material nonlinearity and its interaction with geometric instabilities. The downside of using CFE models is the increase in computational complexity in the form of the number of degrees-of-freedom and memory requirements to run the model.

One promising method for curtailing the expense of CFE component models, while retaining their fidelity, is through the use of mixed-dimension approaches. Mixed-dimension models are used, for example, in predicting the fatigue life of off-shore oil platforms (Knezevic et al., 2019) and the seismic performance of steel frame structures (Imanpour et al., 2016). This modeling approach is useful in these contexts because it explicitly simulates local effects, such as stress concentrations and local geometric instabilities, in the continuum element domains as well as interactions between local and member (i.e., lateral-torsional and/or flexural buckling) instabilities. Component models combining elements of mixed dimensions (i.e.,

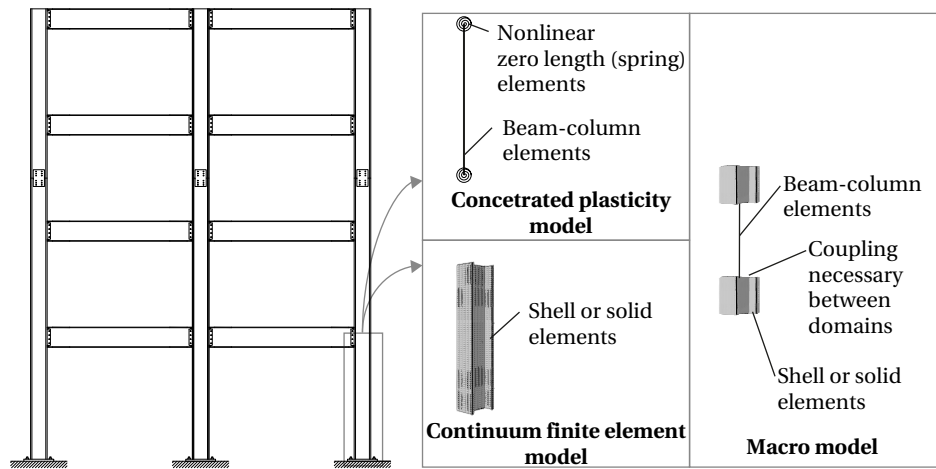


Figure 5.1 – Schematic representation of steel moment-resisting frame and potential component model idealizations.

1D and 2D elements) are herein denoted as “Macro models”, as depicted in Figure 5.1. In particular, the focus of this chapter is narrowed to macro models with applications to steel beam-columns. Such components are well suited to use mixed-dimension models because the beam and column component behavior is well represented by classic beam theories, and the locations of local geometric instabilities under the applied multiaxis loading are well-known (Newell and Uang, 2008; Suzuki and Lignos, 2015; Ozkula et al., 2017; Elkady and Lignos, 2018a).

A mixed-dimension coupling method that can represent the relevant deformations occurring within the member is essential to the development of accurate macro models for steel beam-columns. This chapter focuses on the use of multipoint constraints (MPCs) to couple the domains of differing dimensions. Prior studies have proposed MPC formulations through a variety of different means, see e.g., McCune et al. (2000); Ho et al. (2004); Dassault Systèmes (2014); Liu (2016). However, a limitation in the aforementioned MPC formulations for coupling beam-column and continuum element domains in steel beam-columns is that torsion-warping is not considered. However, torsion-warping significantly affects the torsional stiffness of members featuring wide flange cross sections (i.e., including H- or I-shaped cross sections). Accurately estimating the torsional stiffness is important for predicting the behavior of steel beam-columns that are primarily subjected to torsional loads or that may be susceptible to lateral-torsional buckling.

The problem investigated in this chapter is how to couple beam-column and continuum element domains in a manner that: (1) is computationally efficient by introducing the least number of constraint equations, and (2) includes torsion-warping. To address this problem, a best-fit formulation is proposed based on matching two sets of point clouds. Point cloud

matching is a well-studied problem in several domains, such as the Wahba problem (Wahba, 1965) in the field of spacecraft attitude dynamics, determining the orientation and translation of sets of points in the field of computer vision (Horn, 1987), and more recently determining best-fit corotational frames for 3D continuum finite elements (Mostafa and Sivaselvan, 2014).

This chapter is organized as follows. First, constraint equations are proposed using the best-fit method. These constraint equations are tailored to wide flange cross sections that are set as the scope for this work. The main novelty of the current work is the formulation of the MPC equations as a point cloud transformation problem, and the inclusion of torsion-warping into this framework. Second, the constraint coefficient matrix is derived for use in the nonlinear finite element analysis context. Third, simulation-based examples are provided to validate the proposed coupling method. Lastly, the results from this overall methodology are discussed, its limitations are presented, and prospects for future research are stated.

## 5.2 Development of the multipoint constraint equations

The following steps are used to develop the constraint equations: (1) the assumed beam kinematics are described to provide a basis for the development of the coupling equations; (2) the best-fit coupling concept is introduced, then linked with the beam kinematics; and (3) specific constraint equations, including one for warping, are formulated using the proposed best-fit approach.

### 5.2.1 Beam kinematics

The beam-column element kinematics in the coupling formulation are based on a line of centroids, a plane that rotates about each point on the centroid, and an out-of-plane torsion-warping component—see e.g., Simo and Vu-Quoc (1991). Each node in the beam-column element is assumed to have three displacement degrees of freedom (DOFs), three rotation DOFs, and a warping DOF.

Kinematics of the beam-column element are provided by the equation for  $\mathbf{x}_{mp}$ , in which the subscript  $mp$  indicates the material-point. The material points are defined by

$$\mathbf{x}_{mp}(\xi, \eta, \zeta) = \bar{\mathbf{x}}(\zeta) + \xi \mathbf{n}_1(\zeta) + \eta \mathbf{n}_2(\zeta) + w(\zeta) \psi(\xi, \eta) \mathbf{t}(\zeta), \quad (5.1)$$

where  $\zeta$  is the coordinate along the beam centerline in the deformed configuration,  $\xi$  and  $\eta$  are the distances measured along the  $\mathbf{n}_1$ ,  $\mathbf{n}_2$  axes in the deformed configuration,  $\bar{\mathbf{x}}(\zeta)$  is the position along the beam centerline,  $w(\zeta)$  is the warping amplitude,  $\psi(\xi, \eta)$  is the warping function, and  $\mathbf{t}(\zeta)$  is the axis in the direction of the cross section normal in the deformed configuration. Essentially, the kinematics specify a plane spanned by  $\mathbf{n}_1$  and  $\mathbf{n}_2$ , with a normal vector  $\mathbf{t}$  and centered at  $\bar{\mathbf{x}}(\zeta)$ . The representation of these parameters is shown in Figure 5.2a.

## 5.2. Development of the multipoint constraint equations

The torsion-warping function for elastic, thin-walled, wide flange cross sections is (Chen and Atsuta, 2008):

$$\psi(\xi, \eta) = \xi \eta. \quad (5.2)$$

As stated above, Equation 5.1 is formulated in the deformed configuration. Two other configurations are used in this coupling methodology: the reference and initial configurations, all of which are shown schematically in Figure 5.3. The reference configuration, identified by the prescript  $^r(\cdot)$ , is used to compute cross-sectional properties that remain constant throughout the analysis. The initial configuration, identified by the prescript  $^0(\cdot)$ , is the initial position and orientation of the model. The coupling method, to now be proposed, specifies transformations from the initial to deformed configurations.

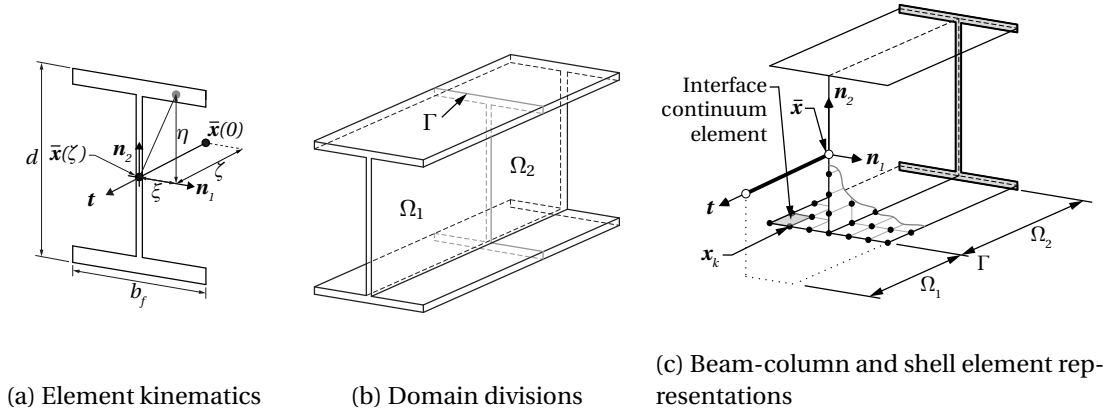


Figure 5.2 – Division of component into domains and beam-column element kinematics.

### 5.2.2 Best-fit coupling approach

First, the best-fit concept is motivated, and afterwards this idea is used to develop the coupling constraint equations. The approach is motivated by considering a plane of best-fit that minimizes the sum of orthogonal distances between the plane and a set of points in 3D. The location of the plane of best-fit is defined by a point on the plane and the orientation is defined by the vector normal to the plane—mimicking the kinematic assumptions of a beam-column element. With reference to Figure 5.4, the coordinates of  $N$  continuum nodes on the interface  $\Gamma$  (see Figure 5.2b) are denoted by the set  $\mathbf{X} = \{\mathbf{x}_k\}_{k=1}^N$ , where  $\mathbf{x}_k$  are the coordinates of the  $k$ -th node. These nodes could be generated, for example, by the shell discretization shown in Figure 5.2c. If a node lays exactly on the best-fit plane, the equation  $\mathbf{t} \cdot (\mathbf{x}_k - \bar{\mathbf{x}}) = 0$  is satisfied, where  $\mathbf{t}$  is the unit normal to the plane, and  $\bar{\mathbf{x}}$  is any point on the plane. The orthogonal distance between a point  $\mathbf{x}_k$  that rests outside of the plane is then defined as  $r_k = \mathbf{t} \cdot (\mathbf{x}_k - \bar{\mathbf{x}})$ .

The best-fit plane is defined as one that minimizes the sum of squared distances  $r_k$  over

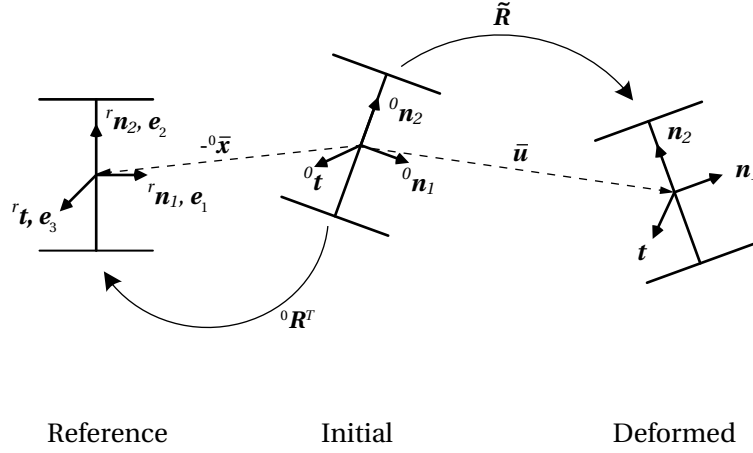


Figure 5.3 – Schematic representation of an wide flange cross section in the reference, initial, and deformed configurations.

all the points in the set  $\mathbf{X}$ . The associated error term  $E(\bar{\mathbf{x}}, \mathbf{t})$  is defined as

$$E(\bar{\mathbf{x}}, \mathbf{t}) = \sum_{k=1}^N r_k^2 = \sum_{k=1}^N \mathbf{t}^T \mathbf{Y} \mathbf{t} \quad (5.3a)$$

$$= \sum_{k=1}^N \mathbf{y}_k^T (\mathbf{t} \mathbf{t}^T) \mathbf{y}_k, \quad (5.3b)$$

where  $\mathbf{y}_k = \mathbf{x}_k - \bar{\mathbf{x}}$  and  $\mathbf{Y} = \mathbf{y}_k \mathbf{y}_k^T$ . The best-fit solution to the plane fitting problem is obtained by minimizing Equation 5.3b with respect to  $\bar{\mathbf{x}}$ :

$$-2(\mathbf{t} \mathbf{t}^T) \sum_{k=1}^N \mathbf{y}_k = 0. \quad (5.4)$$

For a non-trivial solution, the error is minimized with respect to  $\bar{\mathbf{x}}$  when  $\sum_{k=1}^N \mathbf{y}_k = 0$ , therefore,  $\bar{\mathbf{x}} = 1/N \sum_{k=1}^N \mathbf{x}_k$ . This condition implies that the best-fit plane contains the centroid of the point cloud, this point is denoted  $\bar{\mathbf{x}}$ . Furthermore, applying the Rayleigh-Ritz theorem (Gallier and Quaintance, 2020) to Equation 5.3a, the error term  $E$  is minimized when  $\mathbf{t}$  is equal to  $\tilde{\mathbf{t}}$ , where  $\tilde{\mathbf{t}}$  is the normalized eigenvector associated with the minimum eigenvalue of  $\mathbf{Y}$ . The plane of best-fit to a set of points is, therefore, defined by the centroid of these points and the eigenvector  $\tilde{\mathbf{t}}$  (Horn, 1987).

### 5.2.3 The link with beam kinematics

Relating beam-column element kinematics to the coupling problem: if the beam-column centerline initially coincides with the centroid of the point cloud, then the cross-sectional plane is exactly defined by the plane of best-fit if warping is neglected. The translation of



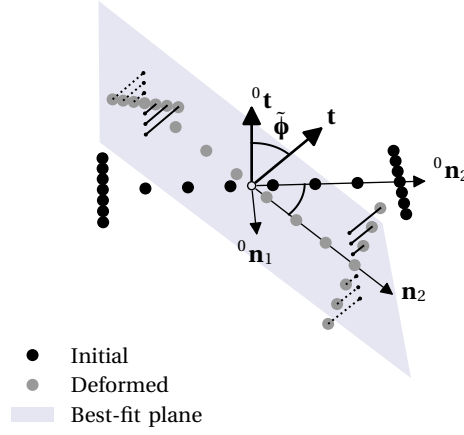


Figure 5.4 – Visualization of the plane of best-fit for wide flange cross sections.

a beam-column node on  $\Gamma$  should then be equal with the translation of the centroid, and the orientation of this beam-column node should be equal to the orientation of the plane of best-fit. As warping is orthogonal to the cross-sectional plane, the orthogonal distance of a point to the plane becomes  $\tilde{r}_k = \mathbf{t} \cdot (\mathbf{x}_k - \bar{\mathbf{x}}) + w\psi_k$ , where  $w$  is the warping amplitude and  $\psi_k$  is the warping function evaluated at  $\mathbf{x}_k$ . The squared error with warping is defined as

$$\tilde{E}(\bar{\mathbf{x}}, \mathbf{t}) = \sum_{k=1}^N \tilde{r}_k^2 = \sum_{k=1}^N \mathbf{y}_k^T (\mathbf{t} \mathbf{t}^T) \mathbf{y}_k + 2w\psi_k r_k + w^2 \psi_k^2. \quad (5.5)$$

Minimizing this error will allow the determination of the best-fit plane to include the deformations due to torsion-warping.

An important assumption to include torsion-warping is that there is a bi-symmetric discretization of continuum nodes on the interface. A bi-symmetric discretization is defined such that for all nodes  $\mathbf{x}_k(\xi, \eta)$  there exist complementary nodes  $\mathbf{x}_l(-\xi, \eta)$  and  $\mathbf{x}_m(\xi, -\eta)$ , where  $k = l = m$  is only possible at  $\xi = \eta = 0$ . Considering the symmetric discretization of nodes, it follows from Equation 5.2 that  $\sum_k \psi_k = 0$  when evaluated over all the nodes. This result is denoted as the antisymmetry of the warping function under a bi-symmetric discretization, or just “antisymmetry of the warping function”. The physical interpretation of this property is that the axial-force resultant is equal to zero when integrating the axial stresses due to torsion warping over the respective cross section.

The best-fit problem can now be stated with warping. First, minimizing the error (5.5)

with respect to  $\bar{\mathbf{x}}$ ,

$$\frac{\partial}{\partial \bar{\mathbf{x}}} \left( \sum_{k=1}^N \mathbf{y}_k^T (\mathbf{t} \mathbf{t}^T) \mathbf{y}_k + 2w\psi_k r_k + w^2 \psi_k^2 \right) = 0 \quad (5.6)$$

$$\Rightarrow -2(\mathbf{t} \mathbf{t}^T) \sum_{k=1}^N \mathbf{y}_k - 2w\mathbf{t} \sum_{k=1}^N \psi_k = -2(\mathbf{t} \mathbf{t}^T) \sum_{k=1}^N \mathbf{y}_k = 0. \quad (5.7)$$

Note that antisymmetry of the warping function is used above. In this case, the centroid of the material points including warping is the centroid of the points without warping. Now, minimizing the error function with respect to  $r_k$ ,

$$\frac{\partial}{\partial r_k} \left( \sum_{k=1}^N r_k^2 + 2w\psi_k r_k + w^2 \psi_k^2 \right) = 0 \quad (5.8)$$

$$\Rightarrow \left( \sum_{k=1}^N r_k \right) + w \left( \sum_{k=1}^N \psi_k \right) = 0, \quad (5.9)$$

again, antisymmetry of the warping function makes the last term in (5.9) equal to zero. This result implies that the best-fit plane is independent of the torsion warping deformations. Intuitively, this conclusion follows from the observation that the residuals due to warping deformations cancel each other out when calculating the plane of best-fit.

The plane of best-fit to the deformed set of nodes is shown in Figure 5.4. In this figure, the initial configuration is subjected to a rotation about the  ${}^0\mathbf{n}_1$  axis in combination with a warping deformation. Residuals in this figure are represented by the dashed (negative warping deformation) or solid lines (positive warping deformation) between the best-fit plane and the deformed points. Notice that each positive residual has a negative counterpart, therefore the best-fit plane coincides with the rotated section without warping deformations. The rotation from the initial to deformed configurations is defined by  $\tilde{\phi}$ —determining this rotation is the crux of the best-fit coupling problem.

#### 5.2.4 Best-fit multipoint constraint equations

Equations are now proposed to relate the interface beam-column element node to the interface continuum element nodes. The beam-column and continuum element domains are defined as  $\Omega_1$  and  $\Omega_2$ , respectively, and the interface between the two domains is denoted as  $\Gamma$ . A schematic representation of these domains is provided in Figure 5.2b for wide flange cross sections. Beam-column and shell element discretization of these domains is shown in Figure 5.2c, this figure also shows a schematic of the point cloud generated by the shell element nodes along  $\Gamma$ .

The interface beam-column node DOFs are treated as dependent, and the interface continuum nodes are treated as independent DOFs to introduce the least number of constraint

## 5.2. Development of the multipoint constraint equations

equations. The constraint equations are posed in a nonlinear form as

$$\mathbf{u}_b^* = \mathbf{f}(\mathbf{U}_c), \quad (5.10)$$

where  $\mathbf{u}_b^* = [\mathbf{u}_b, \boldsymbol{\phi}_b, w_b]^T$  are all the beam-column node DOFs, and  $\mathbf{f}(\mathbf{U}_c)$  are the nonlinear constraint equations dependent on the displacements of the continuum nodes,  $\mathbf{U}_c = \{\mathbf{u}_k\}_{k=1}^N$ . In Equation 5.10, the DOFs are defined in the global coordinate system with respect to the  $\mathbf{e}_1, \mathbf{e}_2, \mathbf{e}_3$  axes. Only the displacement DOFs of the continuum element nodes are considered in the formulation, therefore any continuum element nodal rotations are neglected (e.g., in shell elements).

Multipoint constraint equations are proposed based on the following ideas established in the previous section: (1) the beam-column node is initially located at the centroid of the interface continuum nodes, and the displacement of the beam node follows that of the centroid of the continuum nodes; (2) the rotation of the beam-column node matches the rotation of the best-fit plane; and (3) torsion-warping is determined based on the residuals between the interface continuum nodes and the plane of best-fit. Three MPC equations are specified to constrain the beam-column node to the centroid of the continuum nodes, three equations are specified to constrain the rotation of the beam-column node to the rotation of the plane of best-fit, and one equation is specified to constrain the warping amplitude to account for the residuals between the continuum nodes and the plane of best-fit. Altogether, this formulation necessitates seven equations to couple the seven beam-column node DOF to the  $3N$  continuum node displacement DOFs.

The displacement constraint equations are

$$\mathbf{f}_{1-3} := \mathbf{u}_b = \bar{\mathbf{u}} \quad (5.11)$$

where  $\mathbf{u}_b$  is the displacement of the beam node,  $\bar{\mathbf{u}}$  is the displacement of the centroid of the continuum nodes. The rotation constraint equations are

$$\mathbf{f}_{4-6} := \boldsymbol{\phi}_b = \boldsymbol{\phi}[\tilde{\mathbf{q}}], \quad (5.12)$$

where  $\boldsymbol{\phi}_b$  is the rotation of the beam node,  $\tilde{\mathbf{q}}$  is the rotation quaternion representing the orientation of the best-fit plane, and  $\boldsymbol{\phi}[\cdot]$  indicates the conversion from the quaternion representation to the Euler angle representation. A quaternion representation arises naturally from the eigenvectors of a  $4 \times 4$  eigenvalue problem that represents the rotation from the initial to deformed configurations (Horn, 1987; Mostafa and Sivaselvan, 2014). Computing the rotation from an eigenvector is considered integral to the best-fit MPC formulation as it renders the procedure computationally simple.

Finally, the warping constraint equation is

$$f_7 := w_b = \frac{1}{N_\psi} \sum_{k \in \mathbf{k}_\psi} \frac{1}{\psi_k} \mathbf{t} \cdot (\mathbf{x}_k - \tilde{\mathbf{R}}({}^0\mathbf{x}_k + \tilde{\mathbf{u}})) \quad (5.13)$$

where  $w_b$  is the warping amplitude of the beam node,  $\mathbf{x}_k$  are the locations of the continuum nodes in the deformed configuration,  ${}^0\mathbf{x}_k$  are the locations of the continuum nodes in the initial configuration,  $N_\psi$  is the number of non-zero warping function evaluations,  $\psi_k$  is the warping function evaluated at node  $k$ ,  $\mathbf{t}$  is the normal to the cross-sectional plane, and  $\tilde{\mathbf{R}}$  is the rotation matrix from the initial to the deformed configuration of the best-fit plane. Indices of the non-zero warping function evaluations are defined as the set  $\mathbf{k}_\psi = \{k \mid \psi_k \in \boldsymbol{\psi}, \psi_k \neq 0\}$ , and the number of non-zero evaluations is defined as the cardinality of set  $\mathbf{k}_\psi$  ( $N_\psi = \text{card}[\mathbf{k}_\psi]$ ). Equation 5.13 for the warping amplitude is derived from the average of the residuals from the plane fitting procedure.

Equations 5.11 to 5.13 specify transformations between the initial and deformed configurations, as shown schematically in Figure 5.3. The initial configuration is the undeformed cross section in its initial position and orientation in any space of the user's choosing. The deformed configuration is found by applying a translation then a rotation denoted by  $\tilde{\mathbf{R}}$  to the initial configuration. Additionally, the reference configuration is a convenient space defined by the authors in order to establish basic operations on the interface. It can be found from the initial configuration by applying a translation to the origin and the rotation  ${}^0\mathbf{R}^T$ .

### Orientation of the reference configuration

The orientation of the reference configuration is computed relative to the initial configuration through the matrix  ${}^0\mathbf{R}^T$ . The basis for obtaining  ${}^0\mathbf{R}^T$  is that the reference configuration,  $[{}^r\mathbf{n}_1, {}^r\mathbf{n}_2, {}^r\mathbf{t}]$ , is aligned with the global reference frame,  $[\mathbf{e}_1, \mathbf{e}_2, \mathbf{e}_3] = \mathbf{I}_{3,3}$  where  $\mathbf{I}_{3,3}$  is the  $3 \times 3$  identity matrix (see Figure 5.3). Therefore, the initial configuration is defined as  $[{}^0\mathbf{n}_1, {}^0\mathbf{n}_2, {}^0\mathbf{t}] = {}^0\mathbf{R}\mathbf{I}_{3,3} = {}^0\mathbf{R}$ . From this, the reference configuration is simply obtained from applying  ${}^0\mathbf{R}^T$  to the initial configuration.

The matrix  ${}^0\mathbf{R}$  is computed through Equation 5.3a. First, a set of points  $\mathbf{C} = \{\mathbf{c}_k\} = \{{}^0\mathbf{x}_k - {}^0\tilde{\mathbf{x}}\}_{k=1}^N$  is defined to represent the relative positions of the interface continuum nodes in the initial configuration. Second, the orientation of the initial configuration is found by computing the eigenvalues and eigenvectors of the  $3 \times 3$  matrix  $\mathbf{Y} = [\mathbf{c}_1, \dots, \mathbf{c}_N][\mathbf{c}_1, \dots, \mathbf{c}_N]^T$ . The eigenvector associated with the minimum eigenvalue is the  ${}^r\mathbf{t}$  axis, the eigenvector associated with the maximum eigenvalue is the  ${}^0\mathbf{n}_2$  axis, and the remaining eigenvector is the  ${}^0\mathbf{n}_1$  axis. Third, the orientation of the axes is set such that a right-handed coordinate system is formed. Details for this procedure are provided in Section 5.11.

The ordering of the eigenvalues noted above implies that  ${}^0\mathbf{t}$  is the orientation of the best-fit plane that contains  ${}^0\tilde{\mathbf{x}}$  in the initial configuration. The ordering of axes  ${}^0\mathbf{n}_1$  and  ${}^0\mathbf{n}_2$  is made

## 5.2. Development of the multipoint constraint equations

according to the moments of inertia for the cross section in this best-fit plane. Essentially, the ordering assumes a wide flange cross section; and that  $I_1 > I_2$ , where  $I_1$  and  $I_2$  are the moments of inertia about each axis of the cross section in the best-fit plane. This assumption will hold for most practical cases, however, the axes can easily be defined in a different manner for the cases that it does not hold.

### Computation of the optimal rotation quaternion

The method stated in Mostafa and Sivaselvan (2014) is used to formulate and solve for the best-fit plane's rotation. The rotation quaternion,  $\tilde{\mathbf{q}}$ , is defined by the rotation from the initial to deformed configurations. First, the set of points  $\mathbf{D} = \{\mathbf{d}_k\} = \{\mathbf{x}_k - \bar{\mathbf{x}}\}_{k=1}^N$  is defined for the relative positions of the interface continuum nodes in the deformed configuration. Second, the matrix defining the eigenvalue problem to be solved to obtain the cross-sectional plane's rotation is

$$\mathbf{B} = \sum_k \boldsymbol{\beta}_k^T \boldsymbol{\beta}_k, \quad (5.14)$$

where  $\mathbf{c}_k = {}^0\mathbf{x}_k - {}^0\bar{\mathbf{x}}$  has been previously defined, and the matrix  $\boldsymbol{\beta} = \text{LEFTQUAT}([0, \mathbf{d}_k^T]) - \text{RIGHTQUAT}([0, \mathbf{c}_k^T])$ . The operations LEFTQUAT and RIGHTQUAT, clarified in Section 5.11, are the matrix representations of left- and right-side multiplication of a rotation quaternion (Mostafa and Sivaselvan, 2014). Finally, the optimal rotation quaternion,  $\tilde{\mathbf{q}}$ , is the eigenvector associated with the minimum eigenvalue of  $\mathbf{B}$ . An important distinction between determining  $\tilde{\mathbf{q}}$  from  $\mathbf{B}$  and the eigenvalue problem in Equation 5.3a is that the former gives the *rotation*, while the later gives the *orientation*.

### Rotation quaternion to Euler angle conversion

A conversion from a rotation quaternion to an Euler angle representation is required in Equation 5.12. The method used is the same as the one provided in Abaqus v6.14 (Dassault Systèmes, 2014). The procedure to extract the rotation angle from the rotation quaternion defined by  $\mathbf{q} = [q_0, \mathbf{q}^T]$  is given by

$$\phi[\mathbf{q}] = \|\boldsymbol{\phi}\| \frac{q}{\|\mathbf{q}\|}, \quad (5.15a)$$

$$\|\boldsymbol{\phi}\| = 2 \arctan\left(\frac{\|\mathbf{q}\|}{q_0}\right). \quad (5.15b)$$

The real part of the quaternion  $\mathbf{q}$  is  $q_0$  and the imaginary part is  $\mathbf{q}^T = [q_1, q_2, q_3]$ .

### 5.3 Application of the best-fit constraint equations for nonlinear finite element analysis

The constraint coefficient matrix,  $A$ , where  $\mathbf{u}_b^* = A\mathbf{U}_c$  is used to relate the beam-column and continuum element DOF within the global system of equations. The constraint coefficient matrix is required to account for the constraints within the context of an incremental-iterative solution method for nonlinear finite element problems. For instance, the unconstrained global system of equations can be defined in an unconstrained, partitioned form as

$$\begin{bmatrix} \mathbf{K}_{nn} & \mathbf{K}_{nc} & \mathbf{K}_{nb} \\ \mathbf{K}_{cn} & \mathbf{K}_{cc} & \mathbf{K}_{cb} \\ \mathbf{K}_{bn} & \mathbf{K}_{bc} & \mathbf{K}_{bb} \end{bmatrix} \begin{bmatrix} \mathbf{U}_n \\ \mathbf{U}_c \\ \mathbf{u}_b^* \end{bmatrix} = \begin{bmatrix} \mathbf{P}_n \\ \mathbf{P}_c \\ \mathbf{P}_b \end{bmatrix}, \quad (5.16)$$

where the DOFs  $n$  are not involved in the constraint, the DOFs  $b$  correspond to the dependent beam-column element node, and the DOFs  $c$  correspond to the independent continuum element nodes.

Constraints  $\mathbf{u}_b^* = A\mathbf{U}_c$  are now imposed on the system (5.16). The symmetric, constrained system of equations (Abel and Shephard, 1979) can be defined as

$$\begin{bmatrix} \mathbf{K}_{nn} & \mathbf{K}_{nc} + \mathbf{K}_{nb}A & \mathbf{0} \\ \mathbf{K}_{cn} + A^T\mathbf{K}_{bn} & \mathbf{K}_{cc} + \mathbf{K}_{cb}A & A^T\mathbf{K}_{bb} \\ \mathbf{0} & \mathbf{K}_{bb}A & -\mathbf{K}_{bb} \end{bmatrix} \begin{bmatrix} \mathbf{U}_n \\ \mathbf{U}_c \\ \mathbf{u}_b^* \end{bmatrix} = \begin{bmatrix} \mathbf{P}_n \\ \mathbf{P}_c + A^T\mathbf{P}_b \\ \mathbf{0} \end{bmatrix}. \quad (5.17)$$

In the current context, the constraint coefficient matrix is comprised of three submatrices,  $A = [A^{disp}, A^{rot}, A^{warp}]^T$  that correspond to the interface beam-column node's displacement, rotation, and warping DOFs, respectively. The respective dimensions of the matrices are:  $3 \times 3N$ ,  $3 \times 3N$ , and  $1 \times 3N$ .

It is common to employ the rigid body assumptions to formulate linearized constraint equations to apply the nonlinear constraints in the context of nonlinear finite element analysis solution procedures (Abel and Shephard, 1979). The use of linearized constraint equations implies that each submatrix in the constraint coefficient matrix is computed as  $(A_{ij})_k = (\partial f_i / \partial u_j)_k$ , where  $f_i$  are the constraint equations that impose rigid body motion, and  $u_j$  are the DOFs of the interface continuum node  $k$ . However, this method leads to stress distributions in the interface continuum elements that are substantially incorrect when used with the proposed best-fit approach. The proof of this statement is shown through the derivation of the linearized constraint equations, alongside a simple example to highlight its effect, at the end of this chapter in Section 5.12.

An alternative method, denoted “the nodal force method” is developed to define the constraint coefficient matrix. The use of this alternative method overcomes the limitation

### 5.3. Application of the best-fit constraint equations for nonlinear finite element analysis

of using the linearized equations to define  $\mathbf{A}$ . The nodal force method is based on the interpretation that  $\mathbf{A}^T$  plays the role of distributing forces from the beam-column node to the continuum nodes in (5.17). For instance, see the term  $\mathbf{A}^T \mathbf{P}_b$  on the right-hand side of the system of equations that accomplishes this task. Later examples demonstrate that the nodal load method leads to stresses in the interface continuum elements of macro models that are in fair agreement with full continuum models so long as the assumptions used to derive the method are satisfied.

#### 5.3.1 Overview of the nodal load method for computing the constraint coefficient matrix

The nodal load method is based on beam mechanics and the idea that  $\mathbf{A}^T$  redistributes the forces and moments applied to the interface beam-column node to the interface continuum nodes. Coefficients of the  $\mathbf{A}^T$  matrix are computed by assuming that a unit load is acting on each beam-column node DOF and determining the resulting forces on the continuum element nodes. Only the work-conjugate related to displacements (i.e., forces) acting on the continuum element nodes are required within this framework because only independent displacement DOFs are included in the constraint formulation. The forces acting on each continuum node are determined by integrating the stresses from each unit load over the corresponding nodal area. Beam mechanics implied by the kinematics in Equation 5.1 are used to relate the loads and stresses.

The reference configuration is used to compute the stresses in the nodal load method. The stress in the reference configuration,  ${}^r\boldsymbol{\tau}^i(\xi, \eta)$ , at any point along the interface  $\Gamma$  for a load applied in beam-column DOF  $i$  is defined by

$${}^r\boldsymbol{\tau}^i(\xi, \eta) = {}^r\bar{\boldsymbol{\tau}}^i(\xi, \eta) {}^r\mathbf{p}_i, \quad (5.18)$$

where the prescript  ${}^r(\cdot)$  in (5.18) indicates that all these quantities are defined in the reference configuration,  $\boldsymbol{\tau}$  is the stress tensor,  $\bar{\boldsymbol{\tau}}(\xi, \eta)$  is a stress factor, and  ${}^r\mathbf{p}_i$  represents unit loads in DOF  $i$ . For any DOF, the resulting traction vector on the cross section is then defined as

$${}^r\boldsymbol{\nu}(\xi, \eta) = {}^r\boldsymbol{\tau}(\xi, \eta) {}^r\mathbf{t}. \quad (5.19)$$

The traction vectors are then integrated over an area to obtain a force vector.

The main effort of the nodal force method is to define the stress factors that relate stresses acting on the interface continuum element nodes to the loads applied on the beam-column element node. For instance, stresses on the continuum interface due to torsion applied on the beam-column node are shown in Figure 5.5a. The  $\tau_{31}$  and  $\tau_{32}$  components of the stress tensor are computed on the cross section as a function of a unit torque, the traction vector is

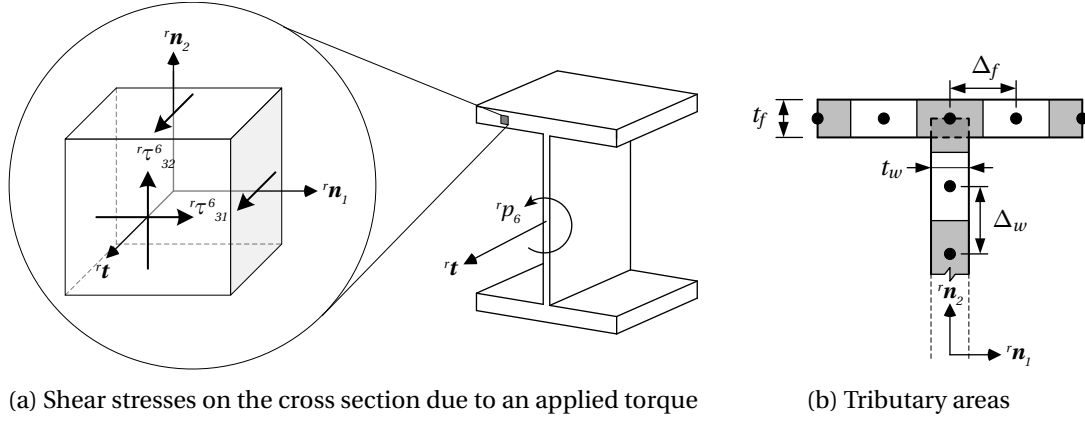


Figure 5.5 – Nodal stresses due to an applied beam-column load and the nodal tributary areas.

computed from the stress tensor, and the stresses are then integrated over each nodal area to obtain a force. A representation of the nodal areas, with respect to a centerline shell element discretization, are shown in Figure 5.5b for a wide flange cross section. The parameters  $t_f$  and  $t_w$  are the flange and web thicknesses, respectively; the parameters  $\Delta_f$  and  $\Delta_w$  are the mesh sizes for the flange and web, respectively. The symmetric cross section discretization established earlier implies that the distances  $\Delta_f$  and  $\Delta_w$  are consistent for all the flange and web elements.

Stresses and their resultants are grouped into axial stresses and shear stress. The axial stresses are induced by axial forces, bi-axial bending, and torsion-warping; shear stresses are induced by bi-axial shear forces and torsion. The summation of all nodal forces derived through this method must satisfy force, moment, and bi-moment equilibrium. Given the reference and global coordinate systems defined in Figure 5.3, the work conjugates to the beam-column nodal loads,  $p_i$ , are the beam-column nodal DOF  $(u_b^*)_i$  ( $i = 1, \dots, 7$ ). As the constraint coefficient matrix is derived in the reference configuration, transformations from the reference to deformed configurations are necessary (see Figure 5.3), and will be discussed upon completion of the description in the reference configuration.

### 5.3.2 Axial force, bi-axial bending, warping

The coefficients in  $\mathbf{A}^T$  related to axial stresses are computed based on the beam-column segment approach presented Chen and Atsuta (2008). The axial stress component in the stress tensor for a continuum node  $k$ ,  $r\bar{\tau}_{33,k}^i$ , is computed for loading in each DOF  $i = 3, 4, 5, 7$  from the section deformations and the stress-strain relation:

$$r\bar{\tau}_{33,k}^i = C_k^{ep} \boldsymbol{\rho}_k^T \mathbf{u}_i^{sec}. \quad (5.20)$$



### 5.3. Application of the best-fit constraint equations for nonlinear finite element analysis

In this equation,  $C_k^{ep}$  is the uniaxial tangent modulus at node  $k$ , the cross section vector,  $\boldsymbol{\rho}_k$ , is defined for each interface continuum node as  $\boldsymbol{\rho}_k = [1, \eta_k, -\xi_k, \xi_k \eta_k]^T$ , and the section deformations  $\mathbf{u}_i^{sec}$  are computed by solving

$$\mathbf{K}^{sec} \mathbf{u}_i^{sec} = \mathbf{p}_i. \quad (5.21)$$

The section deformation vector contains the axial strain, curvatures, and warping due to the applied load  $\mathbf{p}_i$ , where  $\mathbf{p}$  are load vectors with component  $i$  equal to unity, and all others equal to zero. Definition of the cross section stiffness matrix,  $\mathbf{K}^{sec}$ , remains.

The interface continuum elements are herein assumed to exhibit an isotropic elastic response; this may be a significant limitation in certain scenarios, as discussed later in the Limitations section. With the elastic material assumption, i.e.,  $C_k^{ep} = E$ , the section stiffness matrix is

$$\mathbf{K}^{sec} = E \sum_k a_k \boldsymbol{\rho}_k \boldsymbol{\rho}_k^T. \quad (5.22)$$

The diagonal terms in  $\mathbf{K}^{sec}$  are:  $E A$ , where  $A = \sum_k a_k$  is the area of the cross section; and  $E I_1, E I_2, E I_w$ , where  $I_1, I_2, I_w$  are the moments of inertia and the warping constant for the cross section. Bi-symmetry of wide flange cross sections implies that the off-diagonal terms are equal to zero when the material is elastic (Chen and Atsuta, 2008).

#### 5.3.3 Bi-axial shears

From elementary beam theory (Gere, 2004), a shear stress factor  ${}^r\bar{\tau}_{32}^2(\eta) = Q(\eta)/t(\eta)$  is defined for wide flange sections for a unit shear force applied in the direction of the strong axis, and a constant moment of inertia. Again, the assumption of an elastic material behavior is made. Here,  $t(\eta)$  is the part's thickness and  $Q(\eta)$  is the first moment of area. Recall that the stress factor  ${}^r\bar{\tau}_{32}^2(\eta)$  represents the 3,2-component of the shear stress (see Figure 5.5a) due to a shear force applied in beam-column node DOF 2.

Considering  $\eta \in [-d/2, d/2]$  measured from the centroid of the cross section,

$${}^r\bar{\tau}_{32}^2(\eta) = \begin{cases} 1/t_w (0.25b_f t_f (d + d_1) + 0.5t_w (0.5d_1 - \eta)(0.5d_1 + \eta)) & \text{if web} \\ 1/b_f (0.5b_f (0.5d - \eta)(0.5d + \eta)) & \text{if flange,} \end{cases} \quad (5.23)$$

where  $d_1 = d - 2t_f$ . The shear stress factor is computed from the normalized stress as

$${}^r\bar{\tau}_{32,k}^2 = \frac{1}{V_2} {}^r\bar{\tau}_{32}^2(\eta_k), \quad (5.24)$$

where the total shear force is  $V_2 = \sum_k a_k {}^r\bar{\tau}_{32}^2(\eta_k)$ . The distributions of the 3,2-component is shown in Figure 5.6. Strong axis shear also leads to the 3,1-component in the flanges. Considering a constant moment of inertia and a unit shear force, the maximum shear stress

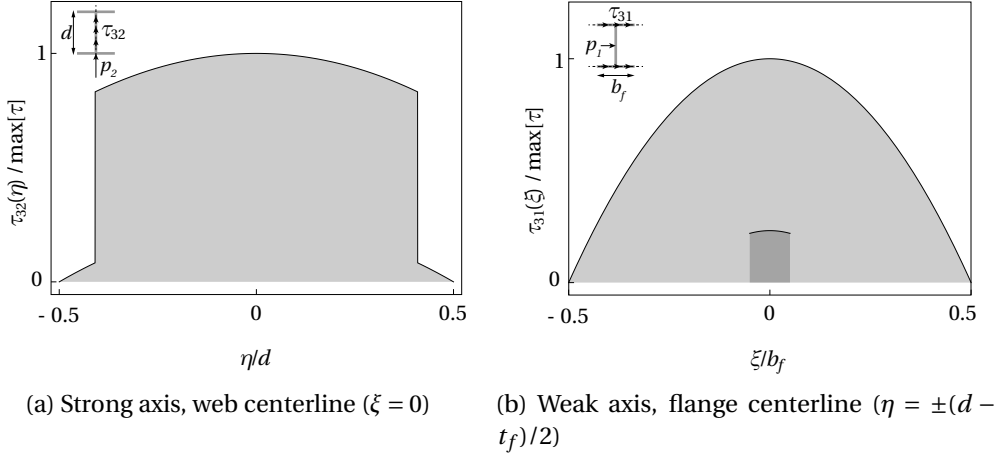


Figure 5.6 – Sample assumed elastic shear stress distribution ( $d = 110$ ,  $b_f = 100$ ,  $t_w = t_f = 10$ ).

factor is

$${}^r\bar{\tau}_{31,max}^2 = \frac{1}{V_2} \frac{b_f(d - t_f)}{4}, \quad (5.25)$$

where  $h_{cl} = h - t_f$  is the centerline depth of the section. Since the distribution is linear, linear interpolation is used between 0 at the flange tips and  ${}^r\bar{\tau}_{31,max}^2$  based on the flange node locations to obtain the value of  ${}^r\bar{\tau}_{31,k}^2$  for flange node  $k$ .

Now considering a shear force applied in the weak axis (DOF 1), the shear stress is

$${}^r\tau_{31}^1(\xi) = \begin{cases} \frac{b^2 - 4(\xi)^2}{8} & \text{if flange} \\ \frac{2b^2 t_f + t_w^2 (h - 2t_f)}{8h_1} & \text{if web (along centerline)}. \end{cases} \quad (5.26)$$

The distribution is shown in Figure 5.6, the darker shaded region in the center are the values on the web. Again, a normalization is used to get the stress factor:

$${}^r\bar{\tau}_{31,k}^1 = \frac{1}{V_1} {}^r\tau_{31}^1(\xi_k), \quad (5.27)$$

where  $V_1 = \sum_k a_k {}^r\tau_{31}^1(\xi_k)$ .

### 5.3.4 Torsion

Forces acting on the continuum nodes due to torsion on the beam-column node are determined by assuming a rigid link between the beam-column node and each continuum node. This assumption is made because the actual shear flow is circuitous throughout the cross section under torsion loading (Gere, 2004). As a result, integrating the shear stress over each nodal area for shell elements will give a resultant near to zero at most points on the cross section. The approach taken here is that the shear force applied to each node is proportional

### 5.3. Application of the best-fit constraint equations for nonlinear finite element analysis

to the distance between the node and the centroid, and is perpendicular to the vector from the centroid to the node.

The shear stress factor in the reference configuration due to torque is computed as

$${}^r\bar{\mathbf{t}}_k^6 = [{}^r\bar{t}_{31,k}^6, {}^r\bar{t}_{32,k}^6]^T = a_k \frac{1}{I_3} \frac{[-\eta_k, \xi_k]^T}{\|[\xi_k, \eta_k]\|} \cdot \|[\xi_k, \eta_k]\| = \frac{1}{I_3} a_k [-\eta_k, \xi_k]^T, \quad (5.28)$$

where the polar moment of inertia for the cross section is computed in a discrete manner as  $I_3 = \sum_k a_k \|[\xi_k, \eta_k]\|^2$ . The division by  $I_3$  is used to satisfy the equilibrium conditions for a unit torque.

#### 5.3.5 Definition of the nodal forces in the deformed configuration

This section establishes how the stress resultants in the nodal force method are transformed from the reference to the deformed configurations. First, the local coordinate system in considered in the reference configuration. The resultant force vector is derived assuming that the stress is constant over the tributary area of each node:

$${}^r s_i = \int a {}^r \tau_{ij}(\xi, \eta) {}^r t_j d = a {}^r \tau_{ij} {}^r t_j, \quad (5.29)$$

where the  $i, j$  indices take values of 1, 2, 3, or in the matrix convention

$${}^r \mathbf{s} = a {}^r \boldsymbol{\tau} {}^r \mathbf{t}. \quad (5.30)$$

Note that specification of an individual node  $k$  is suppressed until the end of this derivation to simplify the notation.

Forces and displacements for each node must be calculated and assigned with respect to the deformed configuration, therefore,

$$\mathbf{s} = a \mathbf{R}^T {}^r \boldsymbol{\tau} {}^r \mathbf{t}. \quad (5.31)$$

The rotation tensor  $\mathbf{R}$  in Equation 5.31 should be interpreted as the relation between the local coordinate system of the cross section and the global coordinate system. Note that the rotation matrix recovered from the optimal rotation quaternion transforms the *vector*  ${}^0 \mathbf{t}$  to  $\mathbf{t}$ , therefore, the following relation is very important,

$$\mathbf{R} = (\tilde{\mathbf{R}}^0 \mathbf{R})^T. \quad (5.32)$$

Recall that  ${}^0 \mathbf{R}$  transforms  ${}^r \mathbf{t}$  to  ${}^0 \mathbf{t}$ . For simplicity, quantities are defined with respect to  $\mathbf{R}$ , and towards the end the relation (5.32) is substituted.

The stress tensor is left in the local reference coordinates since the nodal force method

## Chapter 5. Best-fit constraint equations for coupling mixed-dimension simulation models with wide flange cross sections

---

operates in the reference configuration. The stress tensor of each node is now related to the DOF of the beam node through the stress factors and the vector of applied loads,

$${}^r\boldsymbol{\tau} = {}^r\bar{\boldsymbol{\tau}} {}^r\mathbf{P}, \quad (5.33)$$

Note that the dimensions of  ${}^r\bar{\boldsymbol{\tau}}$  are  $3 \times 3 \times 7$ , and  $\mathbf{P}$  is dimension 7. Substituting the weights,  ${}^r\bar{\boldsymbol{\tau}}$ , into Equation 5.31 and bringing  ${}^r\mathbf{P}$  into the deformed configuration,

$$\mathbf{s} = \mathbf{a} \mathbf{R}^T {}^r\bar{\boldsymbol{\tau}} \mathbf{T} \mathbf{P} \mathbf{R} \mathbf{t}, \quad (5.34)$$

where  $\mathbf{T}$  is the transformation of dimensions  $7 \times 7$  represented by the matrix

$$\mathbf{T} = \begin{bmatrix} \mathbf{R}^T & \mathbf{0}_{3,3} & \mathbf{0}_3 \\ \mathbf{0}_{3,3} & \mathbf{R}^T & \mathbf{0}_3 \\ \mathbf{0}_3^T & \mathbf{0}_3^T & 1 \end{bmatrix}, \quad (5.35)$$

where  $\mathbf{0}_{3,3}$  is a  $3 \times 3$  matrix of zeros,  $\mathbf{0}_3$  is a vector of 3 zeros.

Two key observations regarding the structure of  $\mathbf{T}$  in (5.35) are made. First, the warping amplitude is defined locally based on the direction of  $\mathbf{t}$ , and therefore is not rotated. The physical interpretation is that the stress from warping is always acting in the direction of  $\mathbf{t}$  regardless of the definition of any axes. Second, the displacement, rotation, and warping DOFs can be rotated independently of each other due to the diagonal structure of  $\mathbf{T}$ .

A method to define the constraint coefficient matrix,  $\mathbf{A}$ , in the deformed configuration making use of Equation 5.34 is now outlined. Equation 5.34 is written in indicial notation to assist in understanding the necessary computations,

$$s_i = a R_{ik} {}^r\bar{\tau}_{kl}^m T_{mn} P_n R_{lj} t_j, \quad (5.36)$$

and  $R_{lj} t_j = {}^r t_l$  is the normal to the cross section in the deformed configuration that is known. In (5.36), the indices  $i, j, k, l$  take values of 1, 2, 3, and  $m, n$  take values of 1, 2, ..., 7. The procedure is simplified by first computing the resultant of the stress traction vector in the reference configuration for each DOF by contracting  $\bar{\tau}_{kl}^m {}^r t_l$ :

$${}^r S_k^m = a {}^r\bar{\tau}_{kl}^m {}^r t_l \iff {}^r \mathbf{S} = [a {}^r\bar{\tau}^1 {}^r \mathbf{t}, \dots, a {}^r\bar{\tau}^7 {}^r \mathbf{t}]. \quad (5.37)$$

${}^r \mathbf{S}$  is a  $3 \times 7$  matrix where each column is the matrix-vector product of the traction vector for DOF  $i$  and  ${}^r \mathbf{t}$  times the tributary of the node. Now considering the rest of the terms in Equation 5.34,

$$S_{ij} = R_{ik} {}^r S_{km} T_{mj} \iff \mathbf{S} = \mathbf{R}^T {}^r \mathbf{S} \mathbf{T}, \quad (5.38)$$

where all the quantities are known. Using Equation 5.32 again,

$$\mathbf{S} = \tilde{\mathbf{R}}^0 \mathbf{R}^r \mathbf{S} T, \quad (5.39)$$

recalling that up to this point the specific reference to a node has been suppressed. Finally, the correspondence between the submatrices of the constraint coefficient matrix and Equation 5.39 is

$$(\mathbf{A}^T)_k = (\mathbf{S})_k, \quad (5.40)$$

where the  $k$  subscript is added to denote the continuum node.

## 5.4 Summary of the best-fit coupling method

For fast global convergence, the beam node displacement predicted by the constraint coefficient matrix applied to the continuum node displacements, i.e.,  $\mathbf{A}^{disp} \mathbf{U}_c$ , should agree with  $\mathbf{u}_b$ . To enforce this consistency, the displacement  $\mathbf{u}_b$  in (5.11) is computed as

$$\mathbf{u}_b = \bar{\mathbf{u}} = \mathbf{A}^{disp} \mathbf{U}_c. \quad (5.41)$$

This formulation creates a dependence of  $\mathbf{u}_b$  on the orientation of the cross section since  $\mathbf{A}^{disp}$  depends on  $\tilde{\mathbf{R}}$  via Equation 5.39. The rotation, in-turn, depends on the position of the centroid, creating a nonlinear relation between the centroid displacement and optimal rotation.

This nonlinear relation is addressed through an iterative procedure to determine the centroid displacement termed “inner iterations”. For the first inner iteration, the centroid position is determined using the mean of the shell nodes (i.e.,  $1/N$  factor), this position is used to get an initial estimate of the optimal rotation. Further inner iterations use  $\mathbf{A}^{disp}$  based on the nodal force method including the rotation of the cross section determine the centroid position. Inner iterations are ended when the difference in consecutive centroid displacements is less than a prescribed tolerance, in this case set to  $10^{-8}$ . This procedure typically converges after three iterations.

For clarity, the entire best-fit MPC coupling procedure for wide flange cross sections is summarized using pseudocode in Algorithm 2. The detailed algorithm, along with supporting procedures, is provided in Section 5.11.

## Chapter 5. Best-fit constraint equations for coupling mixed-dimension simulation models with wide flange cross sections

---

---

### Algorithm 2 Summary of the best-fit MPC coupling method.

---

```
1: Compute the reference configuration
2: Compute the nodal areas and cross-sectional properties
3: Compute the nodal forces in the reference configuration
4: Set initial  $A^{disp}$ 
5: while centroid displacements not converged do                                ▷ Inner iterations
6:   Compute the centroid displacement
7:   Compute the optimal rotation
8:   Update  $A^{disp}$ 
9: end while
10: Calculate the warping amplitude
11: Transform the nodal forces into the deformed configuration
12: Calculate the constraint coefficient matrix
13: Assign the exact values of the beam DOF using the constraint equations
```

---

## 5.5 Evaluation of the best-fit coupling method

Two case studies are used to evaluate the proposed best-fit coupling method. For this purpose, the proposed method was implemented using the user MPC subroutine in Abaqus v6.14 (Dassault Systèmes, 2014). The complete source code is provided by the authors (Hartloper, 2021). Descriptions and results are provided for the example; a discussion of the results follows.

For clarity and transparency in simulations, implicit static analysis in Abaqus v6.14 with double floating-point precision is used for both case studies. Nonlinear geometric transformations are assumed (NLGEOM = ON in Abaqus). The nonlinear equilibrium equations are solved using the full-Newton method, and the Abaqus default convergence criteria of 0.5 % on the relative residuals is used.

### 5.5.1 Example 1: Elastic cantilever subjected to large deformations

#### Description

The first example is an elastic cantilever subjected to large deformations. The purpose of this example is to validate the implementation of the proposed coupling method for problems in which the interface elements remain elastic. The beam cross section dimensions are:  $d = 110$  mm,  $b_f = 100$  mm,  $t_f = t_w = 10$  mm, and the length of the cantilever is 2000 mm. Elastic material properties are assumed with modulus of elasticity  $E = 200$  GPa and Poisson's ratio  $\nu = 0.3$ . The model is subjected to a displacement boundary condition at the free end of  $\delta_X = -1000$  mm,  $\delta_Y = 1000$  mm, and  $\delta_Z = 100$  mm, resulting in a maximum displacement magnitude of  $\delta = 1418$  mm. The displacement boundary is selected to induce loading in every

DOF of the interface beam-column node. The basic model is shown in Figure 5.7a with the overall tip displacement,  $\delta$ , and the magnitude of the reaction force at the fixed end,  $F$ . Results are evaluated using the magnitude of the reaction force at the fixed end.

Four model variants are evaluated: the “Full-shell Model”, comprised of shell elements; the “Full-beam Model”, comprised of only beam-column elements; the “KC Model” macro model employing the built in kinematic coupling in Abaqus; and the “BF-MPC Model” macro model employing the proposed best-fit MPC coupling. For both macro models, the beam-column and shell element domains are evenly divided into 1000 mm length. For all models, linear (four-node), reduced integration shell elements (S4R in Abaqus) are used to model the continuum domain. The default of five section points are used throughout the shell thickness. Quadratic, open-section beam-column elements (B32OS in Abaqus) are used to model the beam-column domain. Two S4R elements are used per half-flange, and four in the web; the element aspect ratio is kept at approximately unity along the beam length. The individual B32OS element length is set at 100 mm. A rigid-body constraint is used at the free-end to apply the displacement boundary condition at the centroid of the Full-shell model.

### Results

Tip displacement and reaction force results from the cantilever example are shown in Figure 5.7b, the resulting deformed shape is shown in Figure 5.7a superimposed on the initial shape. The overall force-displacement response of the two macro models (BF-MPC Model and KC-Model) are nearly identical. Good agreement between the macro models and the Full-shell model in terms of reaction force and tip deformation is also apparent. The differences between the macro models and the Full-shell Model are attributed to the beam-column and shell element formulations, as the macro model response lies between the Beam-column Model and the Full-shell Model. This result validates the theory established in this chapter for the best-fit coupling method under the applied loading.

The stresses in the interface shell elements are also reported for the Full-shell Model, KC Model, and BF-MPC Model in Figure 5.8. Each bar in these plots represents the average axial or shear stress computed from the five section points in each shell element on the interface (see Figure 5.2a). In terms of axial stresses, the built-in kinematic coupling (KC) and proposed best-fit MPC (BF-MPC) models perform similarly when compared with the Full-shell Model (see Figures 5.8a and 5.8b). However, in terms of shear stresses, there is a notable improvement over the built-in kinematic coupling when the best-fit MPC is employed as depicted in Figures 5.8c and 5.8d. This result implies that shear stresses are not correctly transferred between the domains when a kinematic coupling such as the one in Abaqus v6.14 is employed.

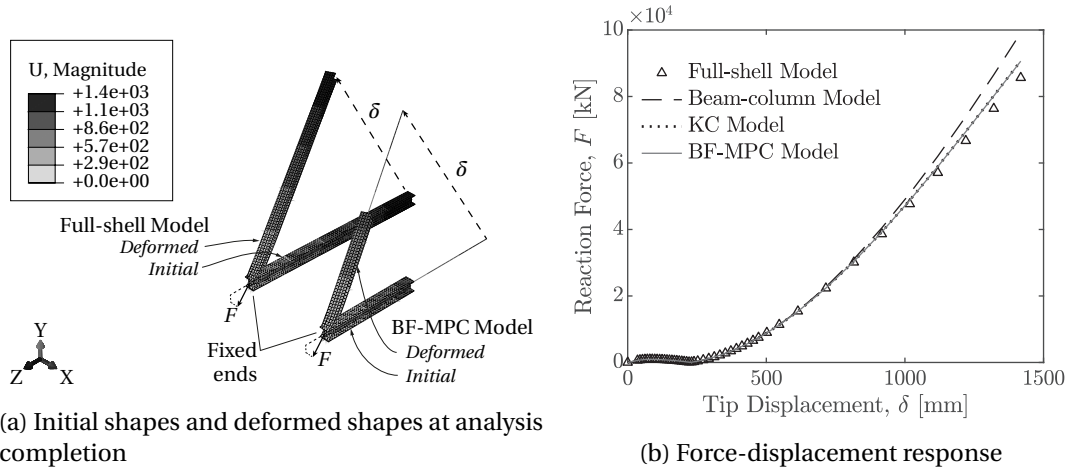


Figure 5.7 – Results from the elastic cantilever model subjected to a large deformation. Figure (a) shows the Full-shell model (left) and BF-MPC model (right).

### 5.5.2 Example 2: Inelastic beam subjected to nonuniform torsion

#### Description

The primary motivation for the implementation of the best-fit MPC is the recognition that coupling methods that do not include warping lead to an incorrect torque-twist response for wide flange cross sections. This issue is demonstrated by comparing the built-in Abaqus v6.14 kinematic coupling with test data. Furthermore, we show that the proposed best-fit MPC coupling method addresses this issue in the elastic domain, although limitations become apparent once the interface elements exhibit yielding.

Experimental data is taken from a beam subjected to non-uniform torsion tested by Farwell and Galambos (1969). A schematic of the set-up is shown in Figure 5.9a. The specimen has a wide flange cross section ( $6 \times 6-25$ ) with a depth of  $d = 152.4$  mm, a flange width of  $b_f = 150.9$  mm, a flange thickness of  $t_f = 12.2$  mm, a web thickness of  $t_w = 8.0$  mm, and a length of 1930 mm. The beam is supported at both ends by the reaction columns that restrict twisting and axial displacements, but allow the specimen to warp. A torque is applied at the center of the beam through a circular loading plate that is rotated using two hydraulic cylinders, the schematic of the load plate profile is inset in Figure 5.9a to show the resulting torque,  $M_Z$  and twist,  $\theta_Z$ . A total torque of  $M_Z = 25$  kN.m is applied at the center of the finite element models.

The same four models discussed earlier (Full-shell, Beam-column, KC, and BF-MPC) are used for this example problem as well. Additionally, another macro model is used with a warping-inclusive kinematic coupling (WIKC) (Hartloper et al., 2021b), denoted the “WIKC Model”. The WIKC Model has a similar formulation to the built-in kinematic coupling in Abaqus v6.14, but is able to transfer torsion-warping deformations as well. The length of



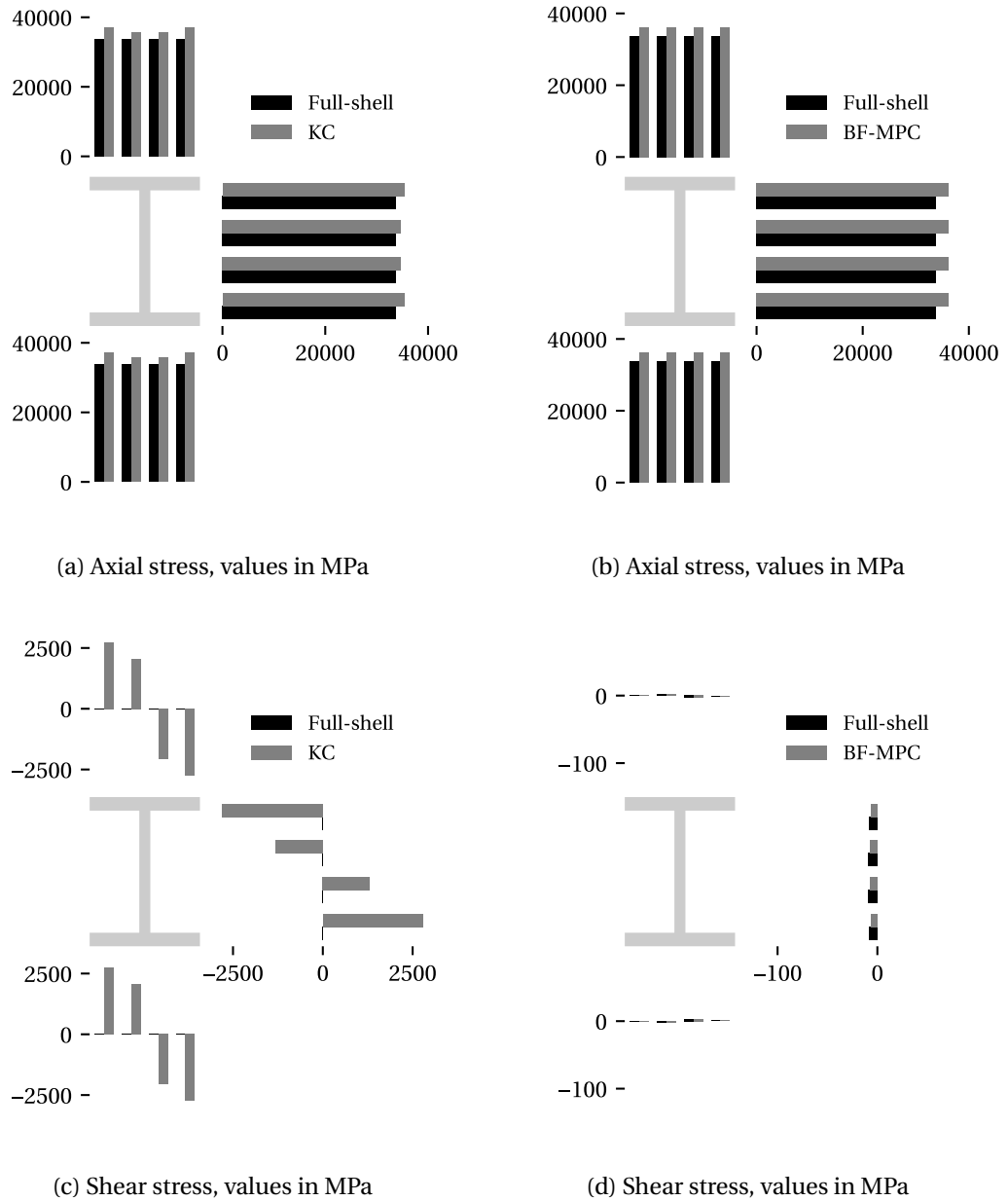


Figure 5.8 – Interface shell element stress distributions for Full-shell, and macro models with built-in Abaqus kinematic coupling (KC) and the proposed MPC (BF-MPC). Values extracted from the final state of Example 1.

the continuum element domain is nominally selected as  $0.25L$  at both ends for the three macro models. The beam-column domain is modeled with ten B32OS elements, and four S4R elements are used in each half-flange and eight in the web. The material properties are  $E = 213400$  MPa,  $\nu = 0.3$ , initial yield stress  $\sigma_{y,0} = 285$  MPa, with linear isotropic hardening defined by 289 MPa at a plastic strain of  $\epsilon^p = 0.01329$  and 876.2 MPa at  $\epsilon^p = 0.094$  (Pi and Trahair, 1995).

## Results

The initial and deformed shape at the end of the analysis are shown for the BF-MPC model in Figure 5.9b, torque-twist results are provided in Figure 5.9c. The average axial stress in the interface continuum elements is shown at an applied torque of  $M_Z = 10^4$  kN.m in Figure 5.9d. The most notable result shown in Figure 5.9c is that the macro model utilizing the built-in Abaqus kinematic coupling (KC Model) does not correctly predict the elastic torsional stiffness. This is because torsion-warping deformations are not transferred at the interface with the built-in Abaqus formulation. All the other models give a good prediction of the test data in the elastic domain. Agreement in the axial stress for the BF-MPC model, as shown in Figure 5.9d, demonstrates that the proposed coupling method adequately transfers torsion-warping deformations.

The beam-column, BF-MPC, and WIKC Models all diverge from the Full-shell Model and test data after around 0.25 rad twist. This is attributed to a limitation in the Abaqus v6.14 beam-column elements in that they are valid for angles of twist up to about 0.2 rad (Dassault Systèmes, 2014). Yielding initiates at a torque of around  $M_Z = 9$  kN.m ( $\theta_Z \approx 0.10$  rad at this point). The BF-MPC model can converge increments up-to around 0.50 rad twist even though the coupling formulation assumes the interface shell elements remain elastic, although the global Newton iterations do not converge after this point (model non-convergence). This may not be a major limitation in beam-columns, as full-scale tests on wide flange beam-columns suggest that the maximum measured twisting angle is around 0.10 rad at relatively large lateral drift demands associated with incipient collapse (Elkady and Lignos, 2018a). However, note that the model employing the WIKC method (Hartloper et al., 2021b) can converge increments in which the interface is inelastic. Moreover, it captures the elastic torsional stiffness of the beam-column under discussion correctly.

## 5.6 Discussion and limitations

The proposed best-fit MPC achieves the objectives set forth, namely: (1) it couples beam-column and continuum element domains utilizing the least number of constraint equations, and (2) it incorporates torsion-warping into the coupling formulation. The best-fit coupling method is validated for simple, large-deformation problems through Example 1. The ability of

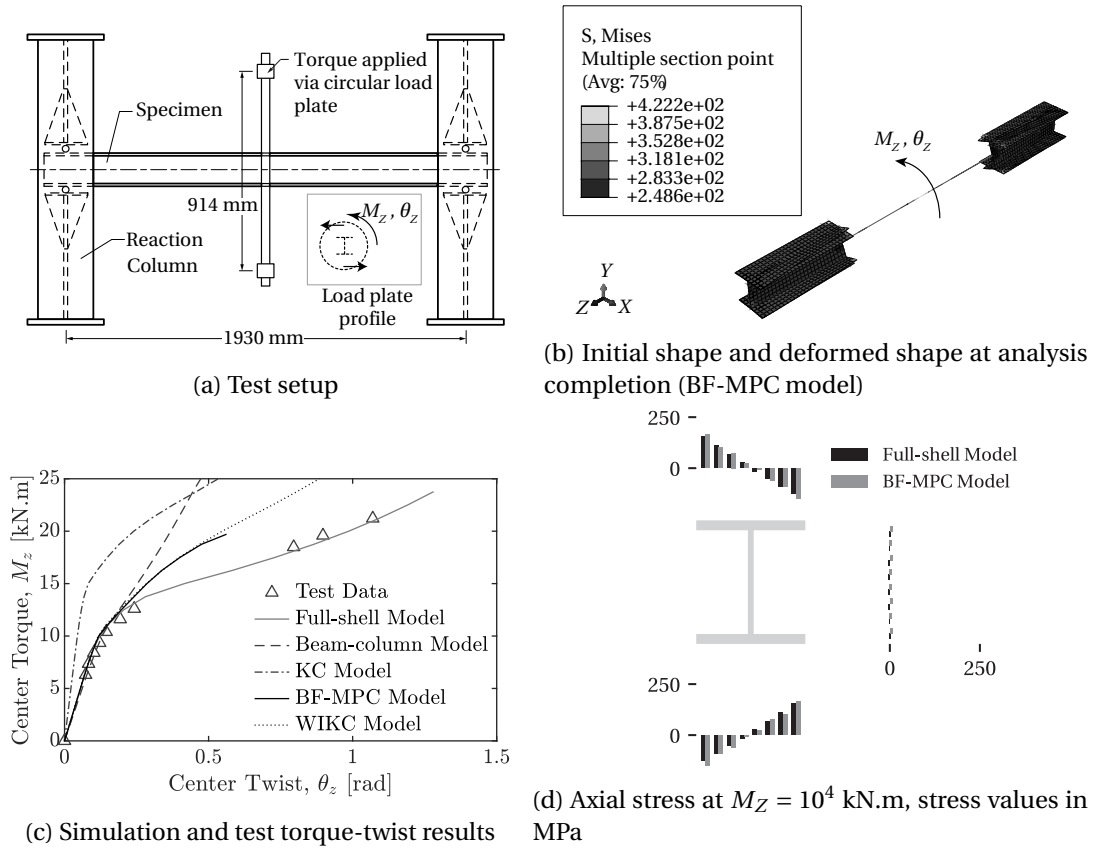


Figure 5.9 – Test setup schematic and results from the Farwell and Galambos (1969) nonuniform torsion test.

the proposed coupling to transfer torsion-warping deformations is demonstrated in Example 2. Furthermore, comparisons of the interface element shear and axial stresses in Example 1, shown in Figure 5.8, demonstrate that the proposed best-fit approach leads to a better agreement with the Full-shell model over the kinematic coupling approach in Abaqus v6.14 in this case. The use of assumed elastic stress distributions appears to be beneficial for transferring shear stresses between domains, so-long as the interface continuum elements remain elastic.

The proposed best-fit MPC utilizes seven equations regardless of the number of interface continuum nodes, whereas kinematic coupling methods require at least  $3N$  equations to couple the two domains. Reducing the number of constraint equations reduces the effort required to impose them (e.g., reduces the number of equations when a Lagrange multiplier method is used (Bathe, 1996)). The trade-off is that additional computations are performed in the best-fit MPC to solve the over-determined problem in a least squares manner and the use of an assumed stress distribution. As this chapter focuses on the formulation of the coupling method, a detailed investigation into the computational efficiency of the proposed best-fit MPC with alternative methods is considered outside the scope of this work.

The elastic stress distribution for determining the constraint coefficient matrix is considered to be a limitation of the proposed coupling method when there is yielding in the interface continuum elements. This issue is highlighted in the results of Example 2 as the BF-MPC model cannot converge many increments after the continuum elements on the interface begin to yield (see Figure 4.8). As the location of the interface is determined by the modeler, this limitation becomes significant in problems where regions of expected yielding go beyond than the location of interface. As such, the WIKC method (Hartloper et al., 2021b) may be advantageous in these cases. Furthermore, the proposed best-fit MPC coupling method may be more suitable for nonlinear elastic problems, such as those encountered in the simulation-assisted design for determining the stability of members, particularly when twist is involved (Ziemian and Abreu, 2018; Ziemian et al., 2018) or in cases where reduced order models are employed for asset evaluation that require a sufficient level of fidelity (Knezevic et al., 2019).

Overcoming the challenge of an assumed elastic interface has a few key components left for future research. First, the effective tangent modulus for each nodal area would have to be known in the computation of the constraint coefficient matrix. This value would replace the elastic modulus in, e.g., Equation 5.20, when computing the nodal forces. Second, the constraint equations, i.e., Equations 5.11–5.13, would be applied on the *increment* of deformation rather than their total value. This consideration is necessary as a result of equilibrium and the definition of the tangent modulus, and is explained as follows.

As yielding occurs under an increasing load, the modulus will reduce from its elastic value to a lower one as governed by the relevant constitutive law. Therefore, under stress gradients, this will result in a reduction of continuum nodal forces in yielded regions under increasing loading, as the nodal force is now proportional to the tangent modulus. Since  $\mathbf{A}^T$

governs the force distribution based on the *total* force applied to the beam-column node (see Equation 5.17), this results in an unloading in yielded regions on the continuum side of the interface. The issue is that yielding does not cause unloading, but rather a reduction in the *increment* in force. To address this, the constraint should be applied on the increment of deformation (and force), rather than the total deformation, as it is currently posed in Equations 5.11–5.13. An efficient formulation to impose the incremental MPC equations remains a challenge itself as classic constraint methods tend to operate on the total nodal forces and deformations (see Equation 5.17).

## 5.7 Summary and conclusions

Seven constraint equations are proposed as a part of a novel best-fit MPC for beam-to-continuum element coupling of members featuring wide flange cross sections. This formulation makes a link between beam-column element kinematics and fitting a plane-of-best-fit to a point cloud. The rotation of the best-fit plane is efficiently computed from the solution to a  $4 \times 4$  eigenvalue problem. Analysis conducted in this chapter provides the basis for a method to deduce the warping amplitude within the proposed framework. Pre-computed elastic stress distributions are used to form the constraint coefficient matrix within the context of nonlinear finite element analysis. The proposed method is implemented as a user MPC in Abaqus v6.14, and the source code is made publicly available (Hartloper, 2021). Two examples are used to validate the method for coupling beam-column and shell elements.

The main conclusions are as follows:

- The proposed method is validated for nonlinear finite element problems coupling beam-column and shell elements. Thus, the objectives set at the outset of (1) using the least number of constraint equations, and (2) including torsion-warping, are satisfied.
- The proposed method can improve the interface stress distribution under certain loading conditions over other methods (e.g., the built-in kinematic coupling method in Abaqus v6.14).
- Global Newton iterations may not converge after the elements on the interfaces begin to yield due to the assumed elastic stress distributions. While this may be a limitation in certain problems of interest, the proposed method could still be used in the context of simulation-assisted design for stability problems (Ziemian and Abreu, 2018; Ziemian et al., 2018). Further work is required to make the method amenable to inelastic interfaces.

## 5.8 Data availability

Some or all data, models, or code generated or used during the study are available in a repository or online in accordance with funder data retention policies. This includes the code for the proposed coupling method and imperfection generation Hartloper (2021). Some or all data, models, or code that support the findings of this study are available from the corresponding author upon reasonable request. This includes the finite element models used in the case studies.

## 5.9 Acknowledgements

This study is based on work supported by EPFL and by the Swiss National Science Foundation (Project No. 200021\_188476) for the first author, and an EPFL internal grant for the second author. The financial support is gratefully acknowledged. Any opinions, findings, and conclusions or recommendations expressed in this chapter are those of the authors and do not necessarily reflect the view of sponsors.

## 5.10 Notation

*The following symbols are used in this chapter:*

- $A = \sum_{k=1}^N a_k$  = cross-sectional area;
- $\mathbf{A}$  = constraint coefficient matrix;
- $a_k$  = tributary area for interface continuum node  $k$ ;
- $b_f$  = section flange width;
- $\mathbf{C} = \{\mathbf{c}_k\}_{k=1}^N$  =  $\{\mathbf{r}\mathbf{x}_k - \mathbf{r}\bar{\mathbf{x}}\}_{k=1}^N$  continuum node relative coordinates, ref. config.;
- $\mathbf{D} = \{\mathbf{d}_k\}_{k=1}^N$  =  $\{\mathbf{x}_k - \bar{\mathbf{x}}\}_{k=1}^N$  continuum node relative coordinates, def. config.;
- $d$  = total section depth;
- $\mathbf{e}_i$  = unit vectors for the global reference frame;
- $\mathbf{p}_i$  = unit load vectors acting on beam-column node DOF  $i$ ;
- $\mathbf{f}$  = constraint equations;
- $I_1, I_2, I_3$  = second moments of area (inertia), polar moment of inertia;
- $I_w$  = and warping constant;
- $\mathbf{K}^{sec}$  = cross section stiffness matrix;
- $N$  = number of interface continuum nodes;
- $\mathbf{n}_1, \mathbf{n}_2$  = vectors spanning the cross section plane;
- $Q_1(\eta), Q_2(\xi)$  = first moments of area;
- $\mathbb{Q} = [q_0, \mathbf{q}^T]$  = rotation quaternion;
- $\mathbf{R}$  = rotation matrix;
- $\mathbf{s}$  = nodal force vector;

$\mathbf{T}$	=	transformation matrix for the interface beam-column loads;
$\mathbf{t}$	=	vector normal to cross-sectional plane;
$t_f$	=	section flange thickness;
$t_w$	=	section web thickness;
$\mathbf{U}_c = \{\mathbf{u}_k\}_{k=1}^N$	=	interface continuum element nodal displacements;
$\mathbf{u}_b^*$	=	$[\mathbf{u}_b, \boldsymbol{\phi}_b, w_b]^T$ interface beam-column nodal DOFs;
$\mathbf{u}^{sec}$	=	cross-sectional deformations for axial stress;
$\mathbf{v}$	=	stress traction vector;
$w$	=	warping amplitude;
$\mathbf{X} = \{\mathbf{x}_k\}_{k=1}^N$	=	continuum node coordinates;
$\mathbf{x}_{mp,b}(\xi, \eta)$	=	material point, beam-column element;
$\bar{\mathbf{x}}$	=	centroid of continuum nodes;
$\delta(\cdot)$	=	infinitesimal quantity;
$\Gamma$	=	beam-column and continuum element interface;
$r_k$	=	residual from best-fit plane at node $k$ ;
$\xi$	=	distance along $\mathbf{n}_1$ axis;
$\boldsymbol{\theta}$	=	infinitesimal rotation vector;
$\Delta_f, \Delta_w$	=	distance between adjacent flange and web nodes, respectively;
$\boldsymbol{\tau}$	=	stress tensor;
$\bar{\boldsymbol{\tau}}$	=	stress factor;
$\eta$	=	distance along $\mathbf{n}_2$ axis;
$\psi(\xi, \eta)$	=	warping function;
$\boldsymbol{\phi}$	=	rotation vector;
$\zeta$	=	distance along the $\mathbf{n}_3$ axis;
$\Omega_1$	=	beam-column element domain;
$\Omega_2$	=	continuum element domain;
$(\cdot)_b$	=	refers to beam-column element domain;
$(\cdot)_c$	=	refers to continuum element domain;
$r(\cdot)$	=	refers to reference configuration;
$^0(\cdot)$	=	refers to initial configuration; and
$\tilde{(\cdot)}$	=	refers to best-fit quantity.

## 5.11 Algorithms

Algorithms 3 and 4 are provided to clarify the best-fit coupling method. The Abaqus user MPC subroutine that implements these algorithms is provided by the Authors at Hartloper (2021). The formulation of the  $4 \times 4$  eigenvalue problem in Algorithm 3, and the supporting procedures LEFTQUAT and RIGHTQUAT in Algorithm 4 are based on methods provided in Mostafa and

## **Chapter 5. Best-fit constraint equations for coupling mixed-dimension simulation models with wide flange cross sections**

---

Sivaselvan (2014). The supporting procedure ROTMAT in Algorithm 4 is based on a method provided in Horn (1987).



**Algorithm 3** Detailed best-fit MPC coupling method using the nodal force method.

---

```

1: inputs:
    •  ${}^0\mathbf{X}$ : The set of continuum nodes in the initial configuration, size  $3 \times N$ .
    •  $\mathbf{U}_c$ : The set of continuum nodal displacements, size  $3 \times N$ .
    •  $N$ : The number of continuum nodes.
    •  $h, b_f, t_f, t_w$ : The cross section dimensions.
2: outputs:
    •  $\mathbf{u}_b, \phi_b, w_b$ : The beam-column node DOF values.
    •  $\mathbf{A}$ : The constraint coefficient matrix for the continuum nodes, size  $7 \times 3N$ .

```

---

```

3:  ${}^0\bar{\mathbf{x}} \leftarrow \text{mean}({}^0\mathbf{X})$ 
4:  $\mathbf{C} \leftarrow \{{}^0\mathbf{x}_i - {}^0\bar{\mathbf{x}}\}_{i=1}^N$ 
5:  ${}^0\mathbf{R} \leftarrow \text{iniConfig}(\mathbf{C})$ 
6: Compute the nodal tributary areas,  $a_k$  and cross-sectional properties  $\{A, I_1, I_2, I_w\}$ 
7: Compute the nodal forces in the reference configuration
8:  $\mathbf{A}^{disp} = 1/N \mathbf{I}_{3 \times 3N}$ 
9: while  $\|\bar{\mathbf{u}}_l - \bar{\mathbf{u}}_{l-1}\| / \|\bar{\mathbf{u}}_l\| < 10^{-8}$  do           ▷ Until convergence of the centroid position
10:    $\bar{\mathbf{u}}_l \leftarrow \mathbf{0}_{1 \times 3}$ 
11:   for  $k \in [1, 2, \dots, N]$  do
12:      $\bar{\mathbf{u}}_l \leftarrow \bar{\mathbf{u}}_l + \mathbf{A}_k^{disp} \mathbf{u}_k$ 
13:   end for
14:    $\bar{\mathbf{x}} \leftarrow {}^0\bar{\mathbf{x}} + \bar{\mathbf{u}}_l$ 
15:    $\mathbf{D} \leftarrow \{\mathbf{x}_i - \bar{\mathbf{x}}\}_{i=1}^N$ 
16:    $\mathbf{B} \leftarrow \mathbf{0}_{4 \times 4}$ 
17:   for  $k \in [1, 2, \dots, N]$  do           ▷ See Mostafa and Sivaselvan (2014)
18:      $\boldsymbol{\beta} \leftarrow \text{leftQuat}[[0, D_{k,1}, D_{k,2}, D_{k,3}]] - \text{rightQuat}[[0, C_{k,1}, C_{k,2}, C_{k,3}]]$ 
19:      $\mathbf{B} \leftarrow \mathbf{B} + \boldsymbol{\beta}^T \boldsymbol{\beta}$ 
20:   end for
21:    $i \leftarrow \text{argmin eigenvalue}[\mathbf{B}]$ 
22:    $\tilde{\mathbf{q}}_1 \leftarrow \text{eigenvector}[\mathbf{B}]_i$ 
23:   Extract  $\tilde{\boldsymbol{\phi}}$  from  $\tilde{\mathbf{q}}_1$  using Equation 5.15a
24:    $\tilde{\mathbf{R}} \leftarrow \text{rotMat}[\tilde{\mathbf{q}}_1]$ 
25:   Update  $\mathbf{A}^{disp}$  using  $\tilde{\mathbf{R}}$  and the nodal forces
26: end while
27:  $\bar{\mathbf{u}} \leftarrow \bar{\mathbf{u}}_l$ 
28: Calculate  $w$  using Equation 5.13
29: Rotate the nodal forces into the current deformed configuration using Equation 5.39
30: Set the active DOF for the beam node
31: for  $k \in [1, \dots, N]$  do
32:   Set the active DOF in the shell node  $k$ 
33:   Assign the  $\mathbf{A}_k$  submatrix from the nodal forces
34: end for
35:  $\mathbf{u}_b \leftarrow \bar{\mathbf{u}}; \phi_b \leftarrow \tilde{\boldsymbol{\phi}}; w_b \leftarrow w$ 

```

---

## Chapter 5. Best-fit constraint equations for coupling mixed-dimension simulation models with wide flange cross sections

---

### Algorithm 4 Supporting procedures.

---

```

1: procedure leftQuat( $\mathbf{q}$ )
2:   inputs:
   •  $\mathbf{q}$ : A quaternion,  $\mathbf{q} = [q_0, \mathbf{q}^T]$ 
3:   outputs:
   •  $\mathbf{Q}_l$ : The left-hand matrix representation, size  $4 \times 4$ 
4:    $\mathbf{Q}_l \leftarrow \begin{bmatrix} q_0 & -\mathbf{q}^T \\ \mathbf{q} & q_0 \mathbf{I}_{3 \times 3} + \hat{\mathbf{q}} \end{bmatrix}$  ▷  $\hat{(\cdot)}$  is the skewsymmetric matrix operator
5: end procedure
6: procedure rightQuat( $\mathbf{q}$ )
7:   inputs:
   •  $\mathbf{q}$ : A quaternion,  $\mathbf{q} = [q_0, \mathbf{q}^T]$ 
8:   outputs:
   •  $\mathbf{Q}_r$ : The right-hand matrix representation, size  $4 \times 4$ 
9:    $\mathbf{Q}_r \leftarrow \begin{bmatrix} q_0 & -\mathbf{q}^T \\ \mathbf{q} & q_0 \mathbf{I}_{3 \times 3} - \hat{\mathbf{q}} \end{bmatrix}$ 
10: end procedure
11: procedure iniConfig( $\mathbf{C}$ )
12:   inputs:
   •  $\mathbf{C}$ : Relative initial position of the shell nodes, size  $3 \times N$ 
13:   outputs:
   •  ${}^0\mathbf{R}$ : The orientation of the initial configuration
14:    $\mathbf{A} \leftarrow \mathbf{C}\mathbf{C}^T$ 
15:    $\mathbf{w} \leftarrow \text{eigenvectors}[\mathbf{A}]; \mathbf{d} \leftarrow \text{eigenvalues}[\mathbf{A}]$ 
16:    ${}^r\mathbf{t} \leftarrow \mathbf{w}_i, i = \arg \min \mathbf{d}; {}^r\mathbf{n}_2 \leftarrow \mathbf{w}_j, j = \arg \max \mathbf{d}$ 
17:    ${}^r\mathbf{n}_1 \leftarrow \mathbf{d}_k$  ▷ The remaining eigenvalue
18:   if  ${}^r\mathbf{n}_1^T ({}^r\mathbf{n}_2 \times {}^r\mathbf{t}) > 0$  then ▷ Ensures a right-handed coordinate system
19:      ${}^0\mathbf{R} \leftarrow [{}^r\mathbf{n}_1, {}^r\mathbf{n}_2, {}^r\mathbf{t}]$ 
20:   else
21:      ${}^0\mathbf{R} \leftarrow [{}^r\mathbf{n}_1, {}^r\mathbf{n}_2, -{}^r\mathbf{t}]$ 
22:   end if
23: end procedure
24: procedure rotMat( $\mathbf{q}$ )
25:   inputs:
   •  $\mathbf{q}$ : A quaternion,  $\mathbf{q} = [q_0, q_1, q_2, q_3]$ 
26:   outputs:
   •  $\mathbf{R}$ : The rotation matrix representation, size  $3 \times 3$ 
27:    $\mathbf{R} \leftarrow \begin{bmatrix} 1 - 2(q_2^2 + q_3^2) & 2(q_1q_2 - q_0q_3) & 2(q_1q_3 + q_0q_2) \\ 2(q_1q_2 + q_0q_3) & 1 - 2(q_1^2 + q_3^2) & 2(q_2q_3 - q_0q_1) \\ 2(q_1q_3 - q_0q_2) & 2(q_2q_3 + q_0q_1) & 1 - 2(q_1^2 + q_2^2) \end{bmatrix}$ 
28: end procedure

```

---

## 5.12 Linearized constraint equations

The first part of this appendix presents key results for the linearized constraint equations. The second part shows a simple example that highlights the limitations of using the direct linearization of the constraint equations to define the constraint coefficient matrix.

### 5.12.1 Derivations

The linearized constraint equations are  $\delta \mathbf{u}_b^* = \mathbf{F} \delta \mathbf{U}_c$ , where the matrix of partial derivatives,  $\mathbf{F}$ , takes the form

$$\mathbf{F} = \begin{bmatrix} \mathbf{F}^{disp} \\ \mathbf{F}^{rot} \\ \mathbf{F}^{warp} \end{bmatrix} = \begin{bmatrix} \frac{\partial \mathbf{f}_{1-3}}{\partial \mathbf{U}_c} \\ \frac{\partial \mathbf{f}_{4-6}}{\partial \mathbf{U}_c} \\ \frac{\partial \mathbf{f}_7}{\partial \mathbf{U}_c} \end{bmatrix}, \quad (5.42)$$

where  $\mathbf{F}^{disp}$ ,  $\mathbf{F}^{rot}$ , and  $\mathbf{F}^{warp}$  correspond to the displacement, rotation, and warping DOFs, respectively. The matrices define  $(\mathbf{F}_{ij})_k = \left( \frac{\partial f_i}{\partial u_j} \right)_k$  for all the continuum nodes included in the MPC where  $i$  is the constraint equation corresponding to beam-column DOFs ( $i = 1, 2, \dots, 7$ ), and  $j$  are the displacement DOFs ( $j = 1, 2, 3$ ) corresponding to the particular continuum node  $k$ .

### Displacement constraints

Linearizing Equation 5.11, noting that  $\bar{\mathbf{u}} = \bar{\mathbf{x}} - {}^r \bar{\mathbf{x}}$  and  $\delta \mathbf{U}_c = \delta \mathbf{X}$ , results in

$$\delta \mathbf{f}_{1-3} = \delta \mathbf{u}_b - \left( \frac{\partial \bar{\mathbf{u}}}{\partial \mathbf{U}_c} \right) \delta \mathbf{U}_c \quad (5.43)$$

$$= \delta \mathbf{u}_b - \left( \frac{\partial \bar{\mathbf{x}}}{\partial \mathbf{X}} - \frac{\partial {}^r \bar{\mathbf{x}}}{\partial \mathbf{X}} \right) \delta \mathbf{U}_c = \delta \mathbf{u}_b - \left( \frac{\partial \bar{\mathbf{x}}}{\partial \mathbf{X}} - \mathbf{0} \right) \delta \mathbf{U}_c \quad (5.44)$$

$$= \delta \mathbf{u}_b - 1/N \text{stack} [\mathbf{I}_3]^T \delta \mathbf{U}_c, \quad (5.45)$$

where  $N$  is the number of shell nodes,  $\text{stack} [\mathbf{I}_3]^T$  is a  $3 \times 3N$  matrix of the repeated identity matrix,  $\mathbf{X} = [\mathbf{x}_1^T, \mathbf{x}_2^T, \dots, \mathbf{x}_N^T]^T$  is a  $3N \times 1$  vector of the location of the shell nodes in the deformed configuration,  $\mathbf{U}_c$  is the vector of displacements defined similarly to  $\mathbf{X}$ , and  $\delta(\cdot)$  denotes infinitesimal quantities. Therefore,  $\mathbf{F}^{disp} = 1/N \text{stack} [\mathbf{I}_3]^T$ .

### Rotation constraints

From Equation 5.12, with the notation  $\tilde{\boldsymbol{\phi}} = \boldsymbol{\phi} [\tilde{\mathbf{q}}]$  we have

$$\boldsymbol{\phi}_b = \tilde{\boldsymbol{\phi}}. \quad (5.46)$$

## Chapter 5. Best-fit constraint equations for coupling mixed-dimension simulation models with wide flange cross sections

---

Linearizing this constraint (see e.g., Dassault Systèmes (2014)),

$$\delta \boldsymbol{\theta}_b = \delta \tilde{\boldsymbol{\theta}} \Rightarrow \delta \boldsymbol{\theta}_b - \delta \tilde{\boldsymbol{\theta}} = \mathbf{0}, \quad (5.47)$$

where  $\theta$  is an infinitesimal rotation. The rotation quantities in Equation 5.47 are rotation vectors, however, the best-fit procedure operates on quaternions. For small angles of rotation, the linearization of the rotation constraint is greatly simplified because the difference between the two angle representations is only a scalar factor of two Hughes (2004):

$$\delta \tilde{\boldsymbol{\theta}} = 2 \operatorname{Im} [\delta \tilde{\mathbf{q}}], \quad (5.48)$$

i.e., the small-angle rotation vector is the imaginary part of the linearized eigenvector. With this consideration, the main effort of the direct linearization of the rotation constraint equations is to relate the linearized eigenvector to the infinitesimal continuum node displacements.

The procedure used herein is based on Mostafa and Sivaselvan (2014), for brevity only the final result is stated here:

$$\delta \mathbf{f}_{4-6} = \delta \tilde{\boldsymbol{\theta}} - \mathbf{F}^{rot} \delta \mathbf{U}_c = \mathbf{0}, \quad (5.49)$$

where

$$\mathbf{F}^{rot} = \operatorname{Im} [[[\tilde{\mathbf{q}}]]_R] \mathbf{G}(\mathcal{D}) (\mathbf{I}_{3N} - \mathbf{P}_T), \quad (5.50)$$

where  $\operatorname{Im} [[[\tilde{\mathbf{q}}]]_R]$  is imaginary part of the right-hand matrix representation of quaternion  $\tilde{\mathbf{q}}$  (i.e.,  $\text{RIGHTQUAT}[\tilde{\mathbf{q}}]$  in Section 5.11),  $\mathbf{G}(\mathcal{D})$  represents the instantaneous rotation of the motion  $\delta \mathcal{D}$  computed using (27) in Mostafa and Sivaselvan (2014), and the matrix of the position of the shell nodes relative to their centroid in the deformed configuration is defined as  $\mathcal{D}$ ,

$$\mathcal{D} = \mathbf{X} - \text{stack} [\bar{\mathbf{x}}] \quad (5.51)$$

$$= (\mathbf{I}_{3N} - \mathbf{P}_T) \mathbf{X}, \quad (5.52)$$

$\mathcal{D}$  is a  $3N \times 1$  vector,  $\mathbf{I}_{3N}$  is the  $3N \times 3N$  identity matrix, and  $\mathbf{P}_T = 1/N$  tile  $[\mathbf{I}_3]$  tile is a  $3N \times 3N$  matrix of repeated  $3 \times 3$  identity matrix multiplied by  $1/N$ .

### Warping Constraint

Restating the warping constraint equation,

$$f_7(w_b, \mathbf{X}) = w_b - \frac{1}{N_\psi} \sum_{k \in \mathbf{k}_\psi} \frac{1}{\psi_k} \mathbf{t} \cdot (\mathbf{x}_k - \tilde{\mathbf{R}}(\mathbf{x}_k + \bar{\mathbf{u}})) = 0, \quad (5.53)$$

Now linearizing this constraint,

$$\begin{aligned}\delta f_7 &= \frac{\partial f_7}{\partial w} \delta w + \frac{\partial f_7}{\partial \mathbf{X}} \delta \mathbf{X} = 0 \\ &= \delta w - \mathbf{F}^{warp} \delta \mathbf{U}_c = 0,\end{aligned}\tag{5.54}$$

where  $\mathbf{F}^{warp}$  is the matrix of coefficients of  $\delta \mathbf{X}$  in Equation 5.54. This matrix represents the instantaneous change in the warping amplitude given a change in the nodal displacement. The final result is

$$\mathbf{F}^{warp} = \frac{1}{N_\psi} \sum_{k \in \mathbf{k}_\psi} \left( \frac{1}{\psi_k} \mathbf{r}^T \frac{\partial \tilde{\mathbf{R}}^T}{\partial \mathbf{X}} \mathbf{x}_k + \frac{1}{\psi_k} \mathbf{r}^T \tilde{\mathbf{R}}^T \frac{\partial \mathbf{x}_k}{\partial \mathbf{X}} \right), \tag{5.55}$$

where  $\frac{\partial \tilde{\mathbf{R}}^T}{\partial \mathbf{X}}$  is the linearized rotation matrix.

### 5.12.2 Example

The same cantilever model geometry, boundary conditions, and mesh as described in Example 1 (Section 5.5.1) is used. However, in this case, only an axial displacement is applied to the free end of  $\delta_Z = -100$  mm (uniform uniaxial tension). A new macro model is considered where  $\mathbf{A}$  is defined using the linearized constraint equations, i.e.,  $\mathbf{A}^{disp} = \mathbf{F}^{disp}$ ,  $\mathbf{A}^{rot} = \mathbf{F}^{rot}$ ,  $\mathbf{A}^{warp} = \mathbf{F}^{warp}$ , rather than through the nodal force method. This model is named “BF-MPC Model (Lin. Eq.)”.

The average interface shell element axial stress results are shown in Figure 5.10, and compared with the results from the Full-shell model. Notice that the stress is not uniform in the BF-MPC Model (Lin. Eq.) since a uniform load is applied to each node due to the  $1/N$  factor in  $\mathbf{F}^{disp}$  (see Equation 5.45). However, the flange tip nodes, for example, should receive half the load as the interior flange nodes because they represent half the area. Therefore, an area weighting is required for loads applied in DOF 3, as is done through the nodal force method. This problem is most severe when shear loading is applied, as in reality, the flange only receives around 5 % of the total shear force under strong axis load (see the stress distribution  $\tau_{32}$  in Figure 5.6).

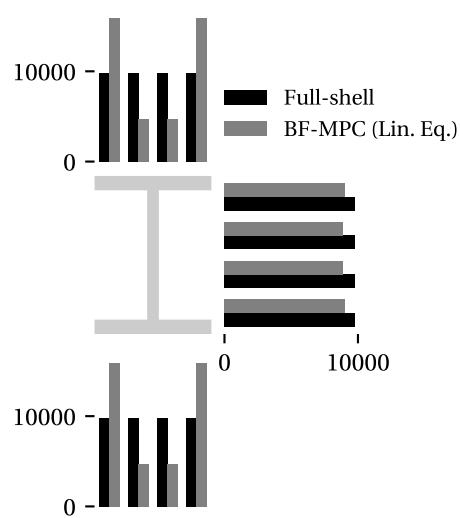


Figure 5.10 – Average axial stress in the interface elements under uniaxial tension when the direct linearization is used in the MPC formulation, values in MPa.

## 6 Mixed-dimension modeling of steel wide flange beam-columns under multiaxis loading

**Authors:** Alexander R. Hartloper, Albano de Castro e Sousa, Dimitrios G. Lignos

**Preprint version of:** Hartloper, A. R., de Castro e Sousa, A., and Lignos, D. G. "Mixed-dimension modeling of steel wide flange beam-columns under multiaxis loading." *Journal of Construction Steel Research*, (In preparation).

**Doctoral candidate's contributions:** Literature review, problem definition, development of methodology for determining model parameters, processing of test data, execution of methodology, evaluation and interpretation of results. Writing and editing of the manuscript. The co-authors supervised the work carried-out by the doctoral candidate and assisted with the editing of the manuscript.

**Abstract:** Continuum finite element (CFE) models with a reduced computational cost that can explicitly simulate material inelasticity and coupled geometric instabilities under multiaxis loading are essential for a number of applications in earthquake and structural engineering. This chapter proposes recommendations for mixed-dimension component macro models as a method to reduce the computational burden of full CFE models for structural wide flange beam-columns. These guidelines are built on objective error metrics and recent advances in material modeling for structural steels. The value of detailed physical material and component information is highlighted throughout this study; we suggest that such data be collected in future testing programs to further improve the state-of-the-art in component simulations. New detailed modeling recommendations (e.g., finite element sizes and imperfection amplitudes) are made to better model the initiation and progression of local buckling for cyclic and monotonic loading, compared to existing approaches. Shell element models are also found to have equivalent accuracy to solid element models for the range of beam-columns investigated. Simulations show that there is an average of 3 % difference in moment-rotation between the full CFE and macro model simulations, while the number of degrees-of-freedom and memory requirements are reduced by about 50 %. Through these recommendations, a validated macro model approach is presented for steel wide flange beam-columns that increases the computational efficiency while retaining the solution fidelity of full CFE models.

**Keywords:** Reduced-order models; Finite element analysis; Coupling; Geometric instabilities; Calibration; Multiaxial plasticity.

## **6.1 Introduction**

### **6.1.1 Background**

Research conducted over the past decade has lead to a solid understanding of steel wide flange beam-column behavior under axial loading coupled with multiaxis lateral loading. A state-of-the-art review on the behavior of these components can be found in Lignos et al. (2019). Important features of note are that flexural strength degradation typically initiates through inelastic flange/web local buckling at the member ends, and later may couple with member twisting and lateral-torsional buckling (LTB). Axial shortening is a consequence of this process that could potentially impact economic loss estimations in steel frame structures in the aftermath of earthquakes (Elkady et al., 2020). Therefore, simulation models that can represent material nonlinearity combined with coupled buckling modes are imperative for modeling steel frame structures subjected to earthquake loading.

Conventional concentrated plasticity (Sivaselvan and Reinhorn, 2000; Ibarra et al., 2005; Lignos and Krawinkler, 2011; Lignos et al., 2019) or fiber-based (Spacone et al., 1996; Le Corvec, 2012; Di Re et al., 2016; Sideris and Salehi, 2016) models have been preferred in the past for nonlinear structural analysis owing to their simplicity and computational efficiency. These approaches come with a number of limitations for modeling steel beam-column components as discussed in Hartloper et al. (2021b). Alternatively, a continuum finite element (CFE) approach using shell or solid elements can be used to overcome these limitations. For example, CFE models can be used for performance-based seismic evaluation and design (Krawinkler et al., 2006), to investigate new structural design concepts, and to research the behavior of critical components within structures (NIST, 2011). The cost in CFE component models is related to the computational expense, in terms of model degrees-of-freedom and computer memory, compared to conventional component modeling methods.

Computational efficiency is desired because multiple analyses need to be run for each structure to obtain statistical information regarding a structure's performance (Vamvatsikos and Cornell, 2002), and to account for the effect of record-to-record uncertainty (Eads et al., 2013). Thus, there is a need to keep the fidelity of CFE approaches, if possible, but at the same time reduce their computational expense. Recently, a mixed-dimension component macro model approach has been advocated by Hartloper et al. (2021b) that mixes beam-column elements with continuum finite elements in critical regions of the component. In this manner, the cost of a purely CFE approach is reduced, while its solution fidelity is retained.

Herein, mixed-dimension component macro models are defined as finite element models that combine elements of varying dimensionality. Dimensionality is measured by the representation of the element: 1D elements are lines (e.g., beam-column elements), 2D elements are surfaces (e.g., shell elements), and 3D elements are volumes (e.g., solid elements). This



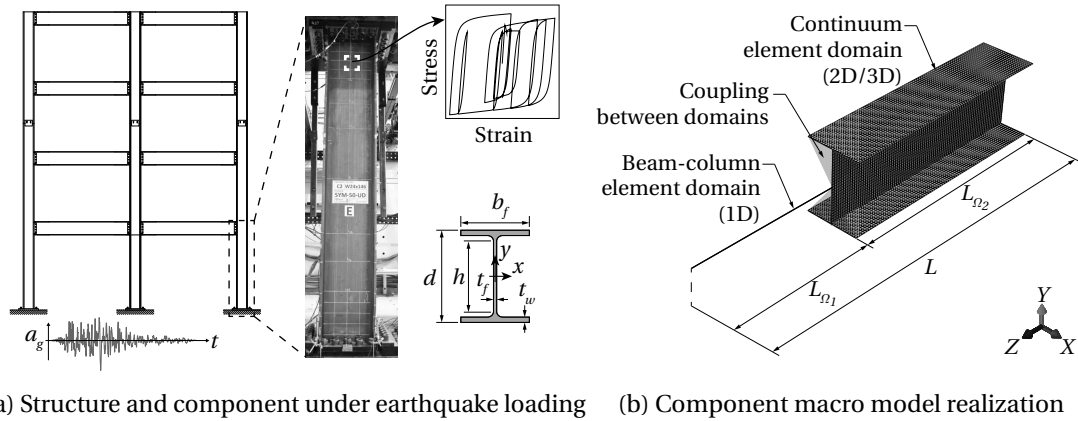


Figure 6.1 – Component macro model representation for beam-columns with wide flange sections subjected to multiaxis cyclic loading. Photo in 6.1a from Elkady and Lignos (2018a).

component modeling approach is shown schematically in Figure 6.1 where 1D beam-column elements are combined with 2D shell or 3D solid elements. The macro model is therefore established by: (a) parameters that define the finite element model within the continuum and beam-column domains (e.g., material model, element type, element size, etc.), (b) the selection of the continuum length,  $L_{\Omega_2}$ , and (c) the method of coupling between the different domains.

Specification of the coupling between domains above was addressed through the warping-inclusive kinematic coupling (WIKC) method (Hartloper et al., 2021b). This work demonstrated the importance of including torsion-warping in the coupling formulation for members with wide flange cross sections. However, further research is required to generalize the macro model approach. The necessary tasks in this regard are to specifically define the modeling guidelines, and to specify the *a priori* division of the component into continuum and beam-column domains. For this purpose, a review of existing guidelines for the CFE modeling of wide flange beam-column components is provided herein to identify potential gaps in the current state-of-the-art.

### 6.1.2 Review of existing modeling recommendations for steel wide flange beam-columns subjected to multiaxis cyclic loading

Recommendations for the continuum finite element modeling of wide flange steel beam-columns are based on a non-exhaustive list from different sources (Newell and Uang, 2008; Gantes and Fragkopoulos, 2010; Elkady and Lignos, 2015a; Fogarty and El-Tawil, 2015; Araújo et al., 2017; Elkady and Lignos, 2018b; Wu et al., 2018; Ziemian et al., 2018; Hartloper et al., 2021b). All of the noted CFE modeling approaches share a few common characteristics: linear shell elements are employed, a nonlinear isotropic/kinematic hardening material model

is utilized, and a combination of local and/or global imperfections may be used to induce geometric instabilities. Aspects from these guidelines will be used as a starting point for the recommendations developed in this study. A variety of member tests have been used in the evaluation and calibration of these guidelines, however, several key experiments on beam-column components have been conducted since their development (Suzuki and Lignos, 2021; Ozkula et al., 2017; Elkady and Lignos, 2018a; Cravero et al., 2020). The above experiments constitute a great source of information to better assess modeling recommendations under a variety of loading and geometric conditions.

### **6.1.3 Modeling structural steels subjected to inelastic cyclic straining**

Strain demands, idealized in Figure 6.1, are expected to be erratic in steel beam-column components subjected to earthquake loads. Defining constitutive model parameters given the uncertainty in earthquake events is, therefore, a primary issue within this context. Notably, the selected constitutive model and its parameters should be reliable for the expected ranges of inelastic stress-strain demands present in beam-column components. Methods for calibrating material models in this context (Cooke and Kanvinde, 2015; de Castro e Sousa et al., 2020) have contributed to the body of knowledge regarding constitutive modeling of structural steels for earthquake-induced inelastic strain demands. The impact of the discontinuous yielding phenomenon (Hall, 1970; Lubliner, 2008) on component behavior is also better understood (Hartloper et al., 2021a). Additionally, methods were recently developed to calibrate material model parameters for cyclic loading with limited information regarding the material response (de Castro e Sousa et al., 2021). These advances in material modeling techniques can be utilized to enhance the aforementioned component modeling guidelines.

### **6.1.4 Objectives**

Computationally efficient methods for modeling steel beam-columns subjected to multiaxis cyclic loading that can represent material inelasticity and coupled geometric instabilities are required for earthquake and general structural engineering applications. Hartloper et al. (2021b) proposed a framework for component macro models of beam-column components based on a few individual tests. General macro modeling recommendations utilizing this framework can now be developed using data from a range of steel beam-column components.

The aim of this chapter is to provide systematic guidelines that satisfy this need for steel wide flange beam-columns under multiaxis loading. Further motivation for this study is provided by recent advances in material modeling and calibration for structural steels, as well as the increased availability of tests that can be used to evaluate these guidelines. With regards to this aim, three main objectives have been identified:

1. provide recommendations for full-continuum modeling of wide flange beam-columns

- considering a larger pool of tests and updated material modeling techniques;
2. provide macro modeling guidelines to match the fidelity of the full-continuum models; and
  3. assess the computational savings for beam-column components using the macro model approach.

Novel aspects of this study are the development of modeling guidelines on the basis of quantifiable metrics, and the proposal of generalized macro model guidelines for steel members subjected to axial loading coupled with lateral drift demands. This research is expected to be valuable to both researchers and practicing engineers for developing CFE models of steel frame buildings at a reduced computational expense.

The chapter is organized as follows. First, the methodology used to complete each of these objectives is provided. Second, results from the finite element simulations are presented and the modeling guidelines are established in support of the main aim. Third, notable outcomes and limitations of the study are discussed. Finally, a summary of the findings is provided along with the primary conclusions.

## 6.2 Methodology

### 6.2.1 Approach

The scope of work conducted in this chapter is summarized in a box depicted in Figure 6.2. Modeling guidelines require definitions for each of the parameters provided in the box. The four labeled parameters will be defined in this study, while the remaining ones have been established in prior work. Continuum finite element model parameters are calibrated to test data to establish a benchmark. Afterwards, the macro model parameters are calibrated to the simulated CFE model response. This methodology is proposed to achieve the overall aim that macro models match the fidelity of full CFE (i.e., full-solid or full-shell) models.

Objective error metrics based on a component's moment-rotation response and axial shortening are used to assist the determination of the modeling parameters. Moment-rotation and axial shortening are considered to be important measures of beam-column component behavior because frame stability is largely dependent on the axial and flexural strength of its members. Therefore, three error metrics are proposed that measure these quantities: (i) an energy metric ( $\epsilon_e$ ), (ii) a peak-strength metric ( $\epsilon_s$ ), and (iii) an axial shortening metric ( $\epsilon_a$ ); these are represented in Figure 6.3. The energy metric measures the overall closeness between two sets of moment-rotation data. The peak strength metric indicates how accurately the finite element model can predict the initiation of flexural strength deterioration. The axial shortening metric indicates how well the model simulates the evolution of axial shortening of the component throughout the imposed loading history.

## Chapter 6. Mixed-dimension modeling of steel wide flange beam-columns under multiaxis loading

COMPONENT MACRO MODEL GUIDELINES	
COMPONENT CONTINUUM MODEL GUIDELINES	
• Geometry, loads, B.Cs.	-Defined by problem
• Residual stresses	-Young (1972)
• Material modeling	-Hartloper et al. (2021a), de Castro e Sousa et al. (2021)
• Continuum element discretization	1. Determined in this study
• Initial imperfections	2. Determined in this study
• Coupling method	-Hartloper et al. (2021b)
• Beam-column element discretization	3. Determined in this study
• Extent of continuum domain(s)	4. Determined in this study

Figure 6.2 – Organization of the steel wide flange column modeling guidelines proposed in this study.

The energy error metric is computed as the normalized, squared accumulated energy bounded between the two results:

$$\epsilon_e(\boldsymbol{\theta}^*, \mathbf{M}_1, \mathbf{M}_2) = \sqrt{\frac{1}{E_1} \int (\mathbf{M}_2 - \mathbf{M}_1)^2 d\boldsymbol{\theta}^*}, \quad (6.1)$$

where  $\mathbf{M}_1$  and  $\mathbf{M}_2$  are the total base moment reaction histories from two cases being compared,  $\theta$  is the chord rotation,  $\boldsymbol{\theta}^*$  is the absolute accumulated chord rotation history, and  $E_1 = \int \mathbf{M}_1^2 d\boldsymbol{\theta}^*$  is the total squared-energy of the “reference/benchmark” case. For this and other metrics, the  $(\cdot)_1$  subscript denote the “reference/benchmark” values, and the  $(\cdot)_2$  subscript denote the “compared” values. No distinction is made between  $\boldsymbol{\theta}_1^*$  and  $\boldsymbol{\theta}_2^*$  since all data are evaluated at the same deformation increments. This metric is computed up to and including the first excursion with  $|\theta| < 0.11$  rad to avoid uncertainty in test data that may arise due to experimental control at large deformations. The error in peak flexural strength is

$$\epsilon_s(\mathbf{M}_1, \mathbf{M}_2) = \frac{|\max \mathbf{M}_2 - \max \mathbf{M}_1| + |\min \mathbf{M}_2 - \min \mathbf{M}_1|}{|\max \mathbf{M}_1 - \min \mathbf{M}_1|}. \quad (6.2)$$

The error in axial shortening is

$$\epsilon_a(\boldsymbol{\delta}_{axial,1}, \boldsymbol{\delta}_{axial,2}) = \frac{\|\boldsymbol{\delta}_{axial,2} - \boldsymbol{\delta}_{axial,1}\|}{\|\boldsymbol{\delta}_{axial,1}\|}, \quad (6.3)$$

where  $\boldsymbol{\delta}_{axial,(.)}$  is the axial shortening history of the considered case. Axial shortening is computed as the extension in the chord:  $\boldsymbol{\delta}_{axial,(.)} = \sqrt{\boldsymbol{\delta}_{x,(.)}^2 + \boldsymbol{\delta}_{y,(.)}^2 + (L + \boldsymbol{\delta}_{z,(.)})^2} - L$ . Similar to  $\epsilon_e$ , this metric is truncated at the first excursion with chord rotation past 11 %rad.

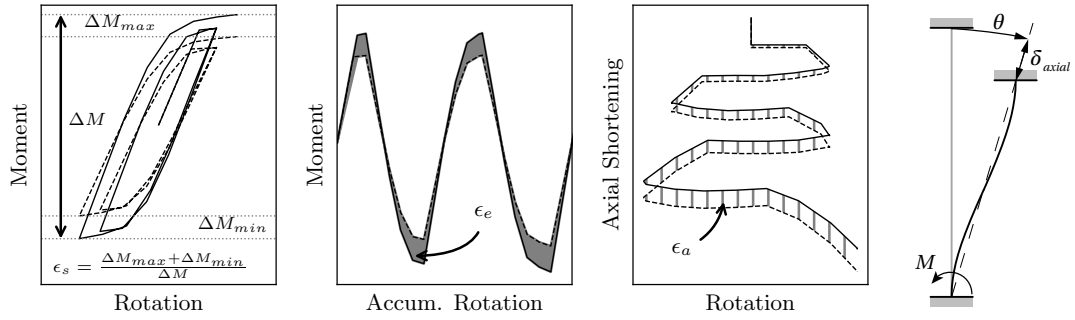


Figure 6.3 – Schematic representation of the error metrics for: peak-strength ( $\epsilon_s$ ), energy ( $\epsilon_e$ ), and axial shortening ( $\epsilon_a$ ).

### 6.2.2 Description of test data

Experimental data is required to calibrate and validate the accuracy of full-continuum modeling guidelines. Test data is taken from Suzuki and Lignos (2021), Elkady and Lignos (2018a), and Cravero et al. (2020). These tests were extracted from a larger set of data collected by Elkady et al. (2018); Lignos et al. (2019) as detailed information regarding the measured member dimensions, boundary conditions, chord rotations, base moments, and axial shortening are available. Data that are not known in all cases consist of the initial geometric imperfections and residual stresses due to hot rolling and fabrication process of the test specimens. Material data for most of these tests largely consist of only standard tensile coupon tests (ASTM, 2016b), however, detailed material information exists for a few specimens; this matter will be discussed in detail below. In total, the database consists of 34 tests on wide flange columns as summarized in Table 6.1.

All selected tests are fixed at the column base, but have differing top boundary conditions (Top B.C.). Specimens from Suzuki and Lignos (2021) and Cravero et al. (2020) were tested in a cantilever configuration (Free), whereas specimens from Elkady and Lignos (2018a) were tested with either a fixed top boundary (Fix), or a rotational boundary (Rot) that simulates the flexible conditions of a first-story steel MRF column (target inflection point at  $3/4L$ ). Three types of lateral load protocols were considered: monotonic (Mon.), symmetric-cyclic (Sym.), and collapse-consistent (C-C); the definitions of each can be found in the cited literature. The majority of tests were conducted with unidirectional lateral loading (Uni.), and three with bidirectional loading (Bi.). Most specimens were tested with constant axial load (Con.), but variable axial loading (Var.) was also present to characterize the behavior of end columns in steel MRFs exhibiting dynamic overturning effects.

The non-dimensional slenderness for lateral-torsional buckling in Table 6.1 is computed

## Chapter 6. Mixed-dimension modeling of steel wide flange beam-columns under multiaxis loading

---

according to Eurocode 3 Part 1-1 (CEN, 2005b) as:

$$\bar{\lambda}_{LT} = \sqrt{Z_x f_{ym} / M_{cr}}, \quad (6.4)$$

where  $Z_x$  is the plastic section modulus for the strong axis,  $f_{ym}$  is the measured yield stress; and

$$M_{cr} = C_1 \pi^2 E I_y / (k_y L)^2 \sqrt{(k_y / k_w)^2 I_w / I_y + (k_y L)^2 G I_t / (\pi^2 E I_y)}, \quad (6.5)$$

where  $G$  is the shear modulus,  $I_y$  is the weak-axis moment of inertia,  $I_w$  is the warping constant,  $I_t$  is the torsional moment of inertia, the reduced length factors are  $k_y = 0.5$ , and  $k_w = 1.0$ . The value of  $C_1$  accounting for the moment distribution throughout the component is taken from Bureau (2008) depending on the top boundary condition (i.e., 2.55 if fixed, 2.57 if rotational, 1.77 if free). The column  $P/P_{ym}$  is the ratio of the compressive axial load to the measured axial yield strength, values with  $0.xx \pm 0.yy$  have a constant load ratio of  $0.xx$  and a transient component of  $0.yy$ . The following range of slenderness and axial load parameters are considered:  $0.19 \leq \bar{\lambda}_{LT} \leq 0.38$ ,  $5.9 \leq b_f / 2t_f \leq 8.1$ ,  $20 \leq h / t_w \leq 44$ , and constant compressive component  $0.15 \leq P / P_{ym} \leq 0.75$ . Definitions of the cross-sectional parameters are set in Figure 6.1. The cantilever specimens have a naturally smaller length (and  $\bar{\lambda}_{LT}$ ) than those with fixed or rotational top B.C. as they represent only the lower portion of the column from the inflection point to the fixed base. Everything considered, the assembled dataset considers a reasonably wide range of cross sections and axial loads, in addition to different lateral load protocols and boundary conditions.

### 6.2.3 Nonlinear finite element modeling guidelines

Procedures for defining the modeling guidelines, summarized in Figure 6.2, are now provided in detail. Afterwards, the results from the applied methodology will be presented. For clarity, all simulations in this study are conducted using implicit static analysis with double-precision in Abaqus v6.14 (Dassault Systèmes, 2014). The nonlinear equilibrium equations are solved using the full-Newton method, nonlinear geometric transformations are considered (NLGEOM=ON), and the Abaqus default convergence criteria is always used.

#### Geometry, loads, boundary conditions, and residual stresses

Finite element models are constructed to represent each specific test. Values for the length and cross-sectional dimensions are always specified as the measured values for all the specimens in the dataset. Column boundary conditions and loading are applied as shown in Figure 6.4. In all cases, all DOFs are restrained at the column base. The torsional and weak-axis rotations are restrained at the top ( $\theta_Y = 0$ ,  $\theta_Z = 0$ ); warping is also restrained at the top. With reference to Figure 6.4, the “Free” condition corresponds to  $\theta_X$  unrestrained, the fixed condition corre-

Table 6.1 – Wide flange column test database used in this study. Top B.C.: Free = cantilever configuration, Fix = fixed, Rot = rotational B.C.. Mon. = Monotonic, Sym. = Symmetric cyclic, C-C = Collapse-consistent; Dir. = Lateral loading direction: Uni. = Unidirectional, Bi. = Bidirectional.  $\bar{\lambda}_{LT}$  from Equation 6.4.

Investigator	Name	Cross Section	Top B.C.	Lateral	Dir.	$\bar{\lambda}_{LT}$	$h/t_w$	$b_f/2t_f$	$P/P_{ym}$
Suzuki and Lignos (2021)	W-6-34-M-C	W14X53	Free	Mon.	Uni.	0.25	28.13	6.24	0.30
	W-6-34-S-C	W14X53	Free	Sym.	Uni.	0.25	28.57	6.28	0.30
	W-6-34-C1-C	W14X53	Free	C-C	Uni.	0.25	27.30	6.27	0.30
	W-6-34-C1-V	W14X53	Free	C-C	Uni.	0.25	27.69	6.28	0.15±0.35
	W-6-34-C2-C	W14X53	Free	C-C	Uni.	0.25	28.01	6.26	0.30
	W-6-34-C2-V	W14X53	Free	C-C	Uni.	0.25	27.69	6.22	0.15±0.35
	W-8-34-S-C	W14X61	Free	Sym.	Uni.	0.20	29.72	8.10	0.31
	W-8-34-C1-C	W14X61	Free	C-C	Uni.	0.20	29.53	8.14	0.31
	W-8-34-C1-V	W14X61	Free	C-C	Uni.	0.20	28.74	8.02	0.15±0.35
	W-6-25-S-C	W14X82	Free	Sym.	Uni.	0.19	20.84	5.98	0.31
	W-6-25-C1-C	W14X82	Free	C-C	Uni.	0.19	19.53	5.98	0.30
	W-6-25-C1-V	W14X82	Free	C-C	Uni.	0.19	20.43	5.93	0.15±0.35
Elkady and Lignos (2018a)	C1	W24X146	Fix	Sym.	Uni.	0.28	30.54	6.08	0.20
	C2	W24X146	Fix	Sym.	Uni.	0.28	30.37	6.10	0.50
	C3	W24X146	Rot	Sym.	Uni.	0.28	30.72	6.12	0.20
	C4	W24X146	Rot	C-C	Uni.	0.28	30.54	6.08	0.20
	C5	W24X146	Rot	C-C	Uni.	0.27	29.85	6.00	0.20
	C6	W24X146	Rot	Sym.	Bi.	0.27	29.57	5.93	0.21
	C7	W24X84	Rot	Sym.	Uni.	0.38	43.05	6.06	0.20
	C8	W24X84	Rot	C-C	Uni.	0.38	43.05	6.06	0.20
	C9	W24X84	Rot	Sym.	Bi.	0.38	43.68	6.06	0.20
	C10	W24X84	Rot	C-C	Bi.	0.38	43.40	6.06	0.20
Cravero et al. (2020)	W-8-34-M-C-30	W14X61	Free	Mon.	Uni.	0.19	27.04	7.83	0.30
	W-8-34-M-C-50	W14X61	Free	Mon.	Uni.	0.19	27.81	7.91	0.50
	W-8-34-C1-C-50	W14X61	Free	C-C	Uni.	0.19	26.17	7.76	0.50
	W-8-34-S-V-30	W14X61	Free	Sym.	Uni.	0.19	27.48	7.94	0.30±0.45
	W-6-25-M-C-30	W14X82	Free	Mon.	Uni.	0.19	21.21	5.91	0.30
	W-6-25-M-C-50	W14X82	Free	Mon.	Uni.	0.19	21.41	5.92	0.50
	W-6-25-S-C-50	W14X82	Free	Sym.	Uni.	0.19	20.61	5.92	0.50
	W-6-25-S-C-75	W14X82	Free	Sym.	Uni.	0.19	22.06	5.93	0.75
	W-6-27-M-C-30	W16X89	Free	Mon.	Uni.	0.19	26.50	5.94	0.30
	W-6-27-M-C-50	W16X89	Free	Mon.	Uni.	0.19	24.35	5.98	0.50
	W-6-27-S-C-50	W16X89	Free	Sym.	Uni.	0.19	26.50	5.99	0.50
	W-6-27-S-V-50	W16X89	Free	Sym.	Uni.	0.19	25.92	5.90	0.50±0.25

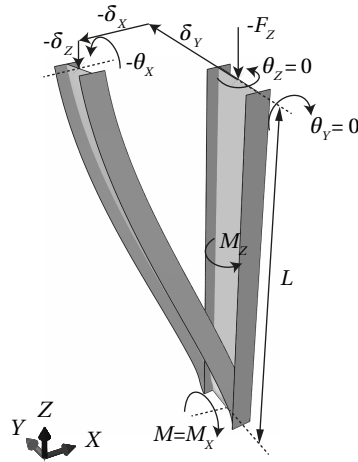


Figure 6.4 – Column boundary conditions, applied loading, and base reaction moment.

sponds to  $\theta_x = 0$ , and the rotational condition corresponds to a specified value of  $\theta_x$  at each point in the loading history. For unidirectional lateral loading  $\delta_x = 0$ , and for bidirectional loading the values of  $\delta_x$  are specified.

As the actual residual stresses are unknown, residual stresses are applied to the models based on the Young (1972) distribution as this was found to be the best match for other rolled members (de Castro e Sousa and Lignos, 2017). Residual stresses are implemented into the finite element models by specifying an initial stress in the elements. For beam-column elements, the uniaxial material model, UVCuni axial, from Hartloper et al. (2021a) was modified in this study to include an initial stress based on the Young (1972) distribution. The use of this modified material model addresses the limitation in Hartloper et al. (2021b) that the residual stress definition should be consistent between the beam-column and continuum domains in macro models. The source code for the modified uniaxial material model is made available online (Hartloper, 2019).

### Material modeling

Two different material models are used in this study. The first model is the classic Voce-Chaboche (VC) model after Voce (1948); Armstrong and Frederick (1966); Chaboche et al. (1979), and the second model is an updated Voce-Chaboche (UVC) model proposed in Hartloper et al. (2021a). In brief, these models have a von Mises yield condition and combine nonlinear isotropic and kinematic hardening rules to represent the material behavior under inelastic cyclic straining; implementation details can be found in the cited literature. An additional term in the UVC model, along with parameter constraints, is intended to simulate the effects of discontinuous yielding in structural steels. The primary benefit of the UVC model over the VC model is that it provides a better estimate of the material's initial yield



stress, with equivalent accuracy in subsequent inelastic loading cycles. A prior study by the authors suggests that even a minor improvement in estimating the material behavior may have a fairly significant impact on the simulated inelastic response (Hartloper et al., 2021a). Therefore, it is desirable to use the UVC model, provided that there is sufficient data to reliably estimate the corresponding material model parameters.

A defining feature of the finite element analyses conducted in this study is that material parameters are fully determined directly from material tests that correspond to the actual column test under consideration. Obtaining model parameters directly from the corresponding material diminishes the uncertainty in the model regarding the material behavior. The reduced uncertainty in the material behavior is considered essential in determining unknown parameters in the modeling guidelines with a greater confidence. The use of accurate material information distinguishes the proposed guidelines from those in prior studies.

Material data for beam-columns in the dataset is divided into two categories: specimens where only uniaxial tension tests are available (31 specimens), and specimens where additional uniaxial cyclic tests have also been conducted (3 specimens). The uniaxial cyclic material tests correspond to those described in de Castro e Sousa et al. (2020) and Hartloper et al. (2021a). This material information allows for a high-quality calibration of the constitutive model for cyclic and monotonic loading. The three specimens with this known data are the W14X82 columns (W-6-25-S-C, W-6-25-C1-C, and W-6-25-C1-V) tested by Suzuki and Lignos (2021). Three different approaches are taken for determining the material parameters depending on the available material data and applied lateral loading:

- For columns with cyclic material data (3 tests, “full information”): the parameters correspond directly to the “A992 Gr. 50 W14X82 flange/web” dataset reported in Hartloper et al. (2021a). Therefore, parameters for the UVC model are taken directly from this reference.
- For columns subjected to monotonic lateral loading (7 tests, “full information”): the UVC model parameters are calibrated to the available tensile coupon tests using the procedure in Hartloper et al. (2021a). This is considered valid as inelastic *cyclic* straining does not occur under monotonic lateral loading.
- For the remaining column tests (24, “limited information”): the calibration procedure described in de Castro e Sousa et al. (2021) is used for the cases where only a tension test is available, but cyclic material behavior is expected. This methodology imposes bounds on the material parameters that are deemed to be representative of the established material response to cyclic loading.

The publicly available Python library RESSPyLab (de Castro e Sousa et al., 2019) is used for all the required material model parameter calibrations.

## **Chapter 6. Mixed-dimension modeling of steel wide flange beam-columns under multiaxis loading**

---

Approaches 1 and 2 are considered “full information” because they either: (a) consist of several heterogeneous (diverse loading protocols) uniaxial coupon tests that allow for the manifestation of cyclic material parameters, or (b) the cyclic behavior of the material is inconsequential for tests subjected to monotonic loading. For this reason, the test database is divided into two sets: (I) the calibration data set consisting of the three column tests under Approach 1 plus two tests from Approach 2 (5 total); and (II) the validation data set consisting of the remaining data. Full-continuum modeling guidelines (see Figure 6.2) are primarily determined using the calibration dataset. The determined parameters are then used to simulate the response of columns within the validation dataset to propose and evaluate new modeling guidelines. The evaluation based on the validation set is believed to be unbiased because each analysis is “blind” in the sense that no information apart from what has been previously established is used in modeling these tests.

### **Finite element discretization**

Both shell and solid element models are investigated in this study. Models are comprised of either linear, reduced-integration shell elements (S4R in Abaqus) with enhanced hourglass stiffness; or quadratic, reduced- integration solid elements (C3D20R in Abaqus). Element sizes for both of these options are based on a mesh convergence study conducted on representative cases. For shell and solid elements, an initial mesh is selected as 50 mm, with an aspect ratio of approximately 1-to-1. This initial size of 50 mm is then subsequently reduced by half to 25 mm, 12.5 mm, and 6.25 mm (shell only). Convergence to the true finite element solution is determined through the normalized difference in energy bounded by the moment-rotation curve. Tests subjected to cyclic lateral loading are selected for the mesh sensitivity as cyclic loading induces greater local curvatures than found in components subjected to monotonic loading. This factor is important as strains tend to be concentrated in regions of local buckling, for this reason, it is also important to conduct the mesh convergence study on a model with initial geometric imperfections.

Linear beam-column elements with torsion-warping (B31OS in Abaqus) are specified in the beam-column element domain of macro models. The number of beam-column elements is selected based on the number required to properly model flexural buckling. The model is initially divided into two elements, then the number of elements is successively doubled until convergence of the solution is obtained.

### **Initial geometric imperfections**

The approach from Hartloper et al. (2021b) is adopted for including imperfections that are critical in the initiation of geometric instabilities. The evolution and coupling of instabilities are assumed to be captured by the finite element model itself (e.g., the later development of a

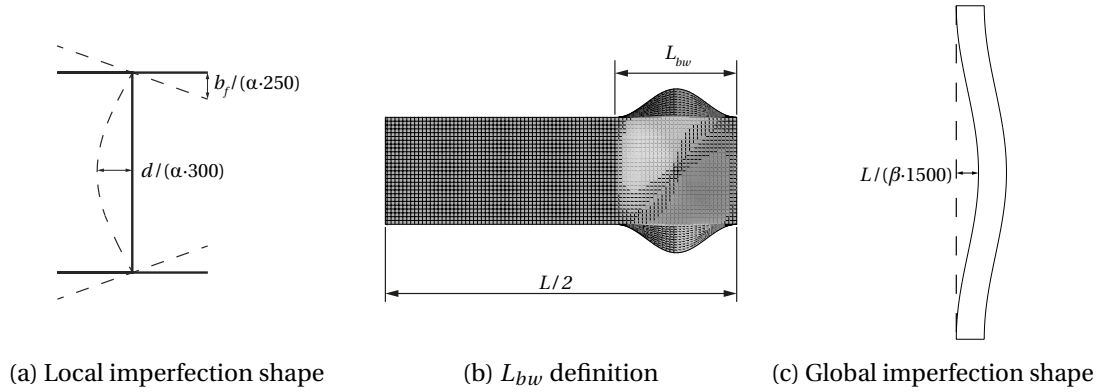


Figure 6.5 – Local and global imperfection shapes and parameter definitions.

second local buckling wave). Local and global initial geometric imperfections are specified by perturbing the initial positions of nodes in the finite element model according to pre-selected imperfection geometries. A twisting imperfection is also applied, as discussed in Hartloper et al. (2021b), by applying a torque ( $M_z$  in Figure 6.4) at the center of the tests by Elkady and Lignos (2018a) based on the measured initial twist angle.

The local imperfection shapes applied to the model are based on plate buckling theory, whereas global imperfections are based on flexural buckling of columns, as shown in Figure 6.5. The selected initial imperfection shapes are in agreement with international standards (CEN, 1993; JISC, 2014; ASTM, 2016a) as well as imperfections measured during manufacturing (Katayama et al., 1998) as they acknowledge web camber and flange out-of-squareness present in wide flange profiles. Local imperfections are defined by the local imperfection wavelength,  $L_{bw}$ , and the amplitude as a function of the scale factor  $\alpha$ . The global imperfection is defined by the amplitude as a function of the scale factor  $\beta$ —the length being automatically fixed by the member itself. Therefore, two parameters are defined in the modeling recommendations for local imperfections ( $L_{bw}$  and  $\alpha$ ), and one parameter for global imperfections ( $\beta$ ).

The general procedure used to determine these three parameters is as follows: (1) select a suitable range of values for each parameter, (2) conduct a finite element analysis given each parameter value and compute the corresponding error metric value, and (3) base the parameter selection on the set that leads to the lowest energy error metric. The local imperfection parameters ( $L_{bw}$  and  $\alpha$ ) are treated as a set and independently of the global imperfection parameter ( $\beta$ ). The following paragraphs outline the ranges of parameters selected and the cases used in determining the values.

The range of local imperfection wavelength values is based on prior analytical and numerical results. Analytical equations for plastic buckling in a structural steel design context can be first attributed to Haaijer (1956) who used a single flange model. These early findings were built upon by Lay (1965); Lay and Galambos (1967) who used a semi-empirical method in conjunction with a torsional buckling model for flanges in wide flange cross sections. The

Lay equation for computing the wavelength is

$$L_{bw} = 2 \cdot 0.713 b_f \frac{t_f}{t_w} \left( \frac{t_w(d - 2t_f)}{b_f t_f} \right)^{1/4}, \quad (6.6)$$

where the 2-factor accounts for two half-wavelengths for buckling under a moment gradient (Lay and Galambos, 1967). The Lay equation has been used extensively in this field (Kemp, 1985; Gioncu and Petcu, 1997; D’Aniello et al., 2012). Objections to the Lay equation have been raised in Möller et al. (1997), who used a yield-line model to establish the yielded length as  $\tan 55^\circ \cdot b_f \approx 1.43 b_f$ . Kolwankar et al. (2018) found  $1.5 b_f$  as the average wavelength through finite element analysis.

The range for  $L_{bw}$  includes the minimum and maximum of aforementioned studies for the local buckle wavelength. The maximum is defined by the Lay equation, as the mean of this equation mapped over the sections in Table 6.1 is  $2.3 b_f$ . Therefore, the final set of values investigated are  $L_{bw} = \{1.0, 1.5, 1.8, 2.0\} \cdot b_f$ , and additionally based on the Lay equation. In total, five values of  $L_{bw}$  will be assessed for each simulation.

The local imperfection amplitude is defined as a function of the scale factor,  $\alpha$ , and the baseline imperfection amplitude. This baseline value is selected as the average *maximum* measured imperfection (Hartloper and Lignos, 2019; Hartloper et al., 2021b). Therefore, the scale factor  $\alpha$  operates on the flange amplitude of  $a_f = b_f / (\alpha \cdot 250)$ , and web amplitude of  $a_w = d / (\alpha \cdot 300)$ . The effect of modifying the local imperfection scale factor,  $\alpha$ , on the moment-rotation from finite element simulations is shown in Figure 6.6. These results are for a column subjected to constant axial load and monotonically increasing lateral displacement at the column tip. As  $\alpha$  increases, the flange/web local buckling mode is delayed due to the smaller imperfection, thus increasing the pre-peak plastic rotation of the column. Flange-only local buckling occurs if no imperfection is included, in this case, the overall component behavior is non-deteriorating until very large lateral drift demands, thereby compromising the accuracy of the predictions.

The local imperfection scale factor is investigated in terms of orders of magnitude:  $\alpha = \{1.0, 10.0, 100.0, inf\}$ , where  $\alpha = inf$  is the case where no local imperfections are applied. Joint combinations of  $L_{bw}$  and  $\alpha$  are applied to all specimens in the “calibration dataset”, for a total of 100 analyses (five specimens, five  $L_{bw}$  values, four  $\alpha$  values). Only local imperfections are applied to the cantilever models (i.e., Top B.C. = Free for all specimens in the calibration dataset) because member buckling modes are not deemed to be critical due to the low member slenderness ratios (e.g.,  $\bar{\lambda}_{LT} < 0.2$ ). Only  $L_{bw}$  and  $\alpha$  are unknown in modeling the calibration dataset tests since the material parameters can be treated as “known” and no global imperfections are applied to these cantilevers.

The global imperfection amplitude,  $a_g = L / (\beta \cdot 1500)$ , is investigated in a manner similar to  $\alpha$  after both the local imperfection parameters have been determined. The range assessed is

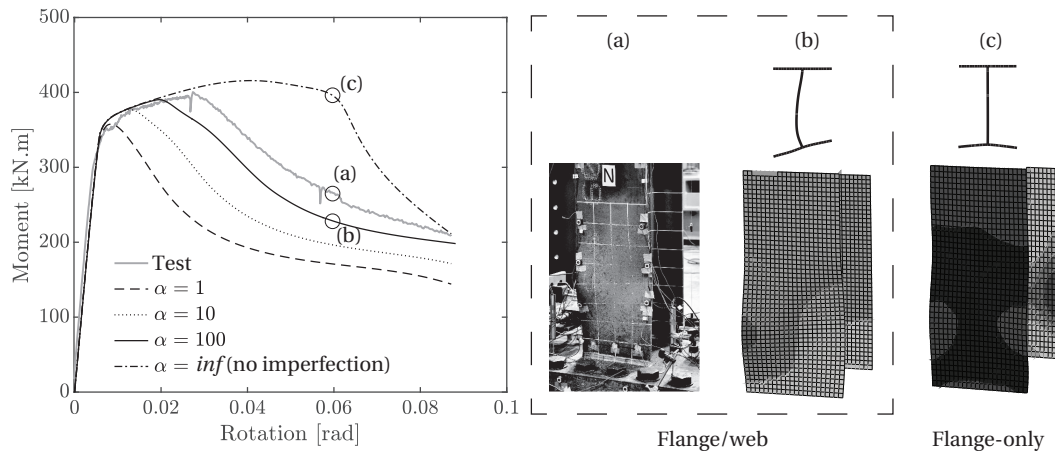


Figure 6.6 – Effect of local imperfection amplitude on full-shell CFE results for the W-8-34-M-C-50 test (W14X61,  $P/P_{ym} = 0.5$ ). Test data and photo from Cravero et al. (2020).

$\beta = \{-1, 1, 10, 100, inf\}$ , where  $\beta = inf$  corresponds to no imperfection, and  $\beta = -1$  is a global imperfection with amplitude  $L/1500$  in the reverse direction shown in Figure 6.5. The selection of  $\beta = -1$  is used to evaluate the effect of applying a global imperfection in the reverse direction with the maximum considered amplitude given the expectation that this effect diminishes as  $\beta$  approaches  $-inf$ . Tests by Elkady and Lignos (2018a) are used to evaluate the effect of global imperfections on columns subjected to multiaxis loading.

### Determination of the continuum length in macro models

The final parameter to determine is the continuum length for macro models,  $L_{\Omega_2}$ , defined in Figures 6.2 and 6.7. The general discretization into continuum and beam-column domains is shown for the cantilever and full-length tests in Figure 6.7. One critical region is modeled at the base of cantilever columns because local buckling only occurs near this location due to the associated moment gradient. Local buckling may also occur at the top end in columns with fixed and rotational top boundary conditions. For these members, a length of  $L_{\Omega_2}$  is assumed at both the top and base of the member.

Recommendations for defining  $L_{\Omega_2}$  are based on error metrics computed between simulated full-continuum and macro model responses given that the accuracy of the former is established on comparisons with data from physical experiments. There are two competing objectives in determining  $L_{\Omega_2}$  that need to be considered. First, lowering  $L_{\Omega_2}$  is expected to reduce the computational effort; second, increasing  $L_{\Omega_2}$  is expected to reduce the macro model error compared to the full-continuum models. Therefore, recommendations for  $L_{\Omega_2}$  are based on the smallest continuum length that leads to an acceptable error between the full-

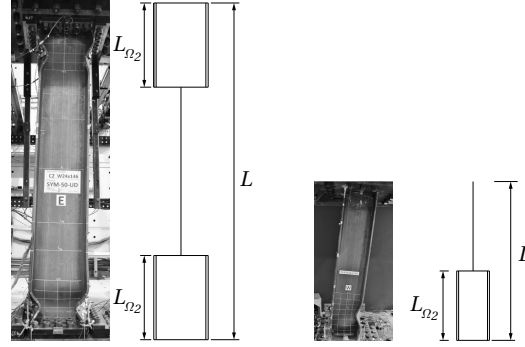


Figure 6.7 – Modeling of critical regions for full-length (Top B.C. = Fixed or Rot; left) and cantilever (Top B.C. = Free; right) members. Photos from Elkady and Lignos (2018a) and Cravero et al. (2020).

continuum and macro models. Hereinafter, acceptable errors are defined when the average error is less than 5 % and no individual error is larger than 10 %. The investigated values are  $L_{\Omega_2} = \{2.0, 3.0, 4.0, 5.0\} \cdot b_f$ .

Hartloper et al. (2021b) found that a longer continuum length is required when modeling columns susceptible to inelastic LTB. As inelastic lateral-torsional buckling is likely not critical in members with  $\bar{\lambda}_{LT} < 0.4$ , and the maximum value of  $\bar{\lambda}_{LT}$  is 0.38 in Table 6.1, fictitious cases are considered with increased LTB slenderness. For this purpose, the C5 ( $L = 3.9$  m,  $P/P_{ym} = 0.2$ , W24X146, collapse-consistent loading), C7 ( $L = 3.9$  m,  $P/P_{ym} = 0.2$ , W24X84, symmetric-cyclic loading), and C8 ( $L = 3.9$  m,  $P/P_{ym} = 0.2$ , W24X84, collapse-consistent loading) tests are modeled with extended length. The C5 column is extended to 5.5 m (new  $\bar{\lambda}_{LT} = 0.37$ ), while the C7 and C8 columns are extended to 5 m (new  $\bar{\lambda}_{LT} = 0.47$ ). The first case acts as a control since  $\bar{\lambda}_{LT} < 0.4$ , whereas the other two cases are to assess if an increase in  $L_{\Omega_2}$  is required when  $\bar{\lambda}_{LT} > 0.4$ . The top boundary is treated as fixed for these additional cases.

## 6.3 Results

### 6.3.1 Material calibration

Results from the tensile coupon fitting using the procedure from de Castro e Sousa et al. (2021) for the VC model are provided in Table 6.2. In this table:  $E$  is the elastic modulus,  $\nu$  is Poisson's ratio,  $\sigma_{y,0}$  is the initial yield stress,  $Q_\infty$  is the magnitude of isotropic hardening at model saturation,  $b$  is the isotropic hardening rate term,  $C_1$  is the kinematic hardening magnitude for backstress 1, and  $\gamma_1$  is the rate term associated with backstress 1. For brevity, the UVC model parameters for the monotonic tests are not shown herein, nor the parameters from Hartloper et al. (2021a) for the W14X82 sections from Suzuki and Lignos (2021).

Predictions of the stress-strain response from the UVC and VC models are shown in

Table 6.2 – Results from the calibration of the Voce-Chaboche model using only tensile tests.

Investigator	Section	$\sigma_{y,0}$ [MPa]	$Q_\infty$ [MPa]	$b$	$C_1$ [MPa]	$\gamma_1$
Suzuki and Lignos (2021)	W14X53-F	356.45	97.16	7.30	2962.48	16.42
	W14X53-W	373.98	112.96	4.38	2065.41	9.85
	W14X61-F	354.93	97.08	9.17	3721.22	20.64
	W14X61-W	374.59	95.29	6.70	2668.69	15.08
Elkady and Lignos (2018a)	W24X146-F <sup>a</sup>	387.44	90.36	6.53	2466.65	14.70
	W24X146-W <sup>a</sup>	392.57	89.85	5.61	2106.30	12.63
	W24X146-F <sup>b</sup>	340.41	88.56	8.64	3198.93	19.45
	W24X146-W <sup>b</sup>	355.08	83.99	8.14	2855.69	18.31
	W24X84-F	322.72	98.89	9.60	3968.36	21.61
	W24X84-W	304.85	112.43	9.13	4290.86	20.55
	W14X61-F	339.52	178.25	1.86	1388.18	4.19
Cravero et al. (2020)	W14X61-W	344.74	181.00	1.58	1197.41	3.56
	W14X82-F	368.67	214.14	3.23	2244.95	10.48
	W14X82-W	395.09	133.47	3.30	1840.38	7.42
	W16X89-F	340.61	162.62	2.45	1663.12	5.51
	W16X89-W	361.34	189.71	1.68	1328.60	3.77

-F: Flange, -W: Web.  $E = 200$  GPa and  $\nu = 0.3$  assumed for all.

<sup>a</sup>C1–C4, <sup>b</sup>C5 and C6.

Figure 6.8. The UVC model parameters are determined using the full dataset for the A992 Gr. 50 (i.e., nominal  $f_y = 345$  MPa) material in Hartloper et al. (2021a) from a W14X82 cross section. The VC parameters determined using the tensile-only (VC, tensile) method from de Castro e Sousa et al. (2021) are shown in these figures for illustrative purposes. The VC model calibrated using the tensile-only method performs reasonably well in predicting the cyclic behavior in this case apart from two notable issues. First, results in Figure 6.8 demonstrate that the VC model tends to underestimate the initial yield stress and the stress up-to around 2 %strain because it does not account for the discontinuous yielding phenomenon. Second, the VC model response shown here does not adequately represent the smooth yielding observed under cyclic loading because only one backstress can reasonably be used in the tensile-only calibration procedure (de Castro e Sousa et al., 2021).

### 6.3.2 Mesh convergence

Selected results from the mesh convergence study are shown in Figures 6.9 and 6.10 for shell and solid element models, respectively. Shell element model results are based on the W-6-25-C1-C test (W14X82, collapse-consistent protocol, constant  $P/P_{ym} = 0.3$ ) whereas the solid element model results are based on the W-6-25-S-C test (W14X82, symmetric cyclic protocol, constant  $P/P_{ym} = 0.3$ ) (Suzuki and Lignos, 2021). These figures display the relative difference in the total energy under the moment-rotation curve of sample element sizes compared to the smallest element size evaluated. For instance, the difference in total energy between the Shell-6 (nominal element size of 6.25 mm) and Shell-12 (nominal element size of 12.5 mm)

## Chapter 6. Mixed-dimension modeling of steel wide flange beam-columns under multiaxis loading

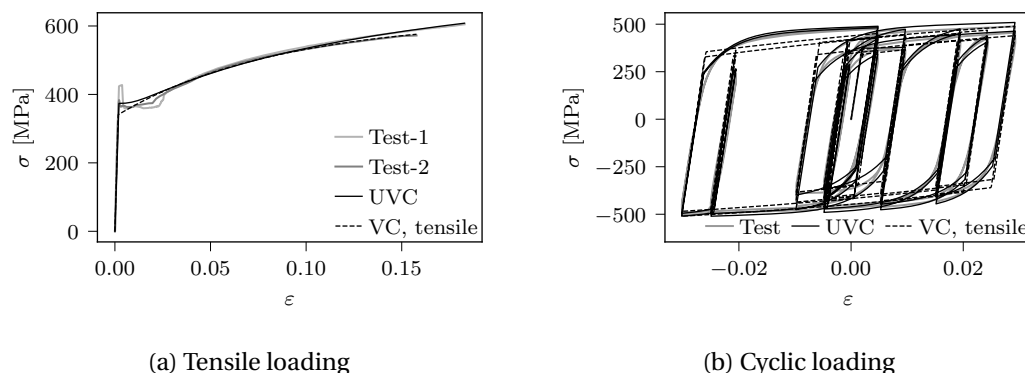


Figure 6.8 – Comparison of A992 Gr. 50 (W14X82 flange) material stress-strain and material model responses using the UVC and VC models. UVC calibrated with tensile and cyclic tests; VC calibrated using only a tensile test. Material data from Suzuki and Lignos (2021).

is around 3 % at the end of the simulation, while the difference between the Shell-6 and the Shell-25 (nominal element size of 25 mm) is more than 10 %. The moment-rotation response from these models is also shown in Figure 6.9. A mesh size of 12.5 mm (Shell-12) is deemed adequate for convergence to the true finite element solution. Thus, the 12.5 mm shell element mesh is selected for use throughout this study.

Four different solid element meshes are displayed in Figure 6.10, where the label “Q” indicates the use of quadratic, reduced-integration elements. The Solid-Q25 model (nominal element size of 25 mm) is similar to the Solid-Q25-1 model, but Solid-Q25-1 only has one element through the flange thickness. Note that a minimum of two elements are required through the web thickness for symmetry of the model. Results shown in Figure 6.10 imply that the governing factors for the solid element modes are the nominal element size and the discretization of the k-area (i.e., the fillet region between the flange and web shown in Figure 6.10) radius. The nominal element size is important because a sufficient number of elements is required along the member’s length, the web depth, and flange width to reliably simulate the onset of local buckling. The finite element results suggest that a reasonably accurate discretization of the k-area curvature provides a more accurate estimation of the cross-sectional stiffness. A difference of around 7 % between the Solid-Q12 (nominal element size of 12.5 mm) and Solid-Q50 (nominal element size of 50 mm) models is observed, thus the Solid-Q50 is rejected for further analyses. The number of elements through the flange thickness is found to have a fairly negligible effect, thus for efficiency reasons, the Solid-Q25-1 model is selected for use throughout this study.

Beam-column element mesh convergence results are shown in Figure 6.11 based on the flexural buckling test by Lamarche and Tremblay (2011). Eight B31OS elements are found to be sufficient for convergence of the finite element solution, or four elements per half-length of the member. For macro model purposes, the following formula is used to define the number



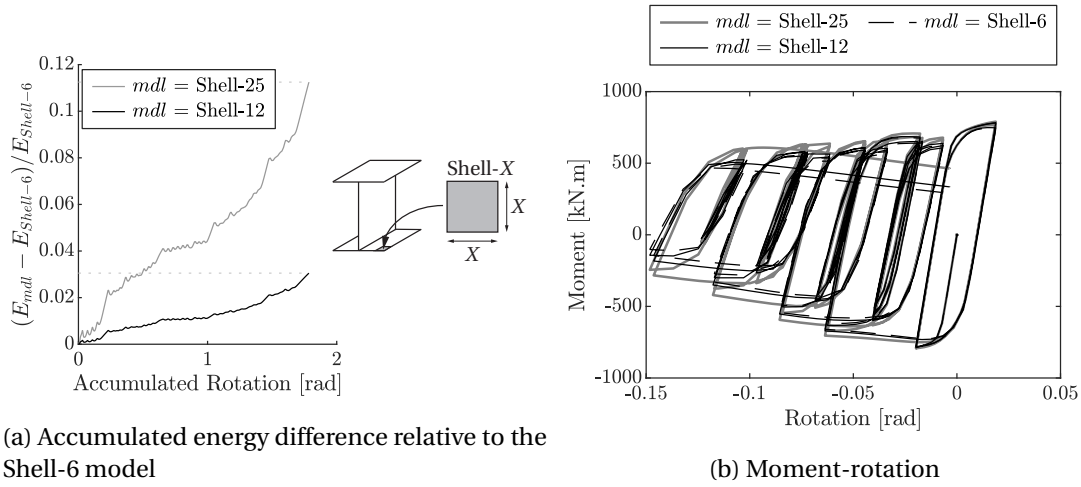


Figure 6.9 – Shell element mesh convergence results ( $E = \int M d\theta^*$ ) based on the W-6-25-C1-C test (W14X82, collapse-consistent,  $P/P_{ym} = 0.3$ ) by Suzuki and Lignos (2021).

of elements per half-length of the member:

$$n_{beam} = \text{ceil} \left[ 4 \cdot (1 - L_{\Omega_2} / L^*) \right], \quad (6.7)$$

where  $\text{ceil}[\cdot]$  is the ceiling function,  $L^* = L/2$  for members in double-curvature, and  $L^* = L$  for members in single-curvature (e.g., cantilevers). Equation 6.7 ensures that there are between 1–4 (2–8 for members in double-curvature) beam-column elements per half-length in macro models depending on the ratio of the continuum length to the total length of the member. This result agrees with the four B31OS elements selected for macro models in Hartloper et al. (2021b).

### 6.3.3 Determination of initial geometric imperfections

#### Local imperfection: shell element models

Results for the full-shell initial geometric imperfection calibration are summarized as a heatmap in Figure 6.12. Each square in this figure represents the average metric of the results from the five simulations in the calibration dataset (W-6-34-M-C, W-8-34-M-C-50, W-6-25-C1-C, W-6-25-C1-V, W-6-25-S-C) at a given  $\alpha$  and  $L_{bw}$  value. The minimum average energy metric is for the combination  $L_{bw} = 1.5b_f$  and  $\alpha = 100$  ( $\epsilon_e = 0.14$ ), thus, it is selected as the best combination of local initial geometric imperfection parameters. This result implies that the overall moment-rotation energy metric difference between simulation and tests is only 14 % over the entire history. Figure 6.13 is provided to give a sense of this level of error. Note that this combination of  $\alpha$  and  $L_{bw}$  also minimizes the peak-strength ( $\epsilon_s = 0.06$ ) and axial shortening ( $\epsilon_a = 0.09$ ) errors.

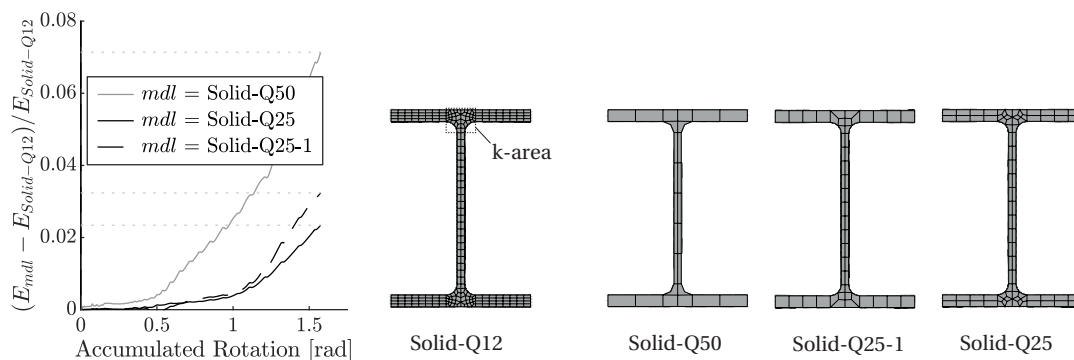


Figure 6.10 – Solid element mesh convergence results ( $E = \int M d\theta^*$ ), relative to the Solid-Q12 model, based on the W-6-25-S-C test (W14X82, symmetric-cyclic,  $P/P_{ym} = 0.3$ ) by Suzuki and Lignos (2021).

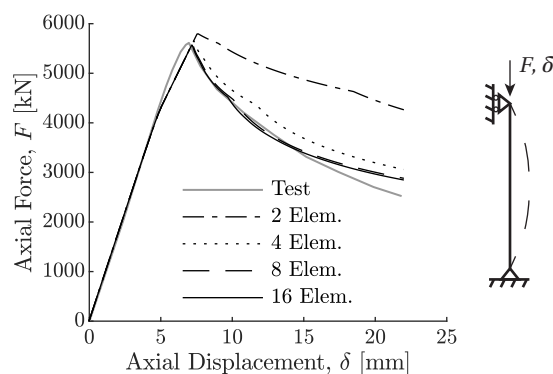


Figure 6.11 – Beam-column element mesh convergence results based on Specimen 1 flexural buckling test by Lamarche and Tremblay (2011).

The largest errors in the full-shell simulations occur when  $\alpha = 1.0$  (i.e.,  $a_f = b_f/250$ ) or  $\alpha = \inf$  (no imperfection), see Figure 6.12. At  $\alpha = 1.0$ , the simulation results underestimate the test results for the modeling conditions described earlier, implying that the specified initial geometric imperfections appear to be too large (see Figure 6.6). At the  $\alpha = \inf$  end, the simulation results overestimate the test results because the flange/web local buckling mode is not triggered. However, a value of  $\alpha = 100$  implies a local imperfection with amplitudes based on  $a_f = b_f/25000$  and  $a_w = d/30000$ . This finding represents a physically unlikely result, as measurements on European cross sections have shown that local initial geometric imperfections have a mean amplitude on the order of, e.g.,  $a_f = b_f/1000$  (Hartloper and Lignos, 2019). Therefore, the authors are of the opinion that the imperfection amplitude be treated as a numerical factor tied the proposed modeling approach; the interpretation of this result in the context of the study is substantiated in Section 6.4.2.

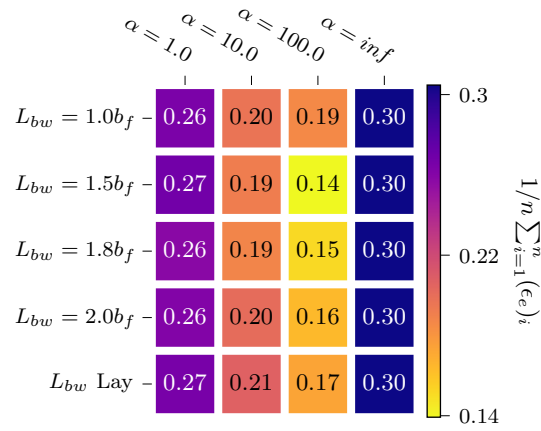
#### Local imperfection: solid element models

A similar procedure as used for shell element models is carried out for the solid element model, under the assumption that  $L_{bw}$  is independent of the element type. Therefore, the value of  $L_{bw} = 1.5b_f$  is also selected for the solid element models based on the preceding section. In this case, the average energy error ( $\epsilon_e$ ) is found to be minimized when  $\alpha = 10$ , as shown in Figure 6.14. This plot shows the average metric values for the calibration dataset for  $L_{bw} = 1.5b_f$  and the varying  $\alpha$  values. The result  $\alpha = 10$  for solid element models compared to  $\alpha = 100$  for shell element models is attributed to the inclusion of the k-area that is not present when a shell element discretization is employed. These results will be discussed in detail in Section 6.4.2.

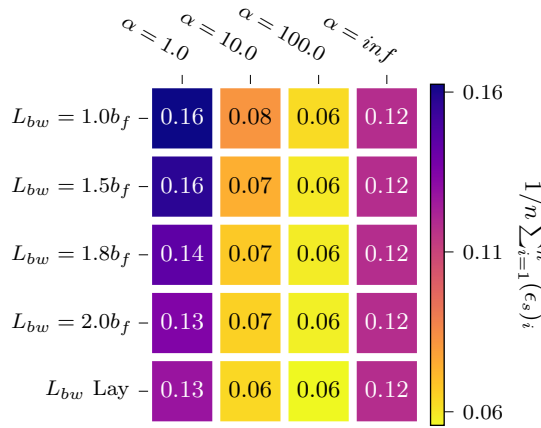
#### Global imperfection

For beam-columns subjected to multiaxis loading tested by Elkady and Lignos (2018a), the influence of the assumed global imperfection amplitude on shell element model results is shown in Figure 6.15 through the proposed error metrics discussed earlier. Fixed values of  $\alpha = 100$  and  $L_{bw} = 1.5b_f$  are used in these simulations. The influence of the assumed global imperfection on the simulated deformations, compared with experimental results, is shown in Figure 6.16. Looking at the side view, the “same direction” local buckling pattern is defined by the flanges buckling “inwards” at both ends, and the “opposite direction” is defined by one end buckling “inwards” and the other “outwards”.

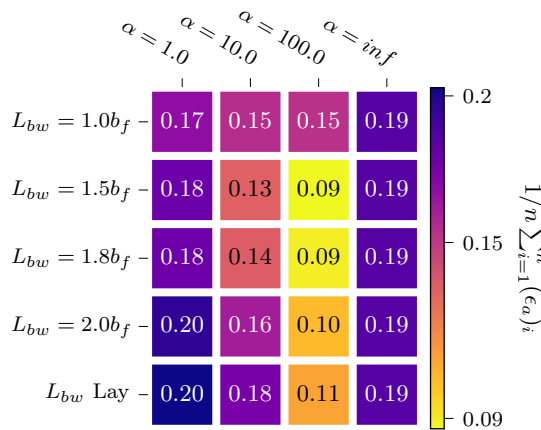
Without data regarding the local and global imperfections in the members, a decision was made to neglect global imperfections in shell element models for the purpose of this study. The main reason for this decision is the observation that local imperfections are sufficient for the adequate shell-element simulation of the given experimental responses. This is attributed to



(a) Energy error

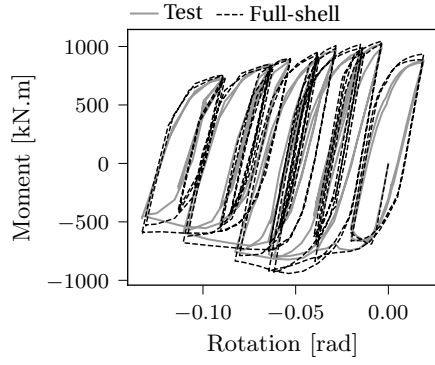


(b) Peak-strength error

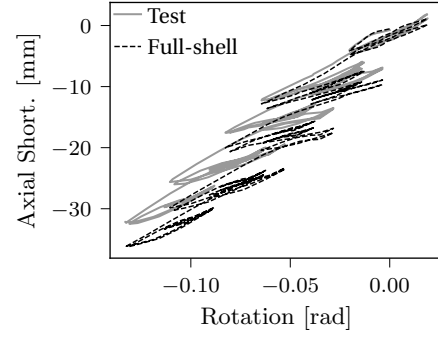


(c) Axial shortening error

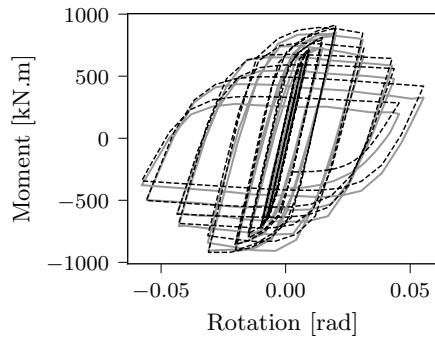
Figure 6.12 – Full-shell model average error metric results from the calibration data set (each square is the average of five tests).



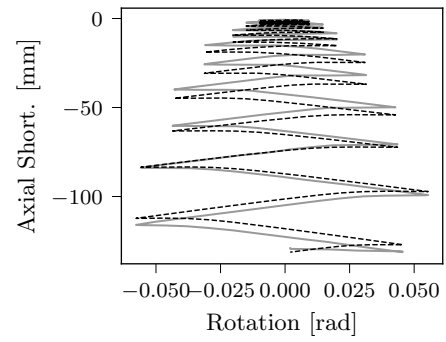
(a) W-6-25-C1-V moment-rotation



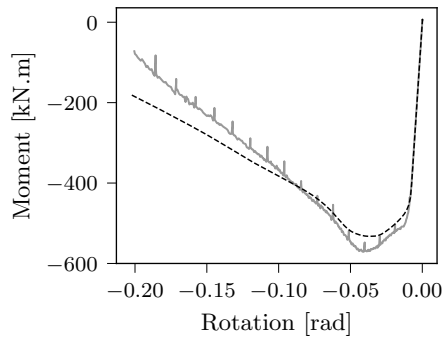
(b) W-6-25-C1-V axial shortening



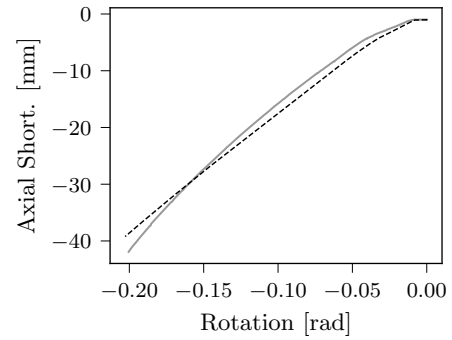
(c) W-6-25-S-C moment-rotation



(d) W-6-25-S-C axial shortening



(e) W-6-34-M-C moment-rotation



(f) W-6-34-M-C axial shortening

Figure 6.13 – Sample results from the full-shell calibration dataset with  $L_{bw} = 1.5b_f$  and  $\alpha = 100$  (solid = Test, dashed = Full-shell).

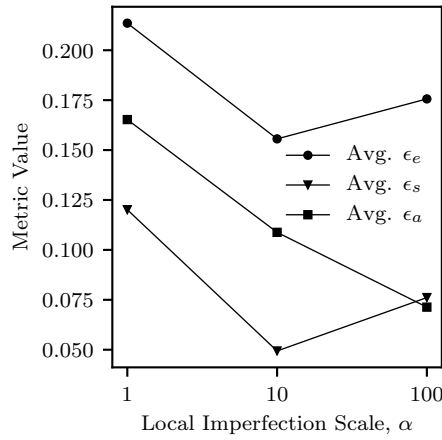


Figure 6.14 – Full-solid model average error metric results from the calibration data set (average of five tests).  $\epsilon_e$  = energy metric,  $\epsilon_s$  = peak-strength metric,  $\epsilon_a$  = axial shortening metric.

geometric instabilities being initiated through local buckling that, later coupled with inelastic twisting/LTB, govern each component's response. Additionally, same-direction local buckling observed in shell element models with  $\beta = 1$  leads to a conflict with the observed deformation in tests (Figure 6.16). However, global imperfections are retained for solid element models because the simulated deformed shapes match with the tests using a global imperfection amplitude scale factor of  $\beta = 1$ . This result is attributed to the larger local imperfection amplitude present in solid element models in connection with the explicit modeling of the k-area.

#### 6.3.4 Summary of full-continuum modeling guidelines and simulation of the validation dataset

Full-shell and full-solid element modeling recommendations determined throughout the previous sections are summarized in Table 6.3 for the employed mesh discretization and imperfection parameters (see Figure 6.2 for other parameters). These recommendations are now evaluated using simulation results of the 29 tests contained in the validation dataset discussed earlier. Voce-Chaboche model parameters used in modeling the validation dataset are contained in Table 6.2. The full-CFE modeling recommendations are assessed through the error metrics computed between the test data and “blind” simulation results that follow.

In assessing the results, the error metrics are found to be sensitive to the ratio of applied axial load ( $P/P_{ym}$ ). For this reason, the validation dataset is split into two categories: tests with moderate axial load ratio (maximum  $P/P_{ym} < 0.5$ ), and tests with very high axial load ratio (minimum  $P/P_{ym} \geq 0.5$ ). The error metrics computed between full CFE simulations and test data in the validation set are summarized in Table 6.4. These errors are largely found to

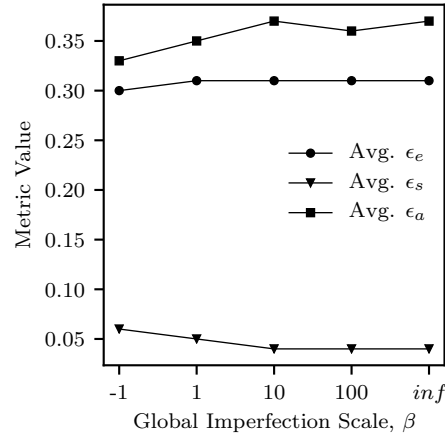


Figure 6.15 – Effect of global imperfection scale factor,  $a_g = L/(\beta \cdot 1500)$ , on columns subjected to multiaxis loading (based on tests from Elkady and Lignos (2018a)).  $\epsilon_e$  = energy metric,  $\epsilon_s$  = peak-strength metric,  $\epsilon_a$  = axial shortening metric.

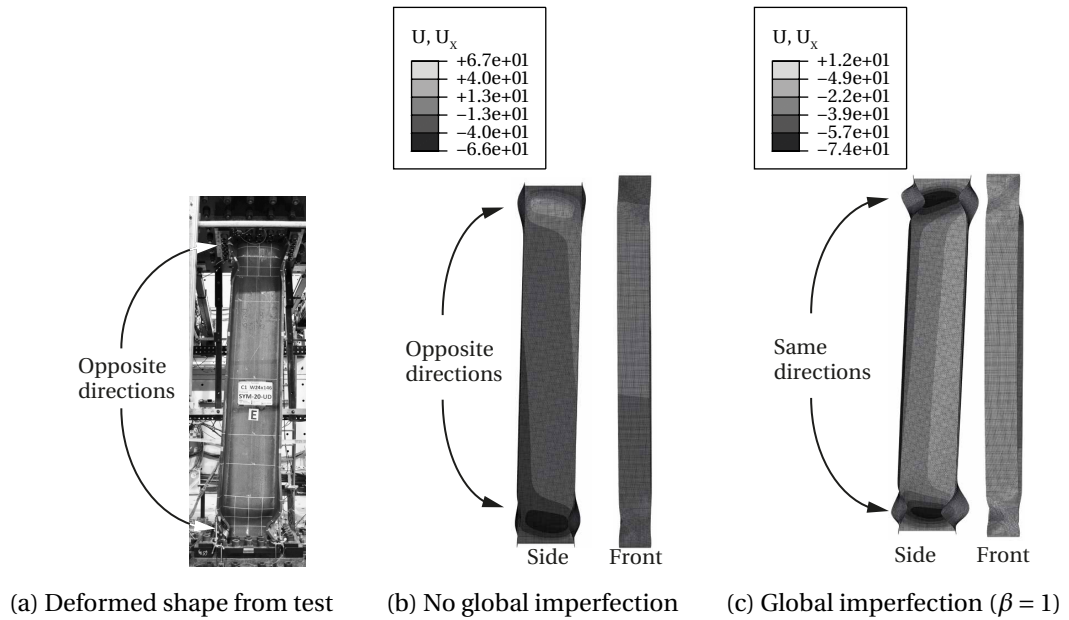


Figure 6.16 – Effect of global imperfection on local buckling orientation for the C1 column. Test photo from Elkady and Lignos (2018a).

## Chapter 6. Mixed-dimension modeling of steel wide flange beam-columns under multiaxis loading

Table 6.3 – Summary of full-continuum modeling parameters determined in this study for modeling columns under multiaxis loading with properties in the ranges of:  $0.19 \leq \bar{\lambda}_{LT} \leq 0.38$ ,  $5.9 \leq b_f/2t_f \leq 8.1$ ,  $20 \leq h/t_w \leq 44$ ,  $0.15 \leq P/P_{ym} \leq 0.75$ .

Item	Shell-domain value	Solid-domain value
Element type	Linear, reduced-integration	Quadratic, reduced-integration
Mesh size	12.5 mm	25.0 mm
Local imperfection scale factor	$\alpha = 100$	$\alpha = 10$
Global imperfection scale factor	No imperfection	$\beta = 1$

Table 6.4 – Error metric results from the validation dataset for full-shell and full-solid models as a function of model type and axial load.

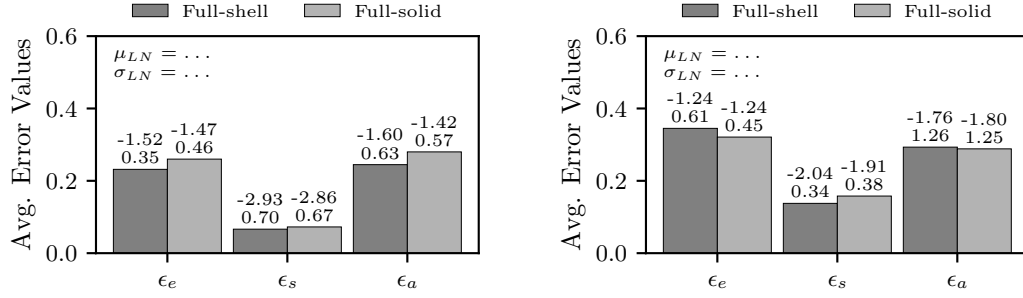
Model	Axial Load	Energy			Peak strength			Axial shortening		
		Avg.	$\mu_{LN}$	$\sigma_{LN}$	Avg.	$\mu_{LN}$	$\sigma_{LN}$	Avg.	$\mu_{LN}$	$\sigma_{LN}$
Full-shell	$P/P_{ym} < 0.5$	0.23	-1.52	0.35	0.07	-2.93 <sup>a</sup>	0.70 <sup>a</sup>	0.24	-1.60	0.63
Full-solid	$P/P_{ym} < 0.5$	0.26	-1.47	0.46	0.07	-2.86	0.67	0.28	-1.42	0.57
Full-shell	$P/P_{ym} \geq 0.5$	0.35	-1.24	0.61	0.14	-2.04	0.34	0.29	-1.76	1.26
Full-solid	$P/P_{ym} \geq 0.5$	0.32	-1.24	0.45	0.16	-1.91	0.38	0.29	-1.80	1.25

Notes: <sup>a</sup> = does not pass Lilliefors test for log-normality.

be log-normally distributed based on a Lilliefors test with a statistical significance of 0.05; the mean ( $\mu_{LN}$ ) and standard deviation ( $\sigma_{LN}$ ) of the associated log-normal distributions are provided in Table 6.4. These statistical parameters can be used in the future, for example, to compare the proposed modeling recommendations with alternative approaches assessed using the same pool of experimental data, which have been made publicly available. Average error metric results are also summarized in a graphical format in Figures 6.17a and 6.17b. Plots comparing the test and simulated moment-rotation and axial shortening response from the full-shell models are provided in Figure 6.18. These figures give a sense of the goodness-of-fit for the simulation results by showing the “worst” (highest  $\epsilon_e$ ) and “best” cases (lowest  $\epsilon_e$ ).

Across both moderate and very-high axial load sets, the shell element models perform equivalently to the solid element models in terms of the average error metrics. Slightly higher error metrics in the solid element models are attributed to the coarse approach used to determine the imperfection scale factors, however, differences on the order of 2 % error are practically considered negligible. In terms of the computational expense, however, shell element models are superior. For instance, in the C1 column (W24X146,  $L = 3.9$  m), the number of DOFs is reduced by around 15 % using a shell element model compared to a solid element model (shell: 200982, solid: 238785) and the memory requirement is reduced by around 80 % (shell: 938 MB, solid: 4470 MB). Only macro shell models are considered going forward in this study, as shell models have just been shown to provide overall equivalent performance to solid element models at significantly reduced computational cost.





(a) Moderate axial load dataset, each bar = average of 20 tests  
 (b) Very-high axial load dataset, each bar = average of 9 tests

Figure 6.17 – Average error metric results from the simulation of the validation dataset. Values above each bar are the mean and standard deviation of the associated log-normal distribution.

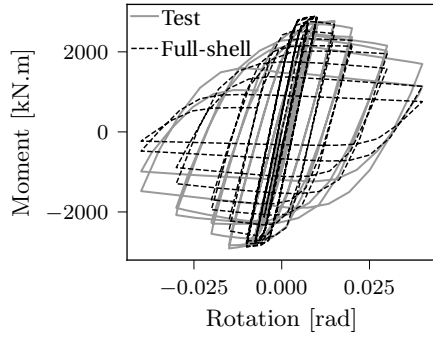
### 6.3.5 Macro model continuum length calibration results

As highlighted previously, only macro shell models are considered due to their efficiency compared to solid element models. Modeling of the shell domains follows the recommendations in Table 6.3, and the number of beam-column elements is set according to Equation 6.7. Thus, the only remaining parameter to be determined is the continuum domain length,  $L_{\Omega_2}$ . Simulations based on all 34 tests in the dataset are considered in the calibration of  $L_{\Omega_2}$ .

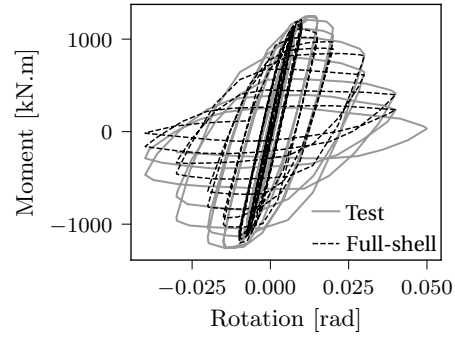
Results for the calibration of  $L_{\Omega_2}$  are summarized in Table 6.5 based on the average error metrics; this table shows that the average error is indifferent when  $L_{\Omega_2} \geq 3.0b_f$ . Moment-rotation and axial shortening plots are provided in Figures 6.19 and 6.20 at different values of  $L_{\Omega_2}$ . These plots indicate the near perfect agreement between the full-shell and macro models at an average energy metric error of 3 %. The energy errors from all the 37 simulations are shown as a histogram in Figure 6.21a for  $L_{\Omega_2} = 3.0b_f$ . The two cases with an energy error over 10 % (C8 and C8-5m with extended length) can be controlled by increasing the length  $L_{\Omega_2}$ .  $L_{\Omega_2}$  values of  $6.0b_f$  are considered to reduce the error below 10 % in these two instances. The two cases are notable due to their comparatively high non-dimensional lateral-torsional slenderness. It is, therefore, proposed to divide the recommendations for the continuum element length into two categories:

$$L_{\Omega_2} = \begin{cases} \max[3.0b_f, 0.25(2L^*)] & \text{if } \bar{\lambda}_{LT} < 0.4 \\ \max[6.0b_f, 0.30(2L^*)] & \text{if } \bar{\lambda}_{LT} \geq 0.4; \end{cases} \quad (6.8)$$

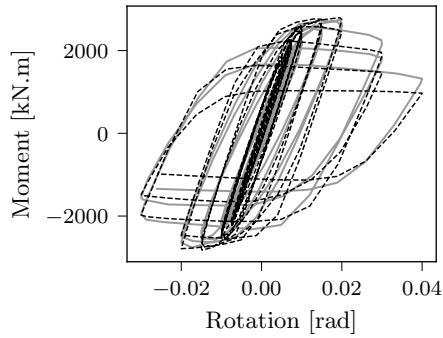
recall that  $L^* = L/2$  for members in double-curvature, and  $L^* = L$  for members in single-curvature (e.g., cantilevers) because two shell domains of length  $L_{\Omega_2}$  are used at the member ends in the case of double-curvature bending, and one domain when the member is in single curvature (i.e., cantilevers). These guidelines essentially specify that half of the member



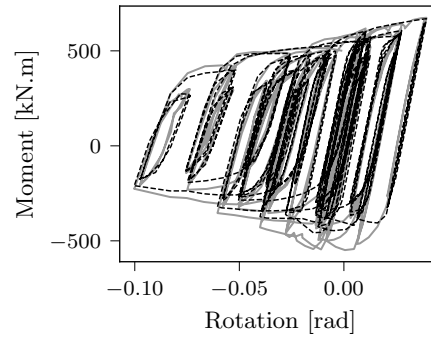
(a) C1 moment-rotation, second-highest  $\epsilon_e$



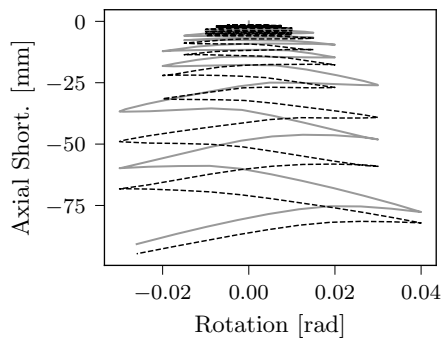
(b) C9 moment-rotation, highest  $\epsilon_e$



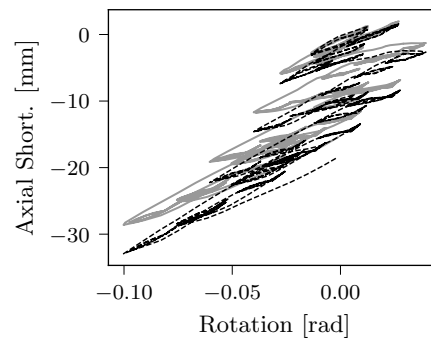
(c) C6 moment-rotation, second-lowest  $\epsilon_e$



(d) W-6-34-C2-V moment-rotation, lowest  $\epsilon_e$



(e) C6 axial shortening



(f) W-6-34-C2-V axial shortening

Figure 6.18 – Representative full-shell model results from the “blind” analysis of tests in the validation dataset (solid = Test, dashed = Full-shell). High values of  $\epsilon_e$  represent worse predictions of moment-rotation.

Table 6.5 – Error metric results for macro-shell models as a function of continuum length ( $L_{\Omega_2}$ ).

$L_{\Omega_2}$	Energy			Peak strength			Axial shortening		
	Avg.	$\mu_{LN}$	$\sigma_{LN}$	Avg.	$\mu_{LN}$	$\sigma_{LN}$	Avg.	$\mu_{LN}$	$\sigma_{LN}$
$2.0b_f$	0.08	-2.98	1.07	0.01	-5.32	0.91	0.06	-3.44	1.13
$3.0b_f$	0.03	-3.85	1.00	0.00	-6.27	1.01	0.03	-4.10	1.06
$4.0b_f$	0.03	-3.89	1.02	0.00	-6.58	1.09	0.03	-4.19	1.18
$5.0b_f$	0.03	-4.10	1.15	0.00	-6.86	0.99	0.03	-4.40	1.22

should be modeled with shell elements, while the other half can be modeled with beam-column elements. If these guidelines are followed, the average error between macro- and full-shell models is only 3 % and no individual error is over 10 %. The histogram of individual errors using Equation 6.8 is shown in Figure 6.21b. Consideration for columns with  $\bar{\lambda}_{LT} > 0.4$  is important, for example, in multi-tiered brace frames (Imanpour et al., 2016) where (1) the axial load can be significant due to the brace demands and (2) the columns may reach lateral-torsional slenderness ratios of  $\bar{\lambda}_{LT} > 0.4$ .

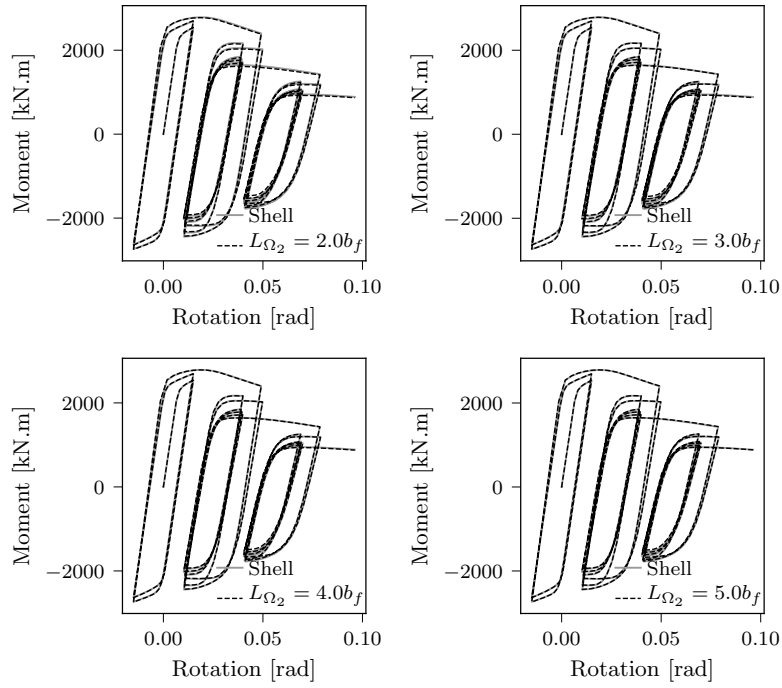
The energy and axial shortening errors shown in Figures 6.21a and 6.21b are found to follow a log-normal distribution, as verified using the Lilliefors test at a significance level of 0.05. The log-normal distributions' means and standard deviations are shown in these plots. The exponential of the log-normal mean is an estimation of the median of the data, i.e.,  $\exp[\mu_{LN}] = \exp[-3.88] = 0.02$  implies that half the macro model simulations have an error compared with their full-shell counterparts less than 2 %.

Computational efficiency of the macro model approach is measured through two metrics: the number of DOFs in the model, and the memory requirements. The first metric indicates the complexity of the problem, and therefore, the effort to complete each iteration of the finite element solution. The second metric represents a baseline requirement to run the simulation on a given computer system. Bar plots for these two metrics are provided in Figure 6.22 based on the Abaqus output for each simulation model. All the values in these plots are normalized by the DOFs and memory of the associated full-shell model. We conclude that modeling wide flange beam-columns components using 50 % length as shell and 50 % length as beam-column elements correlates with a 50 % reduction in both DOFs and memory requirement at the member level.

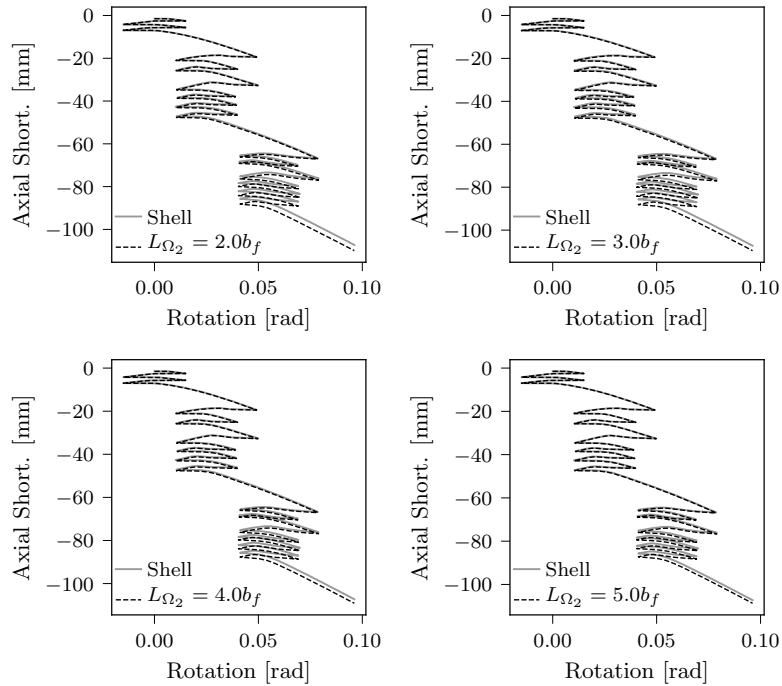
## 6.4 Discussion

### 6.4.1 Influence of constitutive modeling

The quality of the proposed finite element modeling recommendations for predicting the behavior of beam-columns that were physically tested appears to be strongly related to the



(a) Moment-rotation ( $\epsilon_e = 0.014$ )



(b) Axial-shortening ( $\epsilon_a = 0.018$ )

Figure 6.19 – Simulation with lowest error at  $L_{\Omega_2} = 3.0b_f$  between the macro and full-shell models (solid = Full-shell, dashed = Macro-shell).

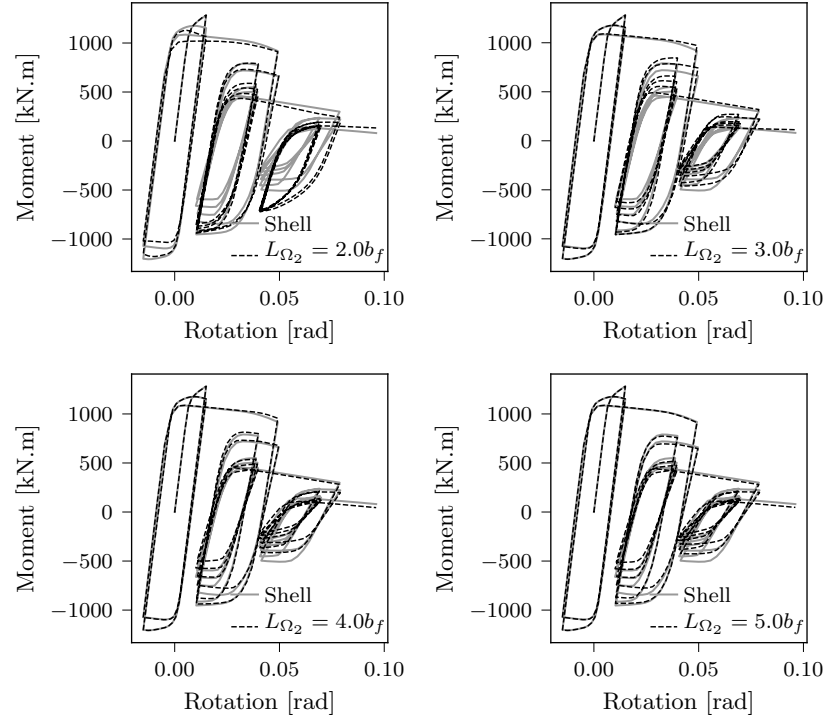


Figure 6.20 – Simulation with highest energy error ( $\epsilon_e = 0.075$ ) at  $L_{\Omega_2} = 4.0b_f$  between the macro and full-shell models (solid = Full-shell, dashed = Macro-shell).

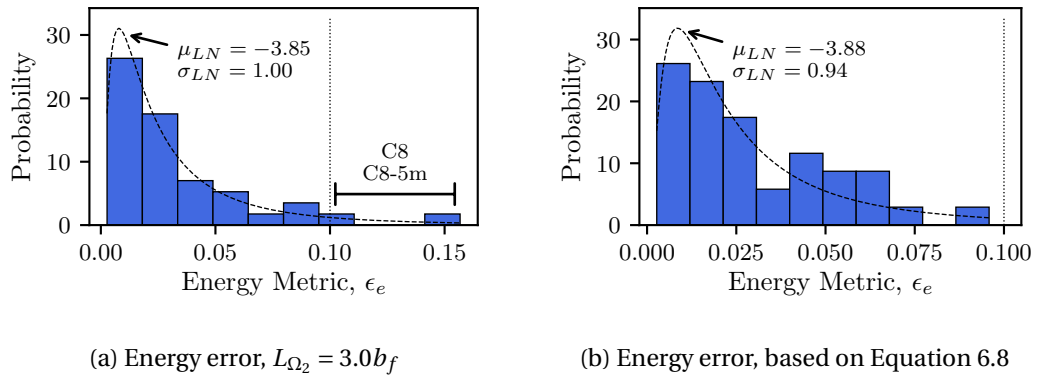


Figure 6.21 – Probability density of individual errors for  $L_{\Omega_2} = 3.0b_f$ , and those when the guidelines proposed in Equation 6.8 are followed.

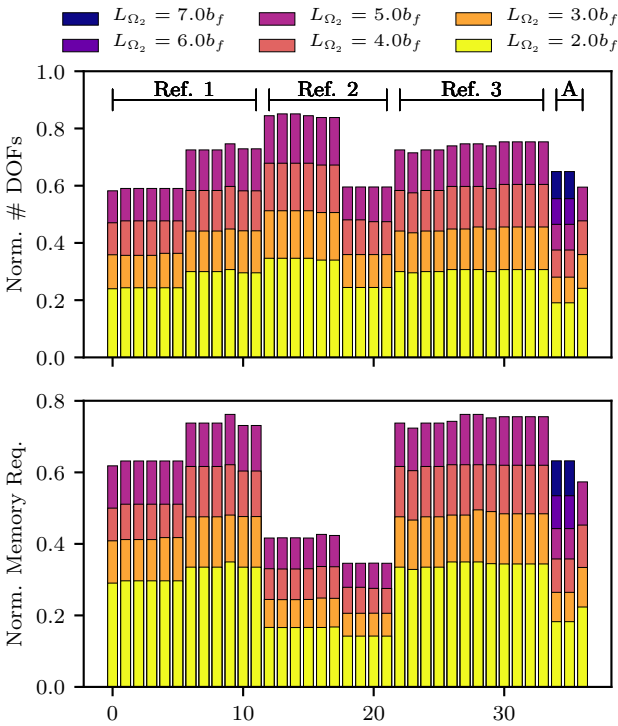


Figure 6.22 – Computational efficiency metrics for the macro models. All values normalized by their respective full-shell values. Ref. 1: Suzuki and Lignos (2021), Ref. 2: Elkady and Lignos (2018a), Ref. 3: Cravero et al. (2020), A: added length analyses.

quality of material data. For instance, the energy error metric is nearly doubled from 14 % in the calibration set to 24 % in the validation set (see Figures 6.13 and 6.18). Fundamentally, the only difference between these two sets of data is knowledge regarding the material behavior. This nearly doubling of the error between tests and simulations can be seen as the cost of having limited material data when modeling a wide flange steel beam-column. These results are further evidence that the tensile-only calibration method should only be used for simulating the hysteretic response of wide flange beam-columns subjected axial load coupled with lateral cyclic drift demands if the full material data are not available (de Castro e Sousa et al., 2021).

Another consequence of the tensile-only calibration methodology is the underestimation of material strength up to strains of around 2 % using the VC model. For instance, material test data and model predictions are shown in Figure 6.23. The VC model calibrated using the tensile-only method (“VC, tensile-only”) lies below the test data until around 2 % (i.e., underestimates the material strength). Underestimating the material strength is expected to lead to an underestimation of pre-buckling component behavior, as material is continuously yielded up-to this point due to hardening. A lower initial yield stress can also affect the simulated buckling mode as shown in Hartloper et al. (2021a). Finally, the error in peak-strength appears to be uniform considering tests with moderate axial load (calibration:  $\epsilon_s = 0.06$ , validation:  $\epsilon_s = 0.07$ ), however, it is notably higher under very high axial loads ( $\epsilon_s = 0.14$ ). This observation, along with generally higher errors in the very high axial load set, implies that simulations with very high axial loading (i.e.,  $P/P_{ym} \geq 0.50$ ) are more sensitive to the accuracy of the material model.

Two avenues of future research are proposed in-light of the importance of material modeling revealed by the preceding discussion. First, the Authors recommend that suites of uniaxial cyclic coupon tests, such as those in de Castro e Sousa et al. (2020), be conducted to calibrate model parameters alongside future component testing programs. Such information is important because full knowledge of the material’s behavior under cyclic loading allows for a better understanding of the component’s behavior through continuum finite element analysis. Second, additional material testing is required to increase the overall knowledge of structural steel materials subjected to inelastic cyclic loading. Such information can be quantified in terms of hardening metrics, for instance, as done in de Castro e Sousa et al. (2021). This knowledge can be used to define a general material behavior when the specific material properties cannot be known (i.e., in design scenarios), and to quantify uncertainty in materials’ cyclic behavior, as has been done for tensile loading (see e.g., Braconi et al. (2013)).

#### 6.4.2 Comparison of shell and solid element modeling

Full-shell and full-solid models provide nearly equivalent accuracy for modeling the tests used in this study, as shown by the error metric results in Figure 6.17. A major consideration in this

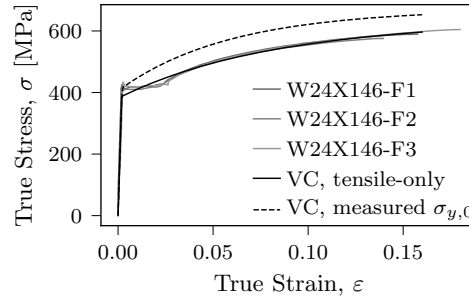


Figure 6.23 – Material results and Voce-Chaboche (VC) model predictions for specimens C1–C4 (W24X146 cross section) tested by Elkady and Lignos (2018a). VC, tensile-only parameters from Table 6.2.

equivalence is the reduction of local imperfection amplitudes in shell models by a factor of ten compared to solid element models. This is particularly evident in Figure 6.14, as the peak strength metric increases at  $\alpha = 100$  for solid element models indicating that the initiation of local buckling is delayed because of a too small imperfection. As previously established, a likely explanation for the lower imperfection amplitude in shell element models is that they do not include the fillet-radius of the k-area, whereas, this region is explicitly modeled by solid elements. The k-area, defined by  $k_1$  in Figure 6.24, is critical because it decreases the local plate slenderness of the flange and web and increases the local torsional restraint in this area. For instance, the length  $b_f/2 - k_1$  in solid element models is approximately 20 % smaller than  $b_f/2 - t_w/2$  in shell element models for a W24X84 section. The lack of the k-area in shell element models increases their proclivity to local buckling and, as such, the optimal local imperfection amplitude for shell element models has more of a model-fitting nature, rather than reflecting a precise physical magnitude. Given this modified local imperfection amplitude, shell element models are still an extremely useful computational tool as they can model beam-column components with equivalent accuracy to solid element models at a reduced computational cost.

The optimal local imperfection amplitude for solid element models of  $a_w = d/(10 \cdot 300)$  ( $\alpha = 10$ ) is explained by two factors. First, the local imperfections are assumed to have a shape that is congruent with the expected local buckling pattern. Second, the baseline local imperfection amplitudes,  $b_f/250$  and  $d/300$ , are specified based on the maximum amplitude of known measured cases. Altogether, these conditions lead to a worst-case scenario for the local imperfection shape, location, and amplitude—an upper bound to the degrading response. It thus seems reasonable that experimental cases would fall below the worst-case simulated response; it is in this context that the imperfection amplitudes are reduced by a factor of 10. Such assumptions regarding the imperfections are necessary in this study because measurements of the actual imperfections were not made for any of the tests in Table 6.1.



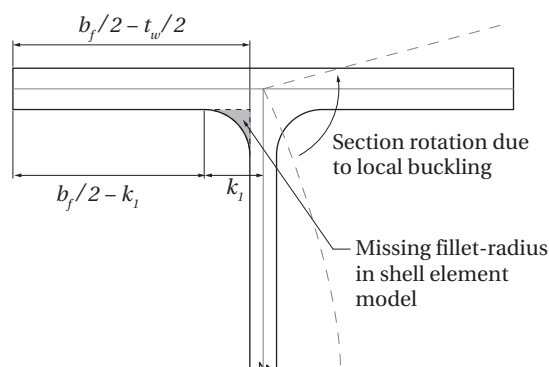


Figure 6.24 – Zoom on k-area of a W24X84 section to highlight the difference between solid and shell element discretizations.

Following the above discussion, it is anticipated that the direct use of measured imperfections is most accurate when combined with a solid element model because the k-area is explicitly modeled and abides by the physical conditions of the problem.

The absence of an explicit consideration of the k-area region can induce important discrepancies between simulated and experimental responses in shell element models (see Figure 6.16). This discrepancy is believed to be related to model shortcomings, rather than solely due to the lack of knowledge of the actual imperfections in tests, as the recommended imperfection amplitudes for shell element models are significantly below baseline magnitudes. Faced with these model shortcomings within the range of specimens assessed in this study, a modeler may make a compromise when using shell element models by either: (a) excluding global imperfections or significantly diminishing their scale; or (b) increasing the local imperfection amplitude (e.g., by setting  $\alpha = 1$ ) and sacrificing accuracy in problems where instabilities initiate through local buckling. Option (a) is used in this study since the global imperfection has a negligible influence on the metric outcomes for the simulated cases investigated in this study (see Figure 6.15) and the measured imperfections are unavailable for the suite of tests examined herein. It is made explicit that this approach *should not* be used for members where strength degradation initiates through flexural buckling (for example, but not limited to, braces and columns subjected to only axial loading) or when the expected behavior is completely unknown to the modeler. While this shortcoming can be avoided altogether by using a solid element model instead of a shell element model, this comes at an important increase to the computational cost.

The discussed shell element model shortcomings may become significant in the assessment of first story end columns within tall steel MRFs subjected to long period ground motions. Under these conditions, end columns experience maximum compressive axial load demands of  $P/P_{ym} \geq 0.50$  (i.e., defined as very high in this study) for more than few seconds due to dynamic overturning effects combined with lateral drift demands (Akcelyan, 2017; Suzuki and

Lignos, 2020). The aforementioned conditions imply that such columns may be susceptible to flexural buckling or coupled local and flexural buckling, in which cases the global imperfection may become influential in predicting the component's response. Appropriate shell element modeling recommendations for beam-columns subjected to these loading conditions motivates further physical experimentation to better comprehend their behavior.

### 6.4.3 Comparison to existing modeling guidelines

The guidelines for full-shell models summarized in Figure 6.2 and Table 6.3 contain a few important differences when compared with existing guidelines identified in the introduction (Newell and Uang, 2008; Fogarty and El-Tawil, 2015; Araújo et al., 2017; Elkady and Lignos, 2018b; Wu et al., 2018). The first difference is the recommendation for material modeling. An approach often used to define the VC model parameters is to use the measured yield stress from a tensile test in conjunction with cyclic hardening parameters from representative tests on the same steel grade. This approach is denoted as “VC, measured  $\sigma_{y,0}$ ” in Figure 6.23, with the parameters  $\sigma_{y,0} = 414$  MPa (Elkady and Lignos, 2018a),  $C_1 = 3378$  MPa,  $\gamma_1 = 20$ ,  $Q_\infty = 90$  MPa, and  $b = 12$  (Elkady and Lignos, 2018b). The “VC, measured  $\sigma_{y,0}$ ” prediction clearly overestimates the tested stress-strain at all points because the VC model does not account for the yield plateau region (i.e., the effects of discontinuous yielding). Modelers should be cognizant that, for the VC model, which has been largely used to date, using the measured yield stress in combination with cyclic hardening parameters calibrated to other coupon tests leads to an *overestimation* of the tensile stress-strain response. Correcting the initial yield stress is motivation to use, e.g., the UVC model (Hartloper et al., 2021a) in-place of the VC model, and conducting cyclic coupon tests to calibrate its parameters.

The second difference is that the shell element size proposed in the current study is smaller than the 20–25 mm proposed elsewhere (Fogarty and El-Tawil, 2015; Araújo et al., 2017; Elkady and Lignos, 2018a; Wu et al., 2018). Element size is important because models built from displacement-based finite elements are overly stiff when the element size is large compared to the size corresponding to the true finite element solution (Bathe, 1996). For instance, the flexural strength shown in Figure 6.9 converges to a lower-bound value as the mesh size decreases (i.e., the model's stiffness decreases as the element size decreases). An appropriately small element size is important to capture the initiation and progression of local buckling and the residual plastic curvature effect (Lee and Lee, 1994) that occurs after the initiation of yielding. This is especially important for cyclic loading because the residual plastic curvature acts as an imperfection upon loading in the opposite direction and local buckling compounds with each cycle.

The third difference is that a smaller local imperfection amplitude is recommended compared to the  $a_{f,prior} = b_f/250$  proposed in, e.g., Araújo et al. (2017) and Elkady and Lignos (2018a). The smaller imperfection amplitude used herein is a product of: (a) calibrating con-

stitutive model parameters in a way that does not overestimate the material's stress-strain response, and (b) using an element size based on results from the mesh convergence study shown in Figure 6.9. Increasing the element size and overestimating the material strengths tends to increase a finite element model's flexural strength and stiffness, therefore, a larger imperfection amplitude appears to be required under these conditions. This justifies the recommendations of prior studies (Elkady and Lignos, 2018b). As already discussed, the proposed imperfection amplitude in solid-element models of  $a_f = b_f/2500$  accounts for the assumptions on the local imperfection geometry, and the amplitude in shell-element models of  $a_f = b_f/25000$  also accounts for the fact that the k-area is not explicitly modeled.

The effect of using a larger imperfection amplitude is most notable when modeling beam-columns subjected to monotonic lateral loading and constant axial load, e.g., see the  $\alpha = 1$  result in Figure 6.6. Simulated results with  $\alpha = 1$  are vastly different from the test data. Similar simulation results are expected in this case even if the element size is increased because monotonic tests are observed to be less sensitive to this parameter. The Authors are of the opinion that these observations regarding the element size and imperfection amplitude were made possible through recently developed methods for calibrating constitutive models to reduce the uncertainty in the material behavior (de Castro e Sousa et al., 2020; Hartloper et al., 2021a; de Castro e Sousa et al., 2021). Furthermore, the guidelines proposed in this study are considered to be general as they unify the modeling of beam-columns subjected to monotonic and cyclic lateral loading.

#### 6.4.4 Recommendations for component macro models

Macro model guidelines are fully defined for the tests in Table 6.1 by: the selection of critical regions shown in Figure 6.7, continuum domain modeling guidelines proposed in Table 6.3, residual stresses according to Young (1972), the number of beam-column elements in Equation 6.7, and the continuum length,  $L_{\Omega_2}$  in Equation 6.8. Conditioned that these guidelines are followed, for the cases investigated, the average energy error between full-shell and macro-shell models is 3 %, the error in peak-strength is 0 %, and the error in axial shortening is 2 %. Perfect agreement in the peak-strength between the macro and the full-shell models indicates that the pre-peak behavior and initiation of local buckling is fully captured by the macro model. These conclusions are stated regardless of the member's geometry, axial load ratio, direction of lateral loading, and employed loading protocol. The component macro model approach is generalized through these recommendations for simulating steel wide flange beam-columns subjected to multiaxis loading.

An alternative to the macro model approach is to use a full-continuum approach and increase the element size outside of the critical regions. In this case, Equation 6.8 may be used to determine the extent of the critical regions in which a fine mesh is to be used. In this light, the macro model is considered to provide an upper bound on the reduction in computational

cost in terms of DOFs and memory use. A detailed study regarding the grading of element sizes is required to provide general recommendations if this alternative method is used, and is therefore, left for future research.

### 6.4.5 Limitations

The most notable limitation in this study is the lack of test data available for calibration of the full-continuum guidelines. The lack of test data for calibration is, in-part, rooted in the lack of cyclic material data corresponding to beam-column tests. For this reason, we suggest that cyclic coupon data, such as that summarized in de Castro e Sousa et al. (2020), be collected in future tests. It is also acknowledged that the recommendations in this chapter apply to the ranges of parameters that are contained in Table 6.1. Although it was not shown in this study, the guidelines are expected to hold for other components, as evidenced by the subassembly macro model simulation in Hartloper et al. (2021b). Moreover, the reliability of modeling recommendations could be increased through further calibration with tests where the material behavior, residual stresses, and initial geometric imperfections are all known, where these tests consist of a wide array of geometries, boundary conditions, and applied loading. Other limitations that can be explored and clarified through additional research are the effects of loading rate (i.e., considering rate-dependent plasticity) and the influence of uncertainty in defined parameters on the component and structural responses.

## 6.5 Summary and conclusions

Recommendations to construct mixed-dimension macro model of steel wide flange columns subjected to multi-axis cyclic loading are proposed in this chapter. Three objectives were met in support of this aim. First, guidelines for full-continuum (shell and solid) finite element models were proposed. These guidelines are summarized in Figure 6.2, where parameters determined in this study are provided in Table 6.3. Second, guidelines for a mixed-dimension macro model were proposed using shell and beam-column elements. The beam-column element mesh recommendations are contained in Equation 6.7, and the length of the continuum domain is contained in Equation 6.8. Third, the computational efficiency of the proposed macro model approach was identified, as summarized in Figure 6.22.

The main conclusions are summarized as follows:

- Reducing the element sizes of current modeling recommendations is deemed to be critical in unifying the accuracy in predicting cyclic and monotonic component-level tests. A linear shell element size of 12.5 mm is recommended for the members evaluated in this study. This element size is smaller than used in previous studies.
- Shell element models that predict test results with the least error have a local imperfec-

tion amplitude that is two orders of magnitude below the maximum permissible amplitude set by international manufacturing standards. This result is primarily attributed to the omission of the k-area in shell element models. Continuum finite element models constructed with quadratic solid elements perform well with imperfection amplitudes close to measured values under the proposed modeling assumptions because they explicitly model the k-area. Therefore, solid element models are expected to provide the best accuracy if measured imperfections are used.

- Tests with well-defined material information were predicted with an overall accuracy of 14 % (calibration dataset), tests with lower-quality material information were predicted with an overall accuracy of 24 % (validation dataset). High-quality material data is deemed fundamental to improve modeling accuracy and is recommended to be included when testing structural steel components to further improve the state-of-the-art in predictive modeling of steel beam-columns.
- For macro models to maintain the fidelity of full-continuum models, a shell-domain length corresponding to 25 % of the entire member length is recommended for beam-columns with  $\bar{\lambda}_{LT} < 0.4$ . A shell-domain length corresponding to 30 % of the entire length is recommended for members with  $\bar{\lambda}_{LT} \geq 0.4$ .
- Following these recommendations, the macro model approach can reduce the computational effort, in terms of memory and degrees of freedom, by around 50 %. The average error between the full-shell and macro models is only 3 %. These observations hold regardless of the beam-column's geometry, loading, and boundary conditions.

## 6.6 Data availability

Some or all data, models, or code generated or used during the study are available in a repository or online in accordance with funder data retention policies. This includes: the code used for material calibration (de Castro e Sousa et al., 2019); the code for the constitutive models (Hartloper, 2019); and the code for the warping-inclusive kinematic coupling (Hartloper, 2020).

Some or all data, models, or code that support the findings of this study are available from the corresponding author upon reasonable request. This includes the finite element models used to generate the results of this study and the beam-column test data.

## 6.7 Acknowledgements

This study is based on work supported by EPFL and by the Swiss National Science Foundation (Project No. 200021\_188476) for the first author, and an EPFL internal grant for the second

author. The financial support is gratefully acknowledged. Any opinions, findings, and conclusions or recommendations expressed in this chapter are those of the authors and do not necessarily reflect the view of sponsors. The Authors sincerely thank Professor Ahmed Elkady from the University of Southampton for allowing the use of the photos in Figures 6.1a, 6.7, and 6.16 and providing the experimental data for the tests in Table 6.1. The Authors sincerely thank Mr. Julien Cravero from Ecole des Ponts ParisTech for allowing the use of the photos in Figures 6.6 and 6.7 and experimental data for tests in Table 6.1. The Authors sincerely thank Dr. Yusuke Suzuki from Nippon Steel Corporation for providing experimental data for tests in Table 6.1.

## 6.8 Notation

*The following symbols are used in this chapter:*

- $a_f$  = maximum local imperfection amplitude at the flange tip;
- $a_w$  = maximum local imperfection amplitude at the web center;
- $b$  = rate of isotropic hardening;
- $b_f$  = flange width;
- $C_1$  = magnitude term for backstress 1;
- $d$  = section depth;
- $E$  = elastic modulus;
- $f_{ym}$  = measured yield stress;
- $h$  = inner web depth;
- $I_t$  = torsion constant;
- $I_w$  = warping constant;
- $I_y$  = moment of inertia about weak axis;
- $k_1$  = distance from center of web to flange toe of fillet;
- $L$  = component length;
- $L_{bw}$  = wavelength for global local imperfection;
- $L_{\Omega_2}$  = length of the continuum element domain;
- $L^*$  =  $L/2$  for members in double-curvature,  $L$  for members in single curvature;
- $M$  = base moment;
- $P$  = applied axial force;
- $P_{ym}$  = measured axial yield strength;
- $Q_\infty$  = magnitude of isotropic hardening at model saturation;
- $t_f$  = flange thickness;
- $t_w$  = web thickness;
- $Z_x$  = plastic section modulus about strong axis;
- $\alpha$  = scale factor for local imperfection amplitude;

$\beta$	=	scale factor for global imperfection amplitude;
$\gamma_1$	=	rate of kinematic hardening for backstress 1;
$\delta_{axial}$	=	axial shortening;
$\epsilon_a$	=	axial shortening metric;
$\epsilon_e$	=	energy metric;
$\epsilon_s$	=	peak-strength metric;
$\epsilon$	=	true strain;
$\theta$	=	chord rotation;
$\theta^*$	=	accumulated chord rotation;
$\bar{\lambda}_{LT}$	=	lateral-torsional slenderness;
$\mu_{LN}$	=	mean of log-normal distribution;
$\nu$	=	Poisson's ratio;
$\sigma$	=	true stress;
$\sigma_{LN}$	=	standard deviation of log-normal distribution; and
$\sigma_{y,0}$	=	constitutive model initial yield stress.





## **Conclusions and backmatter**

### **Part III**



## 7 Conclusion and future work

### 7.1 Summary of work completed in this thesis

The thesis is first summarized on a chapter-by-chapter basis. Each chapter summary includes a brief motivation for each study, pertinent results, and the main conclusions. The expected impact of the work carried out in this thesis is then stated and recommendations are provided for future research building on this thesis.

#### 7.1.1 Chapter 2: Constitutive modeling of structural steels: A nonlinear isotropic/kinematic hardening material model and its calibration

Calibrating the Voce-Chaboche (VC) material model in a consistent manner reveals that the VC model systematically underestimates the initial yield stress in structural steels by at least 10–30 %. This underestimation is attributed to the discontinuous yielding phenomenon in these materials. An updated Voce-Chaboche (UVC) material model is proposed in this chapter to address this issue by modifying the isotropic hardening rule of the VC model. Moreover, sufficient conditions are derived and imposed on the UVC parameters to impose a non-softening response regardless of the applied inelastic strain demands. A consistent calibration procedure is developed for structural steels subjected to earthquake-induced inelastic cyclic straining. The material model implementation is validated in commercial and open-source finite element analysis programs for uniaxial, plane-stress, and multiaxial stress states. The code is made publicly available through Hartloper (2019).

The main conclusions are summarized as follows:

- Parameters for the UVC material model are provided for a database of nine structural steels commonly used in North America, Japan, and Europe. The initial yield stress is increased by nearly 20 % using the UVC model over the VC model. A 19 % relative improvement in the overall material model accuracy is found when compared to the VC

model. The full calibration procedure of the UVC model is made publicly available in the open source Python package RESSPyLab de Castro e Sousa et al. (2019).

- At least two backstresses are necessary for the UVC model to accurately represent the behavior of the investigated steel materials. One backstress leads to an underfitting of the kinematic hardening component of the constitutive material law.
- Results from the conducted parametric study suggest that the simulated geometric instabilities in steel wide flange beam-columns that arise under multiaxis loading are sensitive to the material model and input parameters for the studied column geometry.
- Findings from the presented case study should be supported by full-scale tests where the imperfections, residual stresses within the cross section, and material characteristics are fully quantified beforehand to reliably evaluate the effect of material initial conditions among other considerations. Furthermore, effects that influence the hardening mechanisms and spread of plasticity within the plastic hinge length of beam-columns, such as the rate of applied loading, should also be explored in the future by means of large-scale physical testing.

### 7.1.2 Chapter 3: Cyclic metal plasticity model parameters with limited information: A constrained optimization approach

Information on the cyclic behavior of structural steel materials is fairly scarce, while standard tensile tests are ubiquitous. Material parameters calibrated in a consistent manner reveal that metrics representing the behavior of structural steel materials under inelastic cyclic straining are fairly consistent between several mild steels. A framework is developed to calibrate constitutive model parameters using only standard tension tests in the case that cyclic material tests are not available. This framework uses constrained optimization to impose the *a priori* hardening information on the constitutive model parameters. The procedure is incorporated into the publicly available, open-source Python library, RESSPyLab (de Castro e Sousa et al., 2019).

The main conclusions are summarized as follows:

- The definition of adequate material cyclic-performance metrics is an essential part in the constrained optimization procedure. Metrics are proposed herein that relate typical ratios of isotropic to kinematic hardening and their rates in order to inform the constrained optimization procedure.
- The number of backstresses used in the kinematic part of the models plays a significant role in the accuracy of tensile-only parameter estimates.

- The UVC model does not provide satisfactory results in parameter estimates in the tensile-only constrained optimization, regardless of the number of backstresses employed.
- The VC model with two backstresses does not provide satisfactory estimates of material response for tensile-only calibrations with the constraints presented herein. More data can however motivate different constraints.
- On the other hand, the VC model with one backstress yields satisfactory results when its parameters are calibrated through the proposed methodology. Therefore, this is the recommended material model if a modeler is faced with a situation where only standard tension test data is available.

### 7.1.3 Chapter 4: Warping-inclusive kinematic coupling in mixed-dimension macro models for steel wide flange beam-columns

Component macro models are proposed as a method to reduce the computational complexity of full continuum finite element (CFE) component models. A review of multipoint constraint (MPC) methods for coupling beam-column and continuum element domains reveals that an MPC coupling method that includes torsion-warping is required. The warping-inclusive kinematic coupling (WIKC) method is developed by enhancing a kinematic coupling method with torsion-warping for members featuring wide flange cross sections. The WIKC method is implemented in Abaqus v6.14 using a user defined MPC; open-access source code provided (Hartloper, 2020). Results, validated with test data, demonstrate that the fidelity of CFE models can be maintained at reduced computational expense for isolated beams and columns as well as beam-to-column subassemblies under both static and dynamic multiaxis cyclic loading.

The main conclusions are summarized as follows:

- Including warping in the coupling formulation may be critical in accurately estimating the full-continuum model failure mode and, therefore, should be included for general use. This is especially true for components subjected to nonuniform torsion, or that are susceptible to coupled local and lateral-torsional instabilities, i.e., if the non-dimensional lateral torsional slenderness is  $\bar{\lambda}_{LT} > 0.4$ .
- A nonlinear, finite-rotation constraint formulation appears to be necessary for nonlinear problems, and there do not appear to be any computational advantages offered by the linear coupling method. Linear, small-rotation coupling methods seem to be acceptable for eigenvalue analyses, as well as problems not dominated by torsion if: (i) lateral-torsional buckling (LTB) is not critical, (ii) the angle of twist is less than 0.10 rad, and (iii) the column lateral drift ratio is below 10 %. If twisting is the dominant mode of

deformation, the angle of twist should remain below 0.05 rad if a linear coupling method is employed.

- The macro model approach leads to a reduction in the DOFs and memory usage proportional to the ratio of the beam-column element domain length to the total component length. The macro model approach does not appear to negatively affect the rate of convergence compared to the full-continuum model, therefore, the computational time savings are expected to be a function of the DOF reduction.

### 7.1.4 Chapter 5: Best-fit constraint equations for coupling mixed-dimension simulation models with wide flange cross sections

A new MPC method is developed to couple beam-column and continuum element domains. Seven constraint equations are proposed that couple the degrees-of-freedom of a dependent beam-column element node with the independent interface continuum element nodes. The proposed equations make a link between the kinematics of a beam-column element and the procedure for fitting a plane-of-best-fit to a point cloud. Analysis conducted in this chapter provides the basis for a method to deduce the torsion-warping amplitude within the proposed framework. Elastic stress distributions determined through beam mechanics are used to form the constraint coefficient matrix within the context of nonlinear finite element analysis. The proposed method is implemented as a user MPC in Abaqus v6.14, and the source code is made publicly available (Hartloper, 2021). Two examples are used to validate the method for coupling beam-column and shell elements.

The main conclusions are summarized as follows:

- The proposed method is validated for nonlinear finite element problems coupling beam-column and shell elements. Thus, the objectives set at the outset of (1) using the least number of constraint equations, and (2) including torsion-warping, are satisfied.
- The proposed method can improve the interface stress distribution under certain loading conditions over other methods (e.g., the built-in kinematic coupling method in Abaqus v6.14).
- Global Newton iterations may not converge after the elements on the interfaces begin to yield due to the assumed elastic stress distributions. While this may be a limitation in certain problems of interest, the proposed method could still be used in the context of simulation-assisted design for stability problems (Ziemian and Abreu, 2018; Ziemian et al., 2018). Further work is required to make the method amenable to inelastic interfaces.

### 7.1.5 Chapter 6: Mixed-dimension modeling of steel wide flange beam-columns under multiaxis loading

Macro models for steel beam-column components are defined by parameters such as: the mesh discretization in each domain, the initial geometric imperfections important in the modeling of geometric instabilities, and the proportion of the continuum element domain to the beam-column element domain. General recommendations for the definitions of these parameters allows for the practical use of macro models in frame simulation studies. Recommendations for constructing component models of steel wide flange beam-columns are developed in this chapter on the basis of advancements in constitutive modeling and coupling developed in earlier chapters. These recommendations are developed and validated using comparisons with data from physical experiments on steel beam-columns. Accuracy in predicting physical component behavior is measured in this study through objective metrics, the recommended modeling parameters are those that lead to minimal errors.

The main conclusions are summarized as follows:

- Reducing the element sizes of current modeling recommendations is deemed to be critical in unifying the accuracy in predicting cyclic and monotonic component-level tests. A linear shell element size of 12.5 mm is recommended for the members evaluated in this study. This element size is smaller than used in previous studies.
- Shell element models that predict test results with the least error have a local imperfection amplitude that is two orders of magnitude below the maximum permissible amplitude set by international manufacturing standards. This result is primarily attributed to the omission of the k-area in shell element models. Continuum finite element models constructed with quadratic solid elements perform well with imperfection amplitudes close to measured values under the proposed modeling assumptions because they explicitly model the k-area. Therefore, solid element models are expected to provide the best accuracy if measured imperfections are used.
- Tests with well-defined material information were predicted with an overall accuracy of 14 % (calibration dataset), tests with lower-quality material information were predicted with an overall accuracy of 24 % (validation dataset). High-quality material data is deemed fundamental to improve modeling accuracy and is recommended to be included when testing structural steel components to further improve the state-of-the-art in predictive modeling of steel beam-columns.
- For macro models to maintain the fidelity of full-continuum models, a shell-domain length corresponding to 25 % of the entire member length is recommended for beam-columns with  $\bar{\lambda}_{LT} < 0.4$ . A shell-domain length corresponding to 30 % of the entire length is recommended for members with  $\bar{\lambda}_{LT} \geq 0.4$ .

- Following these recommendations, the macro model approach can reduce the computational effort, in terms of memory and degrees of freedom, by around 50 %. The average error between the full-shell and macro models is only 3 %. These observations hold regardless of the beam-column's geometry, loading, and boundary conditions.

### 7.2 Impact and future research topics

The overarching aim of this thesis was to propose reduced-order simulation models for steel beam-column components that match the fidelity of full continuum element models at a diminished computational expense. On the path to achieve this goal, constitutive modeling of structural steels subjected to earthquake-induced inelastic strain demands was made more accurate compared to the classic Voce-Chaboche model through the development of an updated material model; and two new methods for coupling beam-column and continuum element domains that include torsion-warping were developed. The fidelity of CFE component models is maintained at a reduced computational cost through the proposed component macro model approach that makes use of the updated material model and warping-inclusive kinematic coupling method. The proposed macro model is efficient for the investigated range of steel beam-columns, as it reduces memory requirements and the number of degrees-of-freedom of benchmark CFE analyses by around 50 %. It is also accurate, as the average error between the benchmark CFE and macro model analyses is only 3 %.

The advances in material modeling developed in this thesis can be used to reduce the uncertainty in steel component simulations related to material behavior. Reducing this uncertainty allows analysts to better understand influential modeling parameters, to better comprehend component behavior through simulations, and to better predict component behavior for simulation-assisted design. The development of numerical models that can explicitly simulate coupled geometric instabilities and material inelastic behavior at a lower computational cost is important in scenarios where multiple analyses are required, such as probabilistic assessments and uncertainty quantification. This may be especially useful, for example, in performance-based assessment and design, in benchmarking lower-fidelity simulation models, in the process of developing new structural systems for buildings, and to motivate innovation in high-performance steel materials to target specific performance objectives. The aforementioned impacts of this thesis all ultimately support the objectives of improving the safety and cost efficiency of buildings subjected to earthquake loading.

The contributions of this thesis are further expounded upon through the following research topics.



**7.2.1 Finite element model validation through detailed physical experiments on beam-columns**

As highlighted throughout this thesis, there is a need for detailed physical component testing for the purpose of further validating and improving upon finite element models of steel beam-columns. For instance, in Chapter 2, the importance of future physical experiments for validating the differences between simulation models that employ either the VC or UVC material models is stated. In Chapter 6, the importance of physical experiments for expanding on the range of parameters is outlined, particularly members with relatively high lateral-torsional slenderness in terms of  $\bar{\lambda}_{LT}$ . The need for experiments with measured initial geometric imperfections and residual stresses is apparent for further evaluating the proposed macro model recommendations. Furthermore, the time-dependent behavior of structural steel materials (i.e., strain rate effects and strain ageing) have thus-far been neglected in finite element simulations conducted in this thesis.

Potential research aims related to these needs are to conduct physical experiments on steel beam-column components to better validate finite element models, and to better comprehend the influence of time-dependent effects on steel beam-column component behavior through component and material testing. Component tests with known data regarding the geometry, initial geometric imperfections, material, and residual stresses may be used to provide insight into potential gaps in the state-of-the-art for steel beam-column simulations. Meanwhile, strain rates under real-time loading conditions and the strain ageing present in structural steel materials may influence yielding stress on the order of 10 % (Fujimoto et al., 1978; Lamarche and Tremblay, 2011). Both the aforementioned effects warrant investigation as Chapter 2 showed that simulated geometric instabilities may be sensitive to changes in the initial yield stress within this margin. The influence of strain ageing may be particularly important for studying mainshock/aftershock series in earthquake engineering where the material has time to age. Addressing these research topics can improve numerical models for steel beam-column components, and ultimately leads to more reliable simulations of steel structures.

**7.2.2 Advancing the development of fiber-based reduced-order models**

The computational complexity of performance-based earthquake engineering due to its probabilistic nature has been highlighted throughout this thesis. The macro model proposed in this thesis is estimated to reduce computational costs for beam-column components by around 50 %, however, for certain applications users may desire an even more efficient approach. For this reason, a future aim may be to further reduce the computational effort of the macro model proposed in this thesis while still simulating nonlinear material behavior and coupled geometric instabilities. One potential method of achieving this goal is to develop a fiber-based beam-column element that represents strength and stiffness degradation in

steel beam-columns due to coupled geometric instabilities. Computationally, this approach is promising as fiber-based models are expected to result in less degrees-of-freedom and integration points than the continuum elements used in critical regions of macro models.

Strength degradation in fiber-based beam-column elements could be represented through analytical equations in a similar manner to Möller et al. (1997) who developed a model for cruciform sections subjected to monotonic axial loading. Analytical equations to predict local inelastic geometric instabilities in steel beam-columns subjected to multiaxial loading require significant evolution to accomplish this task. Additionally, issues arising from strain localization as well as mesh dependency in the post-peak response should be carefully addressed. Through this proposed research, further lowering the computational cost would be beneficial for probabilistic assessments, such as those in performance-based earthquake engineering. Furthermore, analytical equations for local inelastic instabilities would also prove useful to inform design guidelines for high-performance steel materials for which the current semi-empirical equations are not fully satisfactory (Galambos et al., 1997).

### 7.2.3 Frame simulation studies

Frame simulations within the performance-based earthquake engineering framework are typically conducted using concentrated plasticity component models. Such simulations come with the limitations of concentrated plasticity component models outlined in Chapter 4. The natural extension of the research conducted in this thesis is to study steel frame structures subjected to earthquake loading using the proposed macro model instead of a concentrated plasticity model. Potential aims of a frame simulation study could be to benchmark existing concentrated plasticity methods of constructing structural models, and to investigate the sensitivity of engineering demand parameters (EDPs) to model variables that cannot be easily assessed using a lower-fidelity modeling approach.

A methodology for modeling steel frame structures evolving from the recommendations in Chapters 4 and 6 is required to achieve the aforementioned aims. The realization of this methodology entails several research objectives. For instance, macro models for beam-to-column subassemblies in steel frame structures should be further validated with experimental data using the framework established in Chapter 6. Additionally, recommendations are required for factors such as the influence of composite action in the beams of moment-resisting frames due to the presence of the concrete floor slab (El Jisr et al., 2020), and the incorporation of the gravity load supporting system in the macro modeling context (Elkady and Lignos, 2015b). Recommendations are also required to account for the inherent damping in buildings that is not explicitly represented in a typical structural model (e.g., due to non-structural components in buildings, friction within bolted connections, etc.).

Finally, additional methods to increase the computational savings when modeling frames can be explored. As discussed in Chapter 4.5.2, the macro model can be applied selectively

depending on the desired level of fidelity in particular regions (e.g., for first-story columns), whereas it may be possible to model the rest of the frame using a lower fidelity approach. Selective application of the macro model could be further improved through an adaptive meshing strategy (see e.g., Molinari and Ortiz (2002)) to determine where to place continuum element domains throughout the analysis only as they are needed. Such an adaptive meshing strategy may dramatically decrease the overall computational cost while retaining solution accuracy.

One interesting impact of using the proposed macro model in frame simulations is to benchmark existing concentrated plasticity modeling approaches. Benchmarking existing approaches is important in understanding the efficacy of these models for risk and loss assessment. Furthermore, the influence of effects that are not explicitly modeled by current concentrated plasticity approaches, such as axial shortening (Elkady et al., 2020), can be directly accounted for using the proposed macro model approach. In terms of sensitivity analyses, studies such as Ibarra and Krawinkler (2005); Liel et al. (2009); Vamvatsikos and Fragiadakis (2010) have shown that the most influential parameters in the prediction of structure's response up-to collapse are those associated with components' strength/stiffness degradation. The use of the macro model allows for uncertainty in structural performance to be quantified through parameters that conventional beam-column elements cannot easily incorporate into the degrading response; examples being: the material hardening characteristics, the initial geometric imperfections, and the residual stresses. Uncertainty quantification is important to determine how the most sensitive parameters can be best controlled to improve the safety and cost-efficiency of designs through the use of, for example, high-performance materials, novel structural systems, and improved construction practices.



## Bibliography

- Abel, J. F. and Shephard, M. S. (1979). "An algorithm for multipoint constraints in finite element analysis." *International Journal for Numerical Methods in Engineering*, 14(3), 464–467.
- AISC (2016a). "Seismic provisions for structural steel buildings." *ANSI/AISC 341-16*, American Institute of Steel Construction, Chicago, IL, USA.
- AISC (2016b). "Specification for structural steel buildings." *ANSI/AISC 360-16*, American Institute of Steel Construction, Chicago, IL, USA.
- Akcelyan, S. (2017). "Seismic retrofit of existing steel tall buildings with supplemental damping devices." PhD. Thesis, McGill University, Montreal, Quebec, Canada.
- Araújo, M., Macedo, L., and Castro, J. M. (2017). "Evaluation of the rotation capacity limits of steel members defined in EC8-3." *Journal of Constructional Steel Research*, 135, 11–29.
- Armstrong, P. J. and Frederick, C. (1966). "A mathematical representation of the multiaxial Bauschinger effect." *Report No. RD/B/N731*, Central Electricity Generating Board, Berkeley Nuclear Laboratories, London, UK.
- ASCE (2017). "Seismic evaluation and retrofit of existing buildings." *ASCE 41-17*, American Society of Civil Engineers, Reston, Virginia, USA.
- ASTM (2016a). "Standard specification for general requirements for rolled structural steel bars, plates, shapes, and sheet piling." *A6/A6M-16a*, ASTM International, West Conshohocken, PA, USA.
- ASTM (2016b). "Standard test methods for tension testing of metallic materials." *E8/E8M - 16a*, ASTM International, West Conshohocken, PA, USA.
- ASTM (2018). "Standard terminology relating to steel, stainless steel, related alloys, and ferroalloys." *A941-18*, ASTM International, West Conshohocken, PA, USA.
- ATC (2017a). "Guidelines for nonlinear structural analysis and design of buildings. Part IIa: Steel moment frames." *Report No. NIST GCR 17-917-46v2*, National Institute of Standards and Technology, Gaithersburg, MD, USA.

## Bibliography

---

- ATC (2017b). "Recommended modeling parameters and acceptance criteria for nonlinear analysis in support of seismic evaluation, retrofit, and design." *Report No. NIST GCR 17-917-45*, National Institute of Standards and Technology, Gaithersburg, MD, USA.
- Bathe, K.-J. (1996). *Finite Element Procedures*. Prentice Hall, New Jersey, USA.
- Bierlaire, M. (2015). *Optimization: Principles and algorithms*. EPFL Press, Lausanne, Switzerland.
- Bouaziz, O., Aouafi, A., and Allain, S. (2008). "Effect of grain refinement on the mechanical behaviour of ferritic steels: Evolution of isotropic hardening and kinematic hardening." *Materials Science Forum*, 584-586 PA, 605–609.
- Braconi, A., Finetto, M., Degee, H., Hausoul, N., Hoffmeister, B., Gündel, M., Karmanos, S. A., Varelis, G., Obiala, R., Hjaij, M., Somja, H., Badalassi, M., Caprili, S., Salvatore, W., Pappa, P., and Rinaldi, V. (2013). *Optimising the Seismic Performance of Steel and Steel-Concrete Structures by Standardising Material Quality Control (OPUS)*. European Commission Research Fund for Coal and Steel, Luxembourg.
- Budaházy, V. and Dunai, L. (2013). "Parameter-refreshed Chaboche model for mild steel cyclic plasticity behaviour." *Periodica Polytechnica. Civil Engineering; Budapest*, 57(2), 139–155.
- Bureau, A. (2008). "NCCI: Elastic critical moment for lateral torsional buckling.
- Byrd, R. H., Hribar, M. E., and Nocedal, J. (1999). "An interior point algorithm for large-scale nonlinear programming." *SIAM Journal on Optimization*, 9(4), 877–900.
- CEN (1993). "Structural steel I and H sections. Tolerances on shape and dimensions." *EN 10034:1993*, European Committee for Standards, Brussels, Belgium.
- CEN (2001). "Metallic materials - Tensile testing Part 1: Method of test at ambient temperature." *EN 10002-1:2001*, European Committee for Standardization (CEN).
- CEN (2005a). "Design of steel structures Part 1-1: General rules and rules for buildings." *EN 1993-1-1*, European Committee for Standardization (CEN), Brussels, Belgium.
- CEN (2005b). "Eurocode 3: Design of steel structures - Part 1-1: General rules and rules for buildings." *EN 1993-1-1*, European Committee for Standardization (CEN), Brussels, Belgium.
- CEN (2005c). "Eurocode 8: Design of structures for earthquake resistance - Part 3: Assessment and retrofit of buildings." *EN 1998-3*, European Committee for Standardization, Brussels, Belgium.

- CEN (2005d). “Hot rolled products of structural steels - Part 2: Technical delivery conditions for non-alloy structural steels.” *NF EN 10025-2*, European Committee for Standardization (CEN), Brussels, Belgium.
- CEN (2019a). “Hot rolled products of structural steels - Part 3: Technical delivery conditions for normalized/normalized rolled weldable fine grain structural steels.” *NF EN 10025-3*, European Commission for Standardization (CEN), Brussels, Belgium.
- CEN (2019b). “Hot rolled products of structural steels - Part 6: Technical delivery conditions for flat products of high yield strength structural steels in the quenched and tempered condition.” *NF EN 10025-6*, European Commission for Standardization (CEN), Brussels, Belgium.
- Chaboche, J. L., Van, K. D., and Cordier, G. (1979). “Modelization of the strain memory effect on the cyclic hardening of 316 stainless steel.” *Proceedings of the 5th International Conference on Structural Mechanics in Reactor Technology*, Berlin, Germany, North-Holland Publishing Co.
- Chavan, K. S. and Wriggers, P. (2004). “Consistent coupling of beam and shell models for thermo-elastic analysis.” *International Journal for Numerical Methods in Engineering*, 59(14), 1861–1878.
- Chen, W.-F. and Atsuta, T. (2008). *Theory of beam-columns Volume 2: Space behavior and design*. J. Ross Publishing, Fort Lauderdale, FL, USA.
- Cofie, N. G. and Krawinkler, H. (1985). “Uniaxial cyclic stress-strain behavior of structural steel.” *Journal of Engineering Mechanics*, 111(9), 1105–1120.
- Conn, A. R., Gould, N. I. M., and Toint, P. L. (2000). *Trust region methods*. MOS-SIAM Series on Optimization. Society for Industrial and Applied Mathematics, Philadelphia, PA, USA.
- Cooke, R. and Kanvinde, A. (2015). “Constitutive parameter calibration for structural steel: Non-uniqueness and loss of accuracy.” *Journal of Constructional Steel Research*, 114, 394–404.
- Cornell, C. A. and Krawinkler, H. (2000). “Progress and challenges in seismic performance assessment, <<https://apps.peer.berkeley.edu/news/2000spring/performance.html>>.”
- Cottrell, A. H. and Bilby, B. A. (1949). “Dislocation theory of yielding and strain ageing of iron.” *Proceedings of the Physical Society. Section A*, 62(1), 49–62.
- Cravero, J., Elkady, A., and Lignos, D. G. (2020). “Experimental evaluation and numerical modeling of wide-flange steel columns subjected to constant and variable axial load coupled with lateral drift demands.” *Journal of Structural Engineering*, 146(3), 04019222.

## Bibliography

---

- D’Aniello, M., Landolfo, R., Piluso, V., and Rizzano, G. (2012). “Ultimate behavior of steel beams under non-uniform bending.” *Journal of Constructional Steel Research*, 78(Supplement C), 144–158.
- Dassault Systèmes (2014). *Abaqus standard and Abaqus documentation for version 6.14*. Dassault Systèmes Simulia Corp., Providence, RI, USA.
- de Castro e Sousa, A., Hartloper, A. R., and Lignos, D. G. (2019). “RESSPyLab version 1.0 - Python tools for structural steel research, <<https://pypi.org/project/RESSPyLab/>>.”
- de Castro e Sousa, A., Hartloper, A. R., and Lignos, D. G. (2021). “Cyclic metal plasticity model parameters with limited information: A constrained optimization approach.” *Journal of Engineering Mechanics*, (In-press).
- de Castro e Sousa, A. and Lignos, D. G. (2017). “Residual stress measurements of European hot-rolled I-shaped steel profiles.” *Technical Report 231302*, Resilient Steel Structures Laboratory, École Polytechnique Fédérale de Lausanne (EPFL), Lausanne, Switzerland.
- de Castro e Sousa, A., Suzuki, Y., and Lignos, D. (2020). “Consistency in solving the inverse problem of the Voce-Chaboche constitutive model for plastic straining.” *Journal of Engineering Mechanics*, 146(9), 04020097.
- Deierlein, G. G. and Zsarnóczay, A. (2019). “State-of-art in computational simulation for natural hazards engineering.” *Report No. 2019-01*, NHERI SimCenter, Richmond, California, USA (February).
- Di Re, P., Addessi, D., and Filippou, F. C. (2016). “3D beam-column finite element under non-uniform shear stress distribution due to shear and torsion.” *Proceedings of the VII European Congress on Computational Methods in Applied Sciences and Engineering (ECCOMAS Congress 2016)*, Crete Island, Greece, Institute of Structural Analysis and Antiseismic Research School of Civil Engineering National Technical University of Athens (NTUA) Greece, 4467–4480.
- Di Re, P., Addessi, D., and Filippou, F. C. (2018). “Mixed 3D beam element with damage plasticity for the analysis of RC members under warping torsion.” *Journal of Structural Engineering*, 144(6), 04018064.
- Eads, L., Miranda, E., Krawinkler, H., and Lignos, D. G. (2013). “An efficient method for estimating the collapse risk of structures in seismic regions.” *Earthquake Engineering & Structural Dynamics*, 42(1), 25–41.
- El Jisr, H., Elkady, A., and Lignos, D. G. (2020). “Hysteretic behavior of moment-resisting frames considering slab restraint and framing action.” *Journal of Structural Engineering*, 146(8), 04020145.



- Elkady, A. (2016). "Collapse risk assessment of steel moment resisting frames designed with deep wide-flange columns in seismic regions." PhD Thesis, McGill University, Montreal, Quebec, Canada.
- Elkady, A., Ghimire, S., and Lignos, D. G. (2018). "Fragility curves for wide-flange steel columns and implications for building-specific earthquake-induced loss assessment." *Earthquake Spectra*, 34(3), 1405–1429.
- Elkady, A., Güell, G., and Lignos, D. G. (2020). "Proposed methodology for building-specific earthquake loss assessment including column residual axial shortening." *Earthquake Engineering & Structural Dynamics*, 49(4), 339–355.
- Elkady, A. and Lignos, D. G. (2015a). "Analytical investigation of the cyclic behavior and plastic hinge formation in deep wide-flange steel beam-columns." *Bulletin of Earthquake Engineering*, 13(4), 1097–1118.
- Elkady, A. and Lignos, D. G. (2015b). "Effect of gravity framing on the overstrength and collapse capacity of steel frame buildings with perimeter special moment frames." *Earthquake Engineering & Structural Dynamics*, 44(8), 1289–1307.
- Elkady, A. and Lignos, D. G. (2018a). "Full-scale testing of deep wide-flange steel columns under multiaxis cyclic loading: Loading sequence, boundary effects, and lateral stability bracing force demands." *Journal of Structural Engineering*, 10.1061/(ASCE)ST.1943-541X.0001937, 04017189.
- Elkady, A. and Lignos, D. G. (2018b). "Improved seismic design and nonlinear modeling recommendations for wide-flange steel columns." *Journal of Structural Engineering*, 10.1061/(ASCE)ST.1943-541X.0002166, 04018162.
- Engelhardt, M. D., Fry, G., Jones, S., Venti, M., and Holliday, S. (2000). "Behavior and design of radius-cut, reduced beam section connections." *Report No. SAC/BD-00/17*, SAC Joint Venture, a partnership of the Structural Engineers Association of California, Applied Technology Council, and California Universities for Research in Earthquake Engineering, Sacramento, California, USA.
- Farwell, C. R. and Galambos, T. V. (1969). "Nonuniform torsion of steel beams in inelastic range." *Journal of the Structural Division*, 95(12), 2813–2830.
- Fell, B. V., Kanvinde, A. M., Deierlein, G. G., and Myers, A. T. (2009). "Experimental investigation of inelastic cyclic buckling and fracture of steel braces." *Journal of Structural Engineering*, 135(1), 19–32.
- FEMA (2000). "State of the art report on connection performance." *Report No. 355D*, Federal Emergency Management Agency, Washington, DC, USA.

## Bibliography

---

- FEMA (2009). "Quantification of building seismic performance factors." *P-695*, Federal Emergency Management Agency, Washington, DC, USA.
- Fogarty, J. and El-Tawil, S. (2015). "Collapse resistance of steel columns under combined axial and lateral loading." *Journal of Structural Engineering*, 142(1).
- Fujimoto, M., Aoki, H., and Asaoka, F. (1978). "Influence of plastic strain history on mechanical properties of structural steels (Part 4. Discussion concerning strain aging, Bauschinger effect and yield locus)." *Transaction of the Architectural Institute of Japan*, 53(10).
- Galambos, T. V. (1998). *Guide to stability design criteria for metal structures*. John Wiley & Sons, New York, NY, USA, fifth edition.
- Galambos, T. V., Hajjar, J. F., Earls, C. J., and Gross, J. L. (1997). "Required properties of high-performance steels." *Report No. NIST IR 6004*, National Institute of Standards and Technology, Gaithersburg, MD, USA.
- Gallier, J. H. and Quaintance, J. (2020). *Linear algebra and optimization with applications to machine learning*. World Scientific, New Jersey.
- Gantes, C. J. and Fragkopoulos, K. A. (2010). "Strategy for numerical verification of steel structures at the ultimate limit state." *Structure and Infrastructure Engineering*, 6(1-2), 225–255.
- Gere, J. M. (2004). *Mechanics of materials*. Brooks/Cole-Thomson Learning, Belmont, CA, USA, 6th edition.
- Gioncu, V. and Petcu, D. (1997). "Available rotation capacity of wide-flange beams and beam-columns Part 1. Theoretical approaches." *Journal of Constructional Steel Research*, 43(1–3), 161–217.
- Grigoriou, V. and Lignos, D. G. (2017). "Characterization of the cyclic hardening properties of european steels." *Technical Report*, Resilient Steel Structures Laboratory (RESSLab), EPFL, Lausanne, Switzerland.
- Haaijer, G. (1956). "Local buckling of wf shapes in the plastic range." PhD. Thesis, Lehigh University, Bethlehem, Pennsylvania, USA.
- Haidemenopoulos, G. N. (2018). *Physical metallurgy: Principles and design*. CRC Press, Boca Raton, FL, USA.
- Hajjar, J. F., Schiller, P. H., and Molodan, A. (1998). "A distributed plasticity model for concrete-filled steel tube beam-columns with interlayer slip." *Engineering Structures*, 20(8), 663–676.

- Hall, E. O. (1970). *Yield point phenomena in metals and alloys*. Plenum Press, New York, NY, USA.
- Hartloper, A., de Castro e Sousa, A., and Lignos, D. G. (2019a). "Sensitivity of simulated steel column instabilities to plasticity model assumptions." *Proceedings of the 12th Canadian Conference on Earthquake Engineering*, Quebec City, QC, Canada, 8.
- Hartloper, A. R. (2019). "UVC\_MatMod: Updated Voce-Chaboche (UVC) material model for structural steels, <[https://github.com/ahartloper/UVC\\_MatMod](https://github.com/ahartloper/UVC_MatMod)> (22-10-2019).
- Hartloper, A. R. (2020). "WIKC: Warping-Inclusive Kinematic Coupling Definition and Pre-processing, <<https://github.com/ahartloper/WIKC>>.
- Hartloper, A. R. (2021). "BF-MPC: Best-fit multi-point constraint equations for mixed-dimension coupling of wide-flange cross sections." *GitHub*, <<https://github.com/ahartloper/bf-mpc>>.
- Hartloper, A. R., de Castro e Sousa, A., and Lignos, D. G. (2019b). "A nonlinear isotropic/kinematic hardening model for materials with discontinuous yielding." *Report No. 271062*, Resilient Steel Structures Laboratory (RESSLab), EPFL, Lausanne, Switzerland.
- Hartloper, A. R., de Castro e Sousa, A., and Lignos, D. G. (2021a). "Constitutive modeling of structural steels: Nonlinear isotropic/kinematic hardening material model and its calibration." *Journal of Structural Engineering*, 147(4), 04021031.
- Hartloper, A. R., de Castro e Sousa, A., and Lignos, D. G. (2021b). "Warping-inclusive kinematic coupling in mixed-dimension macro models for wide-flange beam-columns." *Journal of Structural Engineering*, (Under review).
- Hartloper, A. R. and Lignos, D. G. (2019). "Measurement and identification of imperfections in steel wide-flange cross-sections using point cloud data." *Report No. 264781*, Resilient Steel Structures Laboratory, École Polytechnique Fédérale de Lausanne (EPFL), Lausanne, Switzerland.
- Hassan, T. and Kyriakides, S. (1992). "Ratcheting in cyclic plasticity, Part I: Uniaxial behavior." *International Journal of Plasticity*, 8(1), 91–116.
- Hill, H. N. (1940). "Chart for critical compressive stress of flat rectangular plates." *Technical Note 773*, National Advisory Committee for Aeronautics, Langley Aeronautical Lab, Washington, D.C., USA.
- Ho, R. J., Meguid, S. A., and Sauve, R. G. (2004). "Novel coupling constraint technique for explicit finite element analysis." *International Journal of Computational Methods*, 1(02), 309–328.

## Bibliography

---

- Ho, R. J., Meguid, S. A., Zhu, Z. H., and Sauv , R. G. (2010). "Consistent element coupling in nonlinear static and dynamic analyses using explicit solvers." *International Journal of Mechanics and Materials in Design*, 6(4), 319–330.
- Hopperstad, O. S. and Remseth, S. (1995). "A return mapping algorithm for a class of cyclic plasticity models." *International Journal for Numerical Methods in Engineering*, 38(4), 549–564.
- Horn, B. K. P. (1987). "Closed-form solution of absolute orientation using unit quaternions." *Journal of the Optical Society of America A*, 4(4), 629.
- Hsiao, P.-C., Lehman, D. E., and Roeder, C. W. (2012). "Improved analytical model for special concentrically braced frames." *Journal of Constructional Steel Research*, 73, 80–94.
- Hu, F., Shi, G., and Shi, Y. (2018). "Constitutive model for full-range elasto-plastic behavior of structural steels with yield plateau: Formulation and implementation." *Engineering Structures*, 171, 1059–1070.
- Hughes, P. C. (2004). *Spacecraft Attitude Dynamics*. Dover Publications, Mineola, NY, USA.
- Ibarra, L. F. and Krawinkler, H. (2005). "Global collapse of frame structures under seismic excitations." *Report No. 152*, The John A. Blume Earthquake Engineering Research Center, Stanford University, Stanford, California, USA.
- Ibarra, L. F., Medina, R. A., and Krawinkler, H. (2005). "Hysteretic models that incorporate strength and stiffness deterioration." *Earthquake engineering & structural dynamics*, 34(12), 1489–1511.
- Imanpour, A., Tremblay, R., Davaran, A., Stoakes, C. D., and Fahnestock, L. A. (2016). "Seismic performance assessment of multitiered steel concentrically braced frames designed in accordance with the 2010 AISC seismic provisions." *Journal of Structural Engineering*, 142(12), 04016135.
- ISO (2019). "Metallic materials — Tensile testing — Part 1: Method of test at room temperature." *ISO 6892-1:2019*, International Organization for Standardization, Geneva, Switzerland.
- JISC (2014). "Dimensions, mass and permissible variations of hot rolled steel sections." *JIS G 3192:2014*, Japanese Standards Association (JSA), Tokyo, Japan.
- Jones, E., Oliphant, T., Peterson, P., et al. (2001–2018). "SciPy: Open source scientific tools for Python, <<http://www.scipy.org/>> (19-10-2018).
- Kalochairetis, K. E. and Gantes, C. J. (2011). "Numerical and analytical investigation of collapse loads of laced built-up columns." *Computers & Structures*, 89(11), 1166–1176.

- Kanno, R. (2016). "Advances in steel materials for innovative and elegant steel structures in Japan—A review." *Structural Engineering International*, 26(3), 242–253.
- Katayama, N., Anabuki, Y., and Fujimoto, Y. (1998). "Development of online hot profile gauge for accurate dimension of hot-rolling H-shapes." *Kawasaki Steel Giho*, 30(4).
- Kaufmann, E. J., Metrovich, B., and Pense, A. W. (2001). "Characterization of cyclic inelastic strain behavior on properties of A572 Gr. 50 and A913 Gr. 50 rolled sections." *Report No. 01-13*, ATLSS, Lehigh University, Bethlehem, Pennsylvania, USA.
- Kemp, A. R. (1985). "Interaction of plastic local and lateral buckling." *Journal of Structural Engineering*, 111(10), 2181–2196.
- Knezevic, D., Fakas, E., and Riber, H. J. (2019). "Predictive digital twins for structural integrity management and asset life extension – JIP concept and results." *SPE Offshore Europe Conference and Exhibition*, OnePetro (September).
- Koczubiej, S. and Cichoń, C. (2014). "Global static and stability analysis of thin-walled structures with open cross-section using FE shell-beam models." *Thin-Walled Structures*, 82, 196–211.
- Kolwankar, S., Kanvinde, A., Kenawy, M., Lignos, D., and Kunnath, S. (2018). "Simulating local buckling-induced softening in steel members using an equivalent nonlocal material model in displacement-based fiber elements." *Journal of Structural Engineering*, 144(10), 14.
- Kostic, S. M. and Filippou, F. C. (2012). "Section discretization of fiber beam-column elements for cyclic inelastic response." *Journal of Structural Engineering*, 138(5), 592–601.
- Krawinkler, H., Zareian, F., Medina, R. A., and Ibarra, L. F. (2006). "Decision support for conceptual performance-based design." *Earthquake Engineering & Structural Dynamics*, 35(1), 115–133.
- Krishnan, S. (2010). "Modified elastofiber element for steel slender column and brace modeling." *Journal of Structural Engineering*, 136(11).
- Lamarche, C.-P. and Tremblay, R. (2011). "Seismically induced cyclic buckling of steel columns including residual-stress and strain-rate effects." *Journal of Constructional Steel Research*, 67(9), 1401–1410.
- Lay, M. G. (1965). "Flange local buckling in wide-flange shapes." *Journal of the Structural Division*, 91(6), 94–116.
- Lay, M. G. and Galambos, T. V. (1967). "Inelastic beams under moment gradient." *Journal of the Structural Division*, 93(1), 381–391.

## Bibliography

---

- Le Corvec, V. (2012). "Nonlinear 3D frame element with multi-axial coupling under considerations of local effects." Ph.D. thesis, University of California, Berkeley, Berkeley, CA, USA.
- Lee, G. C. and Lee, E. T. (1994). "Local buckling of steel sections under cyclic loading." *Journal of Constructional Steel Research*, 29(1), 55–70.
- Lemaitre, J. and Chaboche, J.-L. (1990). *Mechanics of solid materials*. Cambridge University Press, Cambridge, UK.
- Liel, A. B., Haselton, C. B., Deierlein, G. G., and Baker, J. W. (2009). "Incorporating modeling uncertainties in the assessment of seismic collapse risk of buildings." *Structural Safety*, 31(2), 197–211.
- Lignos, D. G., Hartloper, A. R., Elkady, A., Deierlein, G. G., and Hamburger, R. O. (2019). "Proposed updates to the ASCE 41 nonlinear modeling parameters for wide-flange steel columns in support of performance-based seismic engineering." *Journal of Structural Engineering*, 145(9), 04019083.
- Lignos, D. G. and Krawinkler, H. (2011). "Deterioration modeling of steel components in support of collapse prediction of steel moment frames under earthquake loading." *Journal of Structural Engineering*, 137(11), 1291–1302.
- Lignos, D. G. and Krawinkler, H. (2013). "Development and utilization of structural component databases for performance-based earthquake engineering." *Journal of Structural Engineering*, 139(8), 1382–1394.
- Liu, H. (2016). "Modeling of frame structures undergoing large deformations and large rotations." PhD Thesis, Purdue University, West Lafayette, Indianapolis, USA.
- Lubliner, J. (2008). *Plasticity theory*. Dover, New York, NY, USA.
- Mahan, M., Dafalias, Y. F., Taiebat, M., Heo, Y., and Kunnath, S. K. (2011). "SANISTEEL: Simple anisotropic steel plasticity model." *Journal of Structural Engineering*, 137(2), 185–194.
- Mari, A. R. (1984). "Nonlinear geometric material and time dependent analysis of three dimensional reinforced and prestressed concrete frames." PhD Thesis, University of California, Berkeley, Berkeley, California, USA.
- Mathur, K., Fahnstock, L. A., Okazaki, T., and Parkolap, M. J. (2012). "Impact of residual stresses and initial imperfections on the seismic response of steel moment frames." *Journal of Structural Engineering*, 138(7), 942–951.

- McCune, R. W., Armstrong, C. G., and Robinson, D. J. (2000). "Mixed-dimensional coupling in finite element models." *International Journal for Numerical Methods in Engineering*, 49(6), 725–750.
- McKenna, F. T. (1997). "Object-oriented finite element programming: Frameworks for analysis, algorithms and parallel computing." Ph.D. thesis, University of California, Berkeley, Berkeley, CA, USA.
- Miyamura, T., Yamashita, T., Akiba, H., and Ohsaki, M. (2015). "Dynamic FE simulation of four-story steel frame modeled by solid elements and its validation using results of full-scale shake-table test." *Earthquake Engineering & Structural Dynamics*, 44(9), 1449–1469.
- Molinari, J. F. and Ortiz, M. (2002). "Three-dimensional adaptive meshing by subdivision and edge-collapse in finite-deformation dynamic-plasticity problems with application to adiabatic shear banding." *International Journal for Numerical Methods in Engineering*, 53(5), 1101–1126.
- Möller, M., Johansson, B., and Collin, P. (1997). "A new analytical model of inelastic local flange buckling." *Journal of Constructional Steel Research*, 43(1), 43–63.
- Monaghan, D. J., Doherty, I. W., Mc Court, D., and Armstrong, C. G. (1998). "Coupling 1D beams to 3D bodies." *Proceedings of the 7th International Meshing Roundtable*, Dearborn, Michigan, USA, Sandia National Lab.
- Mostafa, M. and Sivaselvan, M. (2014). "On best-fit corotated frames for 3D continuum finite elements." *International Journal for Numerical Methods in Engineering*, 98(2), 105–130.
- Neilsen, M. and Schreyer, H. (1993). "Bifurcations in elastic-plastic materials." *International Journal of Solids and Structures*, 30(4), 521–544.
- Newell, J. D. and Uang, C.-M. (2008). "Cyclic behavior of steel wide-flange columns subjected to large drift." *Journal of Structural Engineering*, 134(8).
- Nip, K., Gardner, L., Davies, C., and Elghazouli, A. (2010). "Extremely low cycle fatigue tests on structural carbon steel and stainless steel." *Journal of Constructional Steel Research*, 66(1), 96–110.
- NIST (2010). *Evaluation of the FEMA P-695 methodology for quantification of building seismic performance factors*. US Department of Commerce, Engineering Laboratory, National Institute of Standards and Technology, Gaithersburg, Maryland, USA.
- NIST (2011). "Research plan for the study of seismic behavior and design of deep, slender wide flange structural steel beam-column members." *Report No. NIST GCR 11-917-13*,

## Bibliography

---

- NEHRP Consultants Joint Venture, a partnership of the Applied Technology Council and the Consortium of Universities for Research in Earthquake Engineering for the National Institute of Standards and Technology, Gaithersburg, MD (December).
- NIST/ATC (2018). "ATC-106-1 beam column blind prediction contest, <<https://www.atcouncil.org/atc-106-blind-contest>> (30-09-2019).
- Ohno, N. (1982). "A constitutive model of cyclic plasticity with a nonhardening strain region." *Journal of Applied Mechanics*, 49(4), 721–727.
- Ozkula, G., Harris, J., and Uang, C.-M. (2017). "Observations from cyclic tests on deep, wide-flange beam-columns." *Engineering Journal*, 54(1), 45–59.
- Pi, Y. L. and Trahair, N. S. (1995). "Inelastic torsion of steel I-beams." *Journal of structural Engineering*, 121(4), 609–620.
- Rodrigues, O. (1840). "Des lois géométriques qui régissent les déplacements d'un système solide dans l'espace, et de la variation des coordonnées provenant de ces déplacements considérés indépendamment des causes qui peuvent les produire.." *Journal de mathématiques pures et appliquées*, 5, 62.
- Sadeghian, V., Kwon, O.-S., and Vecchio, F. (2018). "Modeling beam-membrane interface in reinforced concrete frames." *ACI Structural Journal*, 115(3).
- Schafer, B. W., Li, Z., and Moen, C. D. (2010). "Computational modeling of cold-formed steel." *Thin-Walled Structures*, 48(10), 752–762.
- Shim, K. W., Monaghan, D. J., and Armstrong, C. G. (2002). "Mixed dimensional coupling in finite element stress analysis." *Engineering with Computers; Heidelberg*, 18(3), 241–252.
- Sideris, P. and Salehi, M. (2016). "A gradient inelastic flexibility-based frame element formulation." *Journal of Engineering Mechanics*, 142(7).
- Simo, J. C. and Hughes, T. J. R. (1998). *Computational inelasticity*. Interdisciplinary applied mathematics. Springer-Verlag New York, Inc., New York, NY, USA.
- Simo, J. C. and Vu-Quoc, L. (1991). "A Geometrically-exact rod model incorporating shear and torsion-warping deformation." *International Journal of Solids and Structures*, 27(3), 371–393.
- Sivaselvan, M. and Reinhorn, A. M. (2000). "Hysteretic models for deteriorating inelastic structures." *Journal of Engineering Mechanics*, 126(6), 633–640.
- Sivaselvan, M. V. and Reinhorn, A. M. (2002). "Collapse analysis: Large inelastic deformations analysis of planar frames." *Journal of Structural Engineering*, 128(12), 1575–1583.



- Song, H. (2010). "Rigorous joining of advanced reduced-dimensional beam models to three-dimensional finite element models." PhD. Thesis, Georgia Institute of Technology, Atlanta, Georgia, USA.
- Sowerby, R., Uko, D., and Tomita, Y. (1979). "A review of certain aspects of the Bauschinger effect in metals." *Materials Science and Engineering*, 41(1), 43–58.
- Spacone, E., Filippou, F. C., and Taucer, F. F. (1996). "Fibre beam–column model for non-linear analysis of R/C frames: Part I. Formulation." *Earthquake Engineering & Structural Dynamics*, 25(7), 711–725.
- Sreenath, S., Saravanan, U., and Kalyanaraman, V. (2011). "Beam and shell element model for advanced analysis of steel structural members." *Journal of Constructional Steel Research*, 67(12), 1789–1796.
- Stoakes, C. D. and Fahnestock, L. A. (2016). "Strong-axis stability of wide flange steel columns in the presence of weak-axis flexure." *Journal of Structural Engineering*, 142(5), 04016004.
- Suzuki, T., Yoshida, Y., Shimura, Y., Suzuki, Y., Kubota, S., and Nagata, M. (2008). "Development of building structural steel with high yield ratio and high yield point leading to innovative steel structural system." *Report No. 97*, Nippon Steel, Tokyo, Japan.
- Suzuki, Y. (2018). "Earthquake induced collapse of steel moment resisting frames with conventional and high performance steel columns." Ph.D. thesis, McGill University, Montreal, QC, Canada.
- Suzuki, Y. and Lignos, D. G. (2015). "Large scale collapse experiments of wide flange steel beam-columns." *8th International Conference on Behaviour of Steel Structures in Seismic Areas*, Vol. 4, Shanghai, China.
- Suzuki, Y. and Lignos, D. G. (2020). "Development of collapse-consistent loading protocols for experimental testing of steel columns." *Earthquake Engineering & Structural Dynamics*, 49(2), 114–131.
- Suzuki, Y. and Lignos, D. G. (2021). "Experimental evaluation of steel columns under seismic hazard-consistent collapse loading protocols (In press)." *Journal of Structural Engineering*.
- Tada, M., Tamai, H., Ohgami, K., Kuwahara, S., and Horimoto, A. (2008). "Analytical simulation utilizing collaborative structural analysis system." *Proceedings of 14th World Conference on Earthquake Engineering*.
- Trahair, N. S. (1993). *Flexural-torsional buckling of structures*. CRC Press, Boca Raton, Florida, USA (July).

## Bibliography

---

- Ucak, A. and Tsopelas, P. (2011). "Constitutive model for cyclic response of structural steels with yield plateau." *Journal of Structural Engineering*, 137(2), 195–206.
- Vamvatsikos, D. and Cornell, C. A. (2002). "Incremental dynamic analysis." *Earthquake Engineering & Structural Dynamics*, 31(3), 491–514.
- Vamvatsikos, D. and Fragiadakis, M. (2010). "Incremental dynamic analysis for estimating seismic performance sensitivity and uncertainty." *Earthquake Engineering & Structural Dynamics*, 39(2), 141–163.
- Virtanen, P., Gommers, R., Oliphant, T. E., Haberland, M., Reddy, T., Cournapeau, D., Burovski, E., Peterson, P., Weckesser, W., Bright, J., van der Walt, S. J., Brett, M., Wilson, J., Millman, K. J., Mayorov, N., Nelson, A. R. J., Jones, E., Kern, R., Larson, E., Carey, C. J., Polat, İ., Feng, Y., Moore, E. W., VanderPlas, J., Laxalde, D., Perktold, J., Cimrman, R., Henriksen, I., Quintero, E. A., Harris, C. R., Archibald, A. M., Ribeiro, A. H., Pedregosa, F., van Mulbregt, P., and SciPy 1.0 Contributors (2020). "SciPy 1.0: Fundamental algorithms for scientific computing in Python." *Nature Methods*, 17, 261–272.
- Voce, E. (1948). "The relationship between stress and strain for homogeneous deformation." *Journal of the Institute of Metals*, 74, 537–562.
- Wagner, W. and Gruttmann, F. (2002). "Modeling of shell-beam transitions in the presence of finite rotations." *Computer Assisted Mechanics and Engineering Sciences*, 9(3), 405–418.
- Wahba, G. (1965). "A least squares estimate of satellite attitude." *SIAM Review*, 7(3), 409–409.
- Whyte, C. A., Mackie, K. R., and Stojadinovic, B. (2016). "Hybrid simulation of thermomechanical structural response." *Journal of Structural Engineering*, 142(2), 04015107.
- Wu, T.-Y., El-Tawil, S., and McCormick, J. (2018). "Seismic collapse response of steel moment frames with deep columns." *Journal of Structural Engineering*, 144(9), 04018145.
- Yoshida, F. and Uemori, T. (2002). "A model of large-strain cyclic plasticity describing the Bauschinger effect and workhardening stagnation." *International Journal of Plasticity*, 18(5), 661–686.
- Young, B. W. (1972). "Residual stresses in hot rolled members." *International Colloquium on Column Strength*, Vol. 23, Paris, France, International Association for Bridge and Structural Engineering, 25–38.
- Zareian, F. and Krawinkler, H. (2007). "Assessment of probability of collapse and design for collapse safety." *Earthquake Engineering & Structural Dynamics*, 36(13), 1901–1914.

- Ziemian, R. D. (2010). *Guide to stability design criteria for metal structures*. John Wiley & Sons, Inc., New Jersey, USA, sixth edition.
- Ziemian, R. D. and Abreu, J. C. B. (2018). "Design by advanced analysis – 3D benchmark problems." *Steel Construction*, 11(1), 24–29.
- Ziemian, R. D., Batista Abreu, J. C., Denavit, M. D., and Denavit, T.-J. L. (2018). "Three-dimensional benchmark problems for design by advanced analysis: Impact of twist." *Journal of Structural Engineering*, 144(04018220), 12.



# Alexander Hartloper | Curriculum Vitae

## PERSONAL INFORMATION

---

Name	Alexander Riley Hartloper
Citizenship	Canadian
Residence	Switzerland
E-mail	alexander.hartloper@epfl.ch

## EDUCATION

---

01.2017– 03.2021	<b>PhD Civil Engineering</b> EPFL, Lausanne, Switzerland <ul style="list-style-type: none"><li>Thesis: Reduced-order Models for Simulating Coupled Geometric Instabilities in Steel Beam-columns Under Inelastic Cyclic Straining</li><li>Supervisors: Prof. Dimitrios G. Lignos and Dr. Albano de Castro e Sousa</li><li>PhD defense date: 01.03.2021</li></ul>
09.2014– 02.2017	<b>MEng Civil Engineering</b> McGill University, Montreal QC, Canada <ul style="list-style-type: none"><li>Thesis: Updates to the ASCE-41-13 Nonlinear Modelling Procedures for Performance Based Seismic Assessment of New and Existing Steel Moment Resisting Frames</li><li>Supervisor: Prof. Dimitrios G. Lignos</li></ul>
09.2010– 05.2014	<b>BEng Civil Engineering</b> McGill University, Montreal QC, Canada <ul style="list-style-type: none"><li>Specialization in structural engineering</li></ul>

## TEACHING

---

### Course Lecturer

09.2016– 12.2016	<b>CIVE-460: Matrix Structural Analysis</b> McGill University, Montreal QC, Canada <ul style="list-style-type: none"><li>Undergraduate course; 26 students; 3 hours instruction per week; 13 weeks</li><li>Analysis of two and three dimensional frames, structural stability, introduction to finite element analysis</li></ul>
---------------------	---

### Teaching Assistant

09.2019– 01.2019	<b>CIVIL-449: Nonlinear Analysis of Structures</b> EPFL, Lausanne, Switzerland <ul style="list-style-type: none"><li>Graduate course; nonlinear modeling and analysis of structures for static and dynamic loading</li></ul>
02.2017– 07.2017	<b>CIVIL-369: Structural Stability</b> EPFL, Lausanne, Switzerland <ul style="list-style-type: none"><li>Undergraduate course; column and frame stability, lateral-torsional buckling, stability in design codes</li></ul>
01.2015/2016– 04.2015/2016	<b>CIVE-205: Statics</b> McGill University, Montreal QC, Canada <ul style="list-style-type: none"><li>Undergraduate course; equilibrium, force and moment diagrams, centroids and moments of inertia</li></ul>
09.2014/2015– 12.2014/2015	<b>CIVE-460: Matrix Structural Analysis</b> McGill University, Montreal QC, Canada <ul style="list-style-type: none"><li>Undergraduate course; frame analysis, structural stability, introduction to finite element analysis</li></ul>

### Supervision of Junior Researchers

09.2020– 01.2021	<b>Masters Project Advisor</b> EPFL, Lausanne, Switzerland <ul style="list-style-type: none"><li>Student: Selimcan Ozden</li><li>Project: Experimental characterization of cyclic properties of mild European steel materials</li></ul>
02.2017– 07.2020	<b>Masters Level Semester Projects</b> EPFL, Lausanne, Switzerland

- Fundamental Understanding of Structural Stability Using Educational Tools
- Mentoring and evaluation for 2–4 students/semester; 2 hours/week; 14 weeks

09.2018–  
01.2019

#### **Masters Thesis Advisor**

EPFL, Lausanne, Switzerland

- Student: Diego Heredia Rosa
- Thesis: Experimental Behavior and Nonlinear Modeling of Iron-based Shape Memory Alloys (SMAs) Under Inelastic Cyclic Straining

02.2017–  
07.2017

#### **Masters Thesis Advisor**

EPFL, Lausanne, Switzerland

- Student: Valentine Declerck
- Thesis: Steel Frame Buildings Subjected to Multi-Hazards: Nonlinear Modeling and Risk Assessment

### **Interactive Learning Seminars**

07.2017/2018  
07.2019

#### **Design a Seismic Resistant Building**

EPFL, Lausanne, Switzerland

- Annual afternoon seminar given to high school students from the Gymnasium Lerbermatt-Köniz
- Incorporated hands-on activities and basic physics to teach the fundamental principles of structural engineering

### **OTHER EXPERIENCE**

---

01.2019–  
Present

#### **Development of Open-source Engineering Tools**

Work centralized at <https://github.com/ahartloper>

- Contributor to the OpenSees project (C++)
- Co-developer of the RESSPyLab package (Python)
- Developer of various user subroutines for Abaqus finite element simulation platform (Fortran)

05.2015–  
07.2016

#### **Working Group Member**

Applied Technology Council (ATC), Redwood City CA, USA

- Contributed to the NIST GCR 17-917-45 report “Recommended Modeling Parameters and Acceptance Criteria for Nonlinear Analysis in Support of Seismic Evaluation, Retrofit, and Design” as a part of the ATC-114 project for steel moment-resisting frames

### **AWARDS**

---

#### **2018 NIST-ATC Blind Prediction Contest on Deep, Wide-flange Structural Steel Beam-Columns**

National Institute of Standards and Technology (NIST) and Applied Technology Council (ATC), USA

- First place award (Phases I and II) in comprehensive category of the international blind analysis competition

#### **2016 Graduate Excellence Fellowship**

Department of Civil Engineering and Applied Mechanics, McGill University, Montreal QC, Canada

- Value of 3422 CAD

### **REFEREED JOURNAL PUBLICATIONS**

---

- J8. **Hartloper, A. R.**, de Castro e Sousa, A., Lignos, D. G. (n.d.). Mixed-dimension Modeling of Steel Wide Flange Beam-columns Under Multiaxis Loading, Journal of Construction Steel Research (In preparation).
- J7. **Hartloper, A. R.**, de Castro e Sousa, A., Lignos, D. G. (n.d.). Best-fit Constraint Equations for Coupling Mixed-dimension Simulation Models with Wide Flange Cross Sections, Finite Elements in Analysis and Design (In preparation).
- J6. **Hartloper, A. R.**, de Castro e Sousa, A., Lignos, D. G. (n.d.). Warping-inclusive Kinematic Coupling In Mixed-dimension Macro Models for Steel Wide-flange Beam-columns, Journal of Structural Engineering (Under review).
- J5. de Castro e Sousa, A., **Hartloper, A. R.**, Lignos, D. G. (2021). Cyclic Metal Plasticity Model Parameters with Limited Information: A Constrained Optimization Approach, Journal of Engineering Mechanics (In press). [https://doi.org/10.1061/\(ASCE\)EM.1943-7889.0001922](https://doi.org/10.1061/(ASCE)EM.1943-7889.0001922).
- J4. **Hartloper, A. R.**, de Castro e Sousa, A., Lignos, D. G. (2021). Constitutive Modeling of Structural Steels: Nonlinear Isotropic/kinematic Hardening Material Model and Its Calibration, Journal of Structural Engineering. [https://doi.org/10.1061/\(ASCE\)ST.1943-541X.0002964](https://doi.org/10.1061/(ASCE)ST.1943-541X.0002964).

- J3. Heredia Rosa, D., **Hartloper, A. R.**, de Castro e Sousa, A., Lignos, D. G., Motavalli, M, Ghafoori, E. (2021). Experimental Behavior of Iron-based Shape Memory Alloys under Cyclic Loading Histories, *Construction and Building Materials*. <https://doi.org/10.1016/j.conbuildmat.2020.121712>.
- J2. Lignos, D. G., **Hartloper, A. R.** (2020). Steel Column Stability and Implications in the Seismic Assessment of Steel Structures According to Eurocode 8 Part 3, *Stahlbau*. <https://doi.org/10.1002/stab.201900108>.
- J1. Lignos, D. G., **Hartloper, A. R.**, Elkady, A., Deierlein, G. G., Hamburger R. (2018). Proposed Updates to the ASCE 41 Non-linear Modeling Parameters for Wide-Flange Steel Columns in Support of Performance-Based Seismic Engineering, *Journal of Structural Engineering* 145(9), 04019083. [https://doi.org/10.1061/\(ASCE\)ST.1943-541X.0002353](https://doi.org/10.1061/(ASCE)ST.1943-541X.0002353)

#### REFEREED CONFERENCE PUBLICATIONS

---

- C5. Heredia Rosa, D., **Hartloper, A. R.**, de Castro e Sousa, A., Lignos, D. G., Motavalli, M, Ghafoori, E. (2019). Behavior of iron-based Shape Memory Alloys under Cyclic Loading Histories, 5th Conference on Smart Monitoring, Assessment and Rehabilitation of Civil Structures. <https://infoscience.epfl.ch/record/270238>
- C4. **Hartloper, A. R.**, de Castro e Sousa, A., Lignos, D. G. (2019). Sensitivity of Simulated Steel Column Instabilities to Plasticity Model Assumptions, 12th Canadian Conference on Earthquake Engineering. <https://infoscience.epfl.ch/record/267788>
- C3. Lignos, D. G., **Hartloper, A. R.**, Elkady A., Hamburger, R., and Deierlein, G.G. (2018). Revised ASCE-41 Modeling Recommendations for Moment-resisting Frame Systems, 11th U.S. National Conference on Earthquake Engineering. <https://infoscience.epfl.ch/record/255739>
- C2. **Hartloper, A. R.**, Lignos, D. G. (2017). Updates to the ASCE-41-13 Provisions for the Nonlinear Modeling of Steel Wide-Flange Columns for Performance-based Earthquake Engineering, Eurosteel 2017. <https://doi.org/10.1002/cepa.359>
- C1. Lignos, D. G., Elkady A., Suzuki, Y., **Hartloper, A. R.** (2017). Experimental and Numerical Evaluation of Steel Columns for Performance-Based Seismic Assessment of Steel Moment Frames, International Workshop on Performance-Based Seismic Design of Structures. <https://infoscience.epfl.ch/record/231877>